证明材料目录

附件一 已发表论文证明材料

论文 1：Unlocking high photosensitivity direct laser writing and observing atomic clustering in glass （共一）

nature communications

Article

https://doi.org/10.1038/s41467-024-52628-4

Unlocking high photosensitivity direct laser writing and observing atomic clustering in glass

Received: 23 September 2023

Accepted: 17 September 2024

Published online: 27 September 2024

Check for updates

Wenyan Zheng[1], Zhuo Wang[2], Weilin Chen[1], Mengchao Zhang[3], Hui Li[3], Guang Yang[3], Qiang Xu[4], Xvsheng Qiao[1] ✉, Dezhi Tan[1,5] ✉, Junjie Zhang[6], Jianrong Qiu[2], Guodong Qian[1] & Xianping Fan[1]

The direct laser writing (DLW) of photoluminescent metal clusters is inspiring intensive research in functional glasses. However, understanding the influence of the host structure on cluster formation and visualizing DLW-induced clusters at the atomic scale remains challenging. In this work, we develop a highly photosensitive fluorophosphate glass through fluorine incorporation. The addition of fluorine establishes a conducive environment for Ag^+ ions before DLW and enhances the availability of reducing agents and diffusion pathways during DLW. These advantages facilitate the formation of Ag clusters under low-energy single-pulsed DLW. Increasing laser energy results in a combination of Ag clusters and glasses defect, forming a dot + ring photoluminescent pattern. Atom probe tomography (APT), a technique capable of mapping the elemental spatial distribution and identifying clustering, is employed to gain more information on laser-induced clusters. Comparison of APT results between samples without and with DLW reveals the formation of Ag clusters after laser writing. The design concept and characterization enrich the understanding of Ag cluster behavior in glasses. This knowledge opens the possibility of rational design of clusters confined in glasses and inspires their synthesis for various applications.

Direct Laser Writing (DLW) enables precise modifications of transparent materials such as polymer[1], sapphire[2], and glass[3]. This capability allows for the creation of customized 3D microstructures with tailored properties, providing a versatile platform for material engineering and optical device fabrication. Among applications, there is a growing interest in fabricating silver nanoclusters (Ag NCs) inside glass for high-capacity optical data storage (ODS). Consisting of several to tens of atoms, Ag NCs exhibit bright photoluminescence (PL) due to the quantum confinement effect[4,5]. In ODS, DLW is applied to inscribe Ag NCs, with each inscribed PL dot serving as an information recording unit[6]. By tailoring the DLW parameters such as laser energy, duration, and pulse count, tunable PL intensity and multiple grayscales storage can be achieved[7].

Along with laser parameters, the choice of glass matrix also influences ODS performance. An ideal glass for storage application is expected to facilitate the generation of Ag NCs at low energy to reduce writing energy consumption and should be compatible with single-pulse laser processing to enhance the data writing efficiency[8]. The earliest literature on this topic can be traced back to the year 2010[9], subsequent research has mainly focused on refining the DLW

[1]State Key Laboratory of Silicon Materials & School of Materials Science and Engineering, Zhejiang University, Hangzhou, China. [2]State Key Laboratory of Modern Optical Instrumentation College of Optical Science and Engineering, Zhejiang University, Hangzhou, China. [3]School of Materials Science and Engineering, Shanghai University, Shanghai, China. [4]Ocean Academy, Zhejiang University, Zhoushan, China. [5]Zhejiang Lab, Hangzhou, China. [6]College of Optical and Electronic Technology, China Jiliang University, Hangzhou, China. ✉e-mail: qiaoxus@zju.edu.cn; wctdz@zju.edu.cn

Acknowledgements

W.Z. and Z.W. contributed equally to this work. We acknowledge the financial support from the National Natural Science Foundation of China (No. 52172008; 51672243), the Postdoctoral Fellowship Program of CPSF (GZC20241465).

图 1：论文 1 首页

论文 2：3D imprinting of voxel-level structural colors in lithium niobate crystal

RESEARCH ARTICLE

Editor's Choice

ADVANCED MATERIALS
www.advmat.de

3D Imprinting of Voxel-Level Structural Colors in Lithium Niobate Crystal

Zhuo Wang, Bo Zhang, Ziquan Wang, Jie Zhang, Peter G Kazansky, Dezhi Tan,* and Jianrong Qiu**

Advanced coloration methods are of pivotal importance in science, technology, and engineering. However, 3D structural colors that are critical for emerging multidimensional information representation and recording are rarely achievable. Here, a facile voxel-level programmable 3D structural coloration in the bulk lithium niobate ($LiNbO_3$) crystal is reported. This is achieved by engineering wavelength-selective interference between ordinary (O) and extraordinary (E) light in the crystal matrix. To induce effective phase contrast between O and E light for establishing the highly localized interference across the visible band, the presence of a pulse-internal-coupling effect is revealed in the single-pulse ultrafast laser–crystal interaction and an ultrafast-laser-induced micro-amorphization (MA) strategy is thus developed to manipulate local matrix structure. Consequently, micro–nanoscale colorful voxels can be fast inscribed into any spatial position of the crystal matrix in one step. It is demonstrated that the colors can be flexibly manipulated and quickly extracted in 3D space. Multidimensional MA-color data storage with large capacity, high writing and readout speed, long lifetime, and excellent stability under harsh conditions is achieved. The present principle enables multifunctional 3D structural coloration devices inside high-refractive-index transparent dielectrics and can serve as a general platform to innovate next-generation information optics.

1. Introduction

Structural colors originated from the interaction between the polychromatic light and micro–nano photonic structures have been created for various applications in high-resolution optical display, sensing, anti-counterfeiting, information encryption, and recording.[1–6] However, the current structural colors are generally displayed in 2D substrates.[7–9] Although complex bulk photonic crystals have recently been designed to generate quasi 3D colors,[10–12] the color voxels are largely interconnected rather than independent and the spatial extent of coloration is limited to a small scale close to surfaces. Freely imprinting voxel-level controllable structural colors in 3D space enables implanting additional degrees of freedom in light modulation and device functionalization, such as 3D display and high-density data storage. However, due to the lack of a suitable carrier, this vision remains highly challenging and even impossible via traditional coloration approaches.

One way to solve this problem is to develop a principle that can print color voxels in 3D transparent media. Recently, ultrafast laser direct writing (ULDW) in transparent dielectrics has been established as an excellent platform for creating 3D micro–nano functional structures,[13–20] which endows matrix materials with unprecedented functionalities. Representatively, domain engineering at micro–nano scales using ULDW in lithium niobate ($LiNbO_3$) crystals has been used to produce 3D nonlinear photonic crystals.[21–25] However, structural coloration is extremely difficult to generate inside such media, because the high refractive index of the matrix severely impairs the phase modulation capability of photonic structures. Generally, transparent

Z. Wang, B. Zhang, Z. Wang, J. Zhang, J. Qiu
State Key Laboratory of Modern Optical Instrumentation
College of Optical Science and Engineering
Zhejiang University
Hangzhou 310027, China
E-mail: zhangbobo@zju.edu.cn; qjr@zju.edu.cn
P. G Kazansky
Optoelectronics Research Centre
University of Southampton
Southampton SO17 1BJ, UK

D. Tan
Zhejiang Lab
Hangzhou 311100, China
E-mail: wctdz@zju.edu.cn
D. Tan
School of Material Science and Engineering
Zhejiang University
Hangzhou 310027, China
J. Qiu
CAS Center for Excellence in Ultra-intense Laser Science
Chinese Academy of Sciences
Shanghai 201800, China

The ORCID identification number(s) for the author(s) of this article can be found under https://doi.org/10.1002/adma.202303256

DOI: 10.1002/adma.202303256

图 2：论文 2 首页

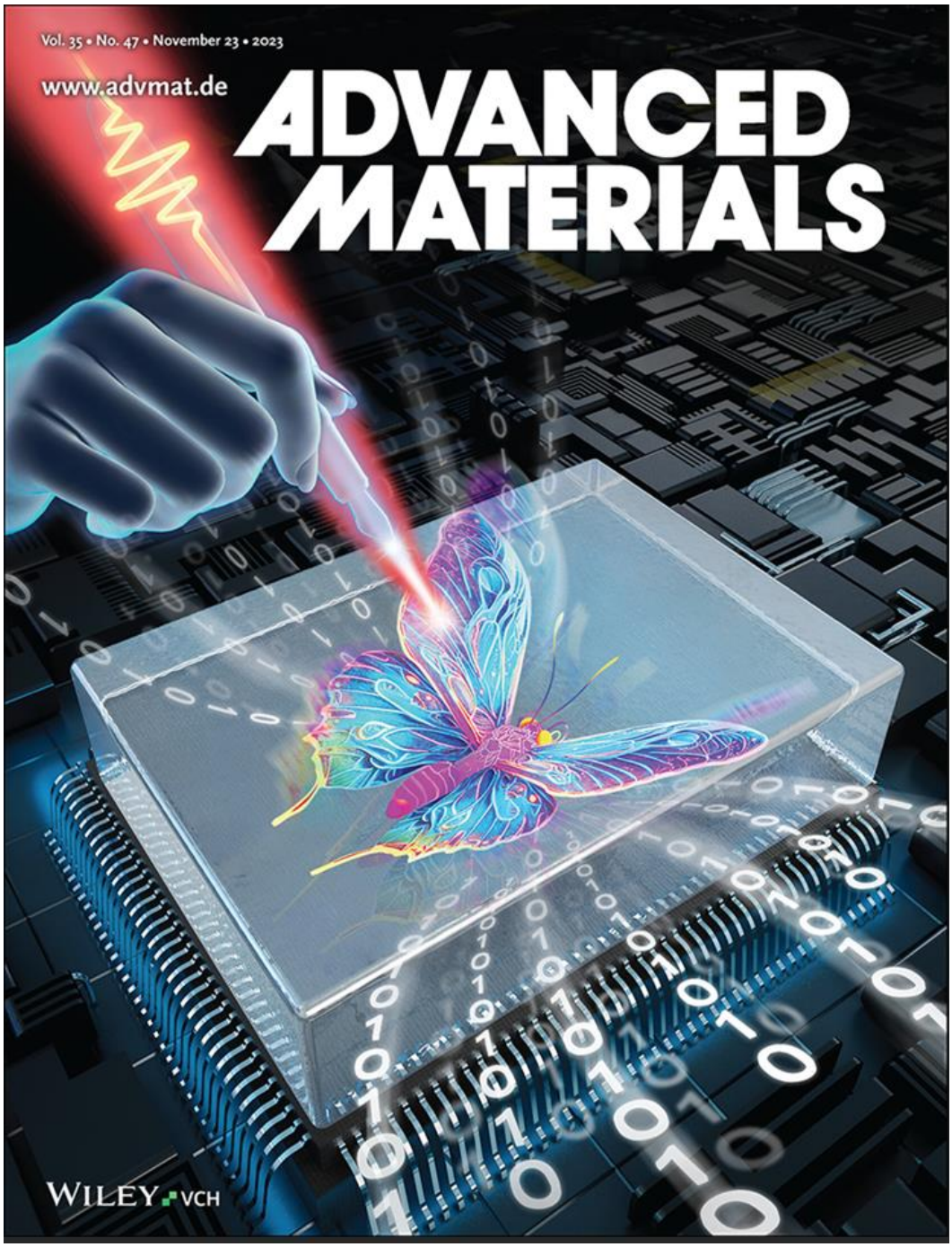

Research Articles

Editor's Choice

3d imprinting of Voxel-Level Structural Colors in Lithium Niobate Crystal

Zhuo Wang, Bo Zhang, Ziquan Wang, Jie Zhang, Peter G Kazansky, Dezhi Tan, Jianrong Qiu

2303256 | First Published: 30 June 2023

https://doi.org/10.1002/adma.202303256

Abstract | PDF

图 3：论文 2 获选期刊封面和主编推荐

论文 3：Ostensibly perpetual optical data storage in glass with ultra-high stability and tailored photoluminescence

Opto-Electronic Advances

Article

January 2023, Vol. 6, No. 1

DOI: 10.29026/oea.2023.220008

Ostensibly perpetual optical data storage in glass with ultra-high stability and tailored photoluminescence

Zhuo Wang[1†], Bo Zhang[1†], Dezhi Tan[2*] and Jianrong Qiu[1,3*]

Long-term optical data storage (ODS) technology is essential to break the bottleneck of high energy consumption for information storage in the current era of big data. Here, ODS with an ultralong lifetime of 2×10^7 years is attained with single ultrafast laser pulse induced reduction of Eu^{3+} ions and tailoring of optical properties inside the Eu-doped aluminosilicate glasses. We demonstrate that the induced local modifications in the glass can stand against the temperature of up to 970 K and strong ultraviolet light irradiation with the power density of 100 kW/cm². Furthermore, the active ions of Eu^{2+} exhibit strong and broadband emission with the full width at half maximum reaching 190 nm, and the photoluminescence (PL) is flexibly tunable in the whole visible region by regulating the alkaline earth metal ions in the glasses. The developed technology and materials will be of great significance in photonic applications such as long-term ODS.

Keywords: ultrafast laser; photoluminescence tailoring; ultralong lifetime; optical data storage

Wang Z, Zhang B, Tan DZ, Qiu JR. Ostensibly perpetual optical data storage in glass with ultra-high stability and tailored photoluminescence. *Opto-Electron Adv* **6**, 220008 (2023).

Introduction

In the development history of human society, data storage plays an indispensable and pivotal role, it has significantly boosted spacious domains from social science to industrial production. With the advent of the Internet of Things and artificial intelligence, the long lifetime and large capacity of information storage are in increasingly high demand. Accordingly, optical data storage (ODS) technique provides a highly fascinating alternative to conventional storage techniques (semiconductor or magnetic-based storage) with lower energy consumption, larger capacity, higher efficiency, and longer lifetime[1–5]. However, accounting for 80% of the total stored data generated by the government, data disaster recovery centers, and archives are not frequently accessed but still need to be available over long periods in an easy access method. The typical lifetime of mature ODS is hundreds of years that is still far from meeting the requirements of next-generation information storage[6–8]. Although the ODS based on ultrafast laser induced volume periodic structures has an ultralong lifetime, multipulse irradiation with the pulse energy up to micro-joule is necessary for writing, which will slow down the writing speed and increase the power consumption[9]. Developing long-term stable ODS based on single pulse writing process can not only notably reduce the energy dissipation

[1]State Key Laboratory of Modern Optical Instrumentation, and College of Optical Science and Engineering, Zhejiang University, Hangzhou 310027, China; [2]Zhejiang Lab, Hangzhou 311100, China; [3]CAS Center for Excellence in Ultra-intense Laser Science, Chinese Academy of Sciences, Shanghai 201800, China.

[†]These authors contributed equally to this work.

*Correspondence: DZ Tan, E-mail: wctdz@zju.edu.cn; JR Qiu, E-mail: qjr@zju.edu.cn

Received: 13 January 2022; Accepted: 26 March 2022; Published online: 31 August 2022

图 4：论文 3 首页

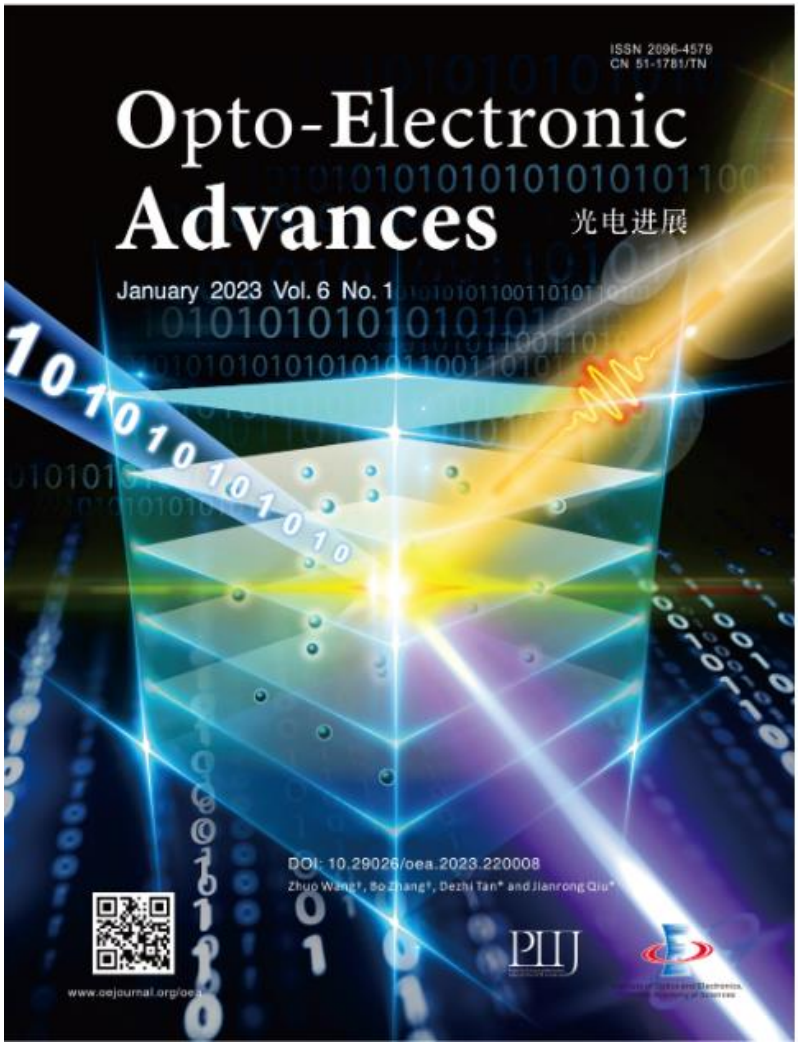

2023年度阅读量TOP 5论文

Opto-Electonic Advances

TOP 1

Ostensibly perpetual optical data storage in glass with ultra-high stability and tailored photoluminescence

作者：Zhuo Wang, Bo Zhang, Dezhi Tan*（谭德志）, Jianrong Qiu*（邱建荣）

Opto-Electron Adv 6, 220008 (2023)

最受欢迎奖

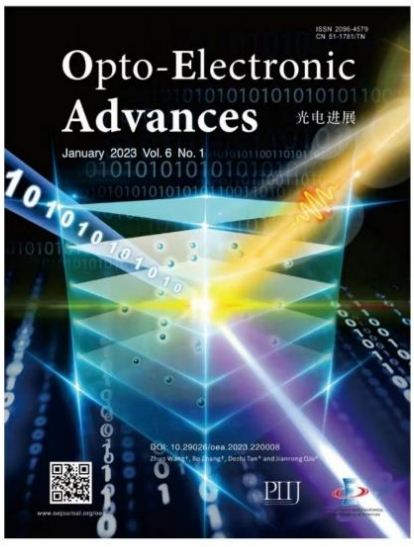

图 5：论文 3 获选期刊封面、年阅读量最高论文和最受欢迎期刊封面

论文 4：Single-pulse-driven frame printing of chromatic pixels in lithium niobate crystal（共一）

RESEARCH ARTICLE

LASER & PHOTONICS REVIEWS

www.lpr-journal.org

Single-Pulse-Driven Frame Printing of Chromatic Pixels in Lithium Niobate Crystal

Jie Zhang, Zhuo Wang, Bo Zhang, and Jianrong Qiu**

Highly efficient and programmable writing of multidimensional optical data is of great value for next-generation high-throughput information technologies but has been rarely achieved. Here, a one-step frame printing of chromatic pixels in lithium niobate crystal by using a single ultrafast laser pulse is reported. In this strategy, a phase superposition-based spatial light modulation strategy is applied to split a single ultrafast laser pulse into multiple son pulses with designated optical properties and spatial distribution patterns. It is demonstrated that these son pulses allow for massively creating micro-amorphous phase transition zones with on-demand structural features that can modulate the intrinsic birefringence of the crystal matrix and generate wavelength-selective interference in the visible band to form pixel-level chromatic patterns, namely, single-pulse-driven frame color printing. The created chromatic pixels can be encoded into computer-recognizable data arrays to play a role in high-efficiency multidimensional information recording. The presented approach enables fast and programmable information batch writing in 3D space and can serve as a versatile tool boosting next-generation information optics.

1. Introduction

The vast majority of information that human beings get from the outside world is transmitted through light where the optical frequency, which can be identified as color by eyes or detectors, is an important information dimension.[1–5] Recently, structural colors that arise from the interference, diffraction, and scattering behaviors of light when interacting with micro-nano structures,[6–11] have been fast-developing and attracted tremendous attention as they lie at the fundamental position in boosting the development of advanced optical display,[12] information recording,[13] sensing,[14] detecting,[15] encryption,[16] and anti-counterfeiting.[17] In principle, the generation of structural colors relies on the optical modulation of illumination polychromatic light by wavelength-scale photonic structures, with each color corresponding to a specific structural feature.[18–21] The generation of pixel-level structural colors that are especially valuable in information optics therefore requires the production of various photonic structural modules,[22–24] where a set of processing parameters generally enables the fabrication of only one structural feature, resulting in the presentation of only one kind of color (**Figure 1a**). Such a one-to-one coloration mode greatly limits the information writing efficiency, as it generally requires frequent adjustment of laser and writing parameters, which will overload the laser and mechanical servo systems. Besides, the spatial scope of pixel-level color printing is largely limited to a 2D plane or near surfaces. 3D embedded micro-nano structures allow for effectively utilizing the vertical spatial dimension and favorable properties of substrates, implanting additional degrees of freedom in light modulation and photonic device functionalization.[25–28] However, a highly efficient structural coloration that enables massively printing multiple chromatic pixels at designated 3D spatial locations with one set of processing parameters has not been achieved.

The key to breaking through this bottleneck lies in the development of a novel one-to-many coloration approach that enables parallel fabricating light modulation structures in 3D space. At present, it is extremely difficult to achieve this goal by relying on conventional micro-nano machining technologies, as they generally require cumbersome processes. Recently, the ultrafast laser has shown great superiority in creating embedded micro-nano photonic structures in various transparent media because of its highly efficient and versatile nonlinear material modification capacity.[29–35] In theory, it is possible to engineer ultrafast laser pulses and manipulate them to fast inscribe desired light modulation structures in a transparent medium, achieving the efficient generation of 3D colors.

Here, we report on a single ultrafast laser pulse-driven frame coloration strategy that enables fast one-to-many production of multiple chromatic pixels in 3D space (Figure 1b). This proposal is built upon two of our pivotal research foundations.[36] First, single-pulse ultrafast laser-induced micro-amorphous phase transition (MAPT) in lithium niobate ($LiNbO_3$) can locally modulate the phase difference of O and E light beams that propagate in the crystal matrix and establish wavelength-selective interference in 3D space by using chromatic polarization effect, namely, pixel-level structural colors. Second, the interference colors can

J. Zhang, Z. Wang, B. Zhang, J. Qiu
State Key Laboratory of Modern Optical Instrumentation
College of Optical Science and Engineering
Zhejiang University
Hangzhou 310027, China
E-mail: zhangbob@zju.edu.cn; qjr@zju.edu.cn

The ORCID identification number(s) for the author(s) of this article can be found under https://doi.org/10.1002/lpor.202400054

DOI: 10.1002/lpor.202400054

Author Contributions

J.Z. and Z.W. contributed equally to this work. J.Z. and B.Z. conceived the idea. J.Q. and B.Z. organized, coordinated, and supervised the project. J.Z. and Z.W. performed the experiments and collected the data. J.Z., Z.W., B.Z., and J.Q. interpreted the results and proposed the color frame printing method. J.Z. and B.Z. wrote the manuscript. J.Z., Z.W., B.Z., and J.Q. discussed and revised the manuscript.

图 6：论文 4 首页

论文5：Long-term optical information storage in glass with ultraviolet-light-preprocessing-induced enhancement of the signal-to-noise ratio

Letter Vol. 46, No. 16 / 15 August 2021 / Optics Letters 3937

Optics Letters

Long-term optical information storage in glass with ultraviolet-light-preprocessing-induced enhancement of the signal-to-noise ratio

ZHUO WANG,[1] BO ZHANG,[1] DEZHI TAN,[2,*] AND JIANRONG QIU[1,2,4]

[1]State Key Laboratory of Modern Optical Instrumentation, College of Optical Science and Engineering, Zhejiang University, Hangzhou 310027, China
[2]Zhejiang Lab, Hangzhou 311100, China
[3]CAS Center for Excellence in Ultra-intense Laser Science, Chinese Academy of Sciences, Shanghai, 201800, China
[4]e-mail: qjr@zju.edu.cn
*Corresponding author: wctdz@zju.edu.cn

Received 8 June 2021; revised 14 July 2021; accepted 14 July 2021; posted 14 July 2021 (Doc. ID 433674); published 9 August 2021

This Letter describes the realization of long-term optical information storage in glass using an enhanced signal-to-noise ratio (SNR). We show that the photo-oxidation of Eu^{2+} ions in the glass matrix induced by ultraviolet light suppresses background signals, thereby enhancing by tenfold the SNR of Eu^{2+} ions photoluminescence (PL) of the dots written by a femtosecond (fs) laser. Thus, smaller dots exhibiting weak PL emission can be detected. In addition, the stored information shows excellent stability under the light irradiation with the power density up to 240 W/cm^2. Accelerated-aging experiments indicate that the stored data can retain stability for more than 115 years at room temperature. The optical storage capacity is approximately 270 Gbit cm^{-3}. This technique enables long-term, high-capacity data storage in glass media.

https://doi.org/10.1364/OL.433674

Over the past two decades, there has been an increasing demand for secure and stable storage of large amounts of information for a long period of time (typically longer than 100 years) [1–6]. Optical storage provides a fascinating alternative to conventional semiconductor- or magnetic-based storage owing to its advantages, including long lifetime [7,8], superb stability [2,9], high storage density [4,8,10], fast speed [11], and low cost [1]. For the traditional non-optical information storage techniques, the stability term is usually shorter than 50 years [12]. Recently, femtosecond (fs) laser-induced modifications in transparent solids, such as refractive index change [13,14], selective precipitation of nanocrystals [9,15–17], regulation of ion valence [18–20], and formation of nanogratings [7,21,22] have been proposed to be useful for three-dimensional or even five-dimensional optical storage with high performance. Generally, glass provides an ideal matrix to stabilize the embedded structural modifications, as well as the stored optical information. For example, the lifetime of nanogratings in silica glass spans seemingly over 3×10^{20} years [7]. However, the lifetime of other structural changes induced by fs laser in glass has not been determined, which is critical for realizing applications of fs laser writing in long-term optical storage.

Three-dimensional optical memory applications always require a high signal-to-noise ratio (SNR), referring to the ratio of photoluminescence (PL) intensity of the written dots to the noise intensity of the storage media (e.g., glass), to decrease the bit error rate (BER) when reading the stored data. In fact, a low SNR could be one of the main issues that limit the recording capacity, reading accuracy, and reading speed of optical memory. Typically, the SNR worsens after long-term storage. Furthermore, there may be a noise signal from the matrix, which would lead to a reduction in SNR and an increase in BER. For example, modifying the valence of active ions, such as the reduction of Eu^{3+} ions in glass by using fs laser irradiation is established as an effective strategy to record optical information [23,24]. However, partially active Eu^{3+} ions doped in glass could also be changed to Eu^{2+} ions during the high-temperature glass preparation process [25–28], which is detrimental to the SNR in ion valence modulation-mediated optical storage. As a result, reducing the noise signal from Eu^{2+} ions in the area without fs laser irradiation is of great importance, not only for improving the SNR and decreasing the BER, but also for reading smaller dots in high-capacity storage.

Here, we propose enhancing the SNR by tenfold in Eu^{3+}-doped sodium aluminoborate glass for long-term optical storage. Information can be written in the glass by a single fs laser pulse that induces the reduction of Eu^{3+} to Eu^{2+}, while ultraviolet (UV)-light pre-irradiation has been demonstrated to significantly suppress the background signal from Eu^{2+} around the written dots in the glass matrix. Furthermore, accelerated aging demonstrated that the stored data remain stable for more than 115 years at room temperature. The optical storage capacity is approximately 270 Gbit cm^{-3}. Thus, the combination of UV-light preprocessing and fs laser writting allows for long-term stable optical information storage with a high SNR.

The Eu^{3+}-doped sodium aluminoborate glass used in this study was fabricated with a stoichiometric composition (in mol %) of 85 B_2O_3 – 5 Al_2O_3 – 10 Na_2O – 0.1 Eu_2O_3 via

图 7：论文 5 首页

论文 6：Single-shot photon recording for three-dimensional memory with prospects of high capacity

6274 Vol. 45, No. 22 / 15 November 2020 / Optics Letters Letter

Optics Letters

Single-shot photon recording for three-dimensional memory with prospects of high capacity

ZHUO WANG,[1] DEZHI TAN,[1,*] AND JIANRONG QIU[1,2]

[1]State Key Laboratory of Modern Optical Instrumentation, College of Optical Science and Engineering, Zhejiang University, Hangzhou 310027, China
[2]e-mail: qjr@zju.edu.cn
*Corresponding author: wctdz@zju.edu.cn

Received 2 September 2020; revised 10 October 2020; accepted 14 October 2020; posted 14 October 2020 (Doc. ID 409171); published 12 November 2020

Femtosecond laser-induced modification in the glass has drawn considerable interest due to its widespread superiority in the applications of three-dimensional optical storage. In this Letter, we report that a single pulse could be used in optical memory with super-high writing speed. The photoluminescence image and spectrum indicate that one pulse-induced permanent photoreduction of Sm^{3+} to Sm^{2+} in Sm^{3+}-doped sodium aluminoborate glass can be achieved. Consequently, strong emission contrast is obtained, which is used for optical storage. By regulating the fabrication conditions, the fluorescent diameter could be controlled to approximately 800 nm, which demonstrates the feasibility in super-high density optical storage. Besides, multi-layer information is successfully inscribed. The proposed technique of single-pulse writing holds great potential for optical memory with high speed and huge capacity.

https://doi.org/10.1364/OL.409171

The capacity and the writing speed of optical information recording are in increasingly high demand with the development of big data technology [1]. Fs laser-induced localized modifications, such as changes in refractive index [2,3], selective precipitation of crystals [4,5], regulation of ion valence [6–9], ablation of nanorods [10,11], and formation of nanogratings [12–14], are widely accepted as effective media for optical data storage. However, great efforts have been made to increase the capacity of optical memory [15–19], but the importance of writing speed has been neglected. All the achievements for the optical storage are based on multi-pulse fs laser writing, which inevitably results in slow recording speed. Generally, thousands of or even more pulses are necessary to write a single spot. Thus, the primary challenge is the lack of a technique of single-pulse writing with the advantages of both high writing speed and tremendous capacity in optical data storage.

Multi-photon absorption induced by the ultra-high irradiance of an fs laser with low repetition rate pulses can lead to the structural modifications, which shows the promise to realize optical recording with a single pulse. Fs laser-induced-ion valence modulation with multiple pulses has engaged high interest due to its great potential in the application of optical storage with excellent characteristics, such as a high signal-to-noise ratio, high stability, and easy reading [20]. In essence, the electronic excitation of ions and transfer between the different excited species can be triggered by a single pulse. However, up to now, control of ion valence using a single pulse has not been reported.

This Letter is devoted to realizing single-shot photon recording with ultra-fast writing speed, which is extremely necessary for three-dimensional optical memory. To achieve this goal, a single pulse with diverse energy is employed to explore the threshold which could exactly induce the valence conversion of rare-earth ions. This not only fills the gap in single-shot photon recording on optical memory, but also becomes the key to increasing the storage density and writing speed. Our experimental study indicates that a single pulse can induce the permanent stable photoreduction of Sm^{3+} into Sm^{2+} in sodium aluminoborate glass. Single-pulse processing tremendously increases the writing speed in optical data storage, as well as greatly reducing the unit size and increasing the storage density. Finally, three-dimensional optical storage is presented with super-high writing speed and low writing energy threshold. In addition, the photoluminescence (PL) difference in the infrared range between Sm^{3+} and Sm^{2+} ions also may be present, which also would be interesting for applications [21–23].

The Sm^{3+}-doped sodium aluminoborate glass used in this Letter was prepared with a chemical composition of $85B_2O_3-5Al_2O_3-10Na_2O-0.1Sm_2O_3$ using a conventional melting–quenching technique [6]. Powers of reagent grade were mixed together and melted at 1250°C for 30 min in ambient atmosphere. The melted glass was cast on a stainless steel plate and formed a glass block with a thickness of about 1 mm.

Data recording experiments were performed with a fs laser system (PHAROS, Light Conversion Ltd.) that delivers 1030 nm. Typically, the laser beam was focused by a 0.8 NA objective lens at a depth of 100 μm from a surface for writing. The information encoded in glass was detected by a scanning

0146-9592/20/226274-04 Journal © 2020 Optical Society of America

图 8：论文 6 首页

论文 7：Focal volume optics for composite structuring in transparent solids （共一）

OPEN ACCESS
IOP Publishing | IMMT
International Journal of Extreme Manufacturing
Int. J. Extrem. Manuf. 7 (2025) 015002 (10pp)
https://doi.org/10.1088/2631-7990/ad8712

Focal volume optics for composite structuring in transparent solids

Bo Zhang[1,7], Zhuo Wang[1,7], Dezhi Tan[2,3,*], Min Gu[4,5], Yuanzheng Yue[6] and Jianrong Qiu[1,*]

[1] State Key Laboratory of Modern Optical Instrumentation, College of Optical Science and Engineering, Zhejiang University, Hangzhou 310027, People's Republic of China
[2] Zhejiang Lab, Hangzhou 311100, People's Republic of China
[3] School of Materials Science and Engineering, Zhejiang University, Hangzhou 310027, People's Republic of China
[4] Institute of Photonic Chips, University of Shanghai for Science and Technology, Shanghai, People's Republic of China
[5] Centre for Artificial-Intelligence Nanophotonics, School of Optical-Electrical and Computer Engineering, University of Shanghai for Science and Technology, Shanghai, People's Republic of China
[6] Department of Chemistry and Bioscience, Aalborg University, 9220 Aalborg, Denmark

E-mail: wctdz@zju.edu.cn and qjr@zju.edu.cn

Received 12 March 2024, revised 17 June 2024
Accepted for publication 15 October 2024
Published 5 November 2024

Abstract

Achieving high-level integration of composite micro-nano structures with different structural characteristics through a minimalist and universal process has long been the goal pursued by advanced manufacturing research but is rarely explored due to the absence of instructive mechanisms. Here, we revealed a controllable ultrafast laser-induced focal volume light field and experimentally succeeded in highly efficient one-step composite structuring in multiple transparent solids. A pair of spatially coupled twin periodic structures reflecting light distribution in the focal volume are simultaneously created and independently tuned by engineering ultrafast laser-matter interaction. We demonstrated that the generated composite micro-nano structures are applicable to multi-dimensional information integration, nonlinear diffractive elements, and multi-functional optical modulation. This work presents the experimental verification of highly universal all-optical fabrication of composite micro-nano structures with independent controllability in multiple degrees of freedom, expands the current cognition of ultrafast laser-based material modification in transparent solids, and establishes a new scientific aspect of strong-field optics, namely, focal volume optics for composite structuring transparent solids.

Supplementary material for this article is available online

Keywords: ultrafast laser, focal volume light field, composite structuring, transparent solids, advanced manufacturing

[7] These authors contributed equally to this work.
[*] Authors to whom any correspondence should be addressed.

2631-7990/25/015002+10$33.00

图 9：论文 7 首页

论文 8：Ultrafast laser-induced self-organized nanostructuring in transparent dielectrics: fundamentals and applications

Zhang et al. PhotoniX (2023) 4:24
https://doi.org/10.1186/s43074-023-00101-8

PhotoniX

REVIEW Open Access

Ultrafast laser-induced self-organized nanostructuring in transparent dielectrics: fundamentals and applications

Bo Zhang[1*], Zhuo Wang[1], Dezhi Tan[2] and Jiangrong Qiu[1*]

*Correspondence: zhangbob@zju.edu.cn; qjr@zju.edu.cn

[1] State Key Laboratory of Modern Optical Instrumentation, College of Optical Science and Engineering, Zhejiang University, Hangzhou, China
[2] Zhejiang Lab, Hangzhou, China

Abstract

Inscribing functional micro-nano-structures in transparent dielectrics enables constructing all-inorganic photonic devices with excellent integration, robustness, and durability, but remains a great challenge for conventional fabrication techniques. Recently, ultrafast laser-induced self-organization engineering has emerged as a promising rapid prototyping platform that opens up facile and universal approaches for constructing various advanced nanophotonic elements and attracted tremendous attention all over the world. This paper summarizes the history and important milestones in the development of ultrafast laser-induced self-organized nanostructuring (ULSN) in transparent dielectrics and reviews recent research progresses by introducing newly reported physical phenomena, theoretical mechanisms/models, regulation techniques, and engineering applications, where representative works related to next-generation light manipulation, data storage, optical detecting are discussed in detail. This paper also presents an outlook on the challenges and future trends of ULSN, and important issues merit further exploration.

Keywords: Ultrafast laser, Self-organization, Nanostructuring, Transparent dielectrics

Introduction

As Moore's law going close to its limit, integrated photonics aiming for on-chip functionalization is fast-rising and has brought up a boom in searching for next-generation optoelectronic substrate materials. Especially, all-inorganic transparent dielectrics such as various glasses and crystals have been established as excellent modular platforms for light emission [1–5], transmission [6–9], and modulation [10–15]. Predictably, next-generation integrated photonic elements and systems will largely rely on various three-dimensional (3D) micro-nano structures inscribed in transparent dielectrics [16–22], such as optical waveguides [23–26], optical couplers [27–29], photonic crystals [30–32], and optical storage voxels [33–35], which has arisen an ever-growing demand for the fabrication of highly integrated all-inorganic optical devices and systems. Currently, it remains difficult and a major challenge to build complex 3D micro-nano structures in multiple all-inorganic transparent dielectrics by using conventional lithography fabrication technologies, owing to the extremely low linear optical absorption and high

图 10：论文 8 首页

论文 9：Photonic circuits written by femtosecond laser in glass: improved fabrication and recent progress in photonic devices

ADVANCED PHOTONICS

Photonic circuits written by femtosecond laser in glass: improved fabrication and recent progress in photonic devices

Dezhi Tan,[a,*] Zhuo Wang,[a] Beibei Xu,[a] and Jianrong Qiu[a,b,*]
[a]Zhejiang University, College of Optical Science and Engineering, State Key Laboratory of Modern Optical Instrumentation, Hangzhou, China
[b]Chinese Academy of Sciences, CAS Center for Excellence in Ultra-Intense Laser Science, Shanghai, China

Abstract. Integrated photonics is attracting considerable attention and has found many applications in both classical and quantum optics, fulfilling the requirements for the ever-growing complexity in modern optical experiments and big data communication. Femtosecond (fs) laser direct writing (FLDW) is an acknowledged technique for producing waveguides (WGs) in transparent glass that have been used to construct complex integrated photonic devices. FLDW possesses unique features, such as three-dimensional fabrication geometry, rapid prototyping, and single step fabrication, which are important for integrated communication devices and quantum photonic and astrophotonic technologies. To fully take advantage of FLDW, considerable efforts have been made to produce WGs over a large depth with low propagation loss, coupling loss, bend loss, and highly symmetrical mode field. We summarize the improved techniques as well as the mechanisms for writing high-performance WGs with controllable morphology of cross-section, highly symmetrical mode field, low loss, and high processing uniformity and efficiency, and discuss the recent progress of WGs in photonic integrated devices for communication, topological physics, quantum information processing, and astrophotonics. Prospective challenges and future research directions in this field are also pointed out.

Keywords: photonic integrated circuit; waveguides; femtosecond laser direct writing; improved techniques; photonic devices.

Received Dec. 1, 2020; revised manuscript received Jan. 18, 2021; accepted for publication Feb. 5, 2021; published online Mar. 10, 2021.

[DOI: 10.1117/1.AP.3.2.024002]

1 Introduction

Photonic integrated circuits have shown the potential to allow integrating passive and active optical components on one chip in a scalable manner and have been identified to support a plethora of applications, such as data communication, sensing, astrophotonics, quantum information processing, and national security.[1–4] Photonic circuits are indispensable components in modern optical communication networks and lie at the heart of integrated photonic devices. Currently, to this end, one of the biggest challenges in integrated photonics is establishing a general and flexible method to produce photonic circuits with low loss, high integration density, and high tunability. The unique feature of 3D fabrication geometry promises femtosecond laser direct writing (FLDW) as an on-demand solution to these requirements.

Femtosecond (fs) laser-induced multiphoton absorption enables tailoring the material structures and properties inside transparent bulk materials with high processing precision and triggers a great deal of activity in the field of photonics.[5–13] In particular, the fs laser can induce a permanent refractive index change in glass, which indicates a promising tool to fabricate photonic circuits, waveguides (WGs), and basic elements in integrated optics.[5,14,15] FLDW has been identified to be an effective technique for constructing WGs in a 3D fashion over a large depth from the micrometer to millimeter scale.[5,16–18] WG-based 2D and 3D optical devices have also been demonstrated in various glasses. Compared with the 2D fabrication of silicon photonic circuits by planar lithography, FLDW is a rapid prototyping technique to produce WGs in 3D without needing complex procedures. Thus, up to now, FLDW has been exploited to

*Address all correspondence to Dezhi Tan, wctdz@zju.edu.cn; Jianrong Qiu, qjr@zju.edu.cn

图 11：论文 9 首页

附件二：专利证明材料

专利 1：一种晶体内部微尺度位错的光学写入和擦除方法以及系统

国 家 知 识 产 权 局

310013
浙江省杭州市西湖区古墩路 701 号紫金广场 B 座 1103 室 杭州求是专利事务所有限公司
林超(0571-87911726-817)

发文日：
2024 年 09 月 13 日

申请号或专利号：202410762058.3　　发文序号：2024091300620450

申请人或专利权人：浙江大学

发明创造名称：一种晶体内部微尺度位错的光学写入和擦除方法以及系统

发 明 专 利 申 请 进 入 实 质 审 查 阶 段 通 知 书

上述专利申请，根据申请人提出的实质审查请求，经审查，符合专利法第 35 条及实施细则第 113 条的规定，该专利申请进入实质审查阶段。

提示：

1.根据专利法实施细则第 57 条第 1 款的规定，发明专利申请人自收到本通知书之日起 3 个月内，可以对发明专利申请主动提出修改。

2.申请文件修改格式要求：

对权利要求修改的应当提交相应的权利要求替换项，涉及权利要求引用关系时，则需要将相应权项一起替换补正。如果申请人需要删除部分权项，申请人应该提交整理后连续编号的部分权利要求书。

对说明书修改的应当提交相应的说明书替换段，不得增加和删除段号，仅只能对有修改部分段进行整段替换。如果要增加内容，则只能增加在某一段中；如果需要删除一个整段内容，应该保留该段号，并在此段号后注明：“此段删除”字样。段号以国家知识产权局回传的或公布/授权公告的说明书段号为准。

对说明书附图修改的应当以图为单位提交相应的替换附图。

对说明书摘要文字部分修改的应当提交相应的替换页。对摘要附图修改的应当重新指定。

同时，申请人应当在补正书或意见陈述书中标明修改涉及的权项、段号、图、页。

国家知识产权局 专利审查业务章

审 查 员：自动审查
联系电话：010-62356655

210307
2023.03

纸件申请，回函请寄：100088 北京市海淀区蓟门桥西土城路 6 号　国家知识产权局专利局受理处收
电子申请，应当通过专利业务办理系统以电子文件形式提交相关文件。除另有规定外，以纸件等其他形式提交的文件视为未提交。

专利 2：一种透明介质内部彩色像素点阵单脉冲立体写入方法

国 家 知 识 产 权 局

310013
浙江省杭州市西湖区古墩路 701 号紫金广场 C 座 1506 室 杭州求是专利事务所有限公司
林超(0571-87911726-817)

发文日：
2024 年 03 月 04 日

申请号：202410242372.9　　发文序号：2024030401096330

专 利 申 请 受 理 通 知 书

根据专利法第 28 条及其实施细则第 43 条、第 44 条的规定，申请人提出的专利申请已由国家知识产权局受理。现将确定的申请号、申请日等信息通知如下：

申请号：202410242372.9
申请日：2024 年 03 月 04 日
申请人：浙江大学
发明人：张博,王卓,张捷,邱建荣
发明创造名称：一种透明介质内部彩色像素点阵单脉冲立体写入方法
经核实，国家知识产权局确认收到文件如下：
权利要求书 1 份 2 页,权利要求项数 ： 9 项
说明书 1 份 7 页
说明书附图 1 份 3 页
说明书摘要 1 份 1 页
专利代理委托书 1 份 2 页
发明专利请求书 1 份 5 页
实质审查请求书 文件份数：1 份
申请方案卷号：超-241-75-王

提示：

1.申请人收到专利申请受理通知书之后，认为其记载的内容与申请人所提交的相应内容不一致时，可以向国家知识产权局请求更正。

2.申请人收到专利申请受理通知书之后，再向国家知识产权局办理各种手续时，均应当准确、清晰地写明申请号。

国家知识产权局 专利审查业务章

审 查 员：自动受理
联系电话：010-62356655

200101
2023.03

纸件申请，回函请寄：100088 北京市海淀区蓟门桥西土城路 6 号　国家知识产权局专利局受理处收
电子申请，应当通过专利业务办理系统以电子文件形式提交相关文件。除另有规定外，以纸件等其他形式提交的文件视为未提交。

专利 3：一种金刚石内部的三维微区热操控方法

国 家 知 识 产 权 局

310013

浙江省杭州市西湖区古墩路 701 号紫金广场 C 座 1506 室 杭州求是专利事务所有限公司
林超(0571-87911726-817)

发文日：

2023 年 09 月 05 日

申请号或专利号：202310756810.9　　发文序号：2023090500643570

申请人或专利权人：浙江大学

发明创造名称：一种金刚石内部的三维微区热操控方法

发 明 专 利 申 请 进 入 实 质 审 查 阶 段 通 知 书

上述专利申请，根据申请人提出的实质审查请求，经审查，符合专利法第 35 条及实施细则第 96 条的规定，该专利申请进入实质审查阶段。

提示：

1.根据专利法实施细则第 51 条第 1 款的规定，发明专利申请人自收到本通知书之日起 3 个月内，可以对发明专利申请主动提出修改。

2.申请文件修改格式要求：

对权利要求修改的应当提交相应的权利要求替换项，涉及权利要求引用关系时，则需要将相应权项一起替换补正。如果申请人需要删除部分权项，申请人应该提交整理后连续编号的部分权利要求书。

对说明书修改的应当提交相应的说明书替换段，不得增加和删除段号，仅只能对有修改部分段进行整段替换。如果要增加内容，则只能增加在某一段中；如果需要删除一个整段内容，应该保留该段号，并在此段号后注明：“此段删除”字样。段号以国家知识产权局回传的或公布/授权公告的说明书段号为准。

对说明书附图修改的应当以图为单位提交相应的替换附图。

对说明书摘要文字部分修改的应当提交相应的替换页。对摘要附图修改的应当重新指定。

同时，申请人应当在补正书或意见陈述书中标明修改涉及的权项、段号、图、页。

国家知识产权局 专利审查业务章

审 查 员：自动审查
联系电话：010-62356655

审查部门：初审及流程管理部

210307
2022.10

纸件申请，回函请寄：100088 北京市海淀区蓟门桥西土城路 6 号 国家知识产权局专利局受理处收
电子申请，应当通过专利业务办理系统以电子文件形式提交相关文件。除另有规定外，以纸件等其他形式提交的文件视为未提交。

专利 4：用于光存储点阵读取的基于 Sobel 滤波的检测方法

(19)国家知识产权局

(12)发明专利申请

(10)申请公布号 CN 116452433 A
(43)申请公布日 2023.07.18

(21)申请号 202310227231.5

(22)申请日 2023.03.10

(71)申请人 浙江大学
地址 310058 浙江省杭州市西湖区余杭塘路866号

(72)发明人 王梓权 张博 王卓

(74)专利代理机构 杭州求是专利事务所有限公司 33200
专利代理师 林超

(51)Int.Cl.
G06T 5/00(2006.01)
G06T 5/20(2006.01)
G06T 1/60(2006.01)
G06T 1/20(2006.01)
G06T 7/13(2017.01)
G06T 7/11(2017.01)
G06T 7/187(2017.01)

权利要求书5页 说明书11页 附图4页

(54)发明名称

用于光存储点阵读取的基于Sobel滤波的检测方法

(57)摘要

本发明公开了用于光存储点阵读取的基于Sobel滤波的检测方法。方法包括点阵图像区域标定，对点阵图像进行索贝尔算法加强以获得索贝尔边缘增强图，并对索贝尔边缘增强图进行预处理得到二次灰度图，对二次灰度图进行处理得到二值化图像，对二值化图像进行旋转以获得正二值图像，对正二值图像进行连通区域标定以生成若干个连通区域，然后根据不同连通区域的最小最接矩形对正二值图像进行网格划分，最后获得正二值图像中的图像数据，从而获得待测晶体中存储的数据并记录。本发明使用了基于Sobel滤波的检测算法，能克服在深层的点阵图出现的层级间的强串扰，提升点阵数据读取的准确率。

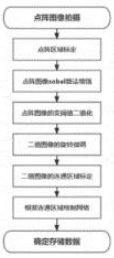

专利 5：一种单脉冲全无机多维光存储方法

证书号第6210788号

发明专利证书

发明名称：一种单脉冲全无机多维光存储方法

发　明　人：张博;王卓;王梓权;邱建荣

专　利　号：ZL 2022 1 0254279.0

专利申请日：2022年03月15日

专利权人：浙江大学

地　　址：310058 浙江省杭州市西湖区余杭塘路866号

授权公告日：2023年08月04日　　授权公告号：CN 114627902 B

国家知识产权局依照中华人民共和国专利法进行审查，决定授予专利权，颁发发明专利证书并在专利登记簿上予以登记。专利权自授权公告之日起生效。专利权期限为二十年，自申请日起算。

专利证书记载专利权登记时的法律状况。专利权的转移、质押、无效、终止、恢复和专利权人的姓名或名称、国籍、地址变更等事项记载在专利登记簿上。

局长
申长雨

国家知识产权局
2023年08月04日

第1页(共2页)

其他事项参见续页

专利 6：一种微型分光元件及其制备方法

证书号第5572695号

发明专利证书

发明名称：一种微型分光元件及其制备方法

发　明　人：张博;王卓;谭德志;邱建荣

专　利　号：ZL 2021 1 1210024.6

专利申请日：2021年10月18日

专利权人：浙江大学

地　　址：310058 浙江省杭州市西湖区余杭塘路866号

授权公告日：2022年11月11日　　授权公告号：CN 113917586 B

国家知识产权局依照中华人民共和国专利法进行审查，决定授予专利权，颁发发明专利证书并在专利登记簿上予以登记。专利权自授权公告之日起生效。专利权期限为二十年，自申请日起算。

专利证书记载专利权登记时的法律状况。专利权的转移、质押、无效、终止、恢复和专利权人的姓名或名称、国籍、地址变更等事项记载在专利登记簿上。

局长
申长雨

国家知识产权局

第1页(共2页)

其他事项参见续页

附件三：参与项目

稀土离子掺杂光存储材料研究项目

委 托 研 发 合 同

甲方：华为技术有限公司

乙方：浙江大学

合同编号：YBN2020015027

签订地点：中国广东省深圳市龙岗区

国家重点研发计划
课题任务书

课题名称：	超分辨光存储介质材料设计与研究
所属项目：	超分辨纳米光信息存储技术研究
所属专项：	信息光子技术
项目牵头承担单位：	上海理工大学
课题承担单位：	浙江大学
课题负责人：	邱建荣
执行期限：	2021 年 12 月 至 2023 年 11 月

中华人民共和国科学技术部制

2021 年 12 月 16 日

0003YF 2021YFB2802001 2021-12-16 11:43:40

nature communications

Article

https://doi.org/10.1038/s41467-024-52628-4

Unlocking high photosensitivity direct laser writing and observing atomic clustering in glass

Received: 23 September 2023

Accepted: 17 September 2024

Published online: 27 September 2024

Check for updates

Wenyan Zheng[1], Zhuo Wang[2], Weilin Chen[1], Mengchao Zhang[3], Hui Li[3], Guang Yang[3], Qiang Xu[4], Xvsheng Qiao[1] ✉, Dezhi Tan[1,5] ✉, Junjie Zhang[6], Jianrong Qiu[2], Guodong Qian[1] & Xianping Fan[1]

The direct laser writing (DLW) of photoluminescent metal clusters is inspiring intensive research in functional glasses. However, understanding the influence of the host structure on cluster formation and visualizing DLW-induced clusters at the atomic scale remains challenging. In this work, we develop a highly photosensitive fluorophosphate glass through fluorine incorporation. The addition of fluorine establishes a conducive environment for Ag^+ ions before DLW and enhances the availability of reducing agents and diffusion pathways during DLW. These advantages facilitate the formation of Ag clusters under low-energy single-pulsed DLW. Increasing laser energy results in a combination of Ag clusters and glasses defect, forming a dot + ring photoluminescent pattern. Atom probe tomography (APT), a technique capable of mapping the elemental spatial distribution and identifying clustering, is employed to gain more information on laser-induced clusters. Comparison of APT results between samples without and with DLW reveals the formation of Ag clusters after laser writing. The design concept and characterization enrich the understanding of Ag cluster behavior in glasses. This knowledge opens the possibility of rational design of clusters confined in glasses and inspires their synthesis for various applications.

Direct Laser Writing (DLW) enables precise modifications of transparent materials such as polymer[1], sapphire[2], and glass[3]. This capability allows for the creation of customized 3D microstructures with tailored properties, providing a versatile platform for material engineering and optical device fabrication. Among applications, there is a growing interest in fabricating silver nanoclusters (Ag NCs) inside glass for high-capacity optical data storage (ODS). Consisting of several to tens of atoms, Ag NCs exhibit bright photoluminescence (PL) due to the quantum confinement effect[4,5]. In ODS, DLW is applied to inscribe Ag NCs, with each inscribed PL dot serving as an information recording unit[6]. By tailoring the DLW parameters such as laser energy, duration, and pulse count, tunable PL intensity and multiple grayscales storage can be achieved[7].

Along with laser parameters, the choice of glass matrix also influences ODS performance. An ideal glass for storage application is expected to facilitate the generation of Ag NCs at low energy to reduce writing energy consumption and should be compatible with single-pulse laser processing to enhance the data writing efficiency[8]. The earliest literature on this topic can be traced back to the year 2010[9], subsequent research has mainly focused on refining the DLW

[1]State Key Laboratory of Silicon Materials & School of Materials Science and Engineering, Zhejiang University, Hangzhou, China. [2]State Key Laboratory of Modern Optical Instrumentation College of Optical Science and Engineering, Zhejiang University, Hangzhou, China. [3]School of Materials Science and Engineering, Shanghai University, Shanghai, China. [4]Ocean Academy, Zhejiang University, Zhoushan, China. [5]Zhejiang Lab, Hangzhou, China. [6]College of Optical and Electronic Technology, China Jiliang University, Hangzhou, China. ✉e-mail: qiaoxus@zju.edu.cn; wctdz@zju.edu.cn

parameter using oxide-based glasses, such as silicate, phosphate, and borosilicate[10–12]. Few attempts have been made to explore alternative glass systems and understand the glass's influence on Ag clustering. Recently, fluorophosphate (PF) glass has emerged as a promising host for Ag clusters, showing potential for high-density storage with enhanced writability[13]. Leveraging the low polarizability of F^- ions, PF glasses could inhibit silver ion reduction and consequent cluster formation. This ensures a uniform distribution of silver ions. During DLW, their large band gap and low refractive index mitigate the self-focusing effect and improve laser resistivity[14]. PF glasses also offer a lower phonon energy environment compared to their oxide counterpart, which reduces the probability of nonradiative transitions of Ag NCs and enhances their PL efficiency[15–17]. These combined properties make PF glass a suitable choice for studying the photochemistry of Ag under laser irradiation and potentially accessing enhanced photosensitivity and PL properties.

Besides understanding glass matrixes, characterizing small clusters poses an additional challenge. Traditional techniques, such as transmission electron microscopy, face limitations due to the electron-beam-induced cluster growth[18]. And scattering methods often require specialized beamlines, making them less accessible[19]. To obtain both spatial and chemical information, a combination of techniques is usually employed, including fluorescence, X-ray absorption fine structure spectroscopy, mass spectrometry, and single-crystal X-ray diffraction[20,21]. Recently, atom probe tomography (APT) has emerged as a powerful high-resolution 3D mapping technique with sub-nanometer precision, offering valuable insights into the distribution of clusters[22–25]. APT offers quantitative information on cluster size and density, thus enhancing our understanding of their structural characteristics.

In this study, we began with a facile approach to enhance the glass photosensitivity by incorporating fluorine into the glass matrix. The addition of fluorine brought two benefits. Firstly, the high electronegativity of fluorine created a less reductant environment, preventing the reduction of Ag^+ ions prior to DLW. This ensured a high concentration of Ag^+ ions available for cluster formation during laser irradiation. Secondly, fluorine disrupted the glass network, increasing the diffusion channels and the availability of reducing agents under DLW (Fig. 1a, b). As the laser energy increased, the PL pattern changed from dots made of Ag clusters to a pattern by a combination of clusters and defects, resulting in a dot + ring arrangement (Fig. 1c). For characterizing the laser-induced clusters, APT was used to capture the formation of Ag clusters following laser writing (Fig. 1d).

Results and discussion

Glass preparation and structural analysis

PFx glasses with fluorine concentrations ranging from PF5 to PF25 were synthesized (Supplementary Fig. 1). The difference between T_g (glass transition temperature) and T_c (crystallization temperature), ΔT, is used to estimate their thermal stability. The increased ΔT from PF5 to PF25 implies enhanced glass thermal stability[26], which is favorable for achieving highly durable storage media (Supplementary Fig. 2). The homogeneous dispersion of Ag^+ ions was confirmed through absorption, PL, and decay measurement (Supplementary Figs. 3–5 and Supplementary Note. 1 and 2).

Analysis of ^{31}P NMR spectra revealed the PF glasses network framework comprises metaphosphate chains by PO_4 tetrahedra, Q^2, where the superscripts indicate the number of bridging oxygens (BOs)[27]. With increasing fluorine content, the Q^2 peak transferred into a smaller chemical shift, and a Q^1 signal emerged (Fig. 2a). This transformation suggested that fluorine depolymerized the metaphosphate structure by replacing bridging P-O-P bonds with terminal P-F and P - nonbridging oxygens (P-NBOs) bonds[28].

The substitution of Q^2 by Q^1 indicated a reduction in the connectivity of the phosphate network, which was further supported by observations in Raman spectra (Supplementary Note. 3, Supplementary Fig. 6, and Supplementary Table. 1). This structural change was expected to bring more diffusion pathways for Ag^+ ions during DLW. Moreover, the incorporation of F^- ions along with O^{2-} ions created a

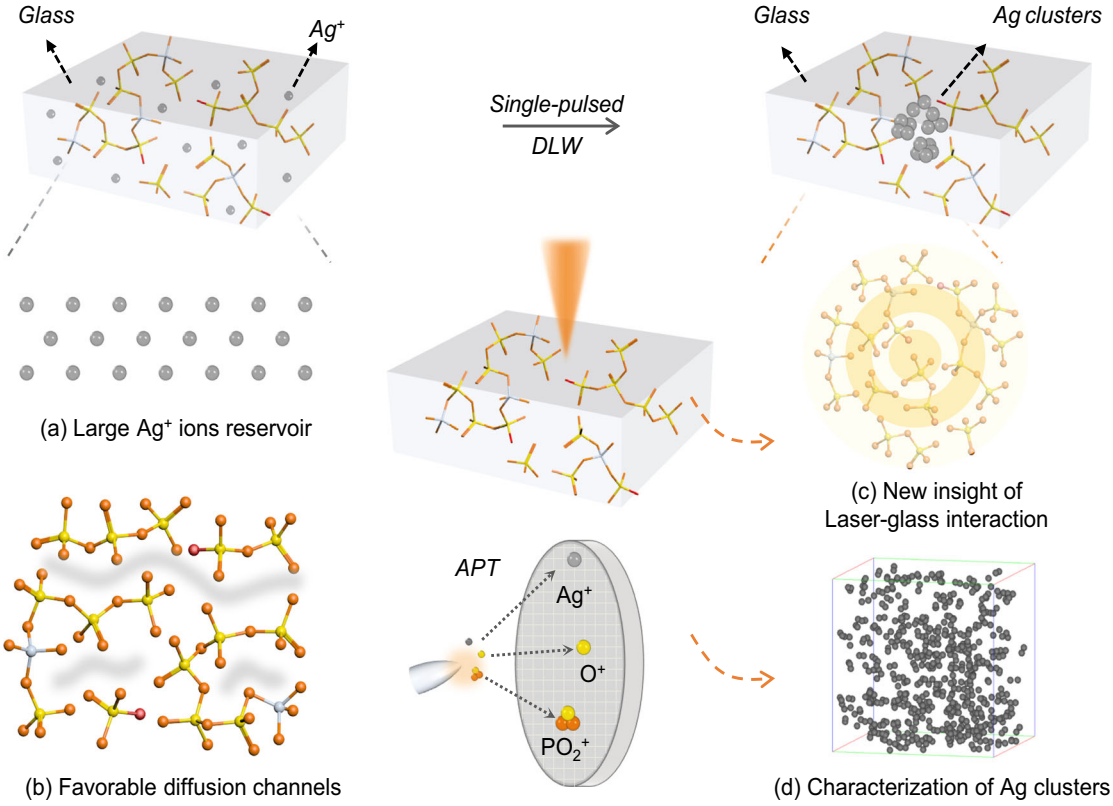

Fig. 1 | Designing glass structures. a large Ag^+ ions reservoir and (**b**) favorable diffusion channels ready for DLW. **c** Single-pulsed DLW transforms Ag^+ ions into Ag clusters, offering insights into laser-glass interactions, and (**d**) enabling APT for cluster observation.

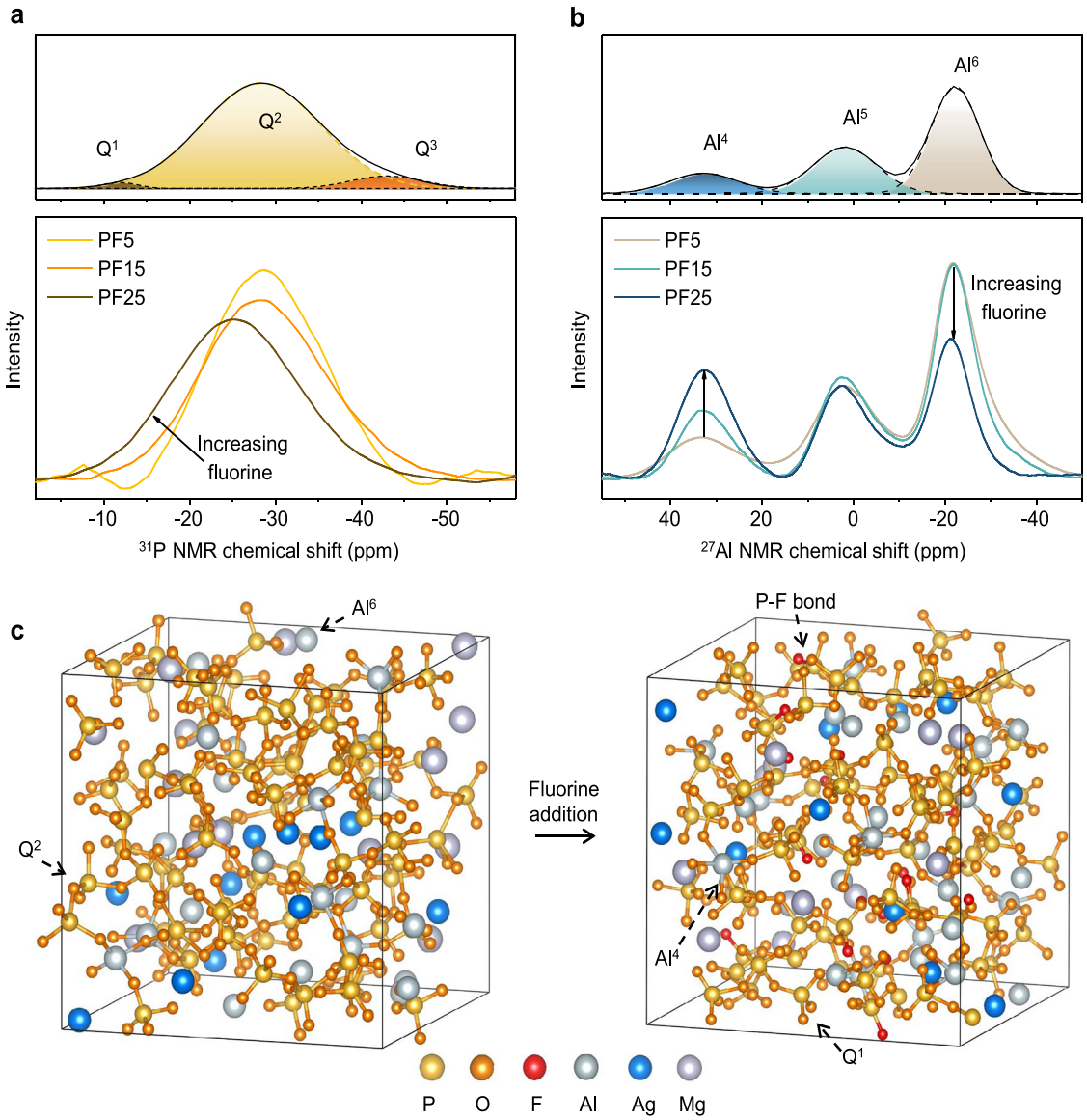

Fig. 2 | Structural analysis of PFx glass. a ^{31}P and (**b**) ^{27}Al NMR spectra and deconvolution of PF5, PF15, and PF25 glasses. **c** Structures of phosphate (oxide-based, left) and fluorophosphate glass (fluorine-modified, right) by AIMD simulation.

mixed-anion environment that exerts asymmetric forces on Ag species and enhances their mobility[29].

Compared to oxygen, the high electronegativity of fluorine resulted in a weak reductant environment, which slowed the reduction of Ag^+ ions and prevented cluster formation before laser irradiation[30]. This was substantiated by the PL enhancement of Ag^+ ions from PF5 to PF25 (Supplementary Fig. 7). In terms of Al element, in PF5, most of Al modified the network interspace in the form of AlO_5 (Al^5) and AlO_6 (Al^6), with a minor fraction participating in glass backbone in the form of AlO_4 (Al^4) (Fig. 2b)[31]. Upon increasing fluorine, the Al^6 gradually converts into Al^4, indicating a growing portion of Al entering the phosphate network via P-O-Al bond linkage. The transformation from Al^6 to Al^4, along with the generation of more chemically durable P-O-Al bonds, counteracted the fluorine-induced depolymerization, contributing to the enhanced glass chemical stability (Supplementary Note. 4 and Supplementary Fig. 8)[32].

To gain deeper insight into the structural change, ab initio molecular dynamics (AIMD) simulations were conducted. Upon fluorine introduction, the glass transformed from a tight-bound phosphate network featuring Q^2 units to an open structure with Q^1 units and P-F bonds (Fig. 2c). At the same time, a growing proportion of Al^4 units emerged, enhancing its role as a glass former. Moreover, in fluorine-modified glasses (right of Fig. 2c), Ag^+ ions were found to be homogenously dispersed throughout the matrix.

Combining experimental and simulated results, the fluorine in PF glass brought two benefits. Firstly, it established a weak reductant environment that prevents premature reduction and ensures sufficient Ag reservoir for subsequent cluster formation. Secondly, the presence of fluorine disrupted the connectivity of metaphosphate chains, introducing more diffusion channels. These channels, in turn, facilitate the aggregation of silver species during laser irradiation and enhance laser responsiveness. These synergistic effects make PF glass a compelling candidate matrix for the fabrication of Ag clusters under low-energy DLW.

Creation and mechanism of Ag nanoclusters under DLW

Drawing on the structural analysis, it was hypothesized that PF25 (with the highest fluorine loading) would present the most favorable photosensitivity. To validate this, a series of single-pulsed femtosecond experiments were conducted (Fig. 3a and Supplementary Fig. 9). The PL of inscribed dots gradually gained its intensity with higher laser energy (Fig. 3b). The minimal energy threshold required to induce PL signal (E_{min}) decreased from 1.0 μJ (PF5) to 0.1 μJ (PF25), indicating enhanced photosensitivity with increasing fluorine.

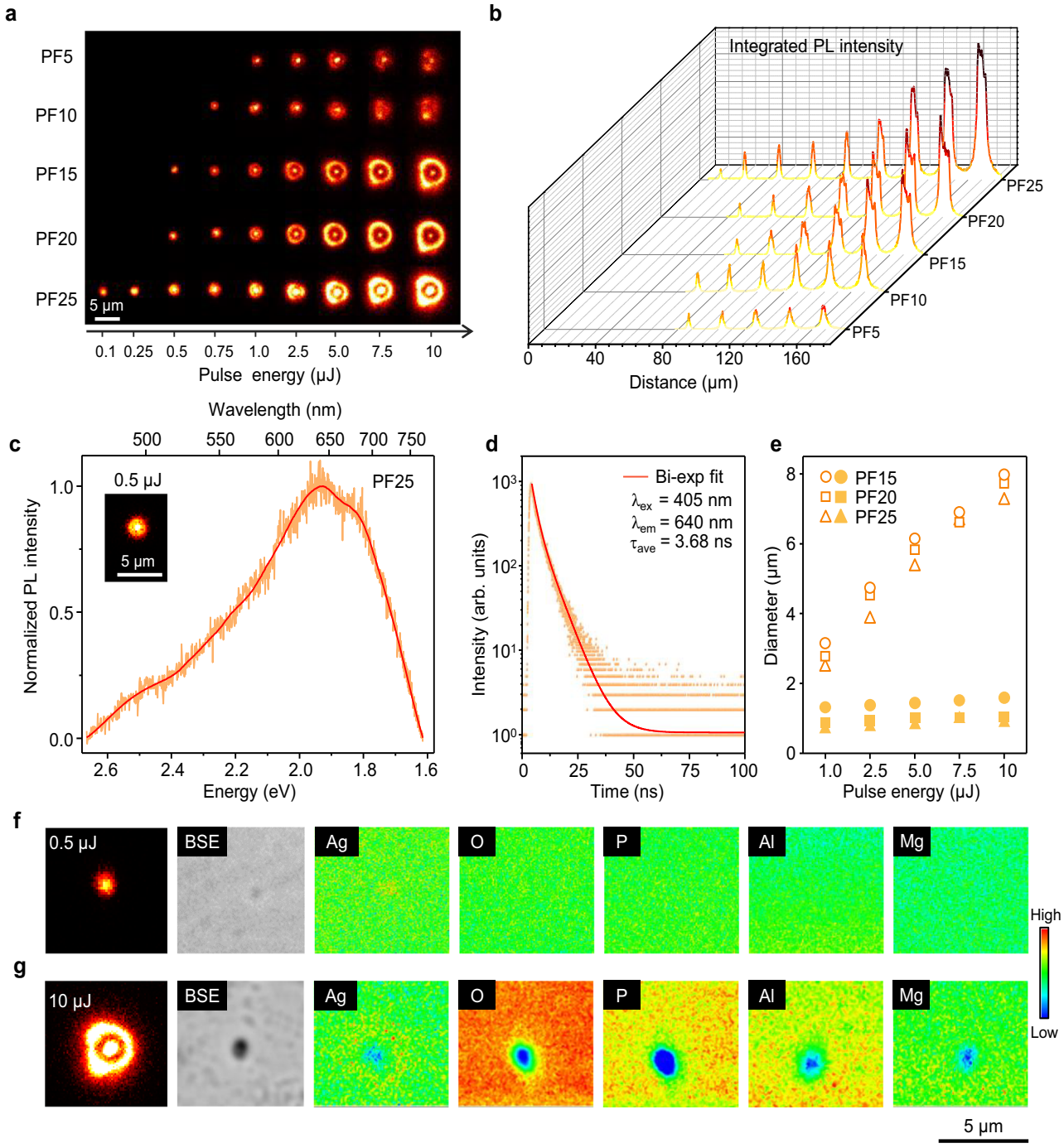

Fig. 3 | Photoluminescence and distribution of DLW-induced Ag clusters. **a** Confocal fluorescence image of PFx glasses, λ_{ex} = 405 nm. **b** Integrated PL intensity. **c** Micro-PL spectrum of the dot written with 0.5 μJ in PF25 (inset: its confocal fluorescence image), smoothing applied without losing intrinsic features (orange line). **d** Emission decay curve monitored at 640 nm (PF25, 0.5 μJ). **e** Dependence of PL dot size (solid symbol) and ring diameter (hollow symbol) on laser energy. **f**, **g** Backscattered electrons image and elemental maps of the irradiated area under 0.5 μJ and 10 μJ energy in PF25.

Micro PL spectra revealed a broad band centered at 640 nm with a smaller shoulder at 520 nm (Fig. 3c and Supplementary Fig. 10). After thermal treatment at 400 °C for 12 h, the primary peak at 640 nm persisted, while the intensity of 520 nm decreased (Supplementary Fig. 11). This indicates that Ag clusters are responsible for the 640 nm emission, while thermally unstable defects contribute to the 520 nm emission[33]. Furthermore, the emission at 640 nm displayed a lifetime of 3.68 ns, consistent with the nanosecond decay characteristic of Ag clusters (Fig. 3d)[9]. These emission features of Ag clusters resemble those of clusters produced by both multi-pulsed femtosecond laser writing and electron/gamma radiation in glasses[34–37]. Moreover, with increasing laser energy, the PL spectrum showed a gradual increase in intensity, indicating a growing number of Ag clusters (Supplementary Fig. 12).

As the writing energy reached 1.0 μJ, peripheral PL rings emerged in PF15 to PF25 (Fig. 3a). With increasing laser energy, the diameter of PL ring (D) presented progressive expansion, while the central dot (d) remained constant (Fig. 3e). This difference suggested that the dot + ring pattern likely originates from two different PL centers. A comparison of electron probe microanalysis (EPMA) revealed that under 1.0 μJ, the Ag enrichment in the outer ring (Fig. 3f, g), while the center exhibits depletion of all elements.

The contrast in element distribution suggested that the PL rings are associated with the migration of Ag species. Conversely, the central dots are likely attributed to intrinsic properties of the glass, possibly arising from laser-induced defects. These defects stem from laser-induced perturbations known as phosphorus oxygen

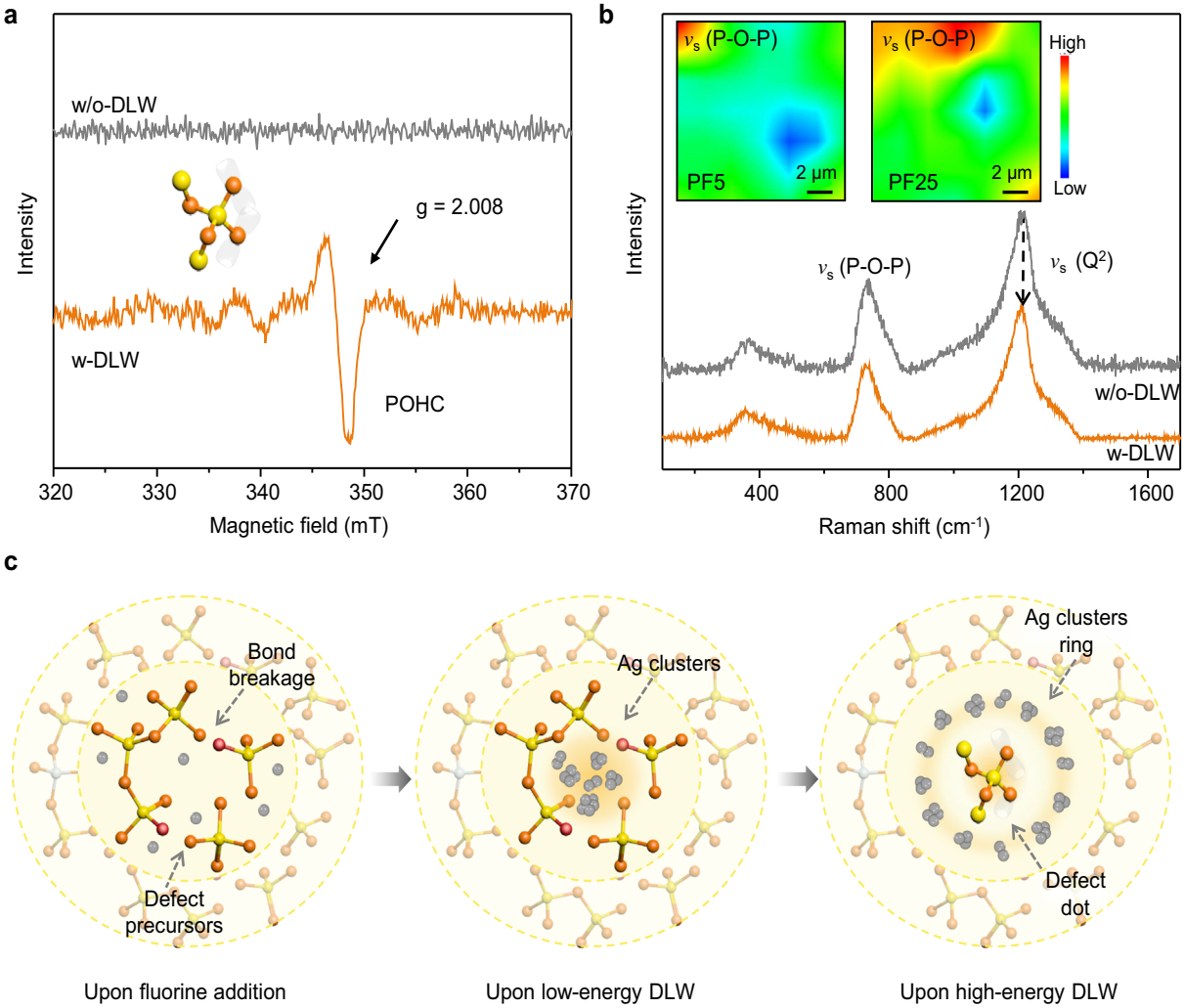

Fig. 4 | Mechanism of Ag clusters formation under DLW. a EPR spectra and (**b**) micro-Raman spectra of the region without and with DLW (w/o-DLW and w-DLW) in PF25, the inset shows the mapping of ν_s (P-O-P) band of the dot written by 0.5 μJ in PF5 and PF25. **c** Schematic diagram of structural evolution upon fluorine modification and increased laser energy.

hole centers (POHCs). They are characterized by an unpaired electron shared between two non-bridging oxygens bound to a phosphorus atom. In addition, they can be resonated at an electron paramagnetic resonance scan (EPR in Fig. 4a and Supplementary Note. 5)[38]. Furthermore, these centers are known to be thermally unstable and can be easily erased by heat treatment at 400 °C for 12 h (Supplementary Fig. 13)[39].

To understand the mechanism behind the dot + ring pattern, a closer examination of the interaction between the laser and the glass becomes necessary. During DLW, the energy deposition begins with a multiphoton absorption process (approximately four-photon), exciting electrons from the valence band into the conduction band[40]. These excited electrons then work as reductants, reducing Ag^+ ions into Ag^0 atoms. Simultaneously, a hole-capturing process takes place by the reaction PO + hole → POHC[41]. In this context, the PO refers to phosphorus-oxygen defect precursors that are considered pre-existing faults in the glass network. Such faults can be oxygen vacancies, nonbridging oxygens, and strained bonds[42].

Recalling PF glass structure, the incorporation of fluorine brings the P-O-P bond breakage, increasing the number of P-NBOs (phosphorus to non-bridging oxygens bonds) and terminal P-F bonds. These NBOs serve as the phosphorus-oxygen defect precursor for POHC formation, capable of capturing holes and inhibiting the recombination of electron-hole[43]. As a result, the retained electrons effectively facilitate the reduction of the Ag^+ ions, leading to the formation of Ag clusters even under low-energy laser irradiation.

When exposed to high-energy DLW, however, the intense laser beam would induce a localized temperature surge, accompanied by a strong shock wave and electron rearrangement at the focal point. This heightened temperature gradient and shock wave facilitate the diffusion of Ag species, leading to the formation of ring-shaped Ag clusters, while the electron rearrangements contribute to the central glass defect[44,45]. Consequently, ring-shaped Ag clusters emerge at the periphery, and thermally erasable defects (POHC) appear in the center.

Further insights into the laser-induced structural changes were obtained from micro-Raman spectra. In Fig. 4b, consistent with the Raman trend upon increasing fluorine, DLW reduced the intensity of both the ν_s (Q^2) peak and ν_s (P-O-P) with a negative Raman shift. The 2D mapping of ν_s(Q^2) displayed a comparable intensity decrease in the regions subjected to DLW for both PF5 and PF25 samples (Supplementary Fig. 14). But for ν_s (P-O-P) – the indicator of phosphate connectivity (Q^2), its reduction in PF25 covered a much smaller area (inset of Fig. 4b). This suggested that the fluorine exerts a pre-break impact, similar to that caused by DLW.

This pre-break effect generates both diffusion pathways and precursors for POHCs: the former prepares the channels for Ag clusters accumulation ready for laser irradiation, and the latter aids in hole scavenging and defect formation (Fig. 4c). It should be noted that our observation differs from previous reports, where the formation of Ag clusters required a thermally assisted process under multiple pulse irradiation[46]. However, during single-pulsed laser irradiation, thermal accumulation was absent, as evidenced by the lack of obvious melted

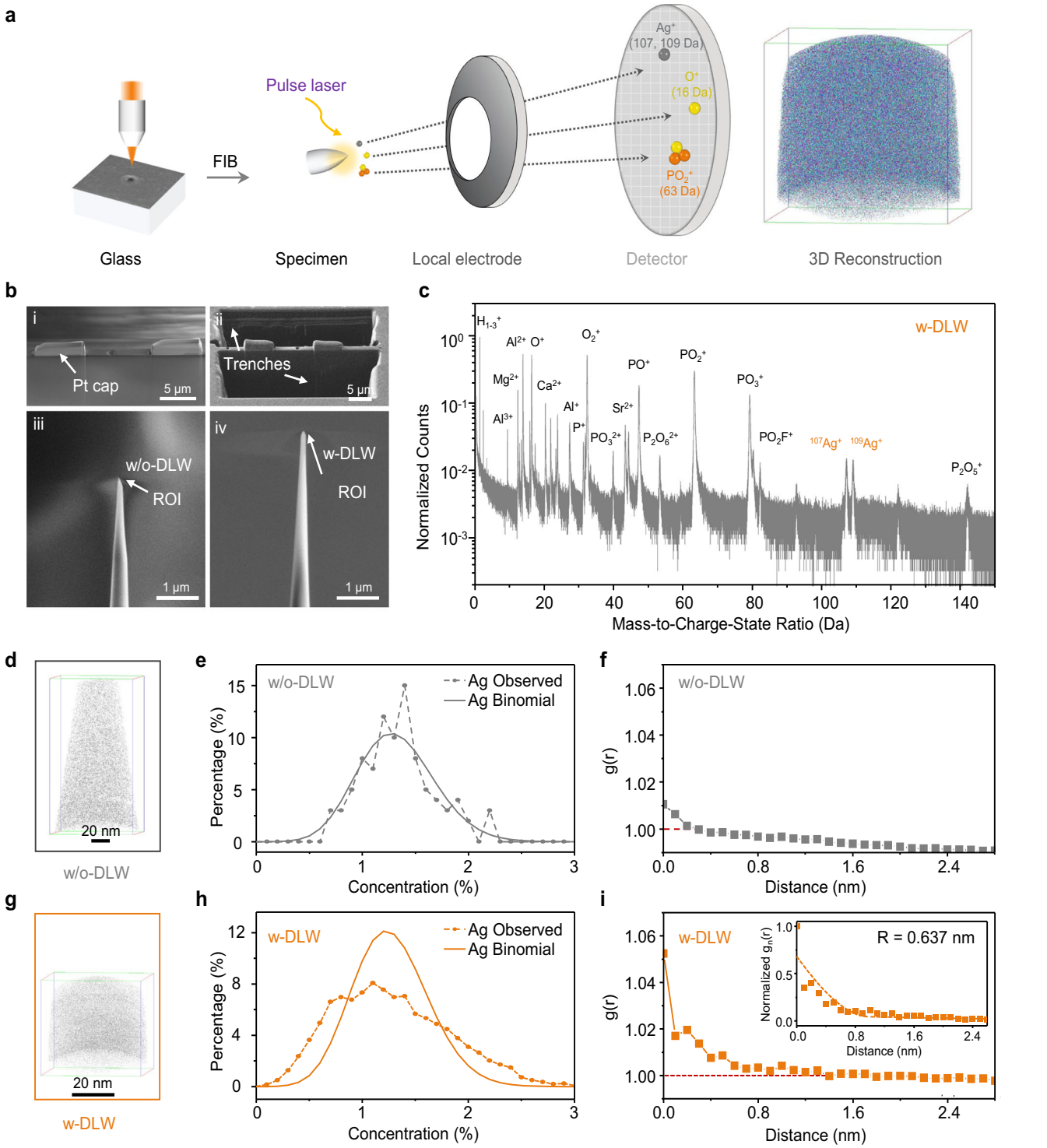

Fig. 5 | Atom probe tomography of Ag clusters. a Schematic illustration of APT measurement. **b** FIB-based APT specimen preparation: i SEM image of a protective Pt cap over the ROI; ii an undercut bar ready for extraction; iii, iv tips of w/o-DLW and w-DLW after annular milling. **c** Mass spectrum of w-DLW tip. **d**, **g** 3D map reconstruction of Ag in w/o-DLW and w-DLW. **e**, **h** FD analysis of Ag: dotted lines with symbols were the experimental data, and solid lines were the modeled binomial distributions. **f**, **i** Ag-Ag pair correlation function, $g(r)$, inset in (**i**) shows normalized $g_n(r)$ and fitted radius result.

structures (Supplementary Fig. S9). The formation of clusters is expected to be limited. In this context, the significance of the glass material becomes evident. The generated Ag clusters evidence the beneficial impact of glass photosensitization, which was facilitated by the introduction of fluorine anions. This reaffirms the effectiveness of the design strategy for PF glasses.

Atom probe tomography of Ag clusters under DLW

To characterize the laser-induced Ag clusters, APT was performed (Fig. 5a). Using a dual-beam focused ion beam, two needle-shaped specimens of the sample without DLW (w/o-DLW) and with direct laser writing (w-DLW) were prepared (Fig. 5b, Supplementary Note. 6and Supplementary Figs. 15–18). Upon laser pulsing, ions in the tip were evaporated from the surface. These ions were directed into a position-sensitive detector with their mass-to-charge ratio recorded by time-of-flight mass spectrometry. Here, the potential for overheating of the specimen tip was deemed minimal, as indicated by the absence of thermal tails in mass spectra (Fig. 5c and Supplementary Fig. 19), suggesting rapid cooling[47,48]. Subsequently, the recorded ion positions on the

detector were utilized to reconstruct the spatial distribution (Supplementary Figs. 20–21).

Visual examination of the 3D reconstructions of Ag revealed no signs of aggregation (Fig. 5d, g). To assess the Ag distribution, frequency distribution (FD) analysis was applied[49]. This analysis begins with a comparison between the FD of Ag experimental data and the theoretical randomized distribution, the latter characterized by binomial probability. As shown in Fig. 5e, the experimental and binomial curves for w/o-DLW were almost overlapped, suggesting a randomized distribution of Ag. However, in w-DLW, the experimental curve presented a broadened peak (Fig. 5h). Given the conservation of the total number of atoms, this broadening indicated that some blocks contain fewer Ag atoms while others contain more than expected. The long tails indicate blocks with high concentrations of Ag atoms, suggesting Ag aggregation[50].

Moreover, the FD analysis incorporates χ^2 statistics to quantify the degree of randomness, assessed by the p-value[51,52]. In w/o-DLW, the Ag experimental curve matched with the theoretical binomial distribution, with a p-value of 0.7, larger than the confidence level typically set at 0.01, suggesting the random distribution of experimental Ag. However, in the w-DLW, a p-value of < 0.001 indicated the aggregation of Ag. Following this, the Pearson coefficient (μ) was used to remove the sample size dependence and give a more accurate estimation, where $\mu = 1$ suggests complete non-randomness and $\mu = 0$ suggests complete randomness. Comparing μ values of w/o-DLW (0.7225) and w-DLW (0.2201) reveals a greater deviation from randomness in w-DLW after laser writing.

Beyond the FD analysis and χ^2 statistics, the Ag aggregation was also reflected in the nearest neighbor distribution (NND) analysis[53]. The Ag NND for w/o-DLW presented a minimal deviation from the randomized distribution (Supplementary Figs. 22, 23). However, in w-DLW, there was a gradual deviation that suggests Ag aggregation. This was further examined using the maximum separation method (Supplementary Note. 7 and Supplementary Figs. 24–26), where Ag clusters with radii larger than 1 nm in w-DLW were found, while clusters in w/o-DLW were smaller than 1 nm (Supplementary Fig. 27). In addition, the Ag-Ag pair correlation functions, $g(r)$, in w-DLW showed a more positive Ag correlation, reflecting the Ag clustering tendency (Fig. 5f, i)[54,55]. Moreover, the Ag-Ag correlation distance (distance at which the correlation approaches unity) was longer in w-DLW than in w/o-DLW, indicating a higher proportion of Ag atoms participating in clusters. For a sphere of radius (R), the normalized correlation function $g_n(r)$ can be fitted to determine the R-value, according to Eq. (1) and (2)[56]:

$$g_n(r) = \begin{cases} 1 - \dfrac{3r}{4R} - \dfrac{r^3}{16R^3}, & if\ r \le 2R) \quad (1) \\ 0, & if\ r > 2R) \quad (2) \end{cases}$$

In the w-DLW region, the radius (R) was determined to be 0.673 nm. These findings collectively confirmed the presence of Ag clusters and offer valuable insights into the aggregation and distribution of Ag clusters in the DLW region.

Optical data storage demonstration

Considering the bright PL and low energy consumption, PF25 and single-pulse laser energy with 0.5 μJ were selected for ODS demonstration (Fig. 6a). A 7 × 7 dot array (Fig. 6b) and the logo of Zhejiang University (Fig. 6c) were written. Figure 6d shows the PL intensity in the array plotted against the horizontal axis. A distinct emissive peak was observed at the inscribed regions, enabling the representation of binary information as emissive dots denoting 1, interspersed with non-emissive intervals representing 0. Each dot occupied a volume of 2×10^{-11} cm^{-3}, corresponding to a storage capacity of 5.82 GB cm^{-3} (or 197 GB per glass disk in 120 × 3 mm^3 form). This capacity exceeds that of traditional DVDs, which typically range from 5 to 25 GB[57]. Notably, there is potential for achieving even higher storage densities by using a more tightly focused laser beam or implementing multilevel encoding within a single data unit[58]. The spatial processing capability of DLW, combined with the homogeneous matrix, enabled the patterning of information at various depths without crosstalk. Three letters, Z, J, and U, were written with a layer interval of 5 μm, demonstrating the potential for high signal-to-noise and multilayer storage (Fig. 6e).

In conclusion, we demonstrated the simultaneous design of photosensitive glass and atomic characterization of DLW-induced Ag clusters by APT. The fluorine-modified fluorophosphate glass facilitated the efficient creation of photoluminescent Ag clusters under low-energy single-pulsed DLW. The introduction of fluorine played a dual role by disrupting the glass network, creating conducive channels for Ag species clustering, and introducing defect precursors that trapped holes, thereby enhancing electron availability for Ag^+ ion reduction. High laser energy resulted in a dot + ring PL pattern, where the central dot was glass defect, and the peripheral ring was Ag clusters. Moreover, the use of APT supported the formation of DLW-induced Ag clusters. These findings, along with the optimization of glass structure and the use of advanced characterization techniques, enhance our understanding of DLW-induced Ag clusters in glass and offer promising prospects for developing photo-functional materials.

Methods

Materials and reagents

Glass samples with the composition of (95-x)$Al(PO_3)_3$-xMF_2–5Ag_2O (M = Mg, Ca, Sr; x = 5–30 mol%) were prepared using the melt-quenching method with $Al(PO_3)_3$, MgF_2, CaF_2, SrF_2, and $AgNO_3$ as raw materials. These are denoted as PFx, where x represents the mol% of MF2. PF0 refers to glass with the composition 70$Al(PO_3)_3$–25MO-5Ag_2O, with MO being alkaline earth metal oxides (M = Mg, Ca, Sr). $Al(PO_3)_3$ (Analytical reagent) were purchased from Thermo Scientific Reagent Co. MgF_2, CaF_2, SrF_2, MgO, CaO, and SrO (Analytical reagent) were purchased from Aladdin Reagent Co. $AgNO_3$ (Analytical reagent) was purchased from Sinopharm Chemical Reagent Co. A 30 g batch of each glass composition was weighed and mixed homogenously in the agate mortar. Then, the mixture was melted in alumina crucibles with closed lips to minimize fluorine loss at 1450 °C for 60 min. The melt was then poured onto a cold stainless-steel plate, annealed, and then immediately pressed with another plate to increase the cooling rate and promote glass formation. The obtained glasses were then cut, ground, and polished for subsequent measurements.

Direct laser writing in glasses

Single-pulsed direct laser writing was conducted on a regeneratively amplified Yb: KGW laser (PHAROS, Light Conversion) with a central wavelength of 1030 nm, pulse duration of 220 fs, and repetition rate of 1 kHz. The laser was focused 100 μm below the glass surface using a 50 × (NA = 0.8) objective lens. The diameter of the laser spot was about 2 μm.

Materials characterizations

X-ray powder diffraction (XRD) was performed using an X-ray diffractometer (Shimadzu XRD-6000) with a 5 °C min^−1 scanning speed. The UV-Vis absorption spectra were recorded in a UV-Vis spectrophotometer (Hitachi U-4100). The glass transition temperature (Tg) and crystallization temperature (Tc) were collected from the differential scanning calorimeter (DSC, Q100 TA). The heating rate was 10 °C min^−1. Photoluminescence (PL), Photoluminescence excitation (PLE), and lifetime decay spectra were recorded by Edinburgh Instruments FLSP920 spectrophotometer. The pH of the glass leachate solutions was measured using a pH meter (FiveEasy PlusTM, FB28). Optical images of the laser-modified regions were captured by a CCD camera attached to a Nikon microscope (Eclipse 80i). PL spectra of the laser-modified region were taken from a confocal microscope (λ_{ex} = 405 nm, LSM780, Zeiss). The PL of Ag clusters after DLW was carried out on a

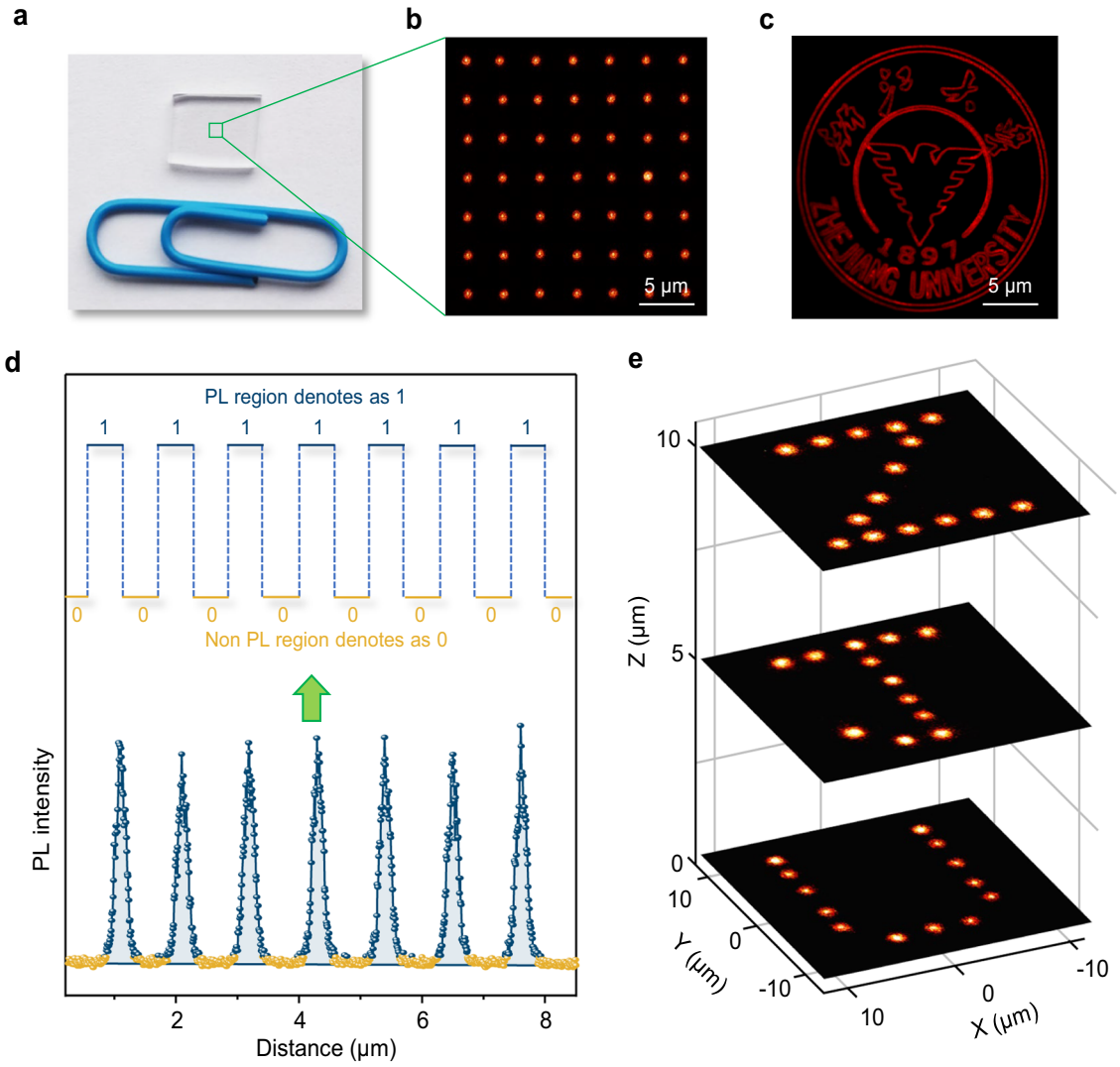

Fig. 6 | Demonstration of 3D optical data storage using PF25 glass. a Photo of PF25, the width was close to that of a paper clip, and the length was one-third of it. **b** A 7 × 7 information points array. **c** Zhejiang University logo. **d** Intensity profile along the horizontal direction of the array, realizing the 0 and 1 state change in binary information. **e** Three-level stack of Z, J, and U with an interval of 5 μm.

homemade confocal microscope. Raman spectra and mapping were collected by Raman spectrometer (LabRAM HR Evolution) with a 532 nm laser excitation. The ^{27}Al nuclear magnetic resonance (NMR) spectra were recorded on an Agilent 600 DD2 spectrometer at a frequency of 156.25 MHz (14.1 T), with 3.6 μs pulses and 10 s recycle time in a 4 mm double-resonance probe. ^{31}P NMR spectra were collected at a frequency of 242.76 MHz (14.1 T) using 3.0 μs pulses and 5 s recycle delays. The $AlCl_3$ and H_3PO_3 were chosen as the chemical shift reference. SEM images and EMPA were carried out on EMPA-1720 (SHIMADZU) at an accelerating voltage of 15 kV and a current of 10 nA. Electron paramagnetic resonance (EPR) spectra were recorded on a Bruker A300 ESR spectrometer in X-ban. The samples were loaded into a quartz tube and cooled to 120 K. A dual-beam SEM/FIB (FEI Helios Nanolab 600i) was used to prepare lift-out samples.

APT experiments were conducted on a CAMECA LEAP 4000H XR operated in laser pulse mode using 355 nm Nd:YVO_4 ultraviolet (UV) laser. The detection efficiency was 37%. Data were acquired in laser pulsing mode at a specimen temperature of 50 K, with a target evaporation rate of 0.5 ions per 100 pulses, pulse duration of 10 ps, pulsing rate of 200 kHz, and laser pulse energy of 60 pJ. The raw data were processed by the commercial IVAS 3.4.4 software to map the position and mass-to-charge ratio of each species.

ab initio Molecular dynamics simulations

ab initio molecular dynamics simulations were carried out on a cubic sample made up of ~1000 atoms with random coordinates by Packmol (v20.14.1)[59]. Two compositions, the 70Al$(PO_3)_3$–5Ag_2O-25CaO (without fluorine) and 70Al$(PO_3)_3$–5Ag_2O-25CaF_2 (with fluorine) were studied. Notably, Ca was chosen to represent the alkaline earth metals (Mg, Ca, Sr), as they all exert as the glass modifier. These two systems were subjected to structural optimization using the Density Functional Theory method based on DZVP-MOLOPT-SR-GTH. Starting from the initial configurations, Born-Oppenheimer Molecular Dynamics (BOMD) was applied[60]. The high-temperature melt at 2000 K was quenched to 300 K over a period of 300 ps in the NPT ensemble (constant number of atoms, constant pressure, and constant temperature). The glass was relaxed at 300 K under atmospheric pressure for 5 ps. Periodic boundary conditions were applied in all directions. The visualization of local atomic structure was facilitated by VESTA (Ver 3.4.5)[61].

Data availability

The data represented in Figs. 2a, b, 3b–e, 4a, b, 5c, e, f, h, i, and 6d are provided as Source Data file. All data in Supplementary Information are available from the corresponding author on request. Source data are provided in this paper.

References

1. Hayashi, S., Tsunemitsu, K. & Terakawa, M. Laser direct writing of graphene quantum dots inside a transparent polymer. *Nano Lett.* **22**, 775–782 (2021).
2. Ródenas, A. et al. Three-dimensional femtosecond laser nanolithography of crystals. *Nat. Photonics* **13**, 105–109 (2018).
3. Sun, K. et al. Three-dimensional direct lithography of stable perovskite nanocrystals in glass. *Science* **375**, 307–310 (2022).
4. Zheng, W. et al. Fluorescence–Phosphorescence manipulation and atom probe observation of fully inorganic silver quantum clusters: imitating from and behaving beyond organic hosts. *Adv. Opt. Mater.* **10**, 2101632 (2021).
5. Grandjean, D. et al. Origin of the bright photoluminescence of few-atom silver clusters confined in LTA zeolites. *Science* **361**, 686–690 (2018).
6. Park, C. H., Petit, Y., Canioni, L. & Park, S. H. Five-dimensional optical data storage based on ellipse orientation and fluorescence intensity in a silver-sensitized commercial glass. *Micromachines* **11**, 1026 (2020).
7. Tan, D., Jiang, P., Xu, B. & Qiu, J. Single-pulse-induced ultrafast spatial clustering of metal in glass: fine tunability and application. *Adv. Photonics Res.* **2**, 2000121 (2021).
8. Lipatiev, A. S. et al. Single-Pulse laser-induced Ag nanoclustering in silver-doped glass for high-density 3D-rewritable optical data storage. *ACS Appl. Nano Mater.* **5**, 6750–6756 (2022).
9. Bellec, M. et al. 3D patterning at the nanoscale of fluorescent emitters in glass. *J. Phys. Chem. C.* **114**, 15584–15588 (2010).
10. Tikhomirov, V. K. et al. Preparation and luminescence of bulk oxyfluoride glasses doped with Ag nanoclusters. *Opt. Express* **18**, 22032–2203240 (2010).
11. Guérineau, T. et al. Structural influence on the femtosecond laser ability to create fluorescent patterns in silver-containing sodium-gallium phosphate glasses. *Opt. Mater. Express* **8**, 3748–3760 (2018).
12. Stalmashonak, A., Abdolvand, A. & Seifert, G. Metal-glass nanocomposite for optical storage of information. *Appl. Phys. Lett.* **99**, 201904 (2011).
13. Fares, H. et al. Femtosecond laser micro-patterning of optical properties and functionalities in novel photosensitive silver-containing fluorophosphate glasses. *J. Non Cryst. Solids* **517**, 51–56 (2019).
14. Gattass, R. R. & Mazur, E. Femtosecond laser micromachining in transparent materials. *Nat. Photonics* **2**, 219–225 (2008).
15. Zhou, R., Calahoo, C., Ding, Y. & Wondraczek, L. Role of Ag^{+} ions in determining Ce^{3+} optical properties in fluorophosphate and sulfophosphate glasses. *ACS Omega* **6**, 30093–30107 (2021).
16. Fares, H., Castro, T., Orives, J. R., Franco, D. F. & Nalin, M. White light and multicolor emission tuning in Ag nanocluster doped fluorophosphate glasses. *RSC Adv.* **7**, 44356–44365 (2017).
17. Kolobkova, E., Kuznetsova, M. S. & Nikonorov, N. Ag/Na ion exchange in fluorophosphate glasses and formation of Ag nanoparticles in the bulk and on the surface of the glass. *ACS Appl Nano Mater.* **2**, 6928–6938 (2019).
18. Li, Y. W. & Jin, R. C. Seeing ligands on nanoclusters and in their assemblies by X-ray crystallography: atomically precise nanochemistry and beyond. *J. Am. Chem. Soc.* **142**, 13627–13644 (2020).
19. Liu, X. et al. Quantifying the solution structure of metal nanoclusters using small-angle neutron scattering. *Angew. Chem. Int. Ed.* **61**, e202209751 (2022).
20. Schneider, C. M. & Colfen, H. High-resolution analysis of small silver clusters by analytical ultracentrifugation. *J. Phys. Chem. Lett.* **10**, 6558–6564 (2019).
21. Aghakhani, S. et al. Atomic scale reversible opto-structural switching of few atom luminescent silver clusters confined in LTA zeolites. *Nanoscale* **10**, 11467–11476 (2018).
22. Gault, B. et al. Atom probe tomography. *Nat. Rev. Methods Prim.* **1**, 51 (2021).
23. Kelly T. F., Geiser B. P., Ulfig R. M., Prosa T. J. & Larson D. J. *Local Electrode Atom Probe Tomography: a User's Guide*. (Springer, 2013).
24. Schreiber, D. & Ryan, J. V. Atom probe tomography of glasses. In *Modern Glass Characterization* (2015).
25. Perea, D. E. et al. Tomographic mapping of the nanoscale water-filled pore structure in corroded borosilicate glass. *Npj Mater. Degrad.* **4**, 8 (2020).
26. Zheng, Q. et al. Understanding glass through differential scanning calorimetry. *Chem. Rev.* **119**, 7848–7939 (2019).
27. Baia, L., Muresan, D., Baia, M., Popp, J. & Simon, S. Structural properties of silver nanoclusters–phosphate glass composites. *Vib. Spectrosc.* **43**, 313–318 (2007).
28. Smedskjaer M. M., Hermansen C. & Youngman R. E. Topological engineering of glasses using temperature-dependent constraints. MRS Bulletin **42**, 29–33 (2017).
29. Aniya, M. Medium range structure and activation energy of ion transport in glasses. *Solid State Ion.* **154**, 343–348 (2002).
30. Möncke, D. & Eckert, H. Review on the structural analysis of fluoride-phosphate and fluoro-phosphate glasses. *J. Non Cryst. Solids. X***3**, 100026 (2019).
31. Wegner, S., van Wüllen, L. & Tricot, G. The structure of alumino-phosphate glasses revisited: Application of modern solid state NMR strategies to determine structural motifs on intermediate length scales. *J. Non Cryst. Solids* **354**, 1703–1714 (2008).
32. Tan, L. et al. Tailoring cluster configurations enables tunable broadband luminescence in glass. *Chem. Mater.* **32**, 8653–8661 (2020).
33. Royon, A., Petit, Y., Papon, G., Richardson, M. & Canioni, L. Femtosecond laser induced photochemistry in materials tailored with photosensitive agents [Invited]. *Opt. Mater. Express* **1**, 866–882 (2011).
34. Pivin, J. C., Roger, G., Garcia, M. A., Singh, F. & Avasthi, D. K. Nucleation and growth of Ag clusters in silicate glasses under ion irradiation. *Nucl. Instrum. Methods Phys. Res. Sect. B Beam Interact. Mater. At.* **215**, 373–384 (2004).
35. Dmitryuk, A. V., Paramzina, S. E., Perminov, A. S., Solov'eva, N. D. & Timofeev, N. T. The influence of glass composition on the properties of silver-doped radiophotoluminescent phosphate glasses. *J. Non Cryst. Solids* **202**, 173–177 (1996).
36. Maurel, C. et al. Luminescence properties of silver zinc phosphate glasses following different irradiations. *J. Lumin* **129**, 1514–1518 (2009).
37. Bourhis, K. et al. Femtosecond laser structuring and optical properties of a silver and zinc phosphate glass. *J. Non Cryst. Solids* **356**, 2658–2665 (2010).
38. Fletcher, L. B. et al. Femtosecond laser writing of waveguides in zinc phosphate glasses [Invited].*Opt. Mater. Express* **1**, 845–855 (2011).
39. Masai, H., Okada, G., Kawaguchi, N. & Yanagida, T. Relationship between defect formation by X-ray irradiation and thermally stimulated luminescence of binary zinc phosphate glasses. *Opt. Mater. Express* **9**, 2037–2045 (2019).
40. Petit, Y. et al. On the femtosecond laser-induced photochemistry in silver-containing oxide glasses: mechanisms, related optical and physico-chemical properties, and technological applications. *Adv. Opt. Techn.* **7**, 291–309 (2018).
41. Petit, L. Radiation effects on phosphate glasses: Review. *Int J. Appl. Glass Sci.* **11**, 511–521 (2019).
42. Griscom, D. L. Defects in amorphous insulators. *J. Non Cryst. Solids* **31**, 241–266 (1978).
43. Belloni, J. Photography: enhancing sensitivity by silver-halide crystal doping. *Radiat. Phys. Chem.* **67**, 291–296 (2003).
44. Glezer, E. N. & Mazur, E. Ultrafast-laser driven micro-explosions in transparent materials. *Appl. Phys. Lett.* **71**, 882–884 (1997).
45. Vailionis, A. et al. Evidence of superdense aluminium synthesized by ultrafast microexplosion. *Nat. Commun.* **2**, 445 (2011).

46. Smetanina, E. et al. Modeling of cluster organization in metal-doped oxide glasses irradiated by a train of femtosecond laser pulses. *Phys. Rev. A* **93**, 013846 (2016).
47. Bachhav, M. N. et al. Evidence of lateral heat transfer during laser assisted atom probe tomography analysis of large band gap materials. *Appl. Phys. Lett.* **99**, 084101 (2011).
48. Kim, S.-H., Stephenson, L. T., Schwarz, T. & Gault, B. Chemical analysis for alkali ion–exchanged glass using Atom Probe Tomography. *Microsc. Microanal.* **29**, 890–899 (2023).
49. Moody, M. P., Stephenson, L. T., Ceguerra, A. V. & Ringer, S. P. Quantitative binomial distribution analyses of nanoscale like-solute atom clustering and segregation in atom probe tomography data. *Microsc. Res. Tech.* **71**, 542–550 (2008).
50. Gault, B., Moody, M. P., Cairney, J. M., Ringer, S. P. Analysis Techniques for Atom Probe Tomography. In *Atom Probe Microscopy*. (Springer New York, 2012).
51. Mitchell, A. L. et al. Nanoscale microstructure and chemistry of transparent gahnite glass-ceramics revealed by atom probe tomography. *Scr. Mater.* **203**, 114110 (2021).
52. Perea, D. E. et al. Determining the location and nearest neighbours of aluminium in zeolites with atom probe tomography. *Nat. Commun.* **6**, 7589 (2015).
53. Stephenson, L. T., Moody, M. P., Liddicoat, P. V. & Ringer, S. P. New techniques for the analysis of fine-scaled clustering phenomena within atom probe tomography (APT) data. *Microsc Microanal.* **13**, 448–463 (2007).
54. De Geuser, F., Lefebvre, W. & Blavette, D. 3D atom probe study of solute atoms clustering during natural ageing and pre-ageing of an Al-Mg-Si alloy. *Philos. Mag. Lett.* **86**, 227–234 (2006).
55. Schmidt, J. E., Oord, R., Guo, W., Poplawsky, J. D. & Weckhuysen, B. M. Nanoscale tomography reveals the deactivation of automotive copper-exchanged zeolite catalysts. *Nat. Commun.* **8**, 1666 (2017).
56. Zhao, H., Gault, B., Ponge, D., Raabe, D. & De Geuser, F. Parameter free quantitative analysis of atom probe data by correlation functions: Application to the precipitation in Al-Zn-Mg-Cu. *Scr. Mater.* **154**, 106–110 (2018).
57. Gao, L., Zhang, Q., Evans, R. A. & Gu, M. 4D Ultra-high-density long data storage supported by a solid-state optically active polymeric material with high thermal stability. *Adv. Opt. Mater.* **9**, 2100487 (2021).
58. Gu, M., Zhang, Q. M. & Lamon, S. Nanomaterials for optical data storage. *Nat. Rev. Mater.* **1**, 16070 (2016).
59. Martinez, L., Andrade, R., Birgin, E. G. & Martinez, J. M. PACKMOL: a package for building initial configurations for molecular dynamics simulations. *J. Comput. Chem.* **30**, 2157–2164 (2009).
60. Ainsworth, R. I., Christie, J. K. & de Leeuw, N. H. On the structure of biomedical silver-doped phosphate-based glasses from molecular dynamics simulations. *Phys. Chem. Chem. Phys.* **16**, 21135–21143 (2014).
61. Momma, K. & Izumi, F. VESTA: a three-dimensional visualization system for electronic and structural analysis. *J. Appl. Crystallogr.* **41**, 653–658 (2008).

Acknowledgements

W.Z. and Z.W. contributed equally to this work. We acknowledge the financial support from the National Natural Science Foundation of China (No. 52172008; 51672243), the Postdoctoral Fellowship Program of CPSF (GZC20241465).

Author contributions

X.Q., D.T., and W.Z. conceived the idea. W.Z. performed the experiments and analyzed the data. W.C. conducted theoretical calculations. Z.W. did the direct laser writing. W.Z., H.L., G.Y., and M.Z. did the APT test. Q.X., J.Z., J.Q., G.Q., and X.F. took part in the discussion and gave important suggestions. W.Z., X.Q., and D.T. wrote the paper. All authors approved the final version of the paper.

Competing interests

The authors declare no competing interests.

Additional information

Supplementary information The online version contains supplementary material available at https://doi.org/10.1038/s41467-024-52628-4.

Correspondence and requests for materials should be addressed to Xvsheng Qiao or Dezhi Tan.

Peer review information *Nature Communications* thanks Yannick Petit and the other anonymous reviewers for their contribution to the peer review of this work. A peer review file is available.

Vol. 35 • No. 47 • November 23 • 2023

www.advmat.de

ADVANCED MATERIALS

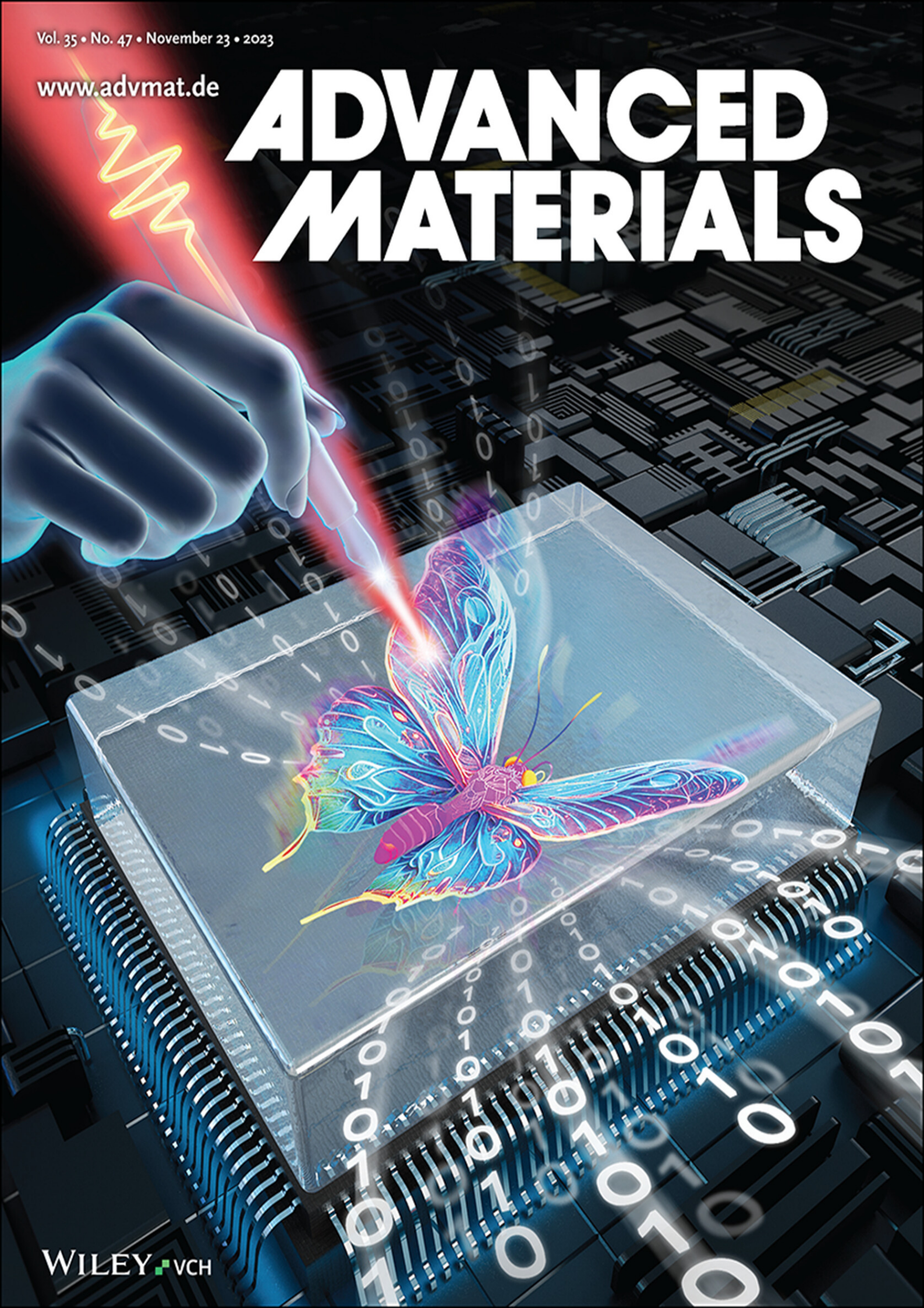

WILEY VCH

3D Imprinting of Voxel-Level Structural Colors in Lithium Niobate Crystal

Zhuo Wang, Bo Zhang, Ziquan Wang, Jie Zhang, Peter G Kazansky, Dezhi Tan,* and Jianrong Qiu**

Advanced coloration methods are of pivotal importance in science, technology, and engineering. However, 3D structural colors that are critical for emerging multidimensional information representation and recording are rarely achievable. Here, a facile voxel-level programmable 3D structural coloration in the bulk lithium niobate ($LiNbO_3$) crystal is reported. This is achieved by engineering wavelength-selective interference between ordinary (O) and extraordinary (E) light in the crystal matrix. To induce effective phase contrast between O and E light for establishing the highly localized interference across the visible band, the presence of a pulse-internal-coupling effect is revealed in the single-pulse ultrafast laser–crystal interaction and an ultrafast-laser-induced micro-amorphization (MA) strategy is thus developed to manipulate local matrix structure. Consequently, micro–nanoscale colorful voxels can be fast inscribed into any spatial position of the crystal matrix in one step. It is demonstrated that the colors can be flexibly manipulated and quickly extracted in 3D space. Multidimensional MA-color data storage with large capacity, high writing and readout speed, long lifetime, and excellent stability under harsh conditions is achieved. The present principle enables multifunctional 3D structural coloration devices inside high-refractive-index transparent dielectrics and can serve as a general platform to innovate next-generation information optics.

1. Introduction

Structural colors originated from the interaction between the polychromatic light and micro–nano photonic structures have been created for various applications in high-resolution optical display, sensing, anti-counterfeiting, information encryption, and recording.[1–6] However, the current structural colors are generally displayed in 2D substrates.[7–9] Although complex bulk photonic crystals have recently been designed to generate quasi 3D colors,[10–12] the color voxels are largely interconnected rather than independent and the spatial extent of coloration is limited to a small scale close to surfaces. Freely imprinting voxel-level controllable structural colors in 3D space enables implanting additional degrees of freedom in light modulation and device functionalization, such as 3D display and high-density data storage. However, due to the lack of a suitable carrier, this vision remains highly challenging and even impossible via traditional coloration approaches.

One way to solve this problem is to develop a principle that can print color voxels in 3D transparent media. Recently, ultrafast laser direct writing (ULDW) in transparent dielectrics has been established as an excellent platform for creating 3D micro–nano functional structures,[13–20] which endows matrix materials with unprecedented functionalities. Representatively, domain engineering at micro–nano scales using ULDW in lithium niobate ($LiNbO_3$) crystals has been used to produce 3D nonlinear photonic crystals.[21–23] However, structural coloration is extremely difficult to generate inside such media, because the high refractive index of the matrix severely impairs the phase modulation capability of photonic structures. Generally, transparent

Z. Wang, B. Zhang, Z. Wang, J. Zhang, J. Qiu
State Key Laboratory of Modern Optical Instrumentation
College of Optical Science and Engineering
Zhejiang University
Hangzhou 310027, China
E-mail: zhangbobo@zju.edu.cn; qjr@zju.edu.cn

P. G Kazansky
Optoelectronics Research Centre
University of Southampton
Southampton SO17 1BJ, UK

D. Tan
Zhejiang Lab
Hangzhou 311100, China
E-mail: wctdz@zju.edu.cn

D. Tan
School of Material Science and Engineering
Zhejiang University
Hangzhou 310027, China

J. Qiu
CAS Center for Excellence in Ultra-intense Laser Science
Chinese Academy of Sciences
Shanghai 201800, China

The ORCID identification number(s) for the author(s) of this article can be found under https://doi.org/10.1002/adma.202303256

DOI: 10.1002/adma.202303256

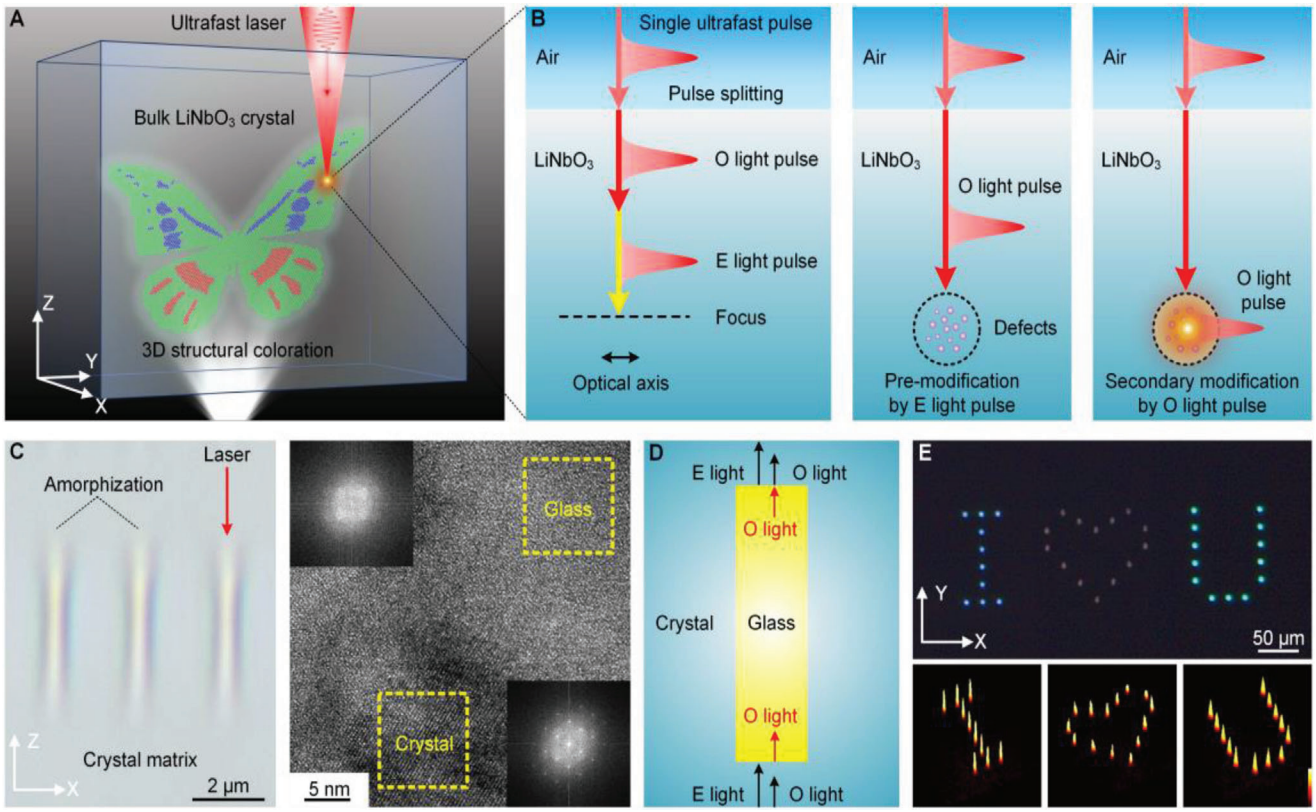

Figure 1. Working principle of MA coloration. A) Schematic illustration showing 3D imprinting of voxel-level structural colors using MA coloration. B) Schematic illustration showing the mechanism of pulse-internal-coupling-assisted ULDW. C) Microscopy image color voxels written in the crystal matrix (left) and high-resolution transmission electron microscopy (HRTEM) image of the crystal-glass phase transition interface (right). Insets: fast Fourier transform (FFT) images of the dotted areas. Selected-area electron diffraction experimental results see Figure S5 (Supporting Information). D) Schematic illustration showing the light propagation behavior at MA zone. E) High SNR structural colors generated by MA voxels (top) and corresponding signal intensity mapping (bottom).

uniaxial crystals possess intrinsic structural anisotropy that allows for splitting one light beam into ordinary (O) and extraordinary (E) light. Using this, it is possible to generate 3D structural colors in high-refractive-index transparent uniaxial crystals by locally modulating the spatial interference of O and E light.

Taking $LiNbO_3$ as an example, we proposed an unprecedentedly facile 3D structural coloration strategy that uses ultrafast laser-induced local amorphization to significantly tune the phase difference of O and E light in the crystal matrix and thus create highly controllable voxelized interference colors in 3D space, which we call micro-amorphization (MA) coloration (**Figure 1**A). In the color imprinting, one color voxel can be fast created by a single ultrafast laser pulse and possesses a considerably high resolution. The color gamut covers the whole visible waveband and can be flexibly manipulated by multiple approaches, enabling programmable 3D full-color patterning. The excellent readability, manufacturability, and stability of MA colors make them fully compatible with current mature data reading and writing technologies and suitable for mass standardized production. Thus, it is highly anticipated to boost the practical applications of 3D structural colors in high-density data storage, encryption, anti-counterfeiting, and 3D display devices.

2. Results and Discussion

2.1. Working Principle of MA Coloration

To fast induce MA structures, we demonstrated a technique of pulse-internal-coupling-assisted ULDW in the $LiNbO_3$ crystal (Figure 1B), where the processing light is incident perpendicular to the optical axis and the intrinsic birefringence of $LiNbO_3$ is used to split the incident single ultrafast laser pulse into spatially coaxial but temporally separated E and O light pulses. As E light pulse transports faster than O light pulse in the $LiNbO_3$ crystal, E light pulse preliminarily modifies the raw material matrix and induces active defects to greatly promote the nonlinear optical absorption (Figures S2 and S3, Supporting Information). Then, O light pulse further irradiates the defective zone, enabling crystal-to-glass phase transition, and creating micro-amorphous structures in the crystal matrix (Figure 1C). Our experiments confirm that the coupling between the E and O light pulses is essential for activating the pulse-internal-coupling-assisted ULDW process (Figure S4, Supporting Information).

The MA color generation is essentially achieved by locally engineering the birefringence property of the crystal matrix. Specifically, when a polychromatic illuminating light beam propagates through MA domains, E light is partially eliminated in the glass

phase (Figure 1D), which will create a giant phase difference jump of O and E light at MA zone (Figure S6A, Supporting Information). By applying the chromatic polarization method to make O and E light possess polarization components in the same direction, constructive interference of specific wavebands and destructive interference of the background signal can be simultaneously achieved,[24] enabling high signal-to-noise ratio (SNR) structural colors (Figure 1E).

2.2. Manipulation of MA Colors

MA colors can be flexibly manipulated by multiple approaches. When probe polychromatic light is incident perpendicular to the optical axis, as there is no E light in the amorphous region, the phase difference of the O and E light beams that propagate through the MA zone can be expressed as:

$$\Delta\varphi = \frac{2\pi\,(d-l)}{\lambda}\,n_{\mathrm{o}} + \frac{2\pi l}{\lambda}n_{\mathrm{g}} - \frac{2\pi\,(d-l)}{\lambda}n_{\mathrm{e}} \tag{1}$$

where $\Delta\varphi$ is the phase difference, λ is the probe light wavelength, d is the sample thickness, l is the length of MA zone, n_{o}, n_{e}, and n_{g} are the refractive indexes of O light, E light, and the light propagating in the glass phase of MA zone, respectively. As refractive index is a dispersion function of wavelength (Figure S6B, Supporting Information), the light wavelength for establishing the constructive interference is essentially dependent on length of MA zone, where the mathematical relationship can be expressed as:

$$l = \frac{k\lambda^2}{2\pi\left(n_{\mathrm{g}}+n_{\mathrm{e}}-n_{\mathrm{o}}\right)} - d\,\frac{\left(n_{\mathrm{o}}-n_{\mathrm{e}}\right)}{\left(n_{\mathrm{g}}+n_{\mathrm{e}}-n_{\mathrm{o}}\right)} = \frac{k}{2\pi}f_1(\lambda) - df_2(\lambda) \tag{2}$$

where k is the interference order, $f_1(\lambda) = \lambda^2/(n_{\mathrm{g}}+n_{\mathrm{e}}-n_{\mathrm{o}})$, and $f_2(\lambda) = (n_{\mathrm{o}}-n_{\mathrm{e}})/(n_{\mathrm{g}}+n_{\mathrm{e}}-n_{\mathrm{o}})$.

From this principle, the color of each MA voxel, controlled by the phase difference of O and E light, can be regulated across the whole visible band by adjusting the length of MA zones (Figure S6C, Supporting Information). Theoretically, a larger MA length corresponds to a redshift of the structural color and a smaller MA length corresponds to a blueshift of the structural color (**Figure 2**A), which is confirmed by experimental results (Figure 2B). Here, we obtained a wide-gamut color manipulation from purple to red across the whole visible band with the corresponding wavelength ranging from 450 to 680 nm (Figure 2C,D) by finely regulating the processing parameters for each color voxel (Figure S8, Supporting Information). Notably, the relative angle of laser polarization to the optical axis of the crystal affects the energy distribution of O and E light (Figure 2E), which can be used to adjust the nonlinear optical absorption of the pulse-internal-coupling-based laser modification process. Specifically, when the energy of O light and E light is balanced, the nonlinear absorption is the strongest, while the nonlinear absorption is weakest when there is only O or E light energy (Figure. S9, Supporting Information). Here, we demonstrated that this energy redistribution process allows for quantitatively manipulating the intensity of the structural color by tuning the laser polarization (Figure 2F), which can provide an additional multiplexing channel for information recording.[25,26]

In addition to processing parameters, the already patterned MA colors can also be dynamically adjusted by introducing external stimuli. For example, the electro-optic effect of $LiNbO_3$ allows for tuning the refractive index contrast between glass phase and crystal matrix, which can be applied to tune the phase shift of the light passing through MA color voxels. Based on this, we further demonstrate the dynamic control of MA colors by electrically modulating the refractive index contrast between amorphous and crystal phases (Figure S10, Supporting Information).

2.3. Cross-Dimension Imprinting of Exquisite Images by Using MA Coloration

As ULDW is a voxel-level programmable patterning technique, each MA-color voxel can be independently decoded into its corresponding imprinting parameters, and thus MA coloration allows for freely imprinting voxels with various colors to form on-demand complex colorful patterns in 3D space. Here, multiple types of MA-color patterning and readout are demonstrated. For example, different monochromatic images of Maxwell's portrait (**Figure 3**A) and the chromatic image of the "Starry Night over the Rhone" are imprinted in $LiNbO_3$ (Figure 3B). By finely regulating the color of each voxel, we can further achieve complex adjustments to the tone style of the chromatic image of "The Starry Night", which is valid for both transmission and reflection viewing modes (Figure 3C). The image resolution can generally exceed 2540 dpi, and the highest resolution can reach ≈50 800 dpi (Figure S11, Supporting Information). Besides planar patterning, 3D color imprinting in the crystal matrix is also demonstrated, including basic (Figure 3D) and customized geometries (Figure 3E), curves, and characters (Figure S12, Supporting Information), whose color voxels are completely independent and their color features can be well controlled at any position in 3D space.

Owing to the wavelength selectivity of the chromatic polarization-based coloration principle, the color of voxels can only be identified by their corresponding illumination wavebands (Figure S13, Supporting Information). Thus, confidential information can be hidden by superimposing different color voxels together. The hidden information (Newton's portrait) is completely unrecognizable under white light illumination or using birefringence imaging (Figure 3F,i,ii) and can only be extracted by illuminating the sample with a specific waveband in a chromatic polarization microscopic system (Figure 3Fiii). Illuminating by a wrong waveband will lead to fake information (Maxwell's portrait) (Figure 3Fiv). By designing more complex color combos, MA colors can be employed for information encryption and anti-counterfeiting with multiple layers of security.

2.4. Comprehensive Performance Characterization of MA Colors

As a recording technique, robust multichannel information recognition is a highly valuable capability and represents the developmental trend of structural colors.[27] The 3D writability of MA coloration and the transparency of $LiNbO_3$ crystal confer at least four readout modes on MA colors (Figure S14A, Supporting

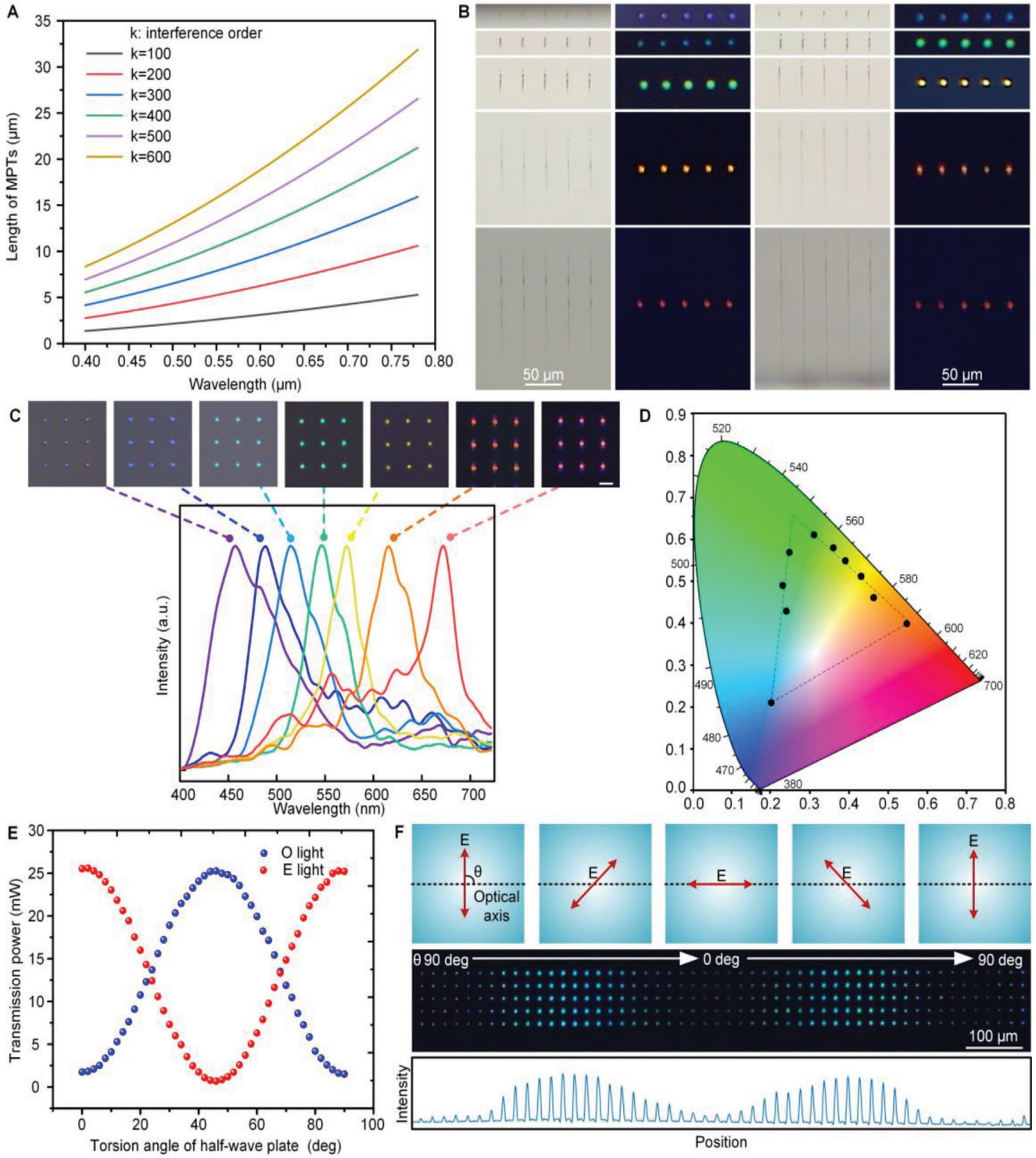

Figure 2. Manipulation of MA colors. A) The length of MA zones as functions of interference wavelengths and interference orders. B) Color regulation by tuning the length of MA zones. C) Multicolor voxels covering the visible band (top) and corresponding spectral features (bottom). Scale bar: 20 μm. D) Gamut of MA coloration in CIE chromaticity coordinates. Original spectral data of the chromaticity points see Figure S7 (Supporting Information). E) Polarization-driven energy distribution control of O and E light. F) Polarization-driven intensity manipulation of the color signal.

Information), including front and back readout using transmission and reflection illumination respectively. Importantly, the color signals extracted under different readout modes are the same because the phase difference of O and E light is essentially generated by the MA region and remains unchanged in both transmission and reflection readout modes (Figure S14B, Supporting Information). As a proof of concept, we demonstrated that the inscribed monochromatic image of Sir Newton's portrait (**Figure 4**A) can be read out from front and back sides in both transmission and reflection modes with good consistency (Figure 4Ai–iv). The reflection mode allows for using epi-illumination to read MA color patterns, which minifies the size of

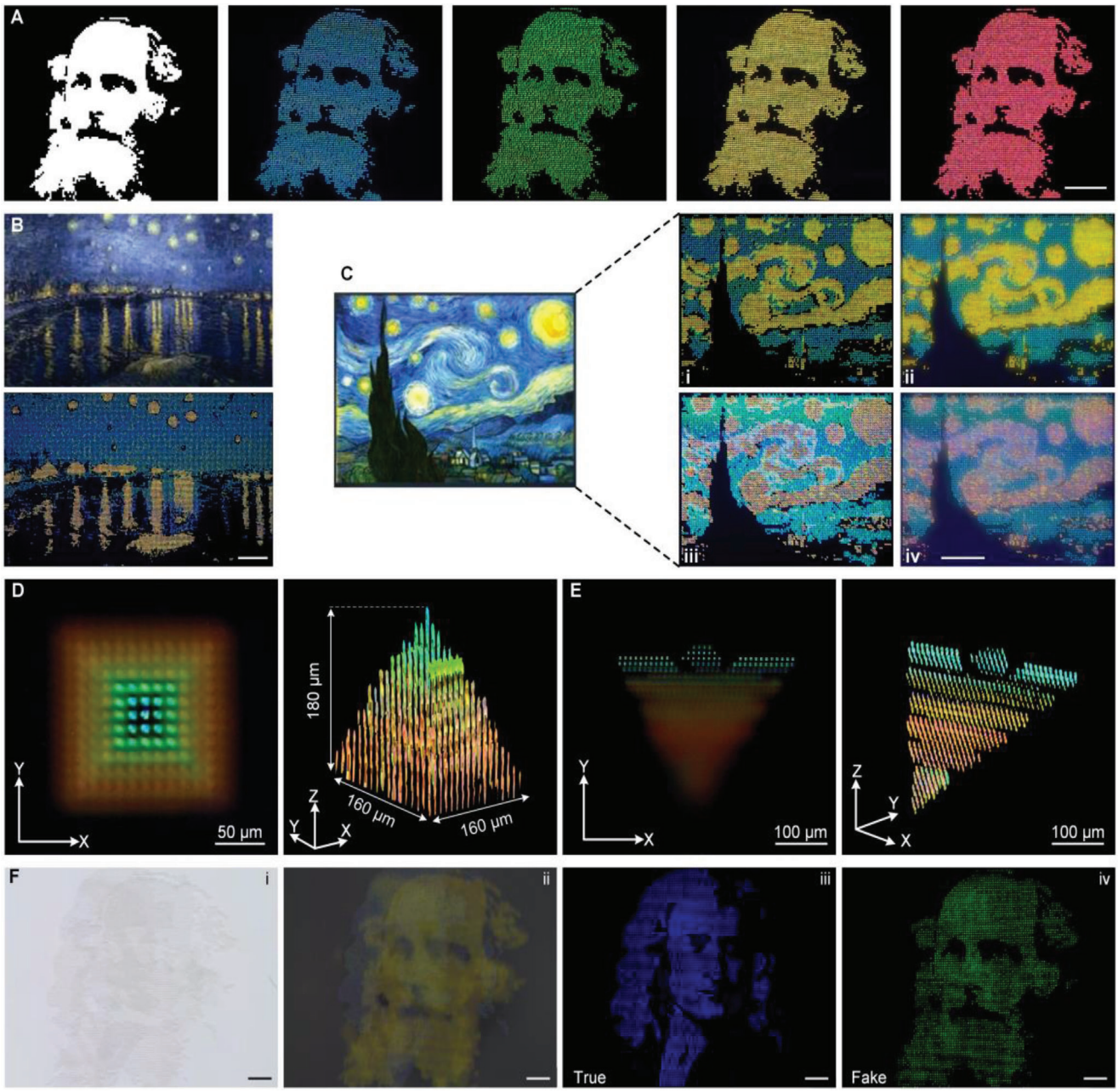

Figure 3. Cross-dimension imprinting of exquisite MA-color images. A) The designed grayscale and experimental monochromatic images of a portrait of Maxwell. B) Complicated chromatic picture patterning. Designed model (top) and experimental result (bottom). C) Voxel-level color tone tuning of a chromatic picture in both transmission mode (i, iii) and reflection mode (ii,iv). Designed model (left) and experimental results (right). Scale bars: (A) to (C), 200 μm. D,E) 3D chromatic patterning of MA colors, including basic geometry (D) and customized geometry (E). F) Optical information encryption where voxels with different color responses are superimposed together and indistinguishable by using white light illumination (i) or birefringence imaging (ii). Extraction of true information by illuminating the sample with specific monochromatic light centered at 445 nm (iii) while a wrong illumination (532 nm) will lead to fake information readout (iv). Scale bars: 100 μm. A,F) "James-Clerk-Maxwell" by Faded Times, Flickr: Public Domain Mark (https://creativecommons.org/publicdomain/mark/1.0). B) Gogh, Vincent van (1853–1890): Starry night. Arles (Starry Night on the Rhone), 1888. Oil on canvas, 72.5×92 cm. 2023©Photo Scala, Florence. Musee d'Orsay, Paris, France. Reproduced with permission. C) Gogh, Vincent van (1853–1890): The Starry Night, 1889. Oil on canvas, 29×36 ¼ (73.7×92.1 cm). Acquired through the Lillie P. Bliss Bequest. Acc. n.: 472.1941. 2023©Photo Scala, Florence. Digital image, The Museum of Modern Art, New York/Scala, Florence. Reproduced with permission.

the MA color reading devices and makes MA colors highly adaptable in mainstream data reading systems. And the transmission mode can provide higher readout accuracy by eliminating the disturbance from the scattering light caused by the reflection illumination. Furthermore, the localized interference-based coloration mechanism makes the identification of MA colors highly independent of the viewing angle (Figure S15, Supporting Information), showing the high robustness of MA color reading. These properties of MA coloration are of great significance for accurate, facile, flexible, and stable information extraction.

In addition to excellent readability, the pulse-internal-coupling assistance endows several appealing advantages for the present

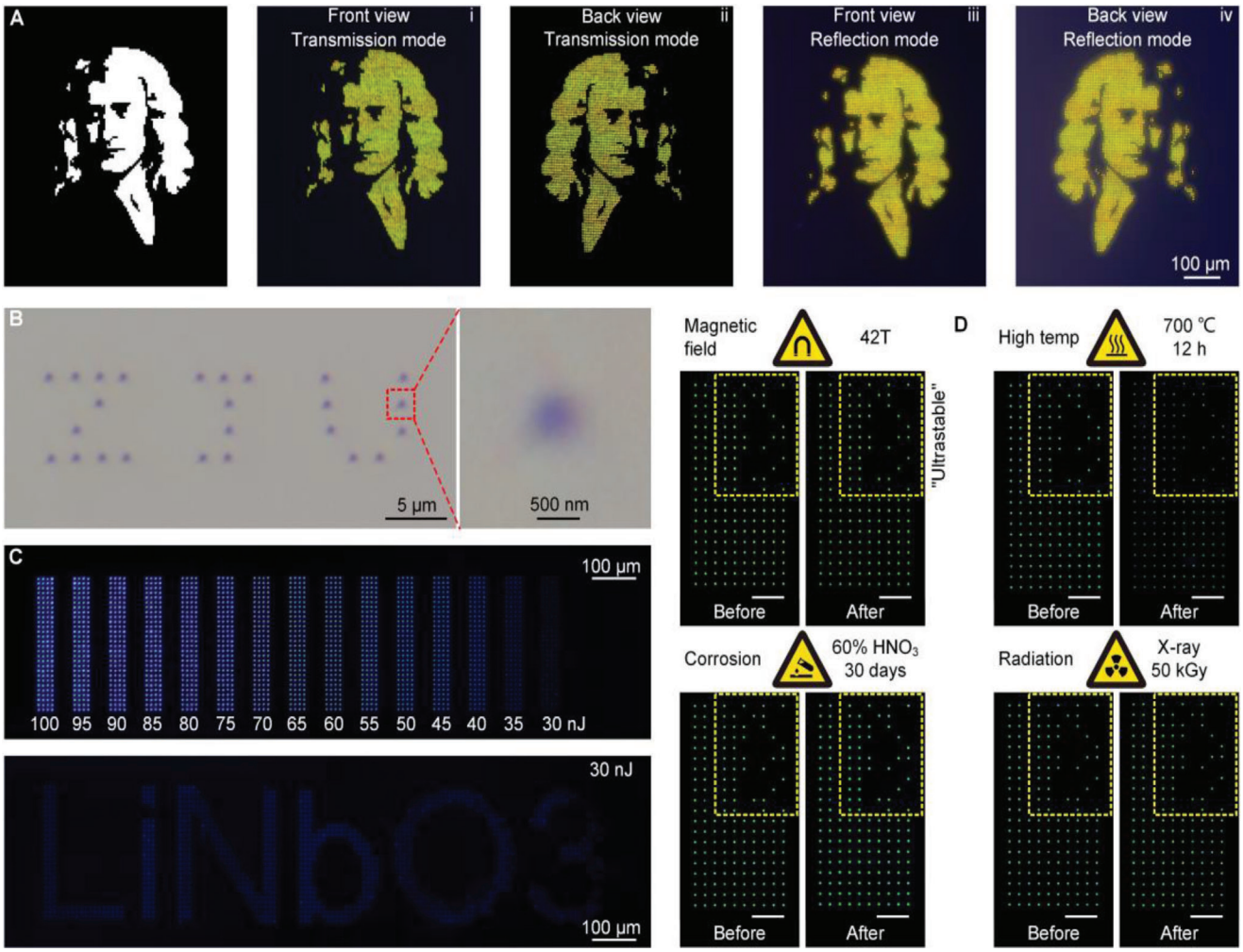

Figure 4. Readability, manufacturability, and stability of MA colors. A) Portrait of Newton (left) and experimental results of four different color readout modes (right), i) Including front reading using transmission illumination, ii) Back reading using transmission illumination, iii) Front reading using reflection illumination, and iv) Back reading using reflection illumination. B) Resolution characterization of MA color voxels. C) Pulse energy limit test for achieving coloration (up) and color patterning by using a pulse energy of 30 nJ (bottom). D) Stability characterization of MA color signal in different harsh conditions, including ultra-intense magnetic field, high temperature, strong acid, and X-ray radiation. Scale bars: 100 μm. A) Sir Isaac Newton. Mezzotint by T. O. Barlow, 1868, after Sir G. Kneller, 1689. Wellcome Collection. Public Domain Mark (https://creativecommons.org/publicdomain/mark/1.0).

MA coloration with high resolution and fabrication efficiency. First, the feature size of MA color voxels can generally reach ≈500 nm (Figure 4B), enabling high display resolution and information density. Second, a single pulse with a strikingly low pulse energy of ≈30 nJ is enough to write one color voxel (Figure 4C), comparable with that for processing organic materials,[28] allowing for splitting a single high-energy pulse into multiple pulses to create color voxel arrays with one shot. Accordingly, the printing efficiency of MA coloration is much higher than traditional approaches that rely on multipulse material modification. Third, the pulse-internal-coupling is spontaneously activated by the structural anisotropy of the crystal matrix rather than relying on external beam control setups, which greatly simplifies the optical system for imprinting color voxels and thus enhances the manufacturability of MA colors.

As the created color voxels are embedded in the stable all-inorganic dielectrics, we can expect high stability of MA colors that inherits the intrinsic stable physicochemical characteristics of $LiNbO_3$ crystals. We tested the produced samples under various harsh conditions (Figure 4D), including ultra-strong magnetic field (42 T), high temperature (700 °C), strong acid corrosion (60% HNO_3), X-ray irradiation (50 kGy), pollution, and mechanical damage (Figure S16, Supporting Information). All the recorded information well survived after these treatments, which was impossible for previous structural colors. We estimated the lifetime of the structural colors to be as long as 10^{13} years by using the accelerating aging experiments at high temperatures (Figure S17, Supporting Information), which is of great value for permanent energy-saving big data storage.[29]

2.5. Demonstration for Multidimensional Data Storage Based on MA Coloration

We demonstrated the great potential of MA coloration in both 2D and 3D data storage by writing the masterpiece "Pride and Prejudice" into binary ASCII data in a 10 × 10 mm $LiNbO_3$ crystal plate (**Figure 5**A–C). The readout of recorded data arrays is easily achieved by photo-reading with a commercial white light-emitting diode (LED) illumination source. Owing to the intrinsic

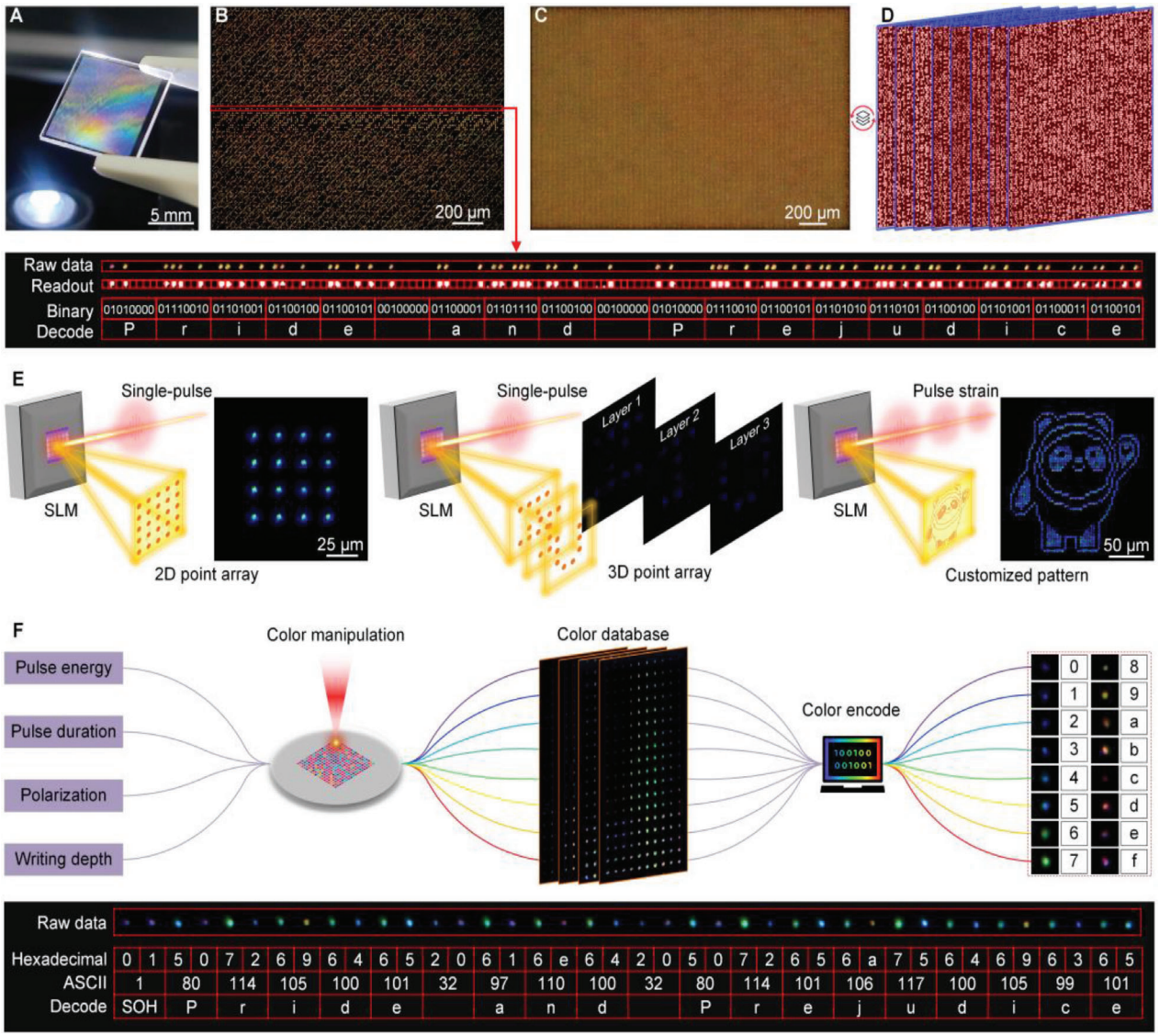

Figure 5. Cross-dimension data storage by MA coloration. A) A $LiNbO_3$ disk full of imprinted color voxels. B) 2D binary color voxels imaging (top) and data readout (bottom). C) 3D color voxels imaging. D) 3D data extraction by image recognition. E) High-efficiency information recording based on SLM technology. For instance, splitting a single pulse into multiple pulses in a single layer (left), splitting a single pulse into multiple pulses in multiple layers (middle), and customized patterning by using pulse train incidence (right). F) 5D data storage by encoding the structural colors and their intensity levels into a hexadecimal system.

high SNR of MA colors, the data arrays in the same layer can be captured in batches by a camera as a whole and the color information can be quickly identified (Figure 5D), without using any complex optical measurements or point-by-point mechanical scanning that is usually used in the traditional data reading process (Figure S18, Supporting Information). Here, intelligent image recognition was adopted to extract the written data with high speed (≈1.2 Gb s^{-1}) and accuracy (up to ≈99.7%), which enables an extremely high readout efficiency for optical data storage (Figures S19 and S20, Supporting Information). Besides the single beam writing, by applying beam shaping tools, such as spatial light modulator (SLM), we can split a single incident pulse into multiple pulses to create color voxel arrays in both 2D layer and 3D space (Figure 5E), which further improve the recording speed by tens of times. Combining high repetition rate laser and galvanometer scanning technology, a 1 Gb s^{-1} level data recording speed can be easily achieved. According to the current extreme resolution of MA coloration, the data capacity of a 127 × 127 × 3 mm $LiNbO_3$ optical disk can theoretically reach ≈24 TB (Equation S7, Supporting Information).

Notably, the highly controllable colors and their signal intensity provide more information multiplexing channels for higher dimensional data storage.[30,31] Here, we preliminarily demonstrate the feasibility of MA-color-based 5D information integration. At the current stage, besides initial 3D coordinates, the signals of a single MA voxel can be further encoded into eight hue states and two intensity levels, corresponding to 4 bits of information per voxel (Figure 5F, up), enabling 5D data storage. By using the hexadecimal ASCII where every two voxels correspond to a character and each voxel represents the number from 0 to f in the hexadecimal system, the text "Pride and Prejudice" can be recorded within a space of 40 voxels in size (Figure 5F, down). Compared with the traditional binary system, the 5D hexadecimal data storage can reduce the number of color voxels needed

to be imprinted, which is expected to further improve the MA-color-based data storage capacity. These results represent an important milestone in achieving optical data storage beyond three dimensions via voxel-level structural colors.

3. Conclusion

The pulse-internal-coupling mechanism makes imprinting MA voxels in the $LiNbO_3$ crystal a conceptually new platform for programmable 3D structural coloration with multiple advantages, including but not limited to fast manufacturability, wide gamut, multichannel recognition, high resolution, energy saving, and excellent stability (Table S1, Supporting Information), which endows new potential with the structural coloration in 3D information display. Especially, MA coloration-based information recording method brings an all-round improvement in optical data storage performances and takes a qualitative leap forward with respect to current technologies (Table S2, Supporting Information), making the writing and readout speed as well as the data density of optical storage comparable to that of magnetic and semiconductor storage. Protected by the all-inorganic crystal matrix, MA coloration can serve as an efficient, green, and perpetual big data storage approach. Importantly, due to the nonlinear processing capability of ultrafast lasers, the principles of this work can be extended to more crystal materials (Figure S21, Supporting Information). Thus, it is expected to develop a general approach to enable a variety of micro–nano phase modulation elements in high-refractive-index media, opening up more advanced micro–nano photonic applications.

For high-dimensional data storage, our experiments have shown that MA colors contain at least 10 color states and 8 intensity states. Thus, more bits of information integration in a MA voxel can be achieved by introducing more states of hue and intensity of MA voxels, which means the full potential of MA-color-based multidimensional information integration is still far from being completely exploited. Notably, with the redshift of MA colors, the length and diameter of MA voxels will also increase, which limits the data capacity improvement brought by multidimensional storage. This problem is expected to be resolved by technologies that can further reduce the length and diameters of MA color voxels and improve the color readout accuracy, such as interference order manipulation (Figure S22, Supporting Information), beam shaping, super-resolution processing, and imaging, which may excite more research works in the future.

In summary, we propose and demonstrate that a single ultrafast laser pulse can create highly localized crystal-to-glass phase transition structures with a micrometer-scaled feature size in all-inorganic uniaxial crystals. The difference in optical properties of the amorphous region and the crystal matrix enables a significant phase difference shift between O and E light, enabling a voxel-level structural coloration with multidimensional controllability in 3D space. The generated colors are revealed to possess a series of excellent performances and hold great potential for multiple applications, including 3D display, information encryption, anti-counterfeit, fast data recording and readout, and low-power long-term multidimensional data storage. It would be exciting to fuse the MA-based coloration with advanced light modulation technologies, novel photoelectric materials, and intelligent image recognition algorithms to develop a versatile 3D color rendering strategy, empowering the development of next-generation information optics.

4. Experimental Section

Materials: Commercially available $10 \times 10 \times 10$ mm Z-cut bulk $LiNbO_3$ crystal was used as the matrix for inducing MA structures. For data storage, the crystal was cut into $10 \times 10 \times 0.5$ mm thin plates along the direction perpendicular to the optical axis. All the crystals were polished on all sides.

MA-Color Sample Preparation: In the pulse-internal-coupling-based MA processing, the optical axis of the $LiNbO_3$ sample was set to be perpendicular to the laser propagation direction where the pulse splitting was spontaneously activated by the intrinsic structural anisotropy (birefringence effect) of the $LiNbO_3$ crystal. Thus, no complex external beam-shaping device was needed. Here, MA color voxels were created by using a standard ultrafast laser direct writing system (Figure S1A, Supporting Information), where the polarization was controlled by a half-wave plate and the 3D position shift of the sample was controlled by using a translation stage. Laser parameters such as pulse energy, pulse duration, and repetition rate were controlled by a computer. The imprinting process of color voxels could be detected in real time by a complementary metal–oxide–semiconductor (CMOS) camera connected to a computer. For high-speed data recording, a spatial light modulator (SLM, X13138 Hamamatsu) and a 4f system were added to the optical circuit to further split a single pulse into multiple pulses and the fixed dichroic could be replaced by a galvanometer for high-speed focal spot movements.

The light source for imprinting MA color voxels in the $LiNbO_3$ crystal was a mode-locked regeneratively amplified Yb: KGW-based ultrafast laser (PHAROS, Light Conversion Ltd.) with a wavelength of 1030 or 515 nm, a pulse duration ranging from 230 fs to 6 ps, and a pulse repetition rate ranging from 1 to 200 kHz. Generally, the laser was focused ≈50 µm below the surface of the sample via a 50× objective lens (NA = 0.8). The MA-based coloration can be achieved by a single laser pulse, the pulse duration, laser polarization, and pulse energy were set according to the desired chrominance and intensity of MA-based coloration (Figure S8, Supporting Information).

Optical Characterization of MA Colors: The color generation and observation were achieved by using a standard chromatic polarization system. As shown in Figure S1B (Supporting Information), the first polarizer (P1) was used to make the probe polychromatic light polarized to split into ordinary (O) light and extraordinary (E) light in crystal. The second polarizer (P2) was used to make the O and E light share a common polarization component in the same direction to establish interference. As the phase difference of O and E light after passing through the crystal was dependent on light frequency, the interference established by chromatic polarization method possessed wavelength selectivity.[24] A filter could be added before the light source to tune the transmission waveband when monochromatic illumination is required. Microscopy images of 3D colorful patterns were obtained by using confocal microscopy where two polarizers were added to the front and back sides of the sample respectively for generating chromatic polarization effect. The spectral characteristics of the color voxels were obtained by a micro-spectroscopy system.

Structural Characterization of MA Voxels: The optical observation of MA color voxels was performed using a microscope (BX53 Olympus). The inner structure of MA region was found and examined by scanning electron microscopy (SEM), using backscattering mode (Gemini300 Zeiss). For the SEM observation, samples were polished so as to expose the single pulse-modified area to air and the polished surface was etched with hydrofluoric acid (5%) to improve the contrast of SEM images. Further phase transition characterization of the crystal-glass heterogeneous interface was performed by focused ion beam (FIB) slice and high-resolution transmission electron microscopy (HRTEM). Electron paramagnetic resonance (EPR) spectroscopy (Bruker, ESRA-300) was applied to examine the defects of the pre-modified area.

Supporting Information

Supporting Information is available from the Wiley Online Library or from the author.

Acknowledgements

The authors wish to thank Nianhang Rong and Xi Zheng of Zhejiang University Analysis Center of Agrobiology and Environmental Sciences for assistance with the SEM examination, Junbo Han of Wuhan National High Magnetic Field Center for assistance with the magnetic disturbance tests, Yanmin Yang and Leipeng Li of Hebei University for assistance with the X-ray irradiation tests. This work was financially supported by the National Key R&D Program of China (No. 2021YFB2800500); the National Natural Science Foundation of China (Grant Nos. U20A20211, 62275233, and 62005164); the Key Research Project of Zhejiang Lab; and China Postdoctoral Science Foundation (2021M702799).

Conflict of Interest

The authors declare no conflict of interest.

Author contributions

B.Z. and Z.W. contributed equally to this work. B.Z. and Z.W. conceived the idea. J.Q. organized, coordinated, and supervised the project. Z.W., B.Z., J.Z., and Z.W. performed the experiments and collected the data. Z.W., B.Z., D.T., and J.Q. interpreted the results and proposed the mechanism of MA coloration. Z.W., B.Z., and D.T. wrote the manuscript. P.G.K. supervised and reviewed the manuscript. Z.W., B.Z., D.T., and J.Q. discussed and revised the manuscript.

Data Availability Statement

The data that support the findings of this study are available from the corresponding author upon reasonable request.

Keywords

3D structural coloration, information optics, lithium niobate crystals, micro-amorphization, ultrafast lasers

Received: April 7, 2023
Revised: June 20, 2023
Published online:

[1] A. H. Dorrah, F. Capasso, *Science* **2022**, *376*, eabi6860.
[2] A. L. Holsteen, A. F. Cihan, M. L. Brongersma, *Science* **2019**, *365*, 257.
[3] L. Shao, X. Zhuo, J. Wang, *Adv. Mater.* **2018**, *30*, 1704338.
[4] C. Liu, Z. Fan, Y. Tan, F. Fan, H. Xu, *Adv. Mater.* **2020**, *32*, 1907569.
[5] H. Huang, H. Li, J. Yin, K. Gu, J. Guo, C. Wang, *Adv. Mater.* **2023**, *35*, 2211117.
[6] K. Zhong, J. Li, L. Liu, S. Van Cleuvenbergen, K. Song, K. Clays, *Adv. Mater.* **2018**, *30*, 1707246.
[7] Z. Yan, Z. Zhang, W. Wu, X. Ji, S. Sun, Y. Jiang, C. C. Tan, L. Yang, C. T. Chong, C.-W. Qiu, R. Zhao, *Nat. Nanotechnol.* **2021**, *16*, 795.
[8] A. Kristensen, J. K. W. Yang, S. I. Bozhevolnyi, S. Link, P. Nordlander, N. J. Halas, N. A. Mortensen, *Nat. Rev. Mater.* **2016**, *2*, 16088.
[9] J.-M. Guay, A. Calà Lesina, G. Côté, M. Charron, D. Poitras, L. Ramunno, P. Berini, A. Weck, *Nat. Commun.* **2017**, *8*, 16095.
[10] Y. Liu, H. Wang, J. Ho, R. C. Ng, R. J. H. Ng, V. H. Hall-Chen, E. H. H. Koay, Z. Dong, H. Liu, C.-W. Qiu, J. R. Greer, J. K. W. Yang, *Nat. Commun.* **2019**, *10*, 4340.
[11] H. Liu, H. Wang, H. Wang, J. Deng, Q. Ruan, W. Zhang, O. A. M. Abdelraouf, N. S. S. Ang, Z. Dong, J. K. W. Yang, H. Liu, *ACS Nano* **2022**, *16*, 8244.
[12] Y. Zhang, L. Zhang, C. Zhang, J. Wang, J. Liu, C. Ye, Z. Dong, L. Wu, Y. Song, *Nat. Commun.* **2022**, *13*, 7095.
[13] A. Ródenas, M. Gu, G. Corrielli, P. Paiè, S. John, A. K. Kar, R. Osellame, *Nat. Photonics* **2019**, *13*, 105.
[14] B. Zhang, D. Tan, Z. Wang, X. Liu, B. Xu, M. Gu, L. Tong, J. Qiu, *Light: Sci. Appl.* **2021**, *10*, 93.
[15] X.-L. Zhang, F. Yu, Z.-G. Chen, Z.-N. Tian, Q.-D. Chen, H.-B. Sun, G. Ma, *Nat. Photonics* **2022**, *16*, 390.
[16] K. Sun, D. Tan, X. Fang, X. Xia, D. Lin, J. Song, Y. Lin, Z. Liu, M. Gu, Y. Yue, J. Qiu, *Science* **2022**, *375*, 307.
[17] R. R. Gattass, E. Mazur, *Nat. Photonics* **2008**, *2*, 219.
[18] T. Xu, K. Switkowski, X. Chen, S. Liu, K. Koynov, H. Yu, H. Zhang, J. Wang, Y. Sheng, W. Krolikowski, *Nat. Photonics* **2018**, *12*, 591.
[19] X. Huang, Q. Guo, D. Yang, X. Xiao, X. Liu, Z. Xia, F. Fan, J. Qiu, G. Dong, *Nat. Photonics* **2020**, *14*, 82.
[20] B. Zhang, L. Wang, F. Chen, *Laser Photonics Rev.* **2020**, *14*, 1900407.
[21] D. Wei, C. Wang, H. Wang, X. Hu, D. Wei, X. Fang, Y. Zhang, D. Wu, Y. Hu, J. Li, S. Zhu, M. Xiao, *Nat. Photonics* **2018**, *12*, 596.
[22] D. Wei, C. Wang, X. Xu, H. Wang, Y. Hu, P. Chen, J. Li, Y. Zhu, C. Xin, X. Hu, Y. Zhang, D. Wu, J. Chu, S. Zhu, M. Xiao, *Nat. Commun.* **2019**, *10*, 4193.
[23] X. Xu, T. Wang, P. Chen, C. Zhou, J. Ma, D. Wei, H. Wang, B. Niu, X. Fang, D. Wu, S. Zhu, M. Gu, M. Xiao, Y. Zhang, *Nature* **2022**, *609*, 496.
[24] H. Kubota, T. Ara, H. Saito, *J. Opt. Soc. Am.* **1951**, *41*, 537.
[25] H. Wang, Y. Lei, L. Wang, M. Sakakura, Y. Yu, G. Shayeganrad, P. G. Kazansky, *Laser Photonics Rev.* **2022**, *16*, 2100563.
[26] Y. Shimotsuma, M. Sakakura, P. G. Kazansky, M. Beresna, J. Qiu, K. Miura, K. Hirao, *Adv. Mater.* **2010**, *22*, 4039.
[27] J. Geng, L. Shi, J. Ni, Q. Jia, W. Yan, M. Qiu, *PhotoniX* **2022**, *3*, 14.
[28] W. Chen, Z. Yan, J. Tian, S. Liu, J. Gao, J. Zhang, *Opt. Lett.* **2021**, *46*, 3211.
[29] M. Gu, X. Li, Y. Cao, *Light: Sci. Appl.* **2014**, *3*, e177.
[30] X. Ouyang, Y. Xu, M. Xian, Z. Feng, L. Zhu, Y. Cao, S. Lan, B.-O. Guan, C.-W. Qiu, M. Gu, X. Li, *Nat. Photonics* **2021**, *15*, 901.
[31] J. Zhang, M. Gecevičius, M. Beresna, P. G. Kazansky, *Phys. Rev. Lett.* **2014**, *112*, 033901.

ISSN 2096-4579
CN 51-1781/TN

Opto-Electronic Advances

光电进展

January 2023 Vol. 6 No. 1

DOI: 10.29026/oea.2023.220008

Zhuo Wang†, Bo Zhang†, Dezhi Tan* and Jianrong Qiu*

www.oejournal.org/oea

Institute of Optics and Electronics, Chinese Academy of Sciences

Opto-Electronic Advances

Article

January 2023, Vol. 6, No. 1

DOI: 10.29026/oea.2023.220008

Ostensibly perpetual optical data storage in glass with ultra-high stability and tailored photoluminescence

Zhuo Wang[1†], Bo Zhang[1†], Dezhi Tan[2*] and Jianrong Qiu[1,3*]

Long-term optical data storage (ODS) technology is essential to break the bottleneck of high energy consumption for information storage in the current era of big data. Here, ODS with an ultralong lifetime of 2×10^7 years is attained with single ultrafast laser pulse induced reduction of Eu^{3+} ions and tailoring of optical properties inside the Eu-doped aluminosilicate glasses. We demonstrate that the induced local modifications in the glass can stand against the temperature of up to 970 K and strong ultraviolet light irradiation with the power density of 100 kW/cm^2. Furthermore, the active ions of Eu^{2+} exhibit strong and broadband emission with the full width at half maximum reaching 190 nm, and the photoluminescence (PL) is flexibly tunable in the whole visible region by regulating the alkaline earth metal ions in the glasses. The developed technology and materials will be of great significance in photonic applications such as long-term ODS.

Keywords: ultrafast laser; photoluminescence tailoring; ultralong lifetime; optical data storage

Wang Z, Zhang B, Tan DZ, Qiu JR. Ostensibly perpetual optical data storage in glass with ultra-high stability and tailored photoluminescence. *Opto-Electron Adv* **6**, 220008 (2023).

Introduction

In the development history of human society, data storage plays an indispensable and pivotal role, it has significantly boosted spacious domains from social science to industrial production. With the advent of the Internet of Things and artificial intelligence, the long lifetime and large capacity of information storage are in increasingly high demand. Accordingly, optical data storage (ODS) technique provides a highly fascinating alternative to conventional storage techniques (semiconductor or magnetic-based storage) with lower energy consumption, larger capacity, higher efficiency, and longer lifetime[1–5]. However, accounting for 80% of the total stored data generated by the government, data disaster recovery centers, and archives are not frequently accessed but still need to be available over long periods in an easy access method. The typical lifetime of mature ODS is hundreds of years that is still far from meeting the requirements of next-generation information storage[6–8]. Although the ODS based on ultrafast laser induced volume periodic structures has an ultralong lifetime, multipulse irradiation with the pulse energy up to micro-joule is necessary for writing, which will slow down the writing speed and increase the power consumption[9]. Developing long-term stable ODS based on single pulse writing process can not only notably reduce the energy dissipation

[1]State Key Laboratory of Modern Optical Instrumentation, and College of Optical Science and Engineering, Zhejiang University, Hangzhou 310027, China; [2]Zhejiang Lab, Hangzhou 311100, China; [3]CAS Center for Excellence in Ultra-intense Laser Science, Chinese Academy of Sciences, Shanghai 201800, China.

†These authors contributed equally to this work.

*Correspondence: DZ Tan, E-mail: wctdz@zju.edu.cn; JR Qiu, E-mail: qjr@zju.edu.cn

Received: 13 January 2022; Accepted: 26 March 2022; Published online: 31 August 2022

associated with frequent data migration but also increase the efficiency of data writing.

Tailoring of optical properties of active centers or dopants in solid matrix has extensively boosted the applications of glasses and crystals in optical communication, information storage, photonic device, and display[2,10–13]. Typically, the spectroscopic features of the active centers or dopants are highly dependent on the local structures of amorphous glass or crystal field and generally tuned via chemical component modulation and homogeneous heat treatment of the matrix[14–17]. Recently, ultrafast laser has also been established to be an effective tool for tailoring optical properties of transparent solids and hence implementing new functionalities with three-dimensional (3D) structuring capability[18–23]. For example, modifying the local structures and valence of active ions in transparent matrix endows writing information in the local volume by distinct photoluminescence (PL) emission properties that enable large capacity ODS with a high signal-to-noise ratio[24–27]. However, the PL is generally induced by multipulse laser irradiation, which limits the writing speed of ODS. Besides, an obvious decrease in the PL intensity of active ions is usually observable at high temperatures, which is detrimental for long-term device operation[28–30]. Hence, the lifetime of ODS based on the distinct PL is limited to only a few hundred years or even several decades[1,31]. It is a challenge to realize ODS that not only possesses a facile method and fast writing speed but also possesses an ultralong lifetime and excellent stability.

In this work, we report long-term and high writing speed ODS by tailoring the valence state of Eu^{3+} ions inside glass with single laser pulse. We demonstrate that the lifetime of stored information is as long as 2×10^7 years and the written local modifications can stand against the temperature of up to 970 K and intense ultraviolet irradiation (100 kW/cm^2). Furthermore, broadband emission of the active Eu^{2+} ions is observed with the full width at half maximum (FWHM) reaching 190 nm and the PL can be tuned in the whole visible region.

Results and discussion

Ordinarily, luminescent materials, a kind of widely employed ODS medium, are composed of a reasonable combination of certain active dopants with an inert matrix. Divalent europium cation (Eu^{2+}) is one of the extensively applied activators due to unequaled 4f-5d transition[32–34]. The emission spectrum of Eu^{2+} is largely dependent on the chemical compositions and structures of hosts as the 5d orbital is sensitive to the surrounding environment. Besides, aluminosilicate glass is considered as an outstanding category of host matrix due to the excellent stability and accessible synthesis method with relatively low cost of raw materials. Eu-doped earth-abundant aluminosilicate glass represents preeminent luminescence characteristics that can meet distinct optoelectronic applications. Therefore, Eu_2O_3 doped calcium-silicon-aluminum (Eu: CSA) glass is employed to serve as ODS matrix, among which intermediate elements including silicium and aluminum act as glass former, whereas the alkaline earth metal element (calcium) serves as glass modifier. Ultrafast laser is used to tailor PL properties of Eu: CSA glass to enable data writing. During laser-matter interaction, three-photon absorption occurs in the laser modified area, and active electrons and holes can be created in glass through multi-photon ionization process. When the electrons are trapped by Eu^{3+}, permanent photoreduction of Eu^{3+} will be achieved to generate Eu^{2+}, and different luminescence characters will be attained.

Figure 1(a) shows the PL spectra from Eu^{3+} in initial Eu: CSA glass before tailoring luminescence by femtosecond (fs) laser. A series of characteristic emission lines between 570 and 750 nm attributed to the $^5D_0-{}^7F_J(J=0,1,2,3,4)$ transition appear[8,35]. The target glass without doping (CSA glass) does not emit PL after ultrafast laser irradiation as illustrated in Fig. 1(b). Typical broadband PL of Eu^{2+} ions arises in Eu: CSA glass after tailoring luminescence with fs laser. The FWHM of the emission spectrum reaches 190 nm, which is much larger than that of the reported value of ~90 nm in the previous reports[30] (such as in the Eu-doped borate (Eu: BAN) glass (Fig. 1(c))). The anomalous spectra broadening can be attributed to the coexistence of Eu^{2+} ions and Eu^{3+} ions in glass (Fig. S4(a)). Besides, the random distribution of Si and Al will enhance the structural disorder and asymmetry thus leading to a broad spectral band. Furthermore, the PL can be stimulated both by 375 nm and 405 nm resulting from the big centroid shift as well as the energy level splitting. The Eu-doped glasses usually have less absorption after 400 nm, the PL of Eu^{2+} excited by 405 nm laser is barely detectable in borate glass as shown in Fig. 1(c). However, by tailoring the optical property of Eu: CSA glass, the absorption in ultraviolet region of Eu^{2+} doped glass becomes higher (Fig. 1(d)), and the PL emission can be excited by 405 nm laser, which provides a new choice of excitation for data

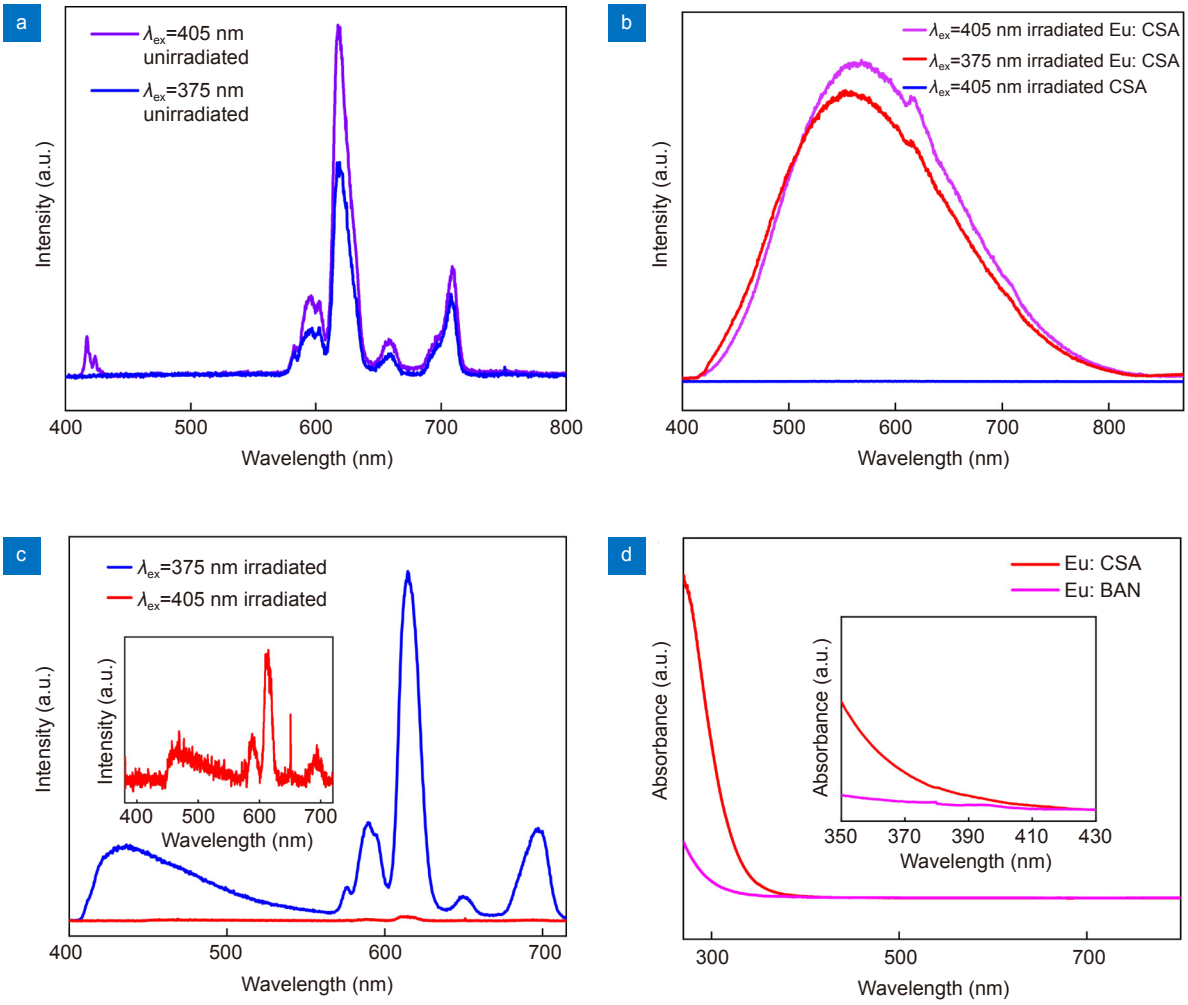

Fig. 1 | (**a**) PL spectra of initial Eu: CSA glass. (**b**) PL spectra of Eu: CSA and CSA glasses after irradiation. (**c**) PL spectra of Eu: BAN glass after ultrafast laser irradiation. The inset is the enlarged PL spectrum excited by 405 nm laser. (**d**) Absorption spectra of Eu: CSA and Eu: BAN glasses. Inset is an enlargement of absorbance from 350 to 430 nm.

reading. Besides, the bandgap of Eu: CSA glass is approximately 3.65 eV according to Fig. 1(d), indicating three-photon absorption during laser-matter interaction. Consequently, reduction of Eu^{3+} and tailoring of optical properties inside glass are achieved simultaneously and allow for tuning the PL of the active ions. The distinct PL in Eu: CSA glass resulting from Eu^{3+} and Eu^{2+} exhibits the possibility to serve as an ODS medium. Besides, potential multi-application of rare earth ions-doped glasses has been proposed, and ODS technology is one of the most important demonstrations.

To further demonstrate the performance of ODS in the devised glass, we systematically investigated the impact of used laser parameters including duration, pulse energy, repetition rate, and pulse number. As illustrated in Fig. 2(a), groups of dots are directly written into Eu: CSA glass by single pulse fs laser with controlled pulse durations and pulse energies. Reading out of dot-array is exhibited in Fig. 2(b) and the result indicates even single pulse can induce local material modifications with PL strong enough to be used for data storage. Figure 2(c) shows that the diameter of the written dots increases with the increase in the pulse energy. The size of written dots can be reduced to 600 nm when the pulse energy is reduced to 96 nJ (Fig. S5(b)), and the density of ODS is approximately 1.4 Tbit cm^{-3}. Figure 2(d) demonstrates the PL intensity of dots written with different pulse energies and pulse durations. The PL intensity increases with the increment in the writing pulse energy. A decrease in pulse duration leads to an increase in the PL intensity of Eu^{2+} and a decrease in the pulse energy threshold for writing emissive dots. Figure 2(e) demonstrates the PL intensity as a function of repetition rate and pulse number, which indicates the presence of a broad grayscale of

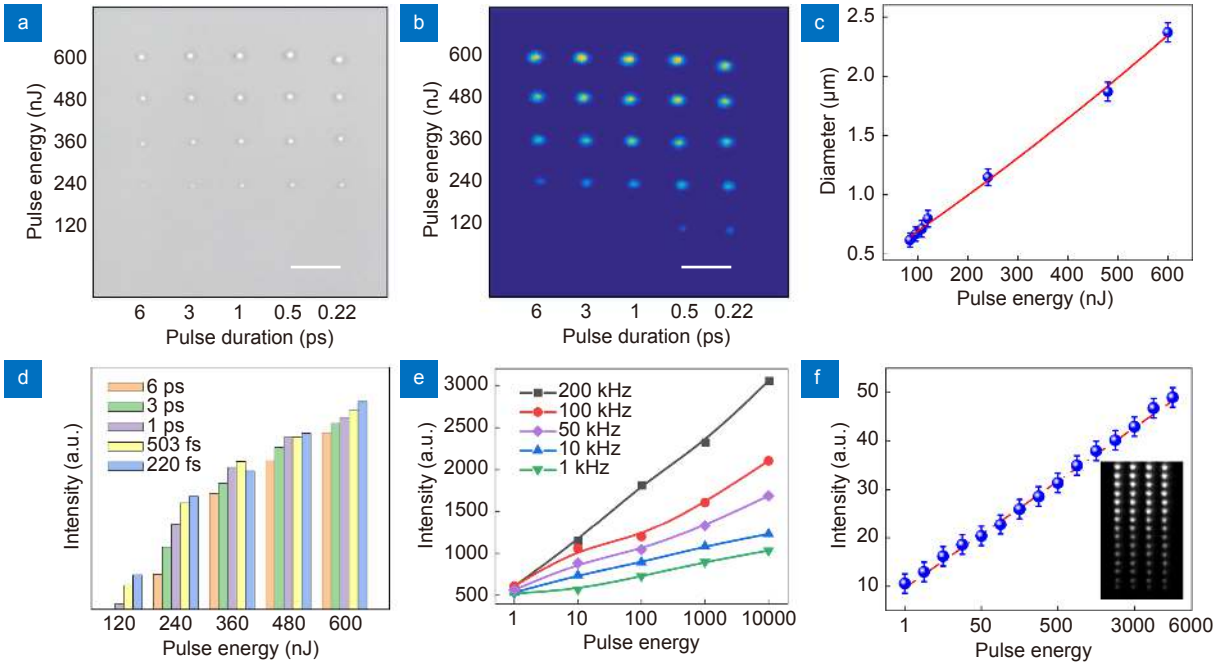

Fig. 2 | (**a**) Optical image of recorded information in the glass. (**b**) Reading out of information by PL mapping. Scale bar: 10 μm. (**c**) Relationship between emissive dot size and pulse energy. (**d**) PL intensity of dots written with diverse pulse durations and pulse energies. (**e**) PL intensity of dots written with various repetition rates and pulse numbers. (**f**) 16 levels of grayscale assignment based on the relation between PL intensity and pulse number.

PL intensity that can serve as another degree of freedom in ODS. Figure 2(f) demonstrates up to 16 levels of grayscales and in this case each written dot can be coded in a 4-bit-format (from 0000 to 1111), which allows further expansion of storage capacity. Dots in a 4-bit format can also be achieved by controlling pulse energy, as shown in Fig. S6. It is worth to note the diameter of writing dots increases with the increase of pulse number and pulse energy. Too small or large bit spacing will lead to a decrease in bit contrast or storage density, as a result, appropriate bit spacing is very crucial to keep the balance between low cross-talk and high storage capacity.

As demonstrated in Fig. 3(a–c), Chinese characters of "zhe jiang da xue" are translated into a binary symbol and recorded in various layers of the transparent Eu:CSA glass. The dots in layer 1 and layer 2 are written by single pulse of fs laser with pulse energy of 200 nJ, and dots in layer 3 and layer 4 are written by 250 nJ and 300 nJ fs laser, respectively. The first layer of dots is written at the depth of 50 μm, and the spacing between adjacent layers in the *z*-direction is 10 μm. Reading out of the recorded information can be achieved by collecting the PL from the dots without and with fs laser writing, which corresponds to the "0" and "1" states in the binary system, respectively. No signal crosstalk is observed between different adjoining layers by controlling the writing pulse number and pulse energy (Fig. 3(b)) and it is also essential for 3D ODS. As the information writing is realized by single pulse incidence, the amount of data written per unit time can be considerably large, which is determined by the laser repetition rate and scanning speed of the stage. Therefore, high repetition frequency in the megahertz range is more favorable for improving information storage efficiency. Besides, a complicated logo pattern is also successfully recorded in glass by selectively tailoring the luminescence with continuous line scanning with 0.5 μJ pulse energy fs laser and the scanning speed is 80 μm/s. The recorded pattern can be read by 405 nm laser stimulation as demonstrated in Fig. 3(d) and it can also be stored in different layers. The non-uniformity of PL intensity, such as the low PL intensity in the bottom right, is due to the non-uniformity of glass thickness, which can be optimized by better polishing. The successful demonstration of 3D information recording and reading demonstrates the feasibility of ODS technology in the Eu_2O_3 doped aluminosilicate glass.

A long-term ODS technology with lifetime longer than a few hundred years can not only significantly reduce the energy dissipation associated with frequent data migration but also increase the savings in expenditures, including electricity and costs of storage devices. Consequently, it is necessary to examine the lifetime of

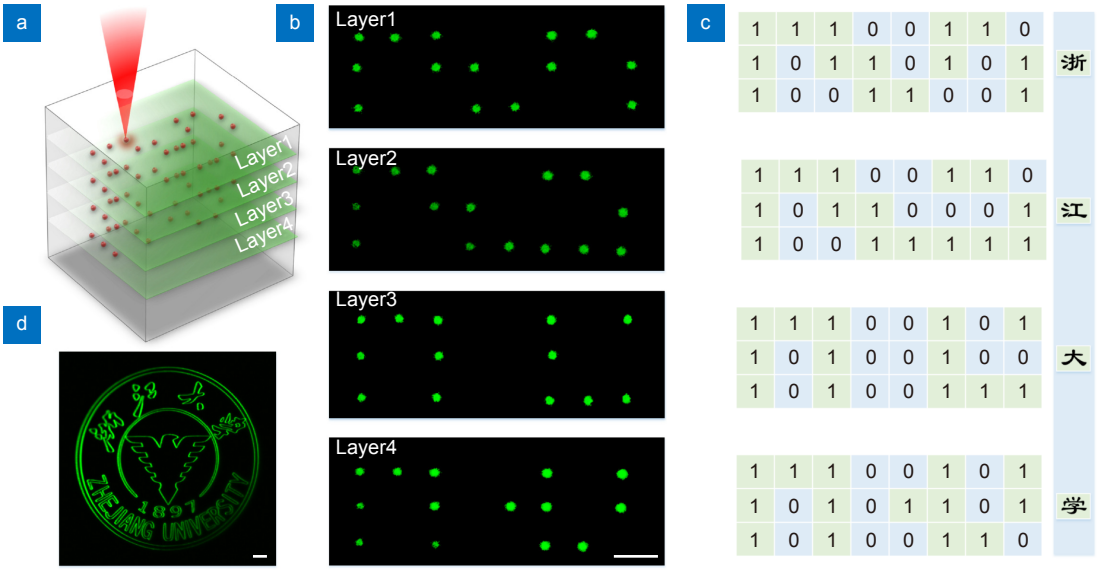

Fig. 3 | Optical information writing and readout. (**a**) Schematic diagram of 3D information writing in the glass. (**b**) Recorded information in glass in different layers. Dots in layer 1 and layer 2 are written by single pulse with 200 nJ. Dots in layer 3 and layer 4 are written by single pulse with 250 nJ and 300 nJ, respectively. Scale bar: 10 μm. (**c**) Encode information by binary format. (**d**) Complicated logo pattern recorded in the glass. Scale bar: 20 μm.

recorded information in the devised material. As illustrated in Fig. 4(a), the stored information in Eu: CSA glass can survive under the temperature of up to 970 K. According to Arrhenius law (Eq. S7), the lifetime (Fig. 4(b)) of the PL signal that can sustain the stability and readability of recorded information is evaluated up to 2×10^7 years which is several orders of magnitude higher than current PL-based ODS approaches (Fig. 4(c))[6,8]. The temperature tolerance of other Eu_2O_3 doped aluminosilicate glasses (Eu: DSA, D represents MgO, CaO, SrO, BaO) is demonstrated in Fig. 4(d), after two-hours heating at 770 K, the PL intensity decreased by only 17%, indicating a generally excellent storage lifetime in similar glass systems. This is because that in Eu: DSA glass, the tetrahedral symmetry around Eu^{2+} will decrease with the incorporation of Al^{3+} and Si^{4+} sites, and the energy level splitting of 5d band increases. Consequently, the activation energy for thermal quenching becomes higher, resulting in a more stable PL. Notably, the recorded information in Eu: CSA glass can withstand highly intense ultraviolet irradiation (~100 kW/cm^2) and be accurately read with an excitation power as low as 6 nW (corresponding to 2 W/cm^2 in Fig. 4(e)). The decay rate of PL intensity is reduced significantly in Eu: CSA glass as compared with the tolerability of ultraviolet irradiation in Ag-doped silicate (Ag: CSA) glass and Eu: BAN glass (Fig. 4(f)). These results firmly confirm the great potential of the Eu: CSA glass-mediated ODS in highly robust long-term information storage.

In addition, the tailoring of luminescence can be universally attained in more glasses, such as employing other alkaline earth metal ions (including Mg, Sr, and Ba) to serve as glass modifiers. Similar broadband PL emitting by Eu^{2+} and several characteristic sharp PL peaks emitting by Eu^{3+} are collected, as shown in Fig. 5(a) and 5(b). It is worth noting that the emission of Eu^{2+} depends on surrounding environment. Hence by regulating the alkaline earth metal ions in aluminosilicate glasses, the PL emitted by Eu^{2+} ions can be tailored and it is flexibly tunable among the whole visible region. The Commission International de L'Eclairage (CIE) chromaticity coordinates of PL spectra in these aluminosilicate glasses changed gradually from (0.29, 0.35) to (0.43, 0.42) with an increase in the ratio of alkaline earth metal ion (Fig. 5(c)). As shown in Fig. 5(d), the energy gap between the 4f ground state and the lowest 5d excited level (E_{fd} (free)) is approximately 4.216 eV (equal to 34000 cm^{-1}) for the free Eu^{2+} ion[36,37]. However, the actual 4f–5d energy position (E_{fd} (A)) is generally smaller than that of the free 4f–5d energy gap when Eu^{2+} ions are doped into the host due to the influence of the surrounding environment on the 5d energy level. Generally, the emission of europium doped luminescence materials is determined by the spectroscopic redshift of the 5d energy position compared with that of free Eu^{2+} ion D (A) consisting of the centroid shift (ε_c) and the energy level splitting ε_s (A)[37]. The

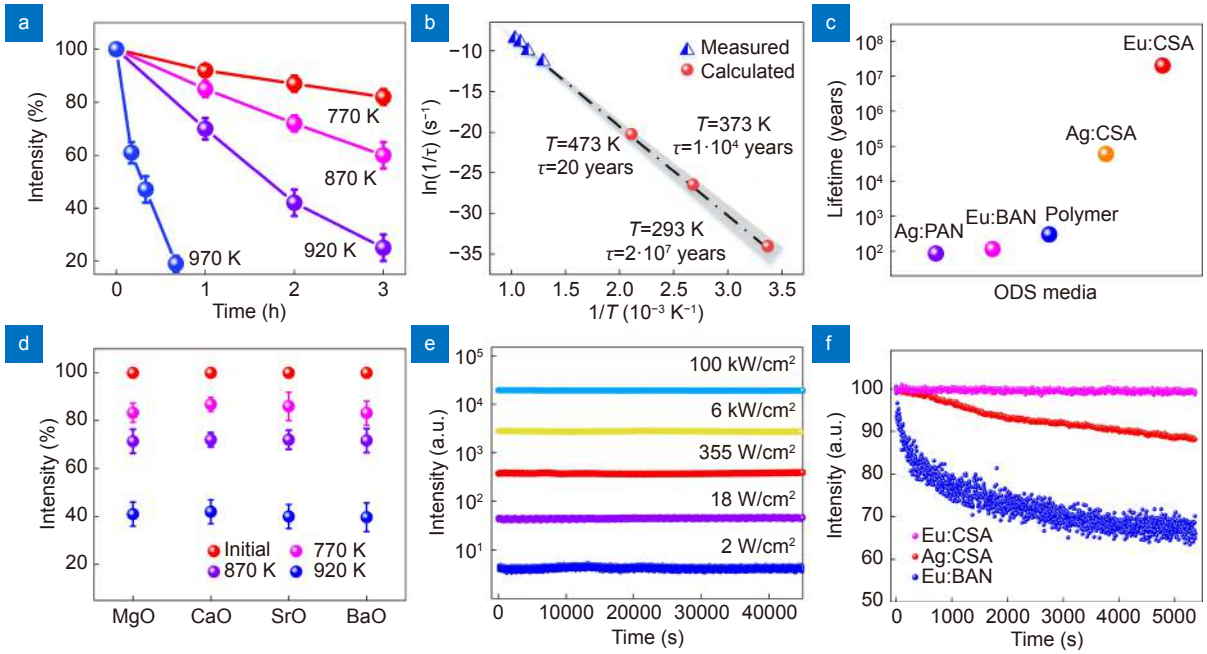

Fig. 4 | Stability of recorded information. (**a**) Thermal stability of PL in Eu: CSA glass. (**b**) Arrhenius plot of the decay rate. Grey area: error estimates. (**c**) Comparison of lifetime in ODS based on different media[6,8]. (**d**) Comparison of thermostability of PL in Eu: DSA glasses. (**e**) PL stability of written dots under various excitation power densities. (**f**) PL stability of different ODS media.

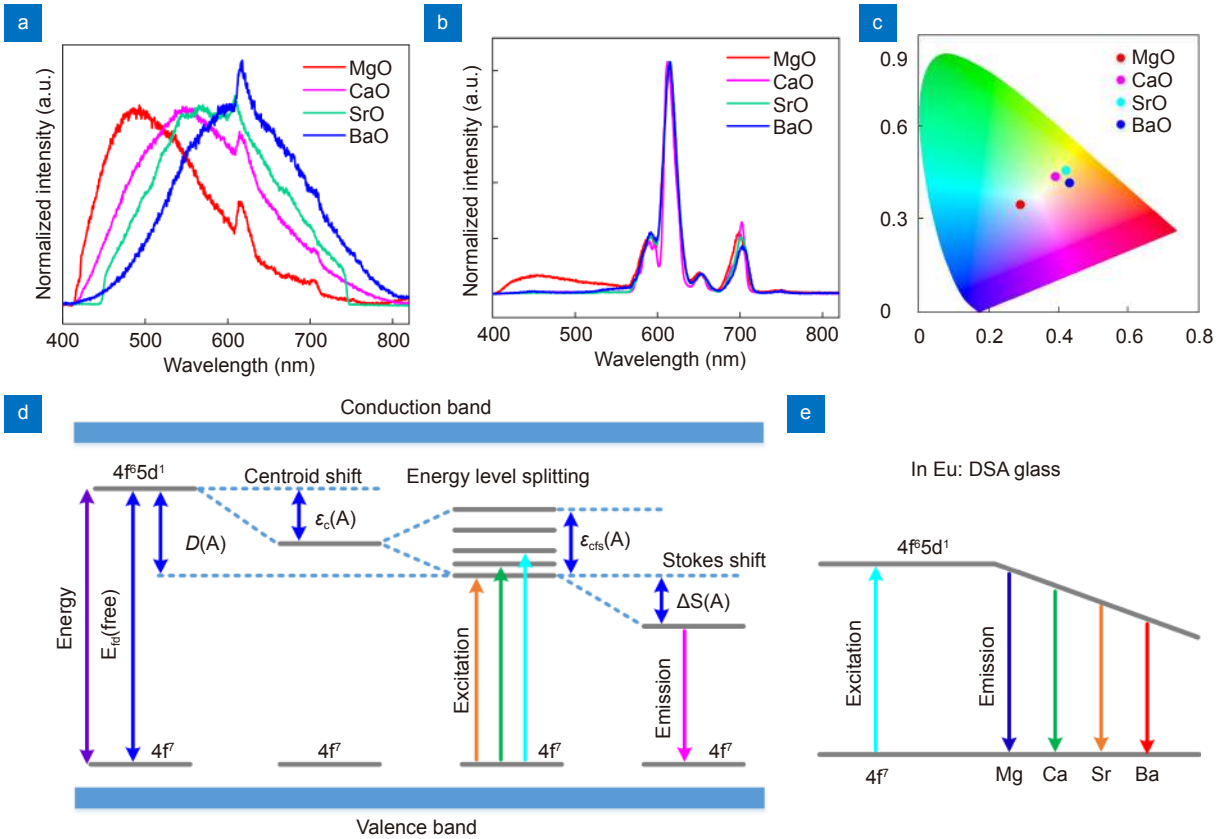

Fig. 5 | (**a**) PL spectra of dots written in the aluminosilicate glasses by fs laser. (**b**) PL spectra of initial glasses. Excitation wavelength: 375 nm. (**c**) Optical emission of Eu^{2+} in CIE coordinates. (**d**) Schematic diagram of the real 5d energy position in an inorganic solid. (**e**) Spectroscopic redshift in Eu: DSA glass.

emission spectrum is influenced by the lowest 5d energy level and Stokes shift (ΔS (A)). The Stokes shift is related to equilibrium position offset and phonon energy. In Eu: DSA glasses, a larger cation ratio results in a bigger spectroscopic redshift, which originates from the synergistic contribution of a large centroid shift, energy level splitting and Stokes shift as illustrated in Fig. 5(e). Typically, when the radius of alkaline earth metal ions increases, the spectral polarizability of the closest anion neighbors increases, the typical coordination number of cations also exhibits an increasing trend, and the distance between Eu^{2+} and O^{2-} also decreases, hence leading to a bigger centroid shift. Thus, the luminescence properties of dopants in solid matrix can be manipulated in a wide range, which can greatly expand the potential applications of aluminosilicate glasses in storage, imaging, and display.

Conclusions

Here, a stable ODS technique with an ultralong lifetime of 2×10^7 years is proposed by ultrafast laser selectively regulating the valence state of doped active ions and tailoring optical properties of Eu^{2+} ions inside the Eu-doped aluminosilicate glasses. It is demonstrated that the stored information exhibits excellent tolerability to temperature (970 K) and ultraviolet irradiation (100 kW/cm^2). Furthermore, the active Eu^{2+} ions emit a broadband PL with FWHM of 190 nm, and the PL can be flexibly tuned in the entire visible range by adjusting the modifiers in glasses. The proposed ODS technique with ultralong lifetime is of great significance for breaking the bottleneck of large energy consumption in practical applications.

References

1. Zhu LW, Cao YY, Chen QQ, Ouyang X, Xu Y et al. Near-perfect fidelity polarization-encoded multilayer optical data storage based on aligned gold nanorods. *Opto-Electron Adv* **4**, 210002 (2021).
2. Zhang B, Wang Z, Tan DZ, Liu XF, Xu BB et al. Ultrafast laser inducing continuous periodic crystallization in the glass activated via laser-prepared crystallite-seeds. *Adv Opt Mater* **9**, 2001962 (2021).
3. Zhang QM, Xia ZL, Cheng YB, Gu M. High-capacity optical long data memory based on enhanced Young's modulus in nanoplasmonic hybrid glass composites. *Nat Commun* **9**, 1183 (2018).
4. Chen WL, Yan Z, Tian J, Liu SY, Gao JC et al. Flexible four-dimensional optical data storage enabled by single-pulse femtosecond laser irradiation in thermoplastic polyurethane. *Opt Lett* **46**, 3211–3214 (2021).
5. Yu JB, Luo MT, Lv ZY, Huang SM, Hsu HH et al. Recent advances in optical and optoelectronic data storage based on luminescent nanomaterials. *Nanoscale* **12**, 23391–23423 (2020).
6. Gao L, Zhang QM, Evans RA, Gu M. 4D Ultra-high-density long data storage supported by a solid-state optically active polymeric material with high thermal stability. *Adv Opt Mater* **9**, 2100487 (2021).
7. Yang ZT, Du JR, Martin LIDJ, Feng A, Cosaert E et al. Designing photochromic materials with large luminescence modulation and strong photochromic efficiency for dual-mode rewritable optical storage. *Adv Opt Mater* **9**, 2100669 (2021).
8. Wang Z, Zhang B, Tan DZ, Qiu JR. Long-term optical information storage in glass with ultraviolet-light-preprocessing-induced enhancement of the signal-to-noise ratio. *Opt Lett* **46**, 3937–3940 (2021).
9. Zhang JY, Gecevicius M, Beresna M, Kazansky PG. Seemingly unlimited lifetime data storage in nanostructured glass. *Phys Rev Lett* **112**, 033901 (2014).
10. Liao HX, Zhao M, Zhou YY, Molokeev MS, Liu QL et al. Polyhedron transformation toward stable narrow-band green phosphors for wide-color-gamut liquid crystal display. *Adv Funct Mater* **29**, 1901988 (2019).
11. Sun K, Tan DZ, Fang XY, Xia XT, Lin DJ et al. Three-dimensional direct lithography of stable perovskite nanocrystals in glass. *Science* **375**, 307–310 (2022).
12. Fernandez TT, Gross S, Privat K, Johnston B, Withford M. Designer glasses—future of photonic device platforms. *Adv Funct Mater* **32**, 2103103 (2022).
13. Xia TF, Cao WQ, Cui YJ, Yang Y, Qian GD. Water-sensitive multicolor luminescence in lanthanide-organic framework for anti-counterfeiting. *Opto-Electron Adv* **4**, 200063 (2021).
14. Yang ZT, Du JR, Martin LIDJ, van der Heggen D, Poelman D. Highly responsive photochromic ceramics for high-contrast rewritable information displays. *Laser Photonics Rev* **15**, 2000525 (2021).
15. Du JR, Feng A, Poelman D. Temperature dependency of trap-controlled persistent luminescence. *Laser Photonics Rev* **14**, 2000060 (2020).
16. Yang ZY, Zhou YY, Qiao JW, Molokeev MS, Xia ZG. Rapid synthesis of red-emitting $Sr_2Sc_{0.5}Ga_{1.5}O_5$: Eu^{2+} phosphors and the tunable photoluminescence via Sr/Ba substitution. *Adv Opt Mater* **9**, 2100131 (2021).
17. Hu T, Ning LX, Gao Y, Qiao JW, Song EH et al. Glass crystallization making red phosphor for high-power warm white lighting. *Light Sci Appl* **10**, 56 (2021).
18. Zhang B, Tan DZ, Liu XF, Tong LM, Kazansky PG et al. Self-organized periodic crystallization in unconventional glass created by an ultrafast laser for optical attenuation in the broadband near-infrared region. *Adv Opt Mater* **7**, 1900593 (2019).
19. Lei YH, Sakakura M, Wang L, Yu YH, Wang HJ et al. High speed ultrafast laser anisotropic nanostructuring by energy deposition control via near-field enhancement. *Optica* **8**, 1365–1371 (2021).
20. Tan DZ, Wang Z, Xu BB, Qiu JR. Photonic circuits written by femtosecond laser in glass: improved fabrication and recent progress in photonic devices. *Adv Photonics* **3**, 024002 (2021).
21. Zhang B, Wang L, Chen F. Recent advances in femtosecond laser processing of $LiNbO_3$ crystals for photonic applications. *Laser Photonics Rev* **14**, 1900407 (2020).
22. Zhang S, Xu LS, Wu J, Yang Y, Zhang CX et al. Femtosecond laser micro-nano processing for boosting bubble releasing of

gas evolution reactions. *Nano Res* **15**, 1672–1679 (2022).
23. Zhang B, Tan DZ, Wang Z, Liu XF, Xu BB et al. Self-organized phase-transition lithography for all-inorganic photonic textures. *Light Sci Appl* **10**, 93 (2021).
24. Gu M, Zhang QM, Lamon S. Nanomaterials for optical data storage. *Nat Rev Mater* **1**, 16070 (2016).
25. Kallepalli DLN, Alshehri AM, Marquez DT, Andrzejewski L, Scaiano JC et al. Ultra-high density optical data storage in common transparent plastics. *Sci Rep* **6**, 26163 (2016).
26. Montelongo Y, Yetisen AK, Butt H, Yun SH. Reconfigurable optical assembly of nanostructures. *Nat Commun* **7**, 12002 (2016).
27. Wang Z, Tan DZ, Qiu JR. Single-shot photon recording for three-dimensional memory with prospects of high capacity. *Opt Lett* **45**, 6274–6277 (2020).
28. Kim YH, Arunkumar P, Kim BY, Unithrattil S, Kim E et al. A zero-thermal-quenching phosphor. *Nat Mater* **16**, 543–550 (2017).
29. Royon A, Bourhis K, Bellec M, Papon G, Bousquet B et al. Silver clusters embedded in glass as a perennial high capacity optical recording medium. *Adv Mater* **22**, 5282–5286 (2010).
30. Wang L, Xie RJ, Li YQ, Wang XJ, Ma CG et al. $Ca_{1-x}Li_xAl_{1-x}Si_{1+x}N_3$: Eu^{2+} solid solutions as broadband, color-tunable and thermally robust red phosphors for superior color rendition white light-emitting diodes. *Light Sci Appl* **5**, e16155 (2016).
31. Gu M, Li XP, Cao YY. Optical storage arrays: a perspective for future big data storage. *Light Sci Appl* **3**, e177 (2014).
32. Dai PP, Li C, Zhang XT, Xu J, Chen X et al. A single Eu^{2+}-activated high-color-rendering oxychloride white-light phosphor for white-light-emitting diodes. *Light Sci Appl* **5**, e16024 (2016).
33. Qiao JW, Zhou GJ, Zhou YY, Zhang QY, Xia ZG. Divalent europium-doped near-infrared-emitting phosphor for light-emitting diodes. *Nat Commun* **10**, 5267 (2019).
34. Joos JJ, van der Heggen D, Martin LIDJ, Amidani L, Smet PF et al. Broadband infrared LEDs based on europium-to-terbium charge transfer luminescence. *Nat Commun* **11**, 3647 (2020).
35. Wang C, Peng MY, Jiang N, Jiang XW, Zhao CJ et al. Tuning the Eu luminescence in glass materials synthesized in air by adjusting glass compositions. *Mater Lett* **61**, 3608–3611 (2007).
36. Dorenbos P. Relation between Eu^{2+} and Ce^{3+} f ↔ d-transition energies in inorganic compounds. *J Phys Condens Matter* **15**, 4797–4807 (2003).
37. Zhao M, Zhang QY, Xia ZG. Structural engineering of Eu^{2+}-doped silicates phosphors for led applications. *Acc Mater Res* **1**, 137–145 (2020).

Acknowledgements

We are grateful for financial supports from the National Key R&D Program of China (No. 2021YFB2802000 and 2021YFB2800500); the National Natural Science Foundation of China (Grant Nos. U20A20211, 51902286, 61775192, 61905215, and 62005164); Key Research Project of Zhejiang Lab; the State Key Laboratory of High Field Laser Physics (Shanghai Institute of Optics and Fine Mechanics, Chinese Academy of Sciences), and China Postdoctoral Science Foundation (2021M702799).

Author contributions

The manuscript was written through contributions of all authors. All authors have given approval to the manuscript.

Competing interests

The authors declare no competing financial interests.

Supplementary information

Supporting information is available for this paper at https://doi.org/10.29026/oea.2023.220008

LASER & PHOTONICS REVIEWS
www.lpr-journal.org

Single-Pulse-Driven Frame Printing of Chromatic Pixels in Lithium Niobate Crystal

Jie Zhang, Zhuo Wang, Bo Zhang, and Jianrong Qiu**

Highly efficient and programmable writing of multidimensional optical data is of great value for next-generation high-throughput information technologies but has been rarely achieved. Here, a one-step frame printing of chromatic pixels in lithium niobate crystal by using a single ultrafast laser pulse is reported. In this strategy, a phase superposition-based spatial light modulation strategy is applied to split a single ultrafast laser pulse into multiple son pulses with designated optical properties and spatial distribution patterns. It is demonstrated that these son pulses allow for massively creating micro-amorphous phase transition zones with on-demand structural features that can modulate the intrinsic birefringence of the crystal matrix and generate wavelength-selective interference in the visible band to form pixel-level chromatic patterns, namely, single-pulse-driven frame color printing. The created chromatic pixels can be encoded into computer-recognizable data arrays to play a role in high-efficiency multidimensional information recording. The presented approach enables fast and programmable information batch writing in 3D space and can serve as a versatile tool boosting next-generation information optics.

1. Introduction

The vast majority of information that human beings get from the outside world is transmitted through light where the optical frequency, which can be identified as color by eyes or detectors, is an important information dimension.[1–5] Recently, structural colors that arise from the interference, diffraction, and scattering behaviors of light when interacting with micro-nano structures,[6–11] have been fast-developing and attracted tremendous attention as they lie at the fundamental position in boosting the development of advanced optical display,[12] information recording,[13] sensing,[14] detecting,[15] encryption,[16] and anti-counterfeiting.[17] In principle, the generation of structural colors relies on the optical modulation of illumination polychromatic light by wavelength-scale photonic structures, with each color corresponding to a specific structural feature.[18–21] The generation of pixel-level structural colors that are especially valuable in information optics therefore requires the production of various photonic structural modules,[22–24] where a set of processing parameters generally enables the fabrication of only one structural feature, resulting in the presentation of only one kind of color (**Figure 1a**). Such a one-to-one coloration mode greatly limits the information writing efficiency, as it generally requires frequent adjustment of laser and writing parameters, which will overload the laser and mechanical servo systems. Besides, the spatial scope of pixel-level color printing is largely limited to a 2D plane or near surfaces. 3D embedded micro-nano structures allow for effectively utilizing the vertical spatial dimension and favorable properties of substrates, implanting additional degrees of freedom in light modulation and photonic device functionalization.[25–28] However, a highly efficient structural coloration that enables massively printing multiple chromatic pixels at designated 3D spatial locations with one set of processing parameters has not been achieved.

The key to breaking through this bottleneck lies in the development of a novel one-to-many coloration approach that enables parallel fabricating light modulation structures in 3D space. At present, it is extremely difficult to achieve this goal by relying on conventional micro-nano machining technologies, as they generally require cumbersome processes. Recently, the ultrafast laser has shown great superiority in creating embedded micro-nano photonic structures in various transparent media because of its highly efficient and versatile nonlinear material modification capacity.[29–35] In theory, it is possible to engineer ultrafast laser pulses and manipulate them to fast inscribe desired light modulation structures in a transparent medium, achieving the efficient generation of 3D colors.

Here, we report on a single ultrafast laser pulse-driven frame coloration strategy that enables fast one-to-many production of multiple chromatic pixels in 3D space (Figure 1b). This proposal is built upon two of our pivotal research foundations.[36] First, single-pulse ultrafast laser-induced micro-amorphous phase transition (MAPT) in lithium niobate ($LiNbO_3$) can locally modulate the phase difference of O and E light beams that propagate in the crystal matrix and establish wavelength-selective interference in 3D space by using chromatic polarization effect, namely, pixel-level structural colors. Second, the interference colors can

J. Zhang, Z. Wang, B. Zhang, J. Qiu
State Key Laboratory of Modern Optical Instrumentation
College of Optical Science and Engineering
Zhejiang University
Hangzhou 310027, China
E-mail: zhangbob@zju.edu.cn; qjr@zju.edu.cn

The ORCID identification number(s) for the author(s) of this article can be found under https://doi.org/10.1002/lpor.202400054

DOI: 10.1002/lpor.202400054

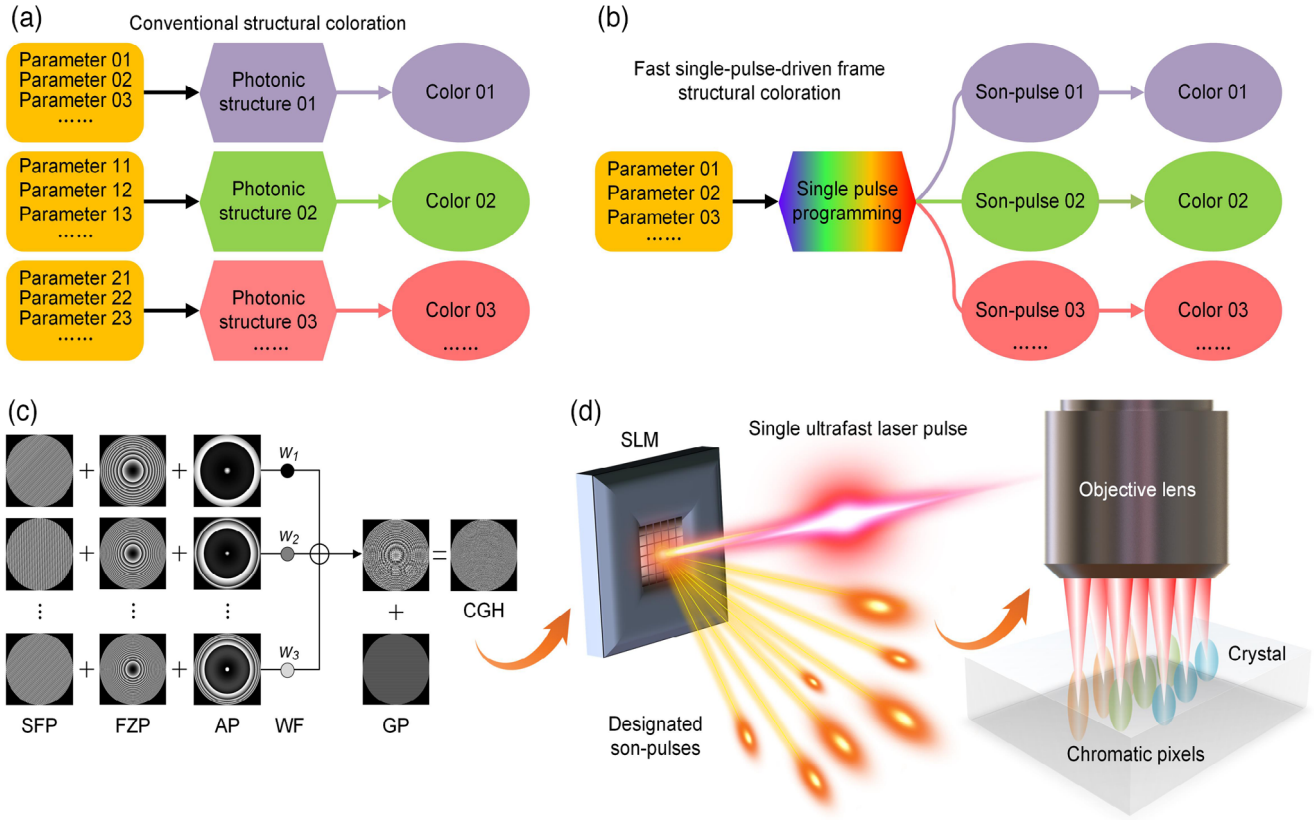

Figure 1. Concept and principle of single-pulse-driven frame printing of chromatic pixels. a) Schematic of conventional one-to-one structural coloration. b) Our fast one-to-many structural coloration based on frame printing. c) Creation principle of a CGH for frame printing. d) Schematic showing a single ultrafast laser pulse is programmed into multiple son pulses that can drive the frame printing of multiple chromatic pixels in 3D space.

be tuned by adjusting the length of the MAPT domain. In our design, a spatial light modulation strategy is applied to add a well-designed multi-focus phase to the original phase of the incident ultrafast laser to create a multi-focal array with designated spatial arrangement, focal-volume length, and energy distribution. Specifically, a single-focus phase (SFP) and Fresnel-zone plate phase (FZP) are added to ensure the 3D spatial positioning of multi-focal arrays. The customization of the structural color is performed by actively introducing an aberration phase (AP) and weighting factor (WF) to adjust focal-volume lengths and energy distributions of multi-focal arrays, respectively (Figure 1c). The grating phase (GP) is introduced to eliminate the influence of the zero-order light.[37,38] In this way, by simply loading a sheet of computer-generated hologram (CGH) to a spatial light modulator (SLM), a single ultrafast laser pulse (parent pulse) can be programmed into multiple designated son pulses that can produce MAPT zones with desired structural features, realizing the frame printing of multiple chromatic pixels in the crystal matrix (Figure 1d). This one-to-many processing mode will endow structural coloration in 3D space with unprecedented efficiency and flexibility.

2. Design and Principle

Generally, the number of pixels that can be printed at a time in frame printing is limited by ultrafast laser output power, objective field of view, and damage threshold of the SLM.[38,39] When printing images with a large number of pixels, it is necessary to perform partition processing, with one partition corresponding to one frame. Here, a three-step algorithm is proposed to obtain the CGH for the generation of a volumetric multi-focal array with required optical properties in 3D space (**Figure 2**): i) Designing the target pattern composed of chromatic pixels, dividing the pattern into a series of frames, and extracting the color and position information of pixels in each frame, where one frame corresponds to one parent pulse and each pixel in a frame corresponds to one son pulse. ii) According to the extracted information, the phase modulation of each frame is programmed to induce the chromatic pixels within it. Specifically, we regard each pixel in one frame as a single focus and further divide a frame into a number of single-focus images. Then, the inverse Fourier transform is applied to calculate these single-focus images into a series of SFPs with lateral position (X/Y coordinates) information. For Z-axis positioning, the SFPs with different vertical depths (Z coordinate) were achieved by introducing FZPs, which are necessary for generating 3D volumetric multi-focal arrays.[40,41] For color manipulation, APs are accordingly superimposed on SFPs, thereby adjusting the focal-volume lengths of son pulses in each frame, and the corresponding son-pulse energy is individually adjusted by multiplying the complex amplitudes of SFPs by WFs. iii) Subjecting these SFPs with FZPs, APs, and WFs to complex amplitude superposition, and thus constructing a complex amplitude hologram that can generate multi-focal arrays with designated

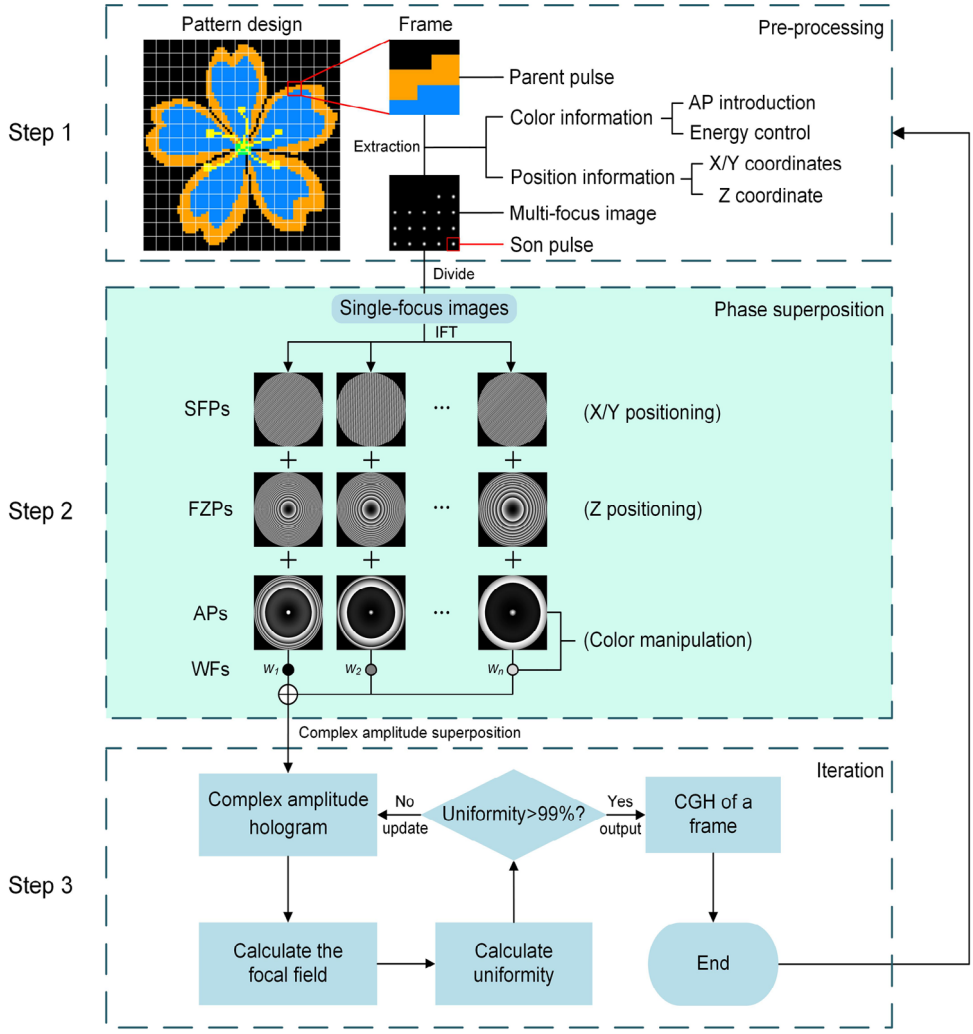

Figure 2. The three-step algorithm for calculating CGHs enables the generation of a volumetric multi-focal array with designated color and position characteristics. IFT: inverse Fourier transform.

parameters, including spatial position, focal-volume length, and energy distribution. Setting this complex amplitude hologram as the initial input and the CGH of a frame can be obtained through an iterative calculation process (Detailed mathematical operation see Text S2, Supporting Information). Therefore, by sequentially loading CGHs into the SLM that drives the laser direct writing system, the single-pulse-driven frame printing of chromatic pixels can be achieved.

This one-to-many coloration mode converts the tedious parameter adjustments of traditional one-to-one coloration into the loading of CGHs. In this way, the laser is tasked solely with emitting single-parameter parent pulses, while the customization of son-pulse parameters is massively handled via the SLM. The 3D writing of multiple color pixels can be achieved by simply loading CGHs and coordinating with simple movements of the translation stage, thereby largely excluding the response time of hardware from the pixel writing process. This method is anticipated to greatly reduce the none-principle limitations on optical information writing efficiency posed by hardware systems, positioning it as a comprehensive platform to propel the advancement of next-generation information optics.

3. Results and Discussion

We demonstrated the effectiveness of the spatial light modulation strategy in generating multi-focal arrays with designated parameters and practically inducing chromatic pixels. Here, we first set a 3 × 3 squared multi-focal array with homogeneous pulse energy distribution in the XY plane as a frame and superposed three APs (denoted as "1", "2", and "3". The detailed generation and optimization of APs see Text S3, Supporting Information) in different rows of this multi-focus image, respectively (**Figure 3a**). The CGH for generating the multi-focal array with desired focal-volume lengths was then calculated by using our algorithm. Simulated spatial light intensity distribution of the multi-focal array shows a significant difference in the focal-volume lengths (Figure 3b). In experimental verification, the obtained CGH was loaded into an SLM to split a parent pulse into designated multiple son pulses that could drive the frame printing of chromatic pixels in a $LiNbO_3$ crystal. The side section image of experimentally induced chromatic pixels is in perfect agreement with the theoretical simulations (Figure 3c), which confirms the feasibility of our approach in generating multi-focal arrays with manageable

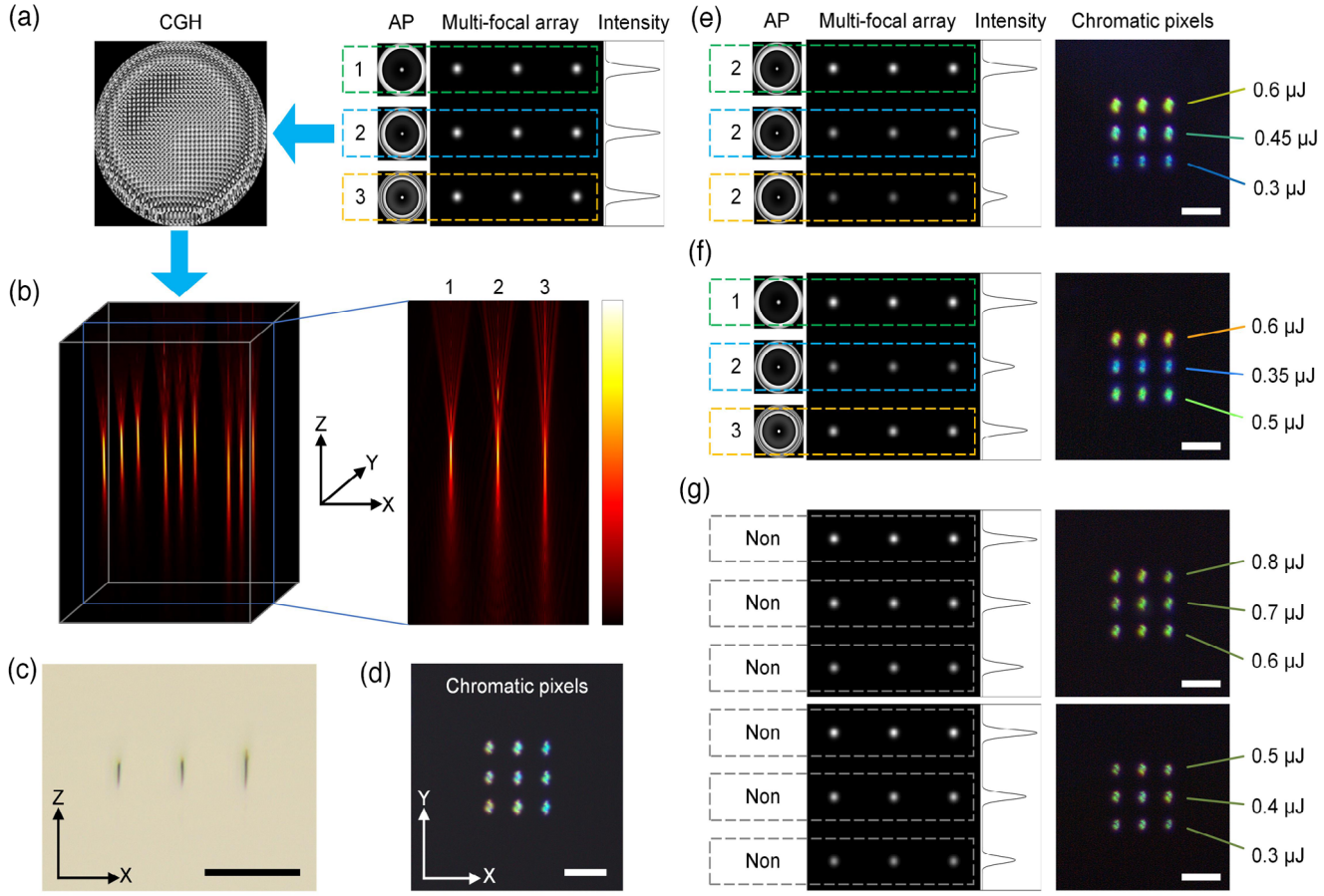

Figure 3. Manipulation of chromatic pixels in frame printing. a) CGH (left) calculated from a designed multi-focus image with three APs superposed on each row (right). b) The 3D simulation of the multi-focal array generated by the calculated CGH. The color bar illustrates light intensity. c) The side section image and d) the top view of experimentally printed chromatic pixels. The energy of each son pulse is 0.42 μJ. e) The designed multi-focal array (left) and experimentally printed chromatic pixels (right) using different son-pulse energies accompanied with a fixed AP. f) The designed multi-focal array (left) and experimentally printed chromatic pixels (right) by engineering the combination of APs and son-pulse energies. g) The results of the frame printing cancel the introduction of APs and only manipulate son-pulse energies. Scale bars: 30 μm.

focal-volume lengths. In theory, a larger focal-volume length can promote the stretching of chromatic pixels in the Z-axis, corresponding to the redshift of the interference signal. However, the experimentally printed pixel array presented the opposite blue shift color variation (Figure 3d), which we call abnormal color manipulation. This is attributed to the absence of corresponding pulse energy adjustment during the focal-volume length manipulation. In this condition, the focal-volume length elongation decreases the energy density in the focal volume, which will instead suppress the extension of the actually induced crystal-to-glass phase transition zone. Then, we fixed AP and arranged the son-pulse energies of three rows in the 3 × 3 multi-focal array as 0.6, 0.45, and 0.3 μJ. Experimental results indicated an obvious red shift in the multi-focal array with pulse energy increased (called normal color manipulation), which confirms the effectiveness of pulse energy-driven color control in frame printing (Figure 3e).

From these results, we realized that the color obtained by individually adjusting AP or pulse energy may not be the optimized result and it is necessary to integrate these two kinds of manipulation modes, namely, simultaneously regulating both the AP and energy distribution, to further enhance color manipulation. Here, we superposed various APs to multi-focus images with different son-pulse energies and conducted a series of process experiments to determine their correspondences, and thus achieve high-quality coloration (Figure S7, Supporting Information). As shown in Figure 3f, by properly engineering the combination of APs and son-pulse energies, we eventually achieve a great improvement in coloration quality, including color saturation, contrast, as well as the distinction between different pixels. As a comparison, we further demonstrated the frame printing that cancels the introduction of APs and only relies on pulse energy control (Figure 3g). Experimental results indicate that color manipulation of chromatic pixels cannot be effectively achieved in frame printing without the introduction of APs, confirming the pivotal role of AP-pulse energy combined control. These results firmly substantiate the capacity of our method in realizing one-step frame printing of designated chromatic pixel arrays in $LiNbO_3$ crystals. In principle, our strategy is universally effective in different single crystals rather than an isolated scheme.

Generally, the physical size of the printed pixels can reach ≈300 nm and the imaged pixel size can reach ≈500 nm (Figure S8, Supporting Information). Since the chromatic pixels are optically read out, their imaged size is limited by the diffraction limit. The further reduction in pixel size will drastically increase the difficulty of data reading, for example, immersion objective and long exposure, which will seriously reduce reading speed

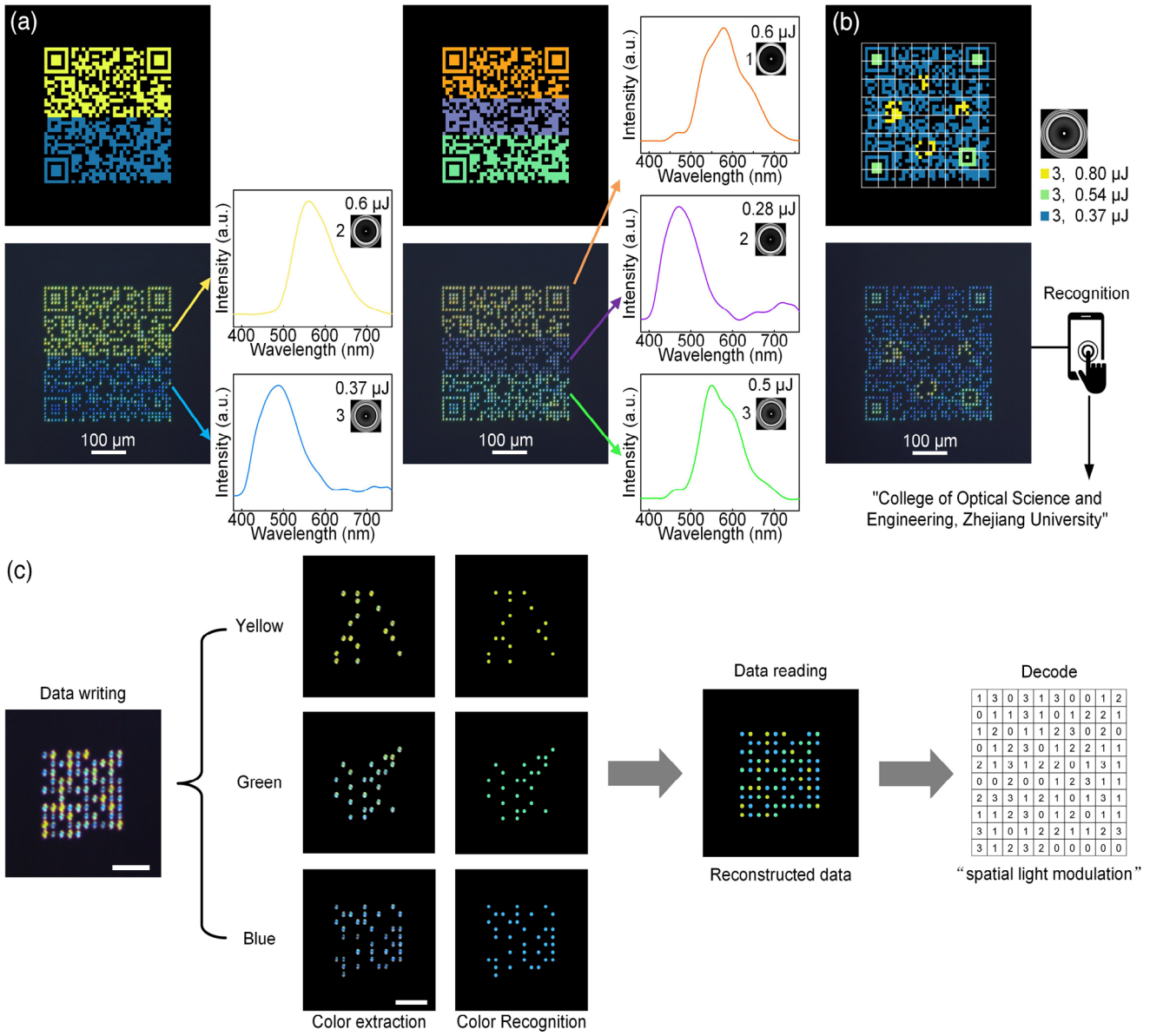

Figure 4. Spectral characteristics and recognizability of chromatic pixels produced by frame printing. a) QR code patterns composed of five colored subareas (top), and the corresponding experimentally printed colorful QR codes (bottom), whose spectra are measured and shown on their right side. b) QR code pattern composed of multiple irregular monochromatic subareas (top), and experimentally printed one with its recognition result (bottom). c) Frame printing of a computer-recognizable data array encoded in quaternary, where yellow equals to "3", green equals to "2", blue equals to "1", and black equals to "0". Scale bars: 50 μm.

and improve application costs. The presented pixel size is the result of a balance among multiple factors at this stage. Protected by the surrounding all-inorganic crystal matrix, these chromatic pixels possess ultra-high stability, making them immune to various harsh environments, such as high temperatures, pollution, and mechanical damage (Figure S9, Supporting Information). These properties make our approach valuable for micro-nano photonic applications that require high robustness, such as next-generation perpetual data storage.

The combination of spectral and positional information forms the essential basis for computer recognition of printed chromatic pixels. In this study, we demonstrated the frame printing of a series of colorful QR codes and investigated the spectral characteristics of printed chromatic pixels. As depicted in **Figure 4**a, several representative spectra centered from 440 to 600 nm are identified in the transmission signals from different colored subareas of the QR codes. This indicates a broad spectral tunability of the chromatic pixels produced through frame printing within the visible range. In addition, we also showcase that the relative positions of different chromatic pixels can be precisely tailored in the single-step fabrication process. As exemplified by a specifically designed colorful QR code composed of three distinct kinds of chromatic pixels, the monochromatic subareas are uneven in shape, size, and pixel number. Even so, the accuracy of the relative positioning of these chromatic pixels is effectively maintained in frame printing, enabling quick recognition and reading of the printed QR code by various intelligent devices (Figure 4b).

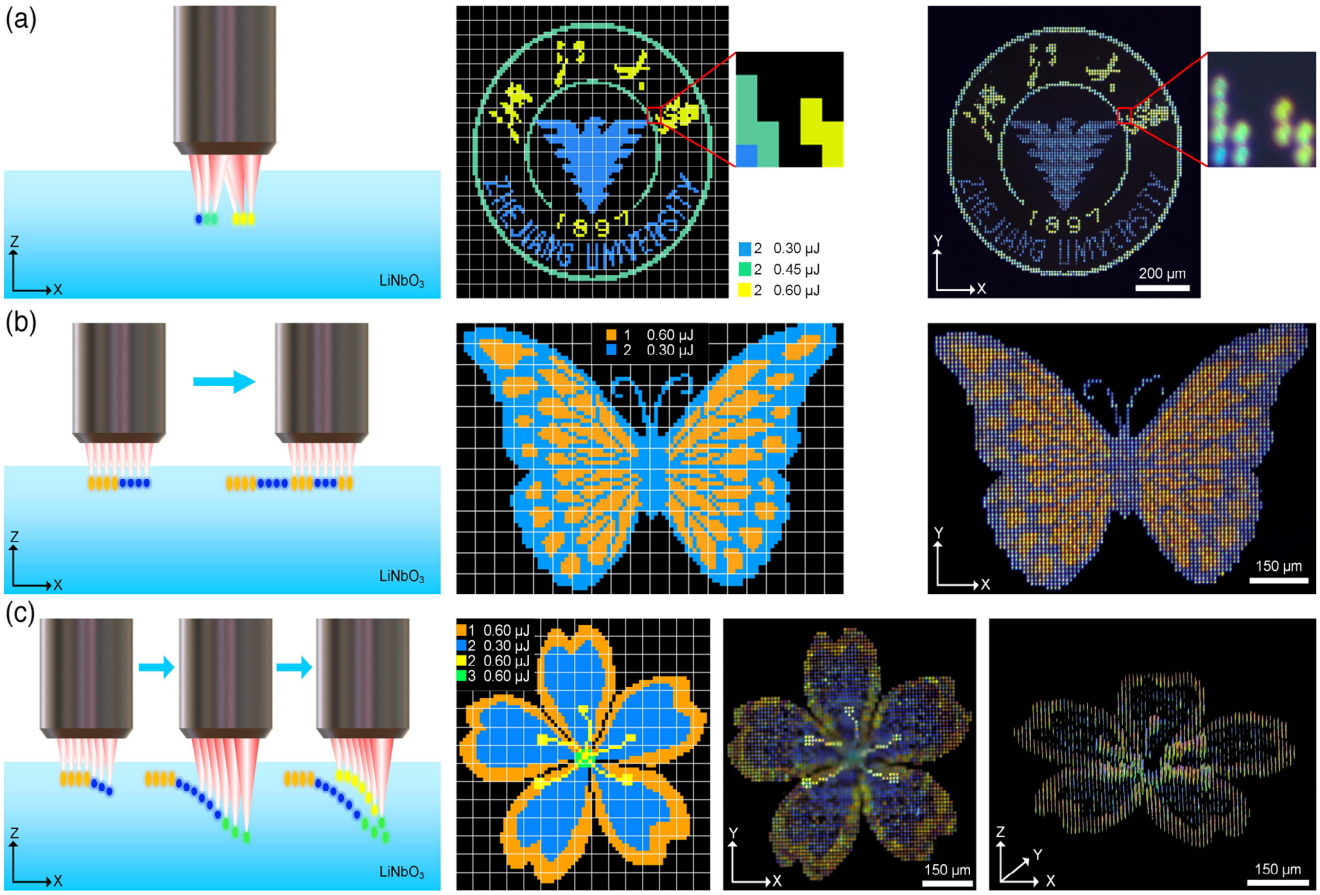

Figure 5. Different types of highly customized frame printing. a) Schematic showing the frame printing of sparse dot-line patterns (left). Designed a sparse dot-line pattern (middle) and experimentally printed one (right). b) Schematic diagram showing the frame printing of complex filling patterns (left). Designed butterfly pattern filled with plenty of irregular subareas (middle) and experimentally printed one (right). c) Schematic showing 3D frame printing of complex 3D patterns without relying on vertical movement (left). Designed 3D flower pattern with multiple subareas (middle). The top view and perspective view of experimentally printed 3D flower pattern (right). Inserted parameter lists indicating the applied APs and son-pulse energies of corresponding subareas.

The spectral features and accurate positioning of chromatic pixels make frame printing an ideal tool for producing computer-recognizable data arrays. As a proof of concept, we demonstrate multidimensional information recording by using the spectral features (reflected in colors) of chromatic pixels as an additional information multiplexing channel beyond traditional spatial dimensions (Figure 4c), where three different chromatic pixels (blue, green, and yellow) were rapidly written by frame printing to construct a quaternary encoded data array. By leveraging color channels, the multidimensional optical data can be precisely decoded by a computer. Owing to the transparency of the crystal matrix, the recorded data arrays can be accurately identified from both the front and back sides of the sample using transmission and reflection illumination modes, respectively (Figure S10, Supporting Information), making our approach widely compatible with different readout systems. These results show that the chromatic pixels written by our frame printing approach possess excellent readability.

Except for standardized patterns like QR codes and data arrays, our method can also perform well in the fast printing of highly customized chromatic patterns with arbitrary shapes. As a proof of concept, we demonstrated three representative types of customized patterning, including sparse dot-line patterning, 2D complex filling patterning, and 3D spatial patterning (**Figure 5**). First, benefiting from the combined color printing strategy of multi-phase superposition and pulse energy distribution, both the pixel positioning and coloration accuracy of irregular sparse dot-line typed patterns can be well guaranteed, achieving pixel-level color control (Figure 5a). Notably, during the frame printing process, the overall energy of the incident parent pulse can be efficiently adjusted according to the pixel numbers and son-pulse energies of each frame, ensuring the color consistency and coherence of different frames, instead of performing frequent parameter regulation like traditional one-to-one coloration modes. We demonstrate that even though the filling pattern with plenty of non-uniform subareas is partitioned into various frames, the target color distribution can be achieved with a considerably high consistency with the original design (Figure 5b), which is advantageous in massive and complex color printing. Importantly, owing to the transparency of $LiNbO_3$ and laser direct writing properties, our methods inherently support the patterning of the chromatic pixels distributed in 3D space, extending the concept of frame printing from 2D to 3D. In 3D frame printing mode, Z-axis positions of chromatic pixels need to be considered. Therefore, FZPs are added in CGHs to adjust the focusing depth of son pulses, thus tuning the Z-axis position of chromatic

pixels. Here, a 3D flower-shaped pattern with pixels distributed in depths ranging from 20 to 180 μm below the crystal surface can be fast printed by simply moving the translation stage in the XY-plane (Figure 5c), which is essentially a volume-by-volume printing process. Unlike traditional layer-by-layer 3D patterning, our 3D frame printing strategy does not require frequent vertical movements or point-by-point processing, which can significantly simplify and speed up the printing process of chromatic pixels in transparent media (Figure S11, Supporting Information). Compared with recently reported multi-pulse and single-pulse-based one-to-one data writing approaches,[42,43] the one-to-many nature of frame printing can significantly improve the writing speed by tens to hundreds of times. These results represent a substantial advance in the efficient writing of 3D visibly chromatic information, which is empowered by our conceptually new color printing strategy. Notably, our strategy aims to improve chromatic information writing and reading efficiency while ensuring computer recognition. Therefore, the printed chromatic pixels may not be optimal for human observation. If necessary, they can be visually improved by optimizing the processing and imaging parameters.

4. Conclusion

In summary, we established a one-step strategy to achieve 3D programmable frame printing of tunable chromatic pixels inside the $LiNbO_3$ crystal matrix. In this strategy, one ultrafast laser pulse corresponds to a frame, and an SLM was applied to split the single incident pulse into multiple son pulses to drive the one-to-many printing process of multiple chromatic pixels in each frame. The crucial of our approach lies in the introduction of various functional phase superposition and pulse energy regulation in spatial light modulation, which enables the generation of volumetric chromatic pixel arrays with designated structural features and spatial distribution. Essentially, the proposed strategy converts the traditional one-to-one coloration process into a fast one-to-many coloration mode, greatly improving the efficiency and flexibility of color patterning in 3D space. The printed chromatic pixels can be encoded into computer-recognizable arrays to play a role in 3D display, encryption, anti-counterfeiting, and multi-dimensional data storage. It would be exciting to fuse the color frame printing approach with various advanced micro-nano machining technologies to achieve quick and programmable information batch writing in 3D space and can serve as a versatile platform to boost next-generation information optics.

Supporting Information

Supporting Information is available from the Wiley Online Library or from the author.

Acknowledgements

This work was financially supported by the National Key R&D Program of China (No. 2021YFB2802001); the National Natural Science Foundation of China (Grant Nos. 12304349, U20A20211); the Postdoctoral Fellowship Program of CPSF (GZB20230628); and "Pioneer" and "Leading Goose" R&D Program of Zhejiang (2023C03089).

Conflict of Interest

The authors declare no conflict of interest.

Author Contributions

J.Z. and Z.W. contributed equally to this work. J.Z. and B.Z. conceived the idea. J.Q. and B.Z. organized, coordinated, and supervised the project. J.Z. and Z.W. performed the experiments and collected the data. J.Z., Z.W., B.Z., and J.Q. interpreted the results and proposed the color frame printing method. J.Z. and B.Z. wrote the manuscript. J.Z., Z.W., B.Z., and J.Q. discussed and revised the manuscript.

Data Availability Statement

The data that support the findings of this study are available from the corresponding author upon reasonable request.

Keywords

chromatic pixels, frame printing, lithium niobate, structural coloration, ultrafast laser

Received: January 11, 2024
Revised: April 12, 2024
Published online:

[1] D. Hu, Y. Lu, Y. Cao, Y. Zhang, Y. Xu, W. Li, F. Gao, B. Cai, B.-O. Guan, C.-W. Qiu, *ACS Nano* **2018**, *12*, 9233.
[2] A. Kristensen, J. K. Yang, S. I. Bozhevolnyi, S. Link, P. Nordlander, N. J. Halas, N. A. Mortensen, *Nat. Rev. Mater.* **2016**, *2*, 16088.
[3] X. Ouyang, Y. Xu, M. Xian, Z. Feng, L. Zhu, Y. Cao, S. Lan, B.-O. Guan, C.-W. Qiu, M. Gu, *Nat. Photonics* **2021**, *15*, 901.
[4] W. Yang, G. Qu, F. Lai, Y. Liu, Z. Ji, Y. Xu, Q. Song, J. Han, S. Xiao, *Adv. Mater.* **2021**, *33*, 2101258.
[5] X. Zhang, M. Pu, Y. Guo, J. Jin, X. Li, X. Ma, J. Luo, C. Wang, X. Luo, *Adv. Funct. Mater.* **2019**, *29*, 1809145.
[6] H. Liu, H. Wang, H. Wang, J. Deng, Q. Ruan, W. Zhang, O. A. M. Abdelraouf, N. S. S. Ang, Z. Dong, J. K. W. Yang, H. Liu, *ACS Nano* **2022**, *16*, 8244.
[7] H. Wang, X. Wang, C. Yan, H. Zhao, J. Zhang, C. Santschi, O. J. F. Martin, *ACS Nano* **2017**, *11*, 4419.
[8] J. Xue, Z.-K. Zhou, Z. Wei, R. Su, J. Lai, J. Li, C. Li, T. Zhang, X.-H. Wang, *Nat. Commun.* **2015**, *6*, 8906.
[9] S. Daqiqeh Rezaei, Z. Dong, J. You En Chan, J. Trisno, R. J. H. Ng, Q. Ruan, C.-W. Qiu, N. A. Mortensen, J. K. W. Yang, *ACS Photonics* **2021**, *8*, 18.
[10] K.-T. Lee, C. Ji, D. Banerjee, L. J. Guo, *Laser Photonics Rev.* **2015**, *9*, 354.
[11] Z. Xuan, J. Li, Q. Liu, F. Yi, S. Wang, W. Lu, *The Innovation* **2021**, *2*, 100081.
[12] W. Fan, J. Zeng, Q. Gan, D. Ji, H. Song, W. Liu, L. Shi, L. Wu, *Sci. Adv.* **2019**, *5*, eaaw8755.
[13] B. Yang, W. Liu, Z. Li, H. Cheng, S. Chen, J. Tian, *Adv. Opt. Mater.* **2018**, *6*, 1701009.
[14] S. Daqiqeh Rezaei, J. Ho, A. Naderi, M. Tavakkoli Yaraki, T. Wang, Z. Dong, S. Ramakrishna, J. K. Yang, *Adv. Opt. Mater.* **2019**, *7*, 1900735.
[15] B. Yang, D. Ma, W. Liu, D.-Y. Choi, Z. Li, H. Cheng, J. Tian, S. Chen, *Optica* **2022**, *9*, 217.

[16] B. Dong, B. Liu, C. Chen, D. Wang, L. Zhang, L. Xu, W. Xiong, J. Li, Y. Hu, J. Chu, D. Wu, *Opt. Lett.* **2023**, *48*, 2508.
[17] C. Ji, M. Chen, L. Wu, *Adv. Opt. Mater.* **2022**, *10*, 2102383.
[18] L. Shi, J. Niu, L. Li, C. Wang, X. Shang, P. Zhang, Y. Liu, Y. Zhang, *Adv. Opt. Mater.* **2022**, *10*, 2200552.
[19] Q. Ruan, W. Zhang, H. Wang, J. Y. E. Chan, H. Wang, H. Liu, D. Fan, Y. Li, C.-W. Qiu, J. K. W. Yang, *Adv. Mater.* **2022**, *34*, 2108128.
[20] Y. Liu, H. Wang, J. Ho, R. C. Ng, R. J. H. Ng, V. H. Hall-Chen, E. H. H. Koay, Z. Dong, H. Liu, C.-W. Qiu, J. R. Greer, J. K. W. Yang, *Nat. Commun.* **2019**, *10*, 4340.
[21] J. Geng, L. Xu, W. Yan, L. Shi, M. Qiu, *Nat. Commun.* **2023**, *14*, 565.
[22] Z. Zhang, T. Guo, Z. Lin, Z. Liu, N. He, X. Xu, Y. Xing, D. Wang, Y. Li, Y. Jin, S. He, *Laser Photonics Rev.* **2023**, *17*, 2200820.
[23] G. Geng, R. Pan, C. Li, R. Zheng, Y. Liu, Z. Zhang, C. Gu, J. Li, *Laser Photonics Rev.* **2023**, *17*, 2300073.
[24] D. Franklin, Y. Chen, A. Vazquez-Guardado, S. Modak, J. Boroumand, D. Xu, S.-T. Wu, D. Chanda, *Nat. Commun.* **2015**, *6*, 7337.
[25] M. Shao, F. Liang, H. Yu, H. Zhang, *Light: Sci. Appl.* **2022**, *11*, 31.
[26] Z. Zhang, M. Shao, F. Liang, H. Yu, H. Zhang, Y. Wu, *Laser Photon. Rev.* 2300664.
[27] D. Wei, C. Wang, H. Wang, X. Hu, D. Wei, X. Fang, Y. Zhang, D. Wu, Y. Hu, J. Li, *Nat. Photonics* **2018**, *12*, 596.
[28] T. Xu, K. Switkowski, X. Chen, S. Liu, K. Koynov, H. Yu, H. Zhang, J. Wang, Y. Sheng, W. Krolikowski, *Nat. Photonics* **2018**, *12*, 591.
[29] K. Sun, D. Tan, X. Fang, X. Xia, D. Lin, J. Song, Y. Lin, Z. Liu, M. Gu, Y. Yue, *Science* **2022**, *375*, 307.
[30] B. Zhang, D. Tan, Z. Wang, X. Liu, B. Xu, M. Gu, L. Tong, J. Qiu, *Light: Sci. Appl.* **2021**, *10*, 93.
[31] X. Xu, T. Wang, P. Chen, C. Zhou, J. Ma, D. Wei, H. Wang, B. Niu, X. Fang, D. Wu, S. Zhu, M. Gu, M. Xiao, Y. Zhang, *Nature* **2022**, *609*, 496.
[32] D. Wei, C. Wang, H. Wang, X. Hu, D. Wei, X. Fang, Y. Zhang, D. Wu, Y. Hu, J. Li, S. Zhu, M. Xiao, *Nat. Photonics* **2018**, *12*, 596.
[33] X.-Q. Liu, Y.-L. Zhang, Q.-K. Li, J.-X. Zheng, Y.-M. Lu, S. Juodkazis, Q.-D. Chen, H.-B. Sun, *PhotoniX* **2022**, *3*, 1.
[34] F. Chen, J. R. V. de Aldana, *Laser Photonics Rev.* **2014**, *8*, 251.
[35] B. Zhang, Z. Wang, D. Tan, J. Qiu, *PhotoniX* **2023**, *4*, 24.
[36] Z. Wang, B. Zhang, Z. Wang, J. Zhang, P. G. Kazansky, D. Tan, J. Qiu, *Adv. Mater.* **2023**, *35*, 2303256.
[37] D. Pan, S. Liu, J. Li, J. Ni, C. Xin, S. Ji, Z. Lao, C. Zhang, B. Xu, R. Li, *Adv. Funct. Mater.* **2022**, *32*, 2106917.
[38] B. P. Cumming, S. Debbarma, B. Luther-Davis, M. Gu, *Optics* **2013**, *21*, 19135.
[39] D. Yang, L. Liu, Q. Gong, Y. Li, *Macromol. Rapid Commun.* **2019**, *40*, 1900041.
[40] S. Hasegawa, Y. Hayasaki, N. Nishida, *Opt. Lett.* **2006**, *31*, 1705.
[41] J. Jia, Y. Wang, J. Liu, X. Li, Y. Pan, Z. Sun, B. Zhang, Q. Zhao, W. Jiang, *Appl. Opt.* **2013**, *52*, 1404.
[42] Z. Wang, B. Zhang, D. Tan, J. Qiu, *Opto-Electronic Adv.* **2023**, *6*, 220008.
[43] H. Wang, Y. Lei, L. Wang, M. Sakakura, Y. Yu, G. Shayeganrad, P. G. Kazansky, *Laser Photonics Rev.* **2022**, *16*, 2100563.

Optics Letters

Single-shot photon recording for three-dimensional memory with prospects of high capacity

ZHUO WANG,[1] DEZHI TAN,[1,*] AND JIANRONG QIU[1,2]

[1]State Key Laboratory of Modern Optical Instrumentation, College of Optical Science and Engineering, Zhejiang University, Hangzhou 310027, China
[2]e-mail: qjr@zju.edu.cn
*Corresponding author: wctdz@zju.edu.cn

Received 2 September 2020; revised 10 October 2020; accepted 14 October 2020; posted 14 October 2020 (Doc. ID 409171); published 12 November 2020

Femtosecond laser-induced modification in the glass has drawn considerable interest due to its widespread superiority in the applications of three-dimensional optical storage. In this Letter, we report that a single pulse could be used in optical memory with super-high writing speed. The photoluminescence image and spectrum indicate that one pulse-induced permanent photoreduction of Sm^{3+} to Sm^{2+} in Sm^{3+}-doped sodium aluminoborate glass can be achieved. Consequently, strong emission contrast is obtained, which is used for optical storage. By regulating the fabrication conditions, the fluorescent diameter could be controlled to approximately 800 nm, which demonstrates the feasibility in super-high density optical storage. Besides, multi-layer information is successfully inscribed. The proposed technique of single-pulse writing holds great potential for optical memory with high speed and huge capacity.

https://doi.org/10.1364/OL.409171

The capacity and the writing speed of optical information recording are in increasingly high demand with the development of big data technology [1]. Fs laser-induced localized modifications, such as changes in refractive index [2,3], selective precipitation of crystals [4,5], regulation of ion valence [6–9], ablation of nanorods [10,11], and formation of nanogratings [12–14], are widely accepted as effective media for optical data storage. However, great efforts have been made to increase the capacity of optical memory [15–19], but the importance of writing speed has been neglected. All the achievements for the optical storage are based on multi-pulse fs laser writing, which inevitably results in slow recording speed. Generally, thousands of or even more pulses are necessary to write a single spot. Thus, the primary challenge is the lack of a technique of single-pulse writing with the advantages of both high writing speed and tremendous capacity in optical data storage.

Multi-photon absorption induced by the ultra-high irradiance of an fs laser with low repetition rate pulses can lead to the structural modifications, which shows the promise to realize optical recording with a single pulse. Fs laser-induced-ion valence modulation with multiple pulses has engaged high interest due to its great potential in the application of optical storage with excellent characteristics, such as a high signal-to-noise ratio, high stability, and easy reading [20]. In essence, the electronic excitation of ions and transfer between the different excited species can be triggered by a single pulse. However, up to now, control of ion valence using a single pulse has not been reported.

This Letter is devoted to realizing single-shot photon recording with ultra-fast writing speed, which is extremely necessary for three-dimensional optical memory. To achieve this goal, a single pulse with diverse energy is employed to explore the threshold which could exactly induce the valence conversion of rare-earth ions. This not only fills the gap in single-shot photon recording on optical memory, but also becomes the key to increasing the storage density and writing speed. Our experimental study indicates that a single pulse can induce the permanent stable photoreduction of Sm^{3+} into Sm^{2+} in sodium aluminoborate glass. Single-pulse processing tremendously increases the writing speed in optical data storage, as well as greatly reducing the unit size and increasing the storage density. Finally, three-dimensional optical storage is presented with super-high writing speed and low writing energy threshold. In addition, the photoluminescence (PL) difference in the infrared range between Sm^{3+} and Sm^{2+} ions also may be present, which also would be interesting for applications [21–23].

The Sm^{3+}-doped sodium aluminoborate glass used in this Letter was prepared with a chemical composition of $85B_2O_3-5Al_2O_3-10Na_2O-0.1Sm_2O_3$ using a conventional melting–quenching technique [6]. Powers of reagent grade were mixed together and melted at 1250°C for 30 min in ambient atmosphere. The melted glass was cast on a stainless steel plate and formed a glass block with a thickness of about 1 mm.

Data recording experiments were performed with a fs laser system (PHAROS, Light Conversion Ltd.) that delivers 1030 nm. Typically, the laser beam was focused by a 0.8 NA objective lens at a depth of 100 μm from a surface for writing. The information encoded in glass was detected by a scanning

confocal fluorescence microscope. It consists of a fiber-coupled light source emitting at 405 nm, an XYZ nanopositioning stage with a 1.3 NA oil objective, and a single-photon counter. A bandpass filter (10 nm bandpass at around 680 nm) was used to eliminate background photoluminescence and improve the signal-to-noise ratio. In our case, the read speed is determined and limited by the moving speed of the nanopositioning stage, which can be improved by using a better detecting system with higher moving speed.

The size of the fs laser written spot and the PL intensity could directly affect the capacity and signal-to-noise ratio of optical storage respectively. Therefore, we systematically explored the effects of laser duration, pulse energy, repetition rate on the size and PL intensity of the irradiated area. Then an optimal parameter that could achieve the smallest memory cell size was determined for single-shot photon recording.

Figure 1(a) shows the optical image of dots written by a single pulse, and this clearly illustrates that optical recording can be realized with irradiation of a single fs laser pulse. Previous reports indicate that the valence of doped ions could be tuned by fs laser pulses [8,9]. Here we mapped PL of the written dots, which is shown in Fig. 1(b), and bright red emission is observable at the dots excited by a 405 nm laser. With the reduction of pulse duration, the single-pulse energy to induce microstructures is in a decreasing tendency, and the PL intensity increases dramatically. It is worth noting that the dots written by a single pulse with energy as low as 0.25 μJ still emit red PL, showing obvious contrast with the nonirradiated area. Figure 1(c) shows the PL spectrum before and after laser irradiation, and this indicates that partial Sm^{3+} ions were photoreducted into Sm^{2+} ions. A new peak attributed to the 4 f − 4 f transition of Sm^{2+} ions appears at around 680 nm [8,9]. Consequently, a novel technique of single-shot writing for optical recording with high speed is established, and the actual speed is only determined by the pulse repetition and stage moving speed. In addition, the reduction efficiency induced by a single fs laser pulse depends on many parameters, such as the nonlinear absorption coefficient of glass matrix, interaction volume, and the number of active electrons trapped by Sm^{3+}; uncovering the intrinsic characteristic of the reduction process will be helpful to determine the reduced percentage of Sm^{3+} [6].

We further analyze the size of the dots with a PL peak at 680 nm. Figure 2(a) compared the PL intensity as a function of pulse energy and duration. Generally, the PL intensity increases with the decrease of pulse duration, which can be assigned to the enhancement of peak power density with shorter pulse duration. Consequently, more Sm^{3+} ions could be reduced to be Sm^{2+} ions, resulting in stronger PL emission. Figure 2(b) revealed that the diameter of the storage unit could be effectively reduced by decreasing the single-pulse energy. When the pulse energy is decreased to 0.25 μJ, the induced structure cannot be distinguished under the optical microscope. However, its emission could still be detected with a diameter of about 800 nm. All the above information demonstrated that the writing speed of optical storage could be greatly improved through single-pulse processing. A low threshold of pulse energy for writing is favorable for huge capacity recording. By using the photoreduction of Sm^{3+} to Sm^{2+}, information not only can be recorded stably in the form of sub-micron size bits inside transparent glass in a three-dimensional manner, but also can be decoded easily by reading out the characteristic PL with a high signal-to-noise

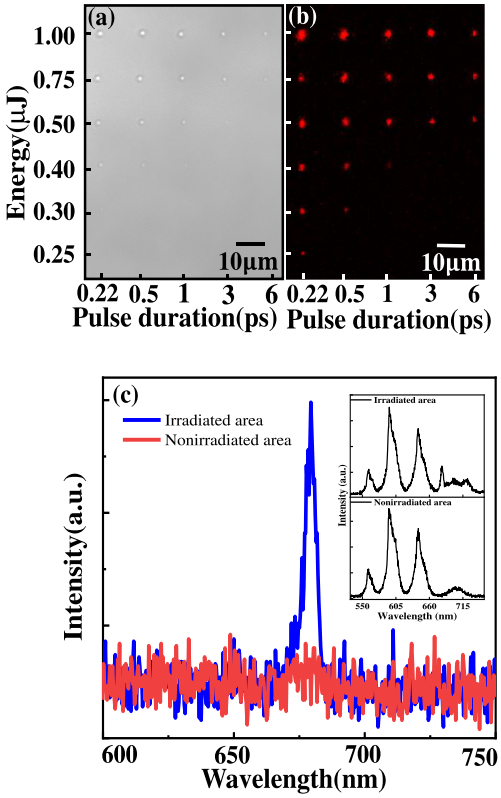

Fig. 1. (a) Optical image and (b) emission image of the dots written by a fs laser with a single pulse. (c) PL spectra before and after fs laser irradiation excited at 405 nm. Inset: PL spectra without a bandpass filter.

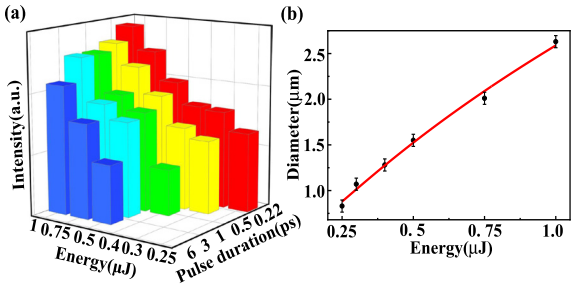

Fig. 2. (a) PL intensity and (b) diameter of emissive dots as a function of pulse duration and energy.

ratio. Furthermore, we suggest that the present technique would be general to induce reduction of Sm^{3+} efficiently in this model glass system with varied doping concentration, and tuning the concentration of Sm^{3+} in the initial glass may adjust the PL intensity and then improve the signal-to-noise ratio. Single-pulse-induced reduction of Sm^{3+} also may be available in the some other systems, such as BaFCl: Sm crystal [24,25]. In addition, we found that the written dots in the glass disappears after annealing the glass sample at about 400 °C for 2 h, and the modified regions finally transform to the initial glass state, which indicates that the written dots are still amorphous.

To reveal the advantage of single-pulse optical recording along with conforming optical properties, we also investigate the features of writing data by varying writing parameters. As illustrated in Fig. 3(a), groups of dots were directly written with diverse repetition rates and a number of pulses. The size

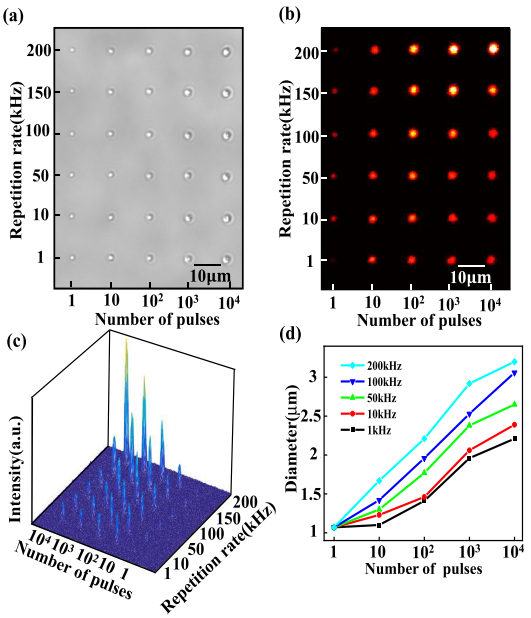

Fig. 3. (a) Optical image, (b) PL image, (c) PL intensity and diameter of the emissive dots written by a fs laser with a diverse number of pulses and various repetition rates. Average fs laser power: 0.5 mw.

of dots was reduced with the decrease of the number of pulses at the same repetition frequency. To read out the information, Fig. 3(b) shows the PL emission of the written dots at about 680 nm, confirming the presence of Sm^{2+} ions. The increment in the number of pulses leads to higher PL intensity [Fig. 3(c)], along with larger luminescent dots [Fig. 3(d)]. At higher repetition frequency, the diameter of the PL region increases in an approximately linear relationship with the exponential growth of the number of pulses. Furthermore, a laser with a higher repetition rate could induce larger microstructure while the number of pulses is the same, which is due to the stronger thermal accumulation effect at a higher repetition rate. An increase of PL intensity as a function of the pulse number or repetition rate originates from larger number of Sm^{2+} generated by photoreaction. It should be noted that although the PL intensity of the memory cell processed by multi pulses is higher, the diameter becomes larger, and the writing time increases at the same time, leading to a limitation in the capacity and writing speed of optical memory. Thus, single-shot photon recording is extremely critical for high-capacity three-dimensional memory storage while ensuring the signal-to-noise ratio.

Figure 4 has provided a proof-of-concept towards single-shot photon recording in three dimensions. Here three layers of bit arrays, consisting of the letter 'Z', 'J', and 'U' on top of each other, were written inside the sodium aluminoborate glass. Each dot was produced by one pulse. In the x or y direction, the distance between the two adjacent points in the same plane is 6 μm. The spacing between layers in the z direction is 8 μm. (z of the middle layer is 100 μm, where z refers to the depth from the upper surface.) From the fluorescent image, it can be found that there is no signal crosstalk between two adjoining layers processed by single-shot photon recording in this system, which is essential for optical memory in three dimensions. More layers of information can be written and stored inside various glasses using this method, and single-shot writing provides the possibility for multi-layer recording optical storage with super capacity.

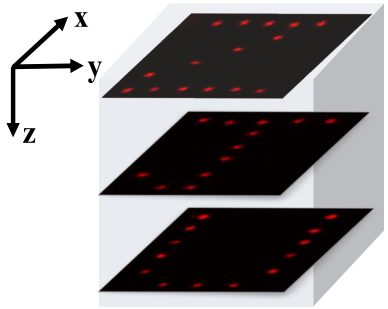

Fig. 4. Demonstration of three-dimensional optical memory recorded by a single pulse.

We report single-shot photon recording for three-dimensional optical memory. Single-pulse-induced photoreduction of Sm^{3+} ions to Sm^{2+} has been achieved, and the written dots exhibit an emissive diameter of 800 nm and distinct PL characteristic compared with the glass, which can be applied in optical storage with a high signal-to-noise ratio. We find that single-pulse processing not only can tremendously increase the writing rate of optical memory, but also can reduce the size of written dots, thus expanding storage capacity. Finally, multi-layer photon recording was demonstrated to illustrate the data-storage possibility in three dimensions. Successful implementation of writing and readout of information categorically reveals the viability of single-shot photon recording in glass as an ultra-fast writing speed, humongous capacity three-dimensional optical memory technique.

Funding. National Natural Science Foundation of China (61775192, 51902286, 61905215, 51772270); National Key Research and Development Program of China (2018YFB1107200); Open Fund of the Wuhan Optoelectronic National Research Center; Huazhong University of Science and Technology; State Key Laboratory of High Field Laser Physics; Shanghai Institute of Optics and Fine Mechanics, Chinese Academy of Sciences; Fundamental Research Funds for the Central Universities.

Disclosures. The authors declare no conflicts of interest.

REFERENCES

1. M. Hilbert and P. Lopez, Science **332**, 60 (2011).
2. E. N. Glezer, M. Milosavljevic, L. Huang, R. J. Finlay, T. H. Her, J. P. Callan, and E. Mazur, Opt. Lett. **21**, 2023 (1996).
3. D. Tan, X. Sun, Q. Wang, P. Zhou, Y. Liao, and J. Qiu, Opt. Lett. **45**, 3941 (2020).
4. J. R. Qiu, X. W. Jiang, C. S. Zhu, M. Shirai, J. Si, N. Jiang, and K. Hirao, Angew. Chem. (Int. Ed.) **43**, 2230 (2004).
5. X. Huan, Q. Guo, D. Yang, X. Xiao, X. Liu, Z. Xiao, F. Fan, J. Qiu, and G. Dong, Nat. Photonics **14**, 82 (2020).
6. J. Qiu, K. Miura, T. Suzuki, T. Mitsuyu, and K. Hirao, Appl. Phys. Lett. **74**, 10 (1999).
7. A. Royon, K. Bourhis, M. Bellec, G. Papon, B. Bousquet, Y. Deshayes, T. Cardinal, and L. Canioni, Adv. Mater. **22**, 5282 (2010).
8. J. Qiu, K. Miura, K. Nouchi, T. Suzuki, Y. Kondo, T. Mitsuyu, and K. Hirao, Solid State Commun. **113**, 341 (1999).
9. K. Miura, J. R. Qiu, S. Fujiwara, S. Sakaguchi, and K. Hirao, Appl. Phys. Lett. **80**, 2263 (2002).
10. H. Ditlbacher, J. R. Krenn, B. Lamprecht, A. Leitner, and F. R. Aussenegg, Opt. Lett. **25**, 563 (2000).
11. P. Zijlstra, J. W. M. Chon, and M. Gu, Nature **459**, 410 (2009).

12. J. Zhang, M. Gecevicius, M. Beresna, and P. G. Kazansky, Phys. Rev. Lett. **112**, 033901 (2014).
13. Y. Shimotsuma, M. Sakakura, P. G. Kazansky, M. Beresna, J. Qiu, K. Miura, and K. Hirao, Adv. Mater. **22**, 4039 (2010).
14. B. Zhang, D. Tan, X. Liu, L. Tong, P. G. Kazansky, and J. Qiu, Adv. Opt. Mater. **7**, 1900593 (2019).
15. Q. Zhang, Z. Xia, Y. B. Cheng, and M. Gu, Nat. Commun. **9**, 1183 (2018).
16. N. Riesen, X. Pan, K. Badek, Y. Ruan, T. M. Monro, J. Zhao, H. Ebendorff-Heidepriem, and H. Riesen, Opt. Express **26**, 12266 (2018).
17. C. Rios, M. Stegmaier, P. Hosseini, D. Wang, T. Scherer, C. D. Wright, H. Bhaskaran, and W. H. P. Pernice, Nat. Photonics **9**, 725 (2015).
18. X. Li, Y. Cao, N. Tian, L. Fu, and M. Gu, Optica **2**, 567 (2015).
19. M. Xian, Y. Xu, X. Ouyang, Y. Cao, S. Lan, and X. Li, "Segmented cylindrical vector beams for massively-encoded optical data storage," Sci. Bull. (to be published).
20. D. Tan, K. N. Sharafudeen, Y. Yue, and J. Qiu, Prog. Mater. Sci. **76**, 154 (2016).
21. R. W. Crane, Ł. Sójka, D. Furniss, J. Nunes, E. Barney, M. C. Farries, T. M. Benson, S. Sujecki, and A. B. Seddon, Opt. Express **28**, 12373 (2020).
22. F. Starecki, A. Braud, N. Abdellaoui, J.-L. Doualan, C. Boussard-Plédel, B. Bureau, P. Camy, and V. Nazabal, Opt. Express **26**, 26462 (2018).
23. P. Němec, J. Jedelský, and M. Frumar, J. Non-Cryst. Solids **326**, 325 (2003).
24. H. Riesen, K. Badek, T. M. Monro, and N. Riesen, Opt. Mater. Express **6**, 3097 (2016).
25. N. Riesen, A. François, K. Badek, T. M. Monro, and H. Riesen, J. Phys. Chem. A **119**, 6252 (2015).

Optics Letters

Long-term optical information storage in glass with ultraviolet-light-preprocessing-induced enhancement of the signal-to-noise ratio

Zhuo Wang,[1] Bo Zhang,[1] Dezhi Tan,[2,*] and Jianrong Qiu[1,3,4]

[1]State Key Laboratory of Modern Optical Instrumentation, College of Optical Science and Engineering, Zhejiang University, Hangzhou 310027, China
[2]Zhejiang Lab, Hangzhou 311100, China
[3]CAS Center for Excellence in Ultra-intense Laser Science, Chinese Academy of Sciences, Shanghai, 201800, China
[4]e-mail: qjr@zju.edu.cn
*Corresponding author: wctdz@zju.edu.cn

Received 8 June 2021; revised 14 July 2021; accepted 14 July 2021; posted 14 July 2021 (Doc. ID 433674); published 9 August 2021

This Letter describes the realization of long-term optical information storage in glass using an enhanced signal-to-noise ratio (SNR). We show that the photo-oxidation of Eu^{2+} ions in the glass matrix induced by ultraviolet light suppresses background signals, thereby enhancing by tenfold the SNR of Eu^{2+} ions photoluminescence (PL) of the dots written by a femtosecond (fs) laser. Thus, smaller dots exhibiting weak PL emission can be detected. In addition, the stored information shows excellent stability under the light irradiation with the power density up to 240 W/cm^2. Accelerated-aging experiments indicate that the stored data can retain stability for more than 115 years at room temperature. The optical storage capacity is approximately 270 Gbit cm^{-3}. This technique enables long-term, high-capacity data storage in glass media.

https://doi.org/10.1364/OL.433674

Over the past two decades, there has been an increasing demand for secure and stable storage of large amounts of information for a long period of time (typically longer than 100 years) [1–6]. Optical storage provides a fascinating alternative to conventional semiconductor- or magnetic-based storage owing to its advantages, including long lifetime [7,8], superb stability [2,9], high storage density [4,8,10], fast speed [11], and low cost [1]. For the traditional non-optical information storage techniques, the stability term is usually shorter than 50 years [12]. Recently, femtosecond (fs) laser-induced modifications in transparent solids, such as refractive index change [13,14], selective precipitation of nanocrystals [9,15–17], regulation of ion valence [18–20], and formation of nanogratings [7,21,22] have been proposed to be useful for three-dimensional or even five-dimensional optical storage with high performance. Generally, glass provides an ideal matrix to stabilize the embedded structural modifications, as well as the stored optical information. For example, the lifetime of nanogratings in silica glass spans seemingly over 3×10^{20} years [7]. However, the lifetime of other structural changes induced by fs laser in glass has not been determined, which is critical for realizing applications of fs laser writing in long-term optical storage.

Three-dimensional optical memory applications always require a high signal-to-noise ratio (SNR), referring to the ratio of photoluminescence (PL) intensity of the written dots to the noise intensity of the storage media (e.g., glass), to decrease the bit error rate (BER) when reading the stored data. In fact, a low SNR could be one of the main issues that limit the recording capacity, reading accuracy, and reading speed of optical memory. Typically, the SNR worsens after long-term storage. Furthermore, there may be a noise signal from the matrix, which would lead to a reduction in SNR and an increase in BER. For example, modifying the valence of active ions, such as the reduction of Eu^{3+} ions in glass by using fs laser irradiation is established as an effective strategy to record optical information [23,24]. However, partially active Eu^{3+} ions doped in glass could also be changed to Eu^{2+} ions during the high-temperature glass preparation process [25–28], which is detrimental to the SNR in ion valence modulation-mediated optical storage. As a result, reducing the noise signal from Eu^{2+} ions in the area without fs laser irradiation is of great importance, not only for improving the SNR and decreasing the BER, but also for reading smaller dots in high-capacity storage.

Here, we propose enhancing the SNR by tenfold in Eu^{3+}-doped sodium aluminoborate glass for long-term optical storage. Information can be written in the glass by a single fs laser pulse that induces the reduction of Eu^{3+} to Eu^{2+}, while ultraviolet (UV)-light pre-irradiation has been demonstrated to significantly suppress the background signal from Eu^{2+} around the written dots in the glass matrix. Furthermore, accelerated aging demonstrated that the stored data remain stable for more than 115 years at room temperature. The optical storage capacity is approximately 270 Gbit cm^{-3}. Thus, the combination of UV-light preprocessing and fs laser writting allows for long-term stable optical information storage with a high SNR.

The Eu^{3+}-doped sodium aluminoborate glass used in this study was fabricated with a stoichiometric composition (in mol %) of $85\,B_2O_3 - 5\,Al_2O_3 - 10\,Na_2O - 0.1\,Eu_2O_3$ via

a conventional melt-quenching route. Reagent grade powders were mixed and melted at 1250°C for 30 min in ambient atmosphere. The melted glass was then removed from the furnace, cast on a stainless steel plate, and formed into a block with a thickness of approximately 1 mm, thereby yielding colorless and transparent glass.

The preprocessing experiments were performed with a 375 nm CW laser, with the laser beam focused by a 1.3 NA oil objective lens. For data recording, a fs laser (PHAROS, Light Conversion Ltd.) with a wavelength of 1030 nm and pulse duration of 220 fs was used. The fs laser beam was focused by a 0.8 NA objective lens for writing data at a depth of 100 μm from the glass surface. The PL of Eu^{2+} ions is recorded using a homemade confocal fluorescence microscope system mainly composed of an excitation light source emitting at 375 nm, an XYZ nanopositioning stage (Physik Instrument), a 1.3 NA oil objective lens (Olympus), and an avalanche photodiode (Excelitas). The typical reading time was 80 ms. In fact, the detector still can collect enough signals for identifying the writing dots when the reading time is shortened to 50 ms, and the reading speed is mainly limited by the moving speed of the stage.

Photo-oxidation induced by a higher-power CW laser was explored for erasable optical recording in active ions-doped glass [29], which presents a facile technique to suppress noise from the glass. Based on this, UV-light irradiation with the power density of 600 W/cm^2 was adopted to induce oxidation of Eu^{2+} and weaken the noise signal from Eu^{2+} in the initial glass before recording data. Figure 1(a) shows the optical image of dots written by a single fs laser pulse of 600 nJ with a reduction of Eu^{3+} to Eu^{2+}. The UV-light preprocessing was only performed in area II. Comparing the two areas, no apparent changes were observed under an optical microscope. We mapped the PL images in both areas, as shown in Fig. 1(b). The characteristic PL of Eu^{2+} ions can be collected in the dots written by the fs laser. We can observe that the background noise signal in area I is much stronger than that in area II, which indicates that the background noise signal is suppressed in the UV-light irradiated area. PL spectra of the written dots and glass matrices are illustrated in Figs. 1(c) and 1(d), respectively. The broadband PL of Eu^{2+} ions, attributed to the 5d–4f transition, appears at around 435 nm, and several sharp peaks between 570 and 750 nm resulting from the $^5D_0 - ^7F_J$ ($J = 0, 1, 2, 3, 4$) transitions of Eu^{3+} ions emerge [Fig. 1(c)] [30]. It is worth noting that there was nearly no change in the PL intensity and peak position of the written dots in both areas. By contrast, Fig. 1(d) demonstrates that the PL peak at around 435 nm is significantly inhibited after the UV-light preprocessing, which is evident in the enlarged PL spectra. This indicates that the Eu^{2+} ions formed in the glass preparation process could be converted to Eu^{3+} ions with UV-light irradiation, in line with the PL mapping images. Consequently, a higher SNR is obtained, and the BER is decreased, both of which are important to read data in optical storage accurately.

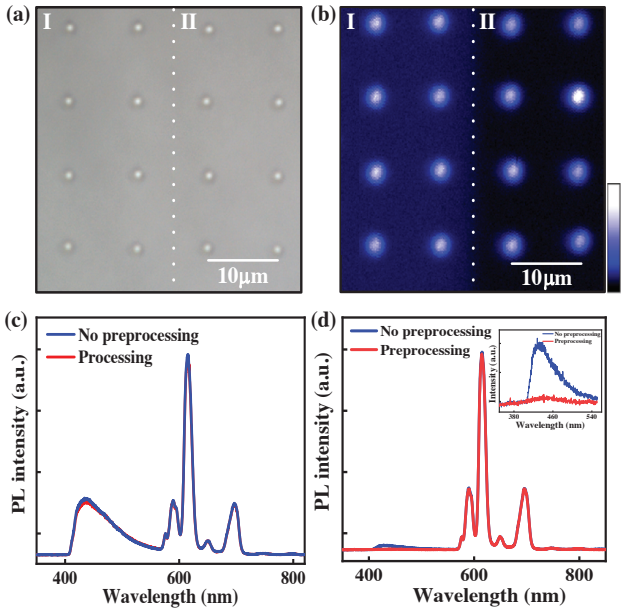

Fig. 1. Optical image (a) and PL mapping (b) of the areas with (area II) and without (area I) preprocessing before recording data. PL spectra of written dots (c) and glass (d) in areas I and II. The color bar shows the intensity of PL: the brighter color represents bigger photon counts and stronger PL intensity. The inset shows enlarged spectra in the range from 350 to 550 nm.

As revealed in Fig. 2(a), the average PL intensity of background noise is 10.97 and 1.07 counts without and with UV-light preprocessing, respectively. The SNR was determined to be 14 (higher than 140) for the case (without/with) UV-light preprocessing, indicating a tenfold enhancement in the SNR, which not only leads to a lower BER, but also implies the feasibility to read smaller dots. Figure 2(b) shows the SNR with different excitation powers in areas I and II, the PL intensities of signal and background noise are revealed in the inset of Fig. 2(b). For all excitation powers, the preprocessing can significantly decrease the background noise and achieve a tenfold enhancement of SNR compared with non-preprocessing.

Because photo-reduction dots are erased when the excitation power exceeds the threshold for Eu^{2+} photo-oxidation, it is of great importance to explore the stability of PL intensity of the written dots at various excitation powers, as shown in Fig. 3(a). The excitation light source was employed to irradiate dots for 10 min. Considering that in a real-world data-reading process these dots would not be constantly exposed to the excitation

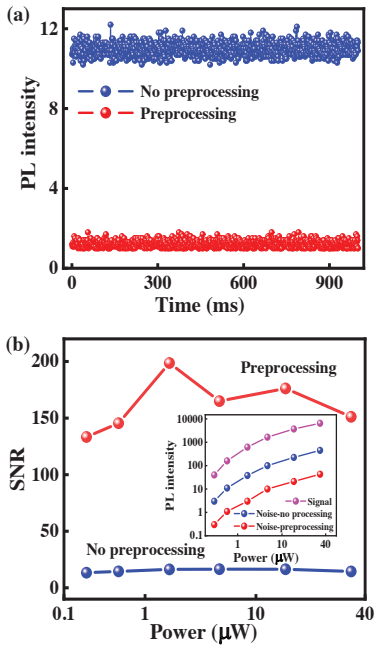

Fig. 2. (a) PL intensity of glass with and without UV-light preprocessing. (b) SNR in areas I and II under diverse excitation power. The inset shows the PL intensity of written dots and glass in areas I and II.

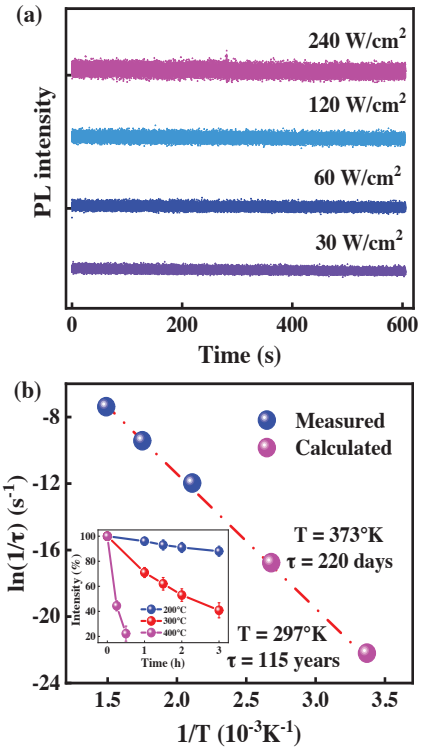

Fig. 3. (a) PL stability of written dots under various excitation power densities. (b) Arrhenius plot of the decay rate.

light, the PL intensity was measured just within 10 min to avoid strong thermal effects. There is no obvious PL change with an excitation power density <240 W/cm^2. It is worth noting that the PL can still be detected accurately with an excitation power as low as 20 nW (corresponding to a power density of 30 W/cm^2). In addition, the intensity of UV light under the indoor conditions and even the outdoor condition (up to $\sim 6.3 \times 10^{-3}$ W/cm^2) is much smaller than that in the current reading process. As a result, the written information is expected to exhibit excellent stability in the preservation environment.

The lifetime of stored data is a crucial factor in optical storage and needs to be further explored. The above discussions indicate that the recorded information remains stable during the normal reading process with the excitation power density below the threshold for UV-light-induced oxidation of Eu^{2+} ions. Here, accelerated aging measurements at different temperatures are adopted to calculate the lifetime through the decay time, which can be estimated by the Arrhenius law:

$$\frac{1}{\tau} = k = A \exp\left(-\frac{E_a}{k_B T}\right),$$

where τ is the lifetime, k is the decay rate, A is the frequency factor, E_a is the activation energy, k_B is the Boltzmann constant, and T is the temperature. This has been proved to be an effective method to predict the storage life [7]. The decay rate can be evaluated by detecting the decrease in PL intensity versus the annealing time at different annealing temperatures [inset of Fig. 3(b)]. As Fig. 3(b) revealed, the lifetime of stored information is determined to be approximately 115 years at room temperature, indicating sufficiently high stability of optical data storage. Even at 373°K, the information can be stored stably for more than 200 days. As a result, the optical information written by a single fs laser pulse in the glass was revealed to show superior stability over conventional semiconductor- or magnetic-based storage. Furthermore, as the recorded information was embedded in the glass matrix, strong protection against the influence of environment such as humidity could be expected, and no obvious change is observed after storing for more than 5 months under room conditions. Data can be steadily stored under room conditions without packing. However, packing is necessary for the protection in the traditional information storage. In addition, it will be interesting to evaluate whether the optical storage system developed here can resist the influence of other harsh environments such as X- and γ-ray radiation [31,32].

To further verify that the preprocessing only inhibits the background noise without changing the glass structure, we measured the Raman spectra of the glass, as shown in Fig. 4(a). No significant changes are observed in the Raman peaks at 770 and 806 cm^{-1}, which are attributed to the BO_4 units and boroxol ring, respectively [26,33]. This confirms that the preprocessing does not destroy the glass structures. The results are also consistent with X-ray photoelectron spectroscopy. Transmittance spectra of glasses before and after writing data by fs laser are depicted in Fig. 4(b). A characteristic absorption band of Eu^{3+} ions is observed at 393 nm assigned to the transition from the ground state $^7F_0$ to excited state $^5L_6$, and it becomes weaker after writing data in the glass, which confirms the reduction of Eu^{3+} ions to Eu^{2+} ions [inset of Fig. 4(b)].

As a further proof-of-concept experiment, a stack of layers with letters were encoded inside the glass. Figure 5 shows how three letters, "Z," "J," and "U," are written in three layers stacked along the z-axis with a 10 μm layer spacing. The distance between adjacent points in the x and y directions is 8 μm. A single 120 nJ fs laser pulse is chosen for data recording, with dot size of 650 nm. The maximum storage capacity is approximately 270 Gbit cm^{-3}, which could be increased by using a

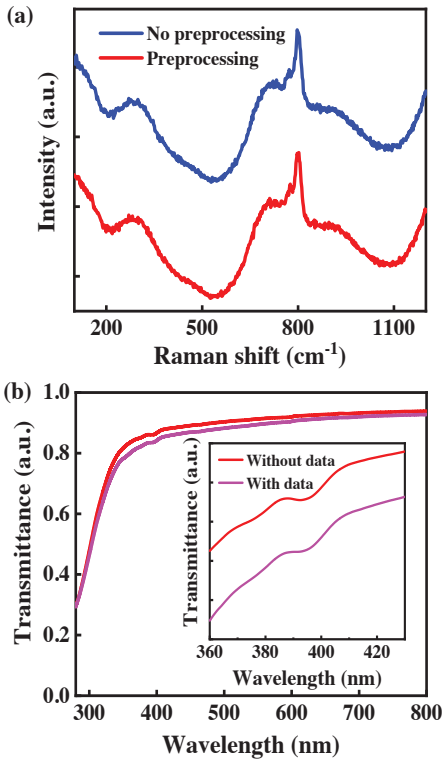

Fig. 4. (a) Raman spectra of the area with and without UV-light preprocessing before writing data. (b) Transmittance spectra of glasses before and after writing data.

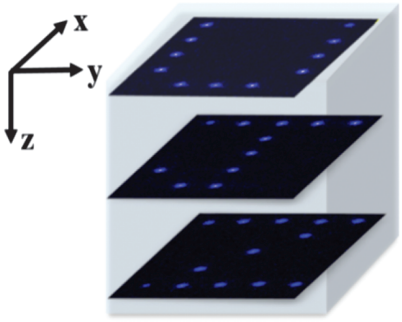

Fig. 5. Demonstration of recorded three-dimensional optical memory.

shaped beam for writing a smaller dot. Furthermore, as all the dots can be written by one fs laser pulse, the writing speed or information storage efficiency can be extremely high, and this is basically determined by the laser repetition rate and scanning speed of the stage. For example, writing 1 million dots in 1 s is achievable for the 1 MHz fs laser if the stage moves fast enough. Considering the low threshold pulse energy (<60 nJ) for writing, it is also possible to write multiple dots with one pulse with the assistance of a spatial light modulator. Furthermore, we have proved that one pulse with the pulse duration in a wide range (e.g., from 220 fs to 6 ps) can write a dot [34]. Consequently, even a low-power fs fiber laser will be enough for optical storage, and a commercial available expensive fs laser system is not necessary. Similar to the glass case, we can also expect to induce valance modification in the crystals using one fs laser pulse [20]. Furthermore, we have confirmed the Sm^{3+} is much more stable than Eu^{2+} in the current glass system, and there is nearly no reduction of Sm^{3+} to Sm^{2+} during the glass preparation process. Consequently, the UV-light preprocessing does not enhance the SNR significantly. However, as the stability of valence state of the rare earth strongly depends on the matrix, it will be meaningful to investigate the effect of matrix on the UV-light preprocessing, such as by adjusting the glass and transparent crystal systems [35]. In addition, super-resolution microscopy is useful for reading smaller dots, and more work is required to improve the reading process.

In conclusion, we propose a novel technique that can significantly improve the SNR and decrease the BER in optical data storage system using glass. To this end, UV-light preprocessing is adopted to induce photo-oxidation of the extraneous Eu^{2+} ions in the glass and subsequently decrease the corresponding emission of Eu^{2+} ions. Thus, the SNR of the PL intensity from the written dots with desirable Eu^{2+} ions generated by a single fs laser pulse can be improved 10 times. To further evaluate the performance of optical storage, the lifetime of the stored information is calculated to be longer than 115 years at room temperature, and the capacity of optical storage is approximately 270 Gbit cm^{-3}. Successful implementation of writing and reading of information categorically reveals the viability of UV light-induced enhancement of SNR for long-term and stable optical information storage.

Funding. National Natural Science Foundation of China (U20A20211, 51902286, 61775192, 61905215, 51772270); State Key Laboratory of High Field Laser Physics; Shanghai Institute of Optics and Fine Mechanics, Chinese Academy of Sciences; Fundamental Research Funds for the Central Universities.

Disclosures. The authors declare no conflicts of interest.

Data Availability. Data underlying the results presented in this paper are not publicly available at this time but may be obtained from the authors upon reasonable request.

REFERENCES

1. M. Gu, X. Li, and Y. Cao, Light Sci. Appl. **3**, e177 (2014).
2. S. Lin, H. Lin, C. Ma, Y. Cheng, and Y. Wang, Light Sci. Appl. **9**, 22 (2020).
3. J. Yu, M. Luo, Z. Lv, S. Huang, H. Hsu, C. Kuo, S. Han, and Y. Zhou, Nanoscale **12**, 23391 (2020).
4. M. Xian, Y. Xu, X. Ouyang, Y. Cao, S. Cao, and X. Li, Sci. Bull. **65**(24), 2072 (2020).
5. N. Riesen, X. Pan, K. Badek, Y. Ruan, T. Monro, J. Zhao, H. Ebendorff-Heidepriem, and H. Riesen, Opt. Express **26**, 12266 (2018).
6. C. Rios, M. Stegmaier, P. Hosseini, D. Wang, T. Scherer, C. D. Wright, H. Bhaskaran, and W. Pernice, Nat. Photonics **9**, 725 (2015).
7. J. Zhang, M. Gecevicius, M. Beresna, and P. G. Kazansky, Phys. Rev. Lett. **112**, 033901 (2014).
8. Q. Zhang, Z. Xia, Y. B. Cheng, and M. Gu, Nat. Commun. **9**, 1183 (2018).
9. T. Nikitin, L. Khriachtchev, M. Raesaenen, and S. Novikov, Appl. Phys. Lett. **94**, 173116 (2009).
10. P. Zijlstra, J. W. M. Chon, and M. Gu, Nature **459**, 410 (2009).
11. X. Li, Y. Cao, N. Tian, L. Fu, and M. Gu, Optica **2**, 567 (2015).
12. M. Gu, Q. Zhang, and S. Lamon, Nat. Rev. Mater. **1**, 16070 (2016).
13. D. Tan, X. Sun, Q. Wang, P. Zhou, Y. Liao, and J. Qiu, Opt. Lett. **45**, 3941 (2020).
14. J. Lapointe, J.-P. Bérubé, and Y. Ledemi, Light Sci. Appl. **9**, 64 (2020).
15. Y. Hu, W. Zhang, Y. Ye, Z. Y. Zhao, and C. Liu, ACS Appl. Nano Mater. **3**, 850 (2019).
16. D. Tan, B. Zhang, and J. Qiu, Laser Photon. Rev. **15**, 202000455 (2021).
17. A. Royon, K. Bourhis, M. Bellec, G. Papon, B. Bousquet, Y. Deshayes, T. Cardinal, and L. Canioni, Adv. Mater. **22**, 5282 (2010).
18. Y. Zheng, Y. Yao, L. Deng, W. Cheng, J. Li, and T. Jia, Photon. Res. **6**, 144 (2018).
19. D. Tan, Z. Wang, B. Xu, and J. Qiu, Adv. Photon. **3**, 024002 (2021).
20. H. Riesen, K. Badek, T. M. Monro, and N. Riesen, Opt. Mater. Express **6**, 3097 (2016).
21. C. Hnatovsky, V. Shvedov, W. Krolikowski, and R. Andrei, Phys. Rev. Lett. **106**, 123901 (2011).
22. B. Zhang, D. Tan, Z. Wang, X. Liu, B. Xu, M. Gu, L. Tong, and J. Qiu, Light Sci. Appl. **10**, 1 (2021).
23. E. Z. Cruzeiro, J. Etesse, A. Tiranov, P. Bourdel, H. Fröwis, P. Goldner, N. Gisin, and M. Afzelius, Phys. Rev. B **97**, 094416 (2018).
24. Z. Zhou, C. Wang, M. Deng, X. Xu, and Q. Liu, Opt. Mater. **111**, 110617 (2021).
25. Q. Zhang, X. Liu, Y. Qiao, B. Qian, G. Dong, J. Ruan, Q. Zhou, J. Qiu, and D. Chen, Opt. Mater. **32**, 427 (2010).
26. Q. Jiao, X. Yu, X. Xu, and D. Zhou, J. Solid State Chem. **202**, 65 (2013).
27. C. Zhu, Y. Yang, X. Liang, S. Yuan, and G. Chen, J. Am. Ceram. Soc. **90**, 2984 (2010).
28. M. Peng, Z. Pei, G. Hong, and Q. Su, Chem. Phys. Lett. **371**, 1 (2003).
29. K. Miura, J. Qiu, S. Fujiwara, S. Sakaguchi, and K. Hirao, Appl. Phys. Lett. **80**, 2263 (2002).
30. C. Wang, M. Peng, N. Jiang, X. Jiang, C. Zhao, and J. Qiu, Mater. Lett. **61**, 3608 (2007).
31. S. Liu, S. Fu, X. Zhang, X. Wang, L. Kang, X. Han, X. Chen, J. Wu, and Y. Liu, Opt. Mater. Express **8**, 1143 (2018).
32. X. Wang, S. Fu, X. Zhang, X. Li, L. Kang, J. Wu, and Y. Liu, Opt. Express **27**, 11991 (2019).
33. B. P. Dwivedi, M. H. Rahman, Y. Kumar, and B. N. Khanna, J. Phys. Chem. Solids **54**, 621 (1993).
34. Z. Wang, D. Tan, and J. Qiu, Opt. Lett. **45**, 6274 (2020).
35. N. Riesen, A. François, K. Badek, T. M. Monro, and H. Riesen, J. Phys. Chem. A **119**, 6252 (2015).

Focal volume optics for composite structuring in transparent solids

OPEN ACCESS
IOP Publishing | IMMT
International Journal of Extreme Manufacturing
Int. J. Extrem. Manuf. 7 (2025) 015002 (10pp)
https://doi.org/10.1088/2631-7990/ad8712

Focal volume optics for composite structuring in transparent solids

Bo Zhang[1,7], Zhuo Wang[1,7], Dezhi Tan[2,3,*], Min Gu[4,5], Yuanzheng Yue[6] and Jianrong Qiu[1,*]

[1] State Key Laboratory of Modern Optical Instrumentation, College of Optical Science and Engineering, Zhejiang University, Hangzhou 310027, People's Republic of China
[2] Zhejiang Lab, Hangzhou 311100, People's Republic of China
[3] School of Materials Science and Engineering, Zhejiang University, Hangzhou 310027, People's Republic of China
[4] Institute of Photonic Chips, University of Shanghai for Science and Technology, Shanghai, People's Republic of China
[5] Centre for Artificial-Intelligence Nanophotonics, School of Optical-Electrical and Computer Engineering, University of Shanghai for Science and Technology, Shanghai, People's Republic of China
[6] Department of Chemistry and Bioscience, Aalborg University, 9220 Aalborg, Denmark

E-mail: wctdz@zju.edu.cn and qjr@zju.edu.cn

Received 12 March 2024, revised 17 June 2024
Accepted for publication 15 October 2024
Published 5 November 2024

Abstract

Achieving high-level integration of composite micro-nano structures with different structural characteristics through a minimalist and universal process has long been the goal pursued by advanced manufacturing research but is rarely explored due to the absence of instructive mechanisms. Here, we revealed a controllable ultrafast laser-induced focal volume light field and experimentally succeeded in highly efficient one-step composite structuring in multiple transparent solids. A pair of spatially coupled twin periodic structures reflecting light distribution in the focal volume are simultaneously created and independently tuned by engineering ultrafast laser-matter interaction. We demonstrated that the generated composite micro-nano structures are applicable to multi-dimensional information integration, nonlinear diffractive elements, and multi-functional optical modulation. This work presents the experimental verification of highly universal all-optical fabrication of composite micro-nano structures with independent controllability in multiple degrees of freedom, expands the current cognition of ultrafast laser-based material modification in transparent solids, and establishes a new scientific aspect of strong-field optics, namely, focal volume optics for composite structuring transparent solids.

Supplementary material for this article is available online

Keywords: ultrafast laser, focal volume light field, composite structuring, transparent solids, advanced manufacturing

[7] These authors contributed equally to this work.
[*] Authors to whom any correspondence should be addressed.

2631-7990/25/015002+10$33.00

1. Introduction

Micro-nano structures lay at the heart of optical components for light manipulation in different dimensions [1–6]. In particular, composite micro-nano structures constructed in 3D have been revealed to enable novel photonic devices with unprecedented control degrees of freedom over the state of electromagnetic waves and have emerged as a new research frontier in nanophotonic science and engineering [7–10]. For example, multi-layer composite micro-nano structures allow for modulating light waves that have wave vectors in 3D space, enabling innovation in stereoscopic display, light manipulation, and data storage [11–15]. Currently, the generation of composite micro-nano structures largely relies on complicated multi-step micro-nano machining processes where the integration of different structural characteristics remains limited. Fast construction of composite micro-nano structures with a higher level of integration in 3D space has long been a bottleneck due to the lack of effective fabrication approaches.

Ultrafast laser-matter interaction has become an excellent platform for preparing functional elements in transparent media [16–22]. For example, ultrafast laser-induced embedded micro-nano structures have been widely studied and utilized in the welding of all-inorganic hard and brittle transparent materials [23, 24]. In particular, 3D material modification capability has become one of the most important attributes inherent in ultrafast laser direct writing (ULDW) technology [25–29]. However, creating different types of micro-nano structures in one step with a single-beam ultrafast laser is traditionally very difficult and even generally not within the scope of ULDW, which is essentially restricted by assuming the typical light distribution as the Gaussian type in the focal volume. Generally, achieving composite structuring with multiple degrees of freedom requires a higher-level manipulation of micro-scale spatial light fields. Up to now, it remains a great challenge to determine and control the microscopic optical behaviors of highly intense light-matter interaction in the focal volume at the micro-nano scale, owing to the multiple complex optical responses and fast ionization process [30–33].

Here, we realize the generation, visualization, and manipulation of the focal volume light fields induced during the ultrafast laser-matter interaction. Combined with ULDW, we proposed that such light fields can be applied for highly integrated and controllable single-step composite structuring within the focus of a single-beam ultrafast laser. Our principles are confirmed to be highly universal and widely applicable in different types of transparent dielectrics. Finally, multiple applications are demonstrated using the fabricated composite structures.

2. Results and discussion

2.1. Working principle of composite structuring

In ultrafast laser-matter interaction, a tightly focused ultrafast laser can induce multi-photon ionization in various transparent dielectrics. This process is highly dependent on the intensity of the laser beam and thus occurs exclusively within the focal volume [34, 35]. During multi-photon ionization, a significant number of free electrons can be quickly excited (figure S2 in the supplementary material), causing the ionized material within the focal volume to exhibit a quasi-metallic state with metal-like optoelectronic properties [36, 37]. Such an ionized zone will disturb the subsequent incident light wave. Here, we proposed that the ionized zone can serve as a tunable scatterer to the incident light and lead to the generation of a tunable scattering light field in the focal volume (figure 1(a)). Generally, a smaller and rounder scatterer leads to an intense forward light field, while a larger and longer scatter leads to a sideward light field in the focal volume (figures S3 and S4 in the supplementary material). The interference between the incident light and the scattered light occurs in the focal volume, resulting in an intense 3D volumetric light field (figures 1(b)–(i)). Both the well-defined intensity distribution and the extremely confined interaction scope make this volumetric light field an ideal secondary driving source to trigger structured spatial nonlinear absorption and selectively modify local material, thereby producing wavelength-scaled periodic interference patterns (PIPs) with a period of $\sim$1 μm (figure 1(b)–(ii)). During the generation process of PIPs, nano-plasmas could be simultaneously excited by ultrafast laser irradiation and their anisotropic growth induced by local field enhancement leads to nano-scale periodic material modification within the volumetric light field-irradiated area, whose orientation depends on the light polarization [38–40]. Therefore, this well-structured volumetric light field can be adopted to further induce subwavelength-scaled nano-gratings (NGs) with a period of $\sim$200 nm, which are embedded inside the PIPs (figure 1(b)–(iii)). This process allows for two parallel material modifications within the extremely compact space of a laser focus and constructing two different yet coupled periodic structures at the same 3D spatial location, namely, single-step composite structuring (figure 1(b)). As a result, we established a fundamentally new principle to achieve highly integrated composite structures relying on the intrinsic light field distribution in the focal volume based on the ultrafast laser-matter interaction.

2.2. Manipulation of composite structuring

Although the PIPs and NGs are spatially coupled together, forming composite structures, they can be manipulated continually and independently (figures 2(a) and (d)), as the orientation of PIPs and NGs depends on the laser scanning direction and polarization, respectively, which is due to the different physical origins (figure S5 and equations (S2)–(S6) in the supplementary material). We identified the formation and orientation of NGs by birefringence intensity mapping (figures 2(b) and (e)) and slow-axis azimuth imaging of the birefringence area (figures 2(c) and (f)), which confirms the optical phase-modulation ability and structural variation of NGs. In addition, we demonstrated that the PIPs and the NGs can be synergistically tuned by simultaneously adjusting the

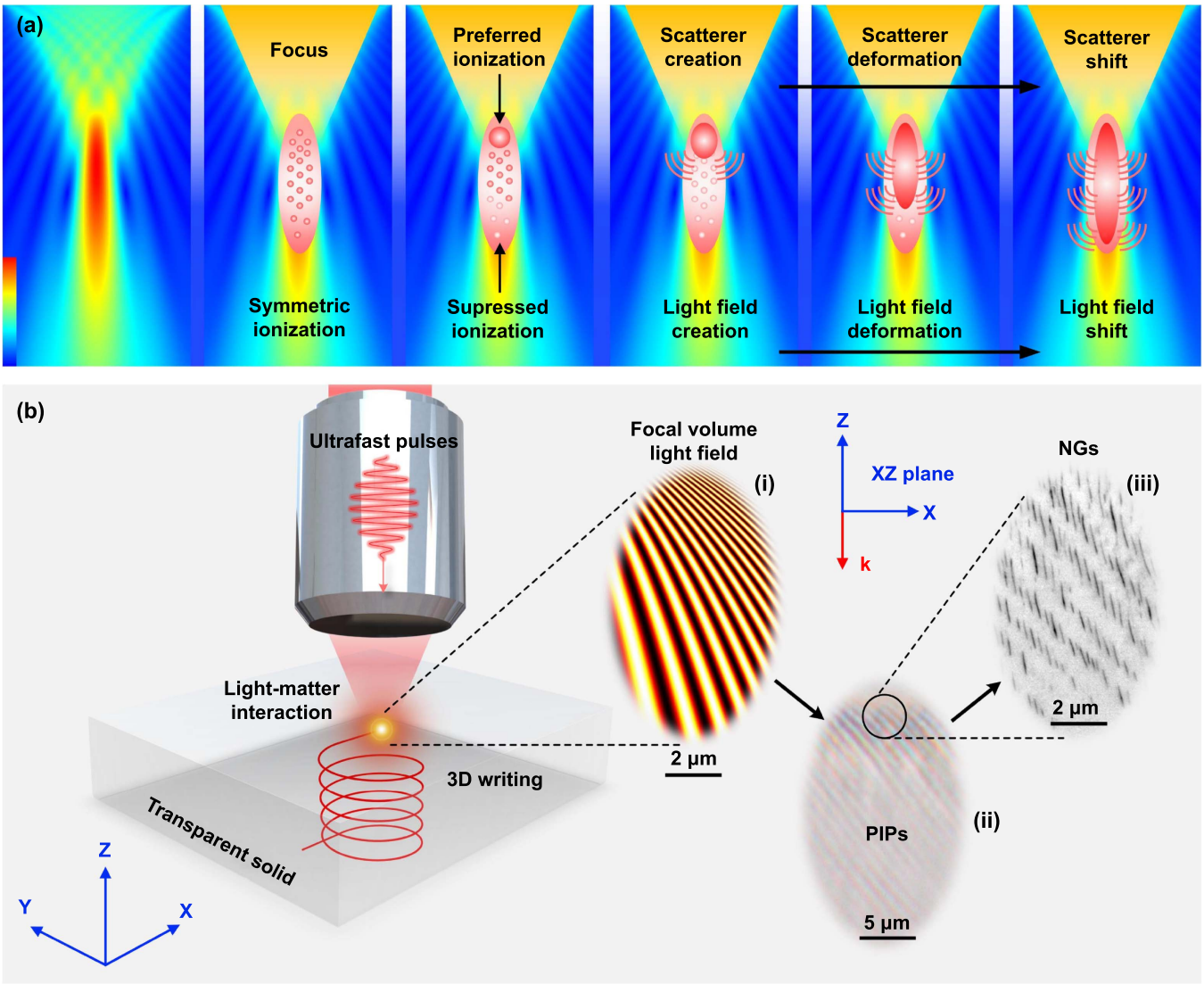

Figure 1. Conceptual model for the principle of composite structuring. (a) Schematic of the light field creation and evolution in the focal volume of a gaussian ultrafast laser beam irradiating in transparent dielectrics. Radiating symbols indicate light scattering. (b) Composite structuring with focal volume light field. Insets: theoretical volume light field in the *XZ* plane (i), experimentally observed periodic interference patterns (PIPs) in the *XZ* plane (ii), and experimentally observed nano-gratings (NGs) inscribed inside the PIPs. (iii) k indicates the laser propagation direction.

scanning direction and laser polarization (figures 2(g) and (i)). Notably, the existence and variation of PIPs do not disturb the birefringence-related optical signals created by NGs, which indicates that both the manipulation and identification of these two structures are completely decoupled. These findings indicate that focal volume light fields enable composite structuring (3D writing, PIPs creation, and NGs creation) with independent controllability in multiple degrees of freedom (3D spatial coordinates, scanning direction, and polarization direction). In contrast to conventional micro-nano machining principles that rely on special materials and multi-step processes to realize the fabrication of different types of micro-nano structures, the composite structuring capacity proposed here is inherent to ultrafast laser processing.

According to our interference model (equations (S2)–(S5)), the spatial distribution of the constructive interference field in the focal volume is theoretically a series of hyperboloids, each of which corresponds to the interference field under a specific interference order. As the focal volume light field is essentially the 3D constructive interference established at the focus, the created PIPs inherit the structural characteristics of the volume light field, which can be verified by their intersecting patterns in the *XZ, YZ*, and *XY* planes (figures S6(a)–(c) in the supplementary material). Based on this, the experimentally observed PIPs can be quantitatively described by the projection of these hyperboloids in observation planes, denoted as constructive interference stripes (CISs). For instance, the CISs in the *XY* plane are a series of circular arcs and the CISs in the *YZ* plane

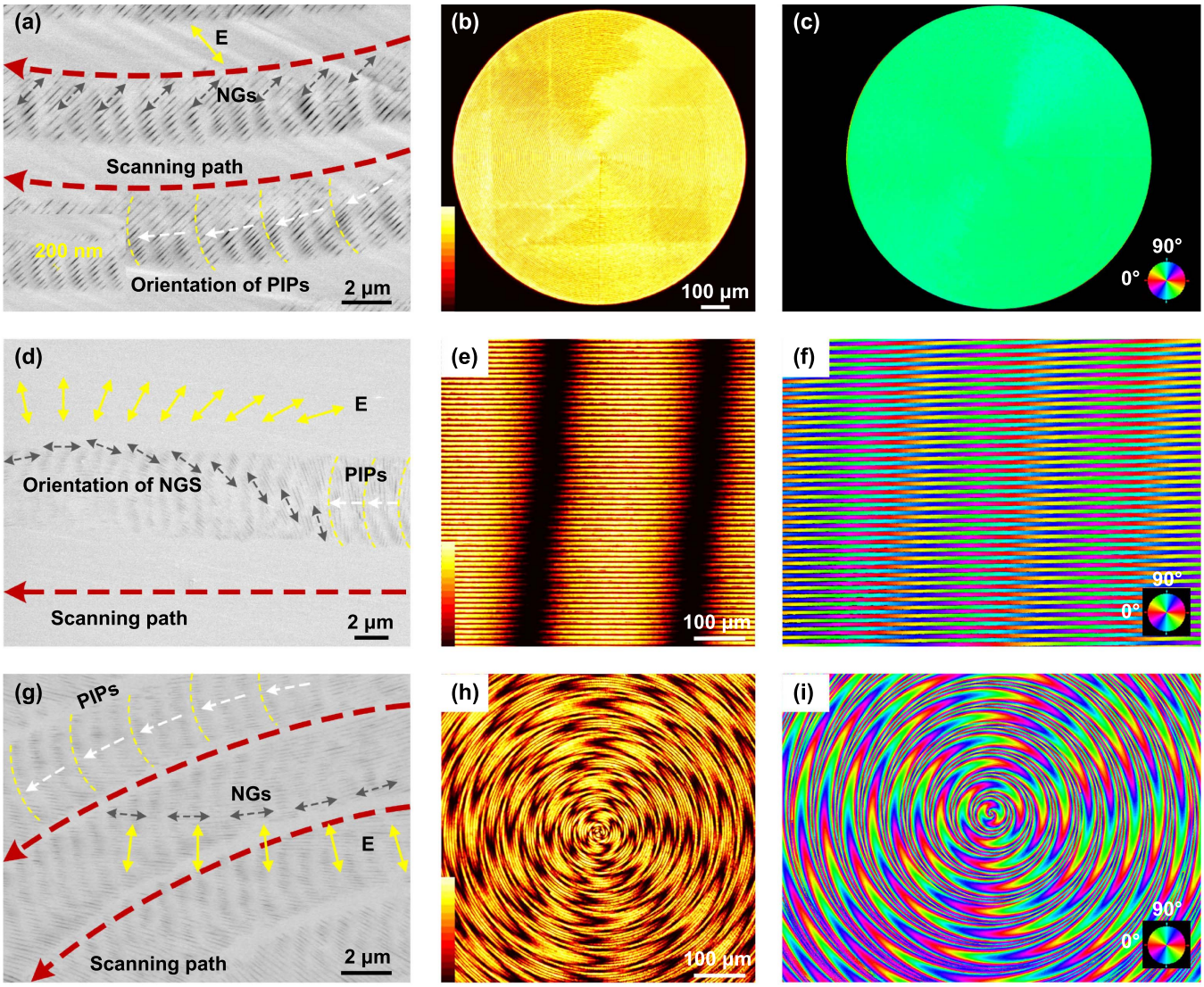

Figure 2. Composite structuring control and corresponding optical characterization in the *XY* plane. (a), (d), and (g) scanning electron microscopy (SEM) images of the composite structures in fused silica. Inset: partially enlarged image. Red dotted arrows indicate the scanning path. White dotted arrows indicate the orientation of the PIPs. Gray dotted arrows indicate the orientation of the NGs. Yellow dotted curves help to visualize the PIPs. E indicates laser polarization. (b), (e), and (h) birefringence imaging, and (c), (f), and (i) imaged azimuth angles of the slow axis of the birefringence area. Color bars illustrate the birefringence intensity. Pseudocolor indicates the orientation of the slow axis. (a), (b), and (c) the scanning direction is continuously changed and the laser polarization is fixed. (d), (e), and (f) the laser polarization is continuously changed and the scanning direction is fixed. (g), (h), and (i) both the laser polarization and the scanning direction are continuously changed.

are a series of symmetrical hyperbolic curves. Notably, the existence of the inclination factor θ (caused by the convergence angle of laser focusing) breaks the symmetry of the CISs in the *XZ* plane (equation (s6)), dividing the CISs into three main categories, namely, positive, negative, and zero-order CISs (figures S6(d)–(f) in the supplementary material). Under the restriction of interference orders, the creation of PIPs must follow specific patterns, which lays the foundation for achieving more complex manipulation of composite structuring.

Here, we propose that this structural manipulation essentially manifests as the shift of CISs that work in composite structuring, which can be demonstrated by examining the PIPs formed in different media. Theoretically, owing to the difference in nonlinear optical response properties between different media, the creation of PIPs should be induced by different types of CISs. Here, we present three representative experimental results of PIPs induced in different media, including positive CISs-induced PIPs in La_2O_3–Nb_2O_5 glass that tilt in the direction opposite to the scanning direction (figure 3(a), left), negative CISs-induced PIPs in La_2O_3–Al_2O_3 glass that tilt along the scanning direction (figure 3(b), left), and zero-order CISs-induced PIPs in fused silica (figure 3(c), left). These experimentally induced PIPs are in good agreement with the simulated CISs in the red-marked regions (figures 3(a)–(c), right).

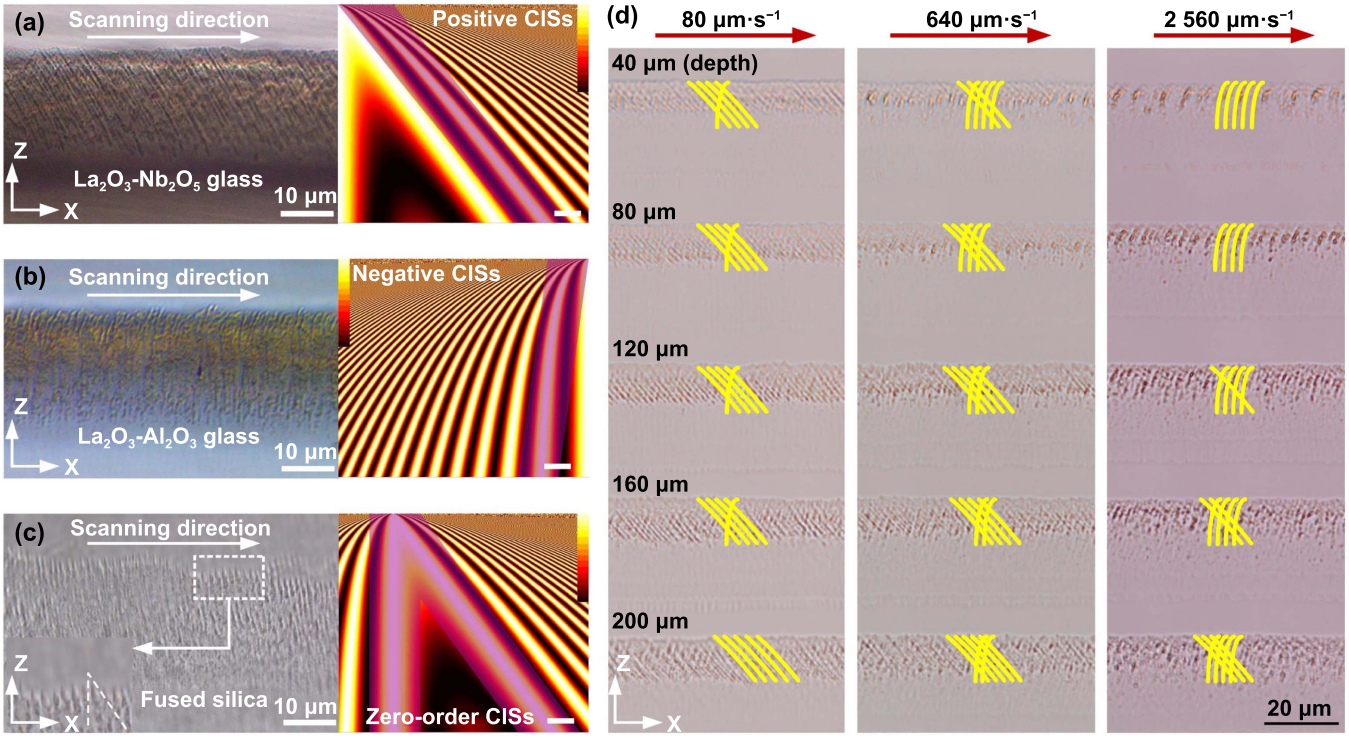

Figure 3. Interference-based composite structuring manipulation. (a) PIPs created in the La_2O_3–Nb_2O_5 glass (left) and simulated positive CISs (right). (b) PIPs created in the La_2O_3–Al_2O_3 glass (left) and simulated negative CISs (right). (c) PIPs created in the fused silica (left) and simulated zero-order constructive interference field (right). The regions marked in red indicate effective CISs that dominate the PIPs formation. Color bars: light intensity. Scale bars in simulation: 1 μm. (d) Parameter-driven structural manipulation of PIPs in fused silica realized by varying laser scanning speed and writing depth. Red arrows: laser scanning direction. Yellow curves help visualize the gradual transition from positive CISs (bottom left) to negative CISs (top right).

Even in the same medium, the CISs that work in the composite structuring can also be effectively controlled by tuning the processing parameters. These parameters generally enable the scatterer deformation by controlling the incident pulse number per unit length or inducing a self-focusing effect, leading to the shift of CISs. From this, more diverse and fine-grained structural manipulation of the composite structures can be realized. For example, by tuning the scanning speed (pulse density), writing depth, and laser power, the inclination direction of PIPs in fused silica can be gradually shifted from opposite to along the laser scanning direction (figures 3(d) and S7 in the supplementary material), indicating the transition from positive CISs to negative CISs. The PIPs can also be manipulated by adjusting the laser polarization state and the numeric aperture of the objective lens (figure S8 in the supplementary material), implying the highly flexible processing capability of composite structuring.

Generally, the processing parameters (high irradiance, large writing depth, pulse number/density, and focal depth) that contribute to the elongation of the focus tend to activate positive CISs-dominated structuring, while the processing parameters (low irradiance, small writing depth, pulse number/density, and focal depth) that restrain the distortion of the focus tend to activate negative CISs-dominated structuring, which agrees with the model we established (section S2) in the supplementary material.

2.3. Universality of composite structuring

We confirmed that composite structuring can serve as a highly universal composite structuring method that enables the creation of composite structures in multiple transparent dielectrics, including but not limited to sapphire, quartz, lithium niobate, lithium tantalite, and silicon carbide (figure S9 in the supplementary material). Notably, the composite structures exhibit designated structural features by utilizing the phase transition properties of target media, resulting in various advanced functional heterostructures that are not achievable with traditional techniques. Generally, the created composite structures can be categorized into four types by characterizing the inner structures and interfaces (figure 4). The first type of PIPs is characterized by alternately arranged glass arrays with and without defects (type I, figures 4(a) and (e)). The type I PIPs are mainly formed in the media that have low crystallization tendency, such as fused silica. An increase in the crystallization tendency of the media leads to the selective crystallization of the original amorphous matrix, thereby producing periodically arranged crystalline structures. The crystallites can be dispersed (type II, figure 4(b)), for example in La_2O_3–ZrO_2–Nb_2O_5 glass, or fully connected (type III, figures 4(c) and (f)), for example in La_2O_3–Ta_2O_5–Nb_2O_5 glass, depending on the crystallization tendency of different glass matrices. Furthermore, similar phase separations can also be induced

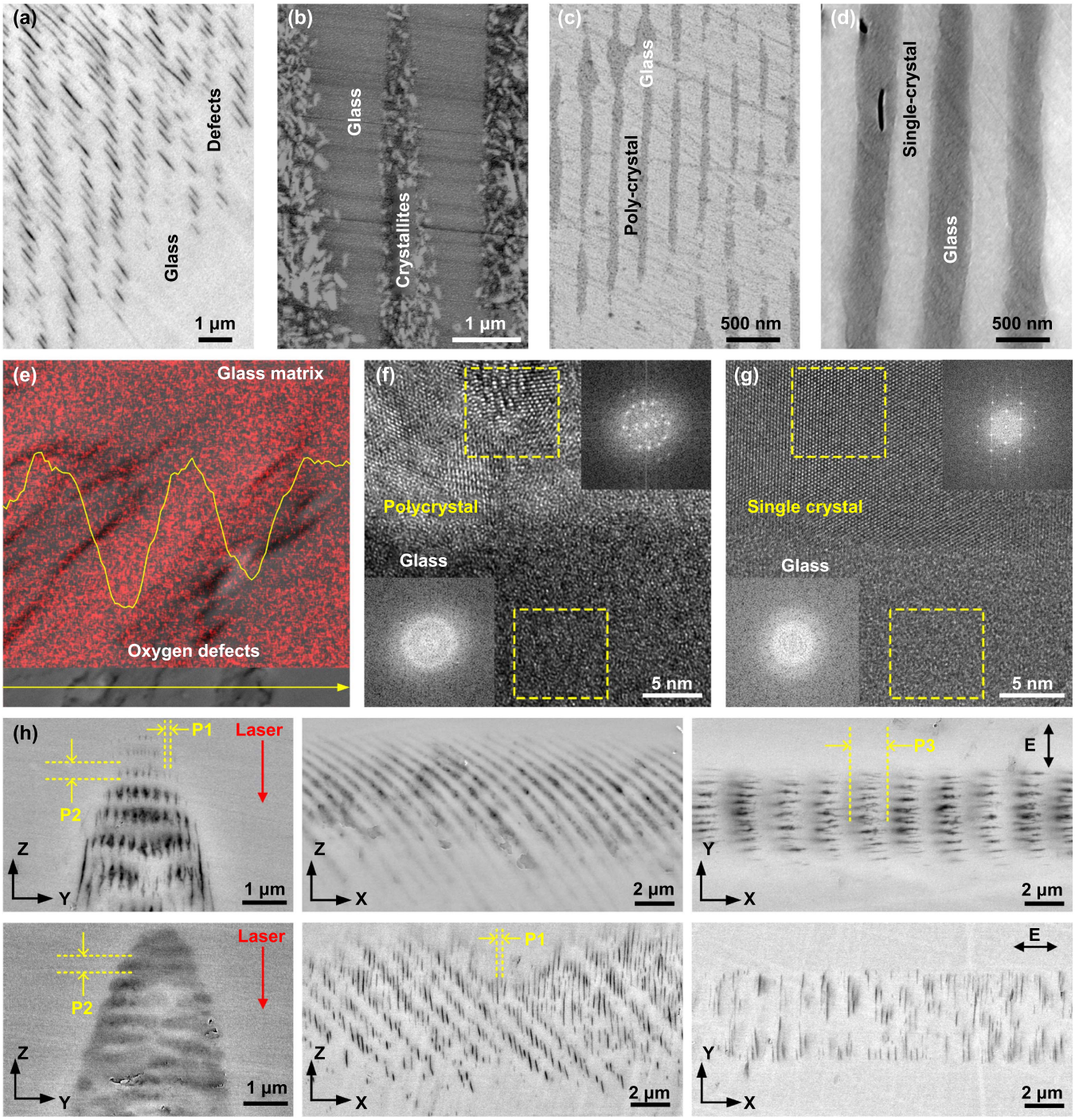

Figure 4. The universality of composite structuring. (a)–(d) SEM images showing the PIPs made of glass-defects (a), glass-crystallites (b), glass-polycrystal (c), and glass-single crystal (d). (e) Mapping of the distribution of O element in the PIPs. The inserted curve indicates O content along the yellow arrow determined by energy dispersive spectroscopy (EDS). (f) High-resolution transmission electron microscopy (HRTEM) image of the heterointerface between glass matrix and polycrystal. (g) HRTEM image of the heterointerface between glass matrix and single crystal. Insets represent the fast Fourier transform (FFT) images of the dotted areas. (h) Cross-section view (right), side view (middle), and top view (left) of the composite structures written with different polarizations. P1, P2, and P3 indicate the periods of PIPs and NGs in different views. E indicates laser polarization direction.

in single crystals (such as quartz and lithium niobate) to produce single crystal-glass PIPs (type IV, figures 4(d) and (g)). Importantly, the structural coupling of PIPs and NGs is also verified to be widely valid in multiple transparent dielectrics, ranging from important glasses to crystals (figure S10 in the supplementary material), and makes the composite structure exhibit multiple periods in 3D space (figure 4(h)), which not only substantiates the universal effectiveness of our principle but also provides a unified mechanism for a series of obscure multi-periodicity phenomena reported before [41–44].

2.4. Potential applications of composite structuring

We presented the potential of the composite structures within multiple aspects of photonics. As the manipulation of PIPs and NGs is completely decoupled, the optical properties of PIPs and NGs can be combined to achieve multi-dimensional information multiplexing. Figures 5(a)–(c) shows that multi-dimensional information integration can be achieved by multiplexing the five dimensions provided by NGs (three spatial dimensions, the azimuth of NGs, and optical retardance) [45, 46], and the sixth dimension, namely the directionality of PIPs, which grants the composite structure with the potential in multi-dimensional information anti-counterfeiting and encryption (figure S11 in the supplementary material). The high universality of composite structuring makes it possible to directly write artificial photonic structures in matrix materials and thus fully utilize the excellent performances of various optical media (figures 5(d) and S12 in the supplementary material), which opens up an avenue to novel optical elements. For example, we demonstrated the fabrication of a planar nonlinear axicon lens with a diameter of about 6 mm in bulk lithium niobate crystal (figure 5(e)). The integration of the nonlinear crystal and the regularly arranged composite structures with sub-wavelength periodicity offers a binary optical manipulation capacity, which allows the element to simultaneously achieve frequency conversion and beam shaping (figure 5(f)). For micro-scale optical modulation, as the period of NGs is sub-wavelength-scaled while that of PIPs is wavelength-scaled, the optical responses of NGs and PIPs can be combined to form a multi-functionally integrated optical modulator that simultaneously possesses polarization and wavelength selectivity (figures 5(g) and (h)).

Compared with the photonic elements that are fabricated by conventional lithography approaches, the created all-inorganic photonic elements embedded in transparent dielectrics generally possess high stability, ultralong service life, and the capacity to work in various extreme environments [47–49]. These photonic elements can potentially be used for the modulation of high-power lasers and effectively work under high temperature, corrosion, and radiation conditions. Predictably, the methodology of focal volume light field-empowered material modification offers an excellent platform for multiple frontier applications, such as optical measurement, information processing, on-chip photonic integration, and space exploration.

3. Discussion and conclusions

For a long time, an ultrafast laser has been applied as a point-typed energy source to trigger various material modifications [50–52], and the profile of light intensity is mainly considered a Gaussian type. Therefore, the actual morphology and evolution of the light field in the focal volume have been overlooked. Our work indicates that the 3D spatial distribution of the light field at the focus can possess finer structures and is tunable, which offers a novel strategy for highly controllable micro-nano fabrication with more degrees of freedom beyond conventional point-by-point optical modification. Furthermore, revealing the actual light field in the focal volume helps understand the ultrafast light-matter interaction physics and may provide the principles for more potential advanced manufacturing technologies.

The proposed models and experimental results may change the traditional cognition of spot-driven laser processing. On the one hand, the focal volume light field can serve as a versatile tool to create various advanced functional composite structures that are not achievable with traditional techniques. On the other hand, the focal volume light field may also become a potentially unfavorable factor in achieving continuous and homogeneous material modification. Therefore, re-examining the current ultrafast laser-based micro-nano manufacturing principle in transparent media would be necessary, and some conventional concepts about behaviors of light in the focal volume need to be improved. This will arouse a series of brand-new research topics about how to activate, manipulate, or eliminate the focal volume light field according to specific application scenarios, which may trigger plenty of research work in the future.

In summary, we proposed and experimentally demonstrated composite material modification in a single step, where the light field in the focal volume can serve as an optical mold for imprinting composite structures and enabling the visualization of the actual energy distribution. The ultrafast laser-excited focal volume light field in transparent dielectrics is revealed to possess a fine distribution rather than being a Gaussian type. The fabricated composite structures are shown to hold great potential for multiple applications, such as multi-dimensional anti-counterfeit, information encryption, nonlinear planar lenses, and multi-functionally integrated photonic crystals. It would be exciting to combine our approach with spatial light modulation technologies, novel photoelectric materials, and intelligent path planning methods to develop a highly generalized strategy to achieve functional photonic elements at the on-demand position in various transparent dielectrics, empowering the construction of next-generation all-inorganic integrated optical systems.

4. Material and methods

4.1. Material preparing

In this study, the unconventional glasses, including La_2O_3–Nb_2O_5 glass, La_2O_3–Al_2O_3 glass, La_2O_3–Ta_2O_5–Nb_2O_5 glass, and La_2O_3–ZrO_2–Nb_2O_5 are prepared using a containerless process where two CO_2 lasers were used to melt the mixture of raw materials levitated by the O_2 airflow. The silica glass and all of the crystals used in this study are commercially available materials.

4.2. Ultrafast laser processing

A ULDW system is used to achieve composite structuring (figure S1 in the supplementary material), where a mode-locked regeneratively amplified Yb: KGW-based ultrafast laser system (PHAROS, Light Conversion Ltd) operating at a wavelength of 1 030 nm was employed as the light source.

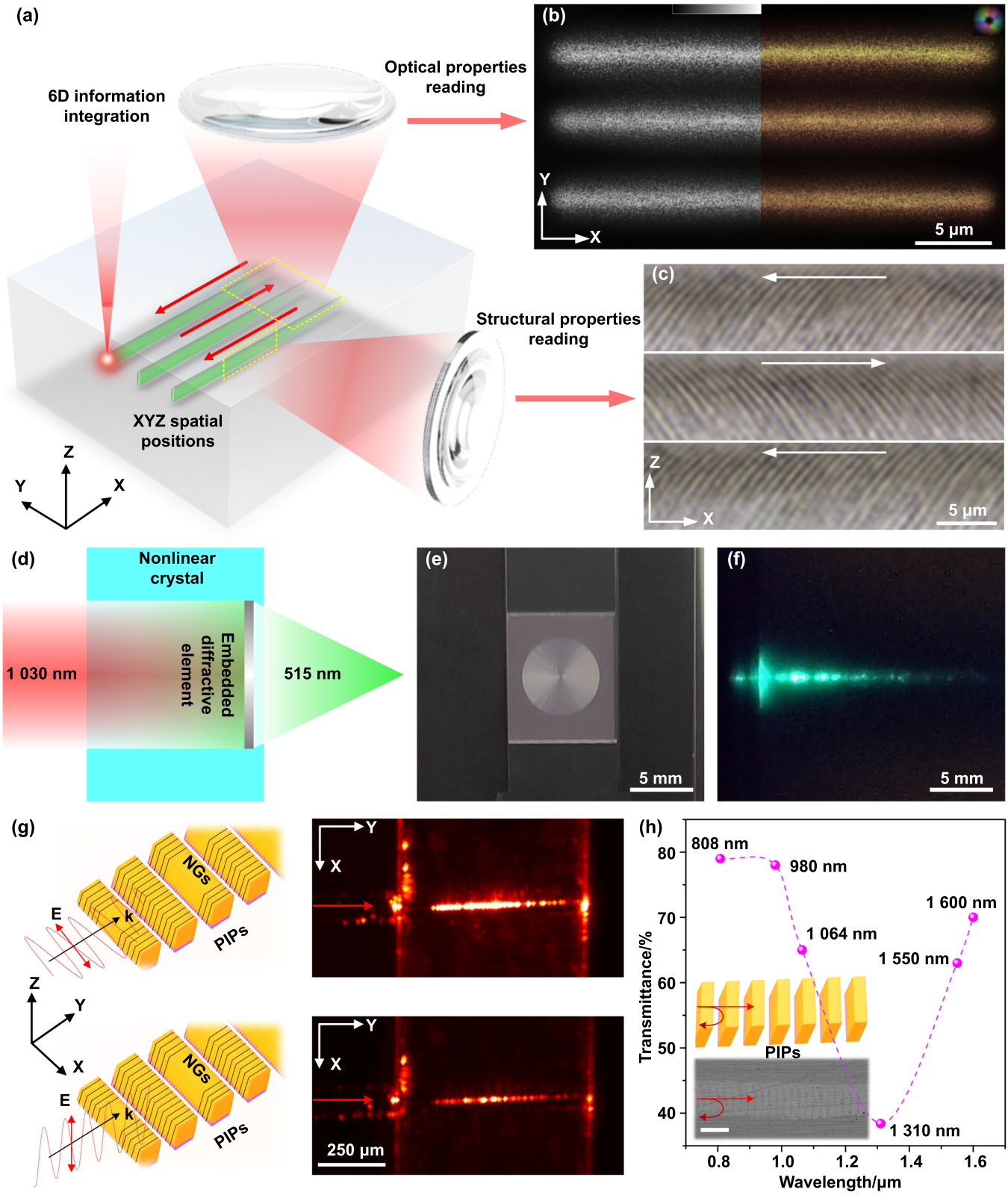

Figure 5. Potential applications of composite structuring. (a) Schematic diagram of multi-dimensional information integration. (b) Optical retardance (left) and azimuth angle (right) of the NGs in fused silica. The color bar illustrates the retardance value (0–250 nm). Pseudocolor indicates the direction of the slow axis. (c) Directional features of the PIPs in fused silica. White arrows indicate the scanning direction. (d) Schematic diagram of the nonlinear diffractive element made of the composite structure. (e) Optical image of a nonlinear planar axicon lens with a diameter of about 6 mm inscribed in lithium niobate crystal. (f) A second harmonic Bessel beam (testing light wavelength: 1 030 nm) was generated by the nonlinear planar axicon lens. (g) Schematic diagram of the polarization selectivity of NGs (left) and corresponding experimental certification (right). E represents the polarization direction. k indicates the wave vector. Probe light wavelength: 980 nm. (h) The wavelength selectivity of PIPs. Insets are schematic diagrams of the selective transmission (upper) and SEM images of PIPs in La_2O_3–Ta_2O_5–Nb_2O_5 glass (lower). Red arrows indicate the incidence of the probe light. Scale bar: 1 μm.

Generally, the laser was focused 10–500 μm below the surface of the sample via a 50 × objective lens (NA = 0.8). For fused silica, the pulse energy is 0.3–2 μJ, the pulse duration is 0.2–4 ps, the repetition rate is 25–200 kHz, and the scanning speed is 10–2000 μm s^{-1}. For unconventional glasses, the pulse energy is 0.5–1.5 μJ, the pulse duration is 0.8–3 ps, the repetition rate is 100–200 kHz, and the scanning speed is 100–2 000 μm s^{-1} (La_2O_3–Nb_2O_5 glass, La_2O_3–ZrO_2–Nb_2O_5 glass, and La_2O_3–Ta_2O_5–Nb_2O_5 glass) and 50–150 μm s^{-1} (La_2O_3–Al_2O_3 glass). For crystals, the pulse energy is 0.5–1 μJ, the pulse duration is 0.5–1 ps, the repetition rate is 50–200 kHz, and the scanning speed is 20–1 600 μm s^{-1}.

4.3. Structural characterization of composite structures

The optical observation of PIPs was performed using a polarizing microscope (BX53 Olympus Ltd). The structural properties of the PIPs and NGs were examined by scanning electron microscopy (SEM), using backscattering mode. For the SEM observation, samples were polished so as to expose the composite structures to air, and the polished surface was etched with hydrofluoric acid to improve the contrast of SEM images. Further phase transition characterization of the crystal-glass heterogeneous interface was performed by focused ion beam slice and transmission electron microscopy.

4.4. Theoretical modelling and simulation

Numerical simulation of the focal light field was performed using a finite-element method mode-solver tool. In the modelling, fused silica is set as the target transparent medium for demonstrating the establishment of the focal-volume interference, and a focused Gaussian beam is set as the original light source. The distance between the light radiation source and the focal plane is determined by the refractive index of the target medium and the numerical aperture of the objective lens.

Data and materials availability

All data needed to evaluate the conclusions in the paper are available in the main text or the supplementary materials.

Acknowledgments

This work was financially supported by the National Key Research and Development Program of China (No. 2021YFB2802001); the National Natural Science Foundation of China (Grant Nos. 12304349, U20A20211, 62275233); the Postdoctoral Fellowship Program of CPSF (GZB20230628, GZC20241465). We wish to thank Nianhang Rong and Xi Zheng of Zhejiang University Analysis Center of Agrobiology and Environmental Sciences for assistance with the SEM examination.

Author contributions

B Z and Z W contributed equally to this work. B Z and Z W conceived the idea. J Q organized, coordinated, and supervised the project. B Z and Z W performed the experiments and collected the data. B Z, Z W, D T and J Q interpreted the results and proposed the structuring mechanism. B Z, Z W and D T wrote the manuscript. M G and Y Y supervised and reviewed the manuscript. B Z, Z W, D T, and J Q discussed and revised the manuscript.

Conflict of interest

The authors declare no competing interests.

ORCID iD

Jianrong Qiu https://orcid.org/0000-0003-3148-2500

References

[1] Zijlstra P, Chon J W M and Gu M 2009 Five-dimensional optical recording mediated by surface plasmons in gold nanorods *Nature* **459** 410–3
[2] Karst J, Floess M, Ubl M, Dingler C, Malacrida C, Steinle T, Ludwigs S, Hentschel M and Giessen H 2021 Electrically switchable metallic polymer nanoantennas *Science* **374** 612–6
[3] Arbabi A, Horie Y, Bagheri M and Faraon A 2015 Dielectric metasurfaces for complete control of phase and polarization with subwavelength spatial resolution and high transmission *Nat. Nanotechnol.* **10** 937–43
[4] Yu N F and Capasso F 2014 Flat optics with designer metasurfaces *Nat. Mater.* **13** 139–50
[5] Hua J Y, Hua E K, Zhou F B, Shi J C, Wang C H, Duan H G, Hu Y Q, Qiao W and Chen L S 2021 Foveated glasses-free 3D display with ultrawide field of view via a large-scale 2D-metagrating complex *Light Sci Appl* **10** 213
[6] Han D D, Zhang Y L, Ma J N, Liu Y Q, Han B and Sun H B 2016 Light-mediated manufacture and manipulation of actuators *Adv. Mater.* **28** 8328–43
[7] Wei D Z *et al* 2018 Experimental demonstration of a three-dimensional lithium niobate nonlinear photonic crystal *Nat. Photonics* **12** 596–600
[8] Zhang Y, Sheng Y, Zhu S N, Xiao M and Krolikowski W 2021 Nonlinear photonic crystals: from 2D to 3D *Optica* **8** 372–81
[9] Chen Y *et al* 2022 Multidimensional nanoscopic chiroptics *Nat. Rev. Phys.* **4** 113–24
[10] Sun L Y *et al* 2019 Separation of valley excitons in a MoS_2 monolayer using a subwavelength asymmetric groove array *Nat. Photonics* **13** 180–4
[11] Li S X, Xia H, Liu T Y, Zhu H, Feng J C, An Y, Zhang X L and Sun H B 2023 In situ encapsulated moiré perovskite for stable photodetectors with ultrahigh polarization sensitivity *Adv. Mater.* **35** 2207771
[12] Lu J F, Tian J, Poumellec B, Garcia-Caurel E, Ossikovski R, Zeng X L and Lancry M 2023 Tailoring chiral optical properties by femtosecond laser direct writing in silica *Light Sci. Appl.* **12** 46
[13] Lu J F, Garcia-Caurel E, Ossikovski R, Courvoisier F, Zeng X L, Poumellec B and Lancry M 2023 Femtosecond laser direct writing multilayer chiral waveplates with minimal linear birefringence *Opt. Lett.* **48** 271–4

[14] Wei D Z *et al* 2019 Efficient nonlinear beam shaping in three-dimensional lithium niobate nonlinear photonic crystals *Nat. Commun.* **10** 4193

[15] Gao J C, Zhao X J, Yan Z, Fu Y H, Qiu J R, Wang L and Zhang J Y 2024 Multi-dimensional shingled optical recording by nanostructuring in glass *Adv. Funct. Mater.* **34** 2306870

[16] Ouyang X *et al* 2021 Synthetic helical dichroism for six-dimensional optical orbital angular momentum multiplexing *Nat. Photon.* **15** 901–7

[17] Zhang B, Tan D Z, Wang Z, Liu X F, Xu B B, Gu M, Tong L M and Qiu J R 2021 Self-organized phase-transition lithography for all-inorganic photonic textures *Light Sci. Appl.* **10** 93

[18] Papadopoulos A, Skoulas E, Mimidis A, Perrakis G, Kenanakis G, Tsibidis G D and Stratakis E 2019 Biomimetic omnidirectional antireflective glass via direct ultrafast laser nanostructuring *Adv. Mater.* **31** 1901123

[19] Zhang B, Wang Z, Tan D Z and Qiu J R 2023 Ultrafast laser-induced self-organized nanostructuring in transparent dielectrics: fundamentals and applications *PhotoniX* **4** 24

[20] Wang Z, Zhang B, Wang Z Q, Zhang J, Kazansky P G, Tan D Z and Qiu J R 2023 3D imprinting of voxel-level structural colors in lithium niobate crystal *Adv. Mater.* **35** 2303256

[21] Djogo G, Li J Z, Ho S, Haque M, Ertorer E, Liu J, Song X L, Suo J and Herman P R 2019 Femtosecond laser additive and subtractive micro-processing: enabling a high-channel-density silica interposer for multicore fibre to silicon-photonic packaging *Int. J. Extrem. Manuf.* **1** 045002

[22] Lu Y, Kai L, Chen C Y, Yang Q, Meng Y Z, Liu Y, Cheng Y, Hou X and Chen F 2022 Nanochannels with a 18-nm feature size and ultrahigh aspect ratio on silica through surface assisting material ejection *Adv. Photon. Nexus* **1** 026004

[23] Hecker S, Blothe M and Graf T 2020 Reproducible process regimes during glass welding by bursts of subpicosecond laser pulses *Appl. Opt.* **59** 11382–8

[24] Hecker S, Blothe M, Grossmann D and Graf T 2020 Process regimes during welding of glass by femtosecond laser pulse bursts *Appl. Opt.* **59** 6452–8

[25] Ródenas A, Gu M, Corrielli G, Paiè P, John S, Kar A K and Osellame R 2019 Three-dimensional femtosecond laser nanolithography of crystals *Nat. Photonics* **13** 105–9

[26] Jia Y C, Wang S X and Chen F 2020 Femtosecond laser direct writing of flexibly configured waveguide geometries in optical crystals: fabrication and application *Opto-Electron. Adv.* **3** 190042

[27] Jin F, Liu J, Zhao Y Y, Dong X Z, Zheng M L and Duan X M 2022 λ/30 inorganic features achieved by multi-photon 3D lithography *Nat. Commun.* **13** 1357

[28] Zhang X L, Yu F, Chen Z G, Tian Z N, Chen Q D, Sun H B and Ma G C 2022 Non-Abelian braiding on photonic chips *Nat. Photon.* **16** 390–5

[29] Sugioka K 2019 Hybrid femtosecond laser three-dimensional micro-and nanoprocessing: a review *Int. J. Extrem. Manuf.* **1** 012003

[30] Von der Linde D, Sokolowski-Tinten K and Bialkowski J 1997 Laser–solid interaction in the femtosecond time regime *Appl. Surf. Sci.* **109–110** 1–10

[31] Stuart B C, Feit M D, Herman S, Rubenchik A M, Shore B W and Perry M D 1996 Nanosecond-to-femtosecond laser-induced breakdown in dielectrics *Phys. Rev.* B **53** 1749–61

[32] Du D, Liu X, Korn G, Squier J and Mourou G 1994 Laser-induced breakdown by impact ionization in SiO_2 with pulse widths from 7 ns to 150 fs *Appl. Phys. Lett.* **64** 3071–3

[33] Tsibidis G D and Stratakis E 2020 Ionisation processes and laser induced periodic surface structures in dielectrics with mid-infrared femtosecond laser pulses *Sci. Rep.* **10** 8675

[34] Schaffer C B, Brodeur A and Mazur E 2001 Laser-induced breakdown and damage in bulk transparent materials induced by tightly focused femtosecond laser pulses *Meas. Sci. Technol.* **12** 1784–94

[35] Itoh K, Watanabe W, Nolte S and Schaffer C B 2006 Ultrafast processes for bulk modification of transparent materials *MRS Bull.* **31** 620–5

[36] Taylor R, Hnatovsky C and Simova E 2008 Applications of femtosecond laser induced self-organized planar nanocracks inside fused silica glass *Laser Photonics Rev.* **2** 26–46

[37] Rajeev P P, Gertsvolf M, Hnatovsky C, Simova E, Taylor R S, Corkum P B, Rayner D M and Bhardwaj V R 2007 Transient nanoplasmonics inside dielectrics *J. Phys. B: At. Mol. Opt. Phys.* **40** S273–82

[38] Bhardwaj V R, Simova E, Rajeev P P, Hnatovsky C, Taylor R S, Rayner D M and Corkum P B 2006 Optically produced arrays of planar nanostructures inside fused silica *Phys. Rev. Lett.* **96** 057404

[39] Hnatovsky C, Taylor R S, Rajeev P P, Simova E, Bhardwaj V R, Rayner D M and Corkum P B 2005 Pulse duration dependence of femtosecond-laser-fabricated nanogratings in fused silica *Appl. Phys. Lett.* **87** 014104

[40] Shimotsuma Y, Kazansky P G, Qiu J R and Hirao K 2003 Self-organized nanogratings in glass irradiated by ultrashort light pulses *Phys. Rev. Lett.* **91** 247405

[41] Zhang F T, Nie Z G, Huang H X, Ma L, Tang H, Hao M M and Qiu J R 2019 Self-assembled three-dimensional periodic micro-nano structures in bulk quartz crystal induced by femtosecond laser pulses *Opt. Express* **27** 6442–50

[42] Yang W J, Bricchi E, Kazansky P G, Bovatsek J and Arai A Y 2006 Self-assembled periodic sub-wavelength structures by femtosecond laser direct writing *Opt. Express* **14** 10117–24

[43] Lu J F, Dai Y, Li Q, Zhang Y L, Wang C H, Pang F F, Wang T Y and Zeng X L 2019 Fiber nanogratings induced by femtosecond pulse laser direct writing for in-line polarizer *Nanoscale* **11** 908–14

[44] Cao J, Mazerolles L, Lancry M, Brisset F and Poumellec B 2017 Modifications in lithium niobium silicate glass by femtosecond laser direct writing: morphology, crystallization, and nanostructure *J. Opt. Soc. Am.* B **34** 160–8

[45] Zhang J Y, Gecevičius M, Beresna M and Kazansky P G 2014 Seemingly unlimited lifetime data storage in nanostructured glass *Phys. Rev. Lett.* **112** 033901

[46] Shimotsuma Y, Sakakura M, Kazansky P G, Beresna M, Qiu J R, Miura K and Hirao K 2010 Ultrafast manipulation of self-assembled form birefringence in glass *Adv. Mater.* **22** 4039–43

[47] Wang Y T, Lancry M, Cavillon M and Poumellec B 2022 Lifetime prediction of nanogratings inscribed by a femtosecond laser in silica glass *Opt. Lett.* **47** 1242–5

[48] Wang Z, Zhang B, Tan D Z and Qiu J R 2023 Ostensibly perpetual optical data storage in glass with ultra-high stability and tailored photoluminescence *Opto-Electron. Adv.* **6** 220008

[49] Wang M H *et al* 2021 Femtosecond laser fabrication of nanograting-based distributed fiber sensors for extreme environmental applications *Int. J. Extrem. Manuf.* **3** 025401

[50] Eaton S M, Zhang H B, Herman P R, Yoshino F, Shah L, Bovatsek J and Arai A Y 2005 Heat accumulation effects in femtosecond laser-written waveguides with variable repetition rate *Opt. Express* **13** 4708–16

[51] Kawata S, Sun H B, Tanaka T and Takada K 2001 Finer features for functional microdevices *Nature* **412** 697–8

[52] Tan D Z, Zhang B and Qiu J R 2021 Ultrafast laser direct writing in glass: thermal accumulation engineering and applications. *Laser Photon. Rev.* **15** 2000455

Review Article

ADVANCED PHOTONICS

Photonic circuits written by femtosecond laser in glass: improved fabrication and recent progress in photonic devices

Dezhi Tan[a,*] Zhuo Wang,[a] Beibei Xu,[a] and Jianrong Qiu[a,b,*]

[a]Zhejiang University, College of Optical Science and Engineering, State Key Laboratory of Modern Optical Instrumentation, Hangzhou, China
[b]Chinese Academy of Sciences, CAS Center for Excellence in Ultra-Intense Laser Science, Shanghai, China

Abstract. Integrated photonics is attracting considerable attention and has found many applications in both classical and quantum optics, fulfilling the requirements for the ever-growing complexity in modern optical experiments and big data communication. Femtosecond (fs) laser direct writing (FLDW) is an acknowledged technique for producing waveguides (WGs) in transparent glass that have been used to construct complex integrated photonic devices. FLDW possesses unique features, such as three-dimensional fabrication geometry, rapid prototyping, and single step fabrication, which are important for integrated communication devices and quantum photonic and astrophotonic technologies. To fully take advantage of FLDW, considerable efforts have been made to produce WGs over a large depth with low propagation loss, coupling loss, bend loss, and highly symmetrical mode field. We summarize the improved techniques as well as the mechanisms for writing high-performance WGs with controllable morphology of cross-section, highly symmetrical mode field, low loss, and high processing uniformity and efficiency, and discuss the recent progress of WGs in photonic integrated devices for communication, topological physics, quantum information processing, and astrophotonics. Prospective challenges and future research directions in this field are also pointed out.

Keywords: photonic integrated circuit; waveguides; femtosecond laser direct writing; improved techniques; photonic devices.

Received Dec. 1, 2020; revised manuscript received Jan. 18, 2021; accepted for publication Feb. 5, 2021; published online Mar. 10, 2021.

[DOI: 10.1117/1.AP.3.2.024002]

1 Introduction

Photonic integrated circuits have shown the potential to allow integrating passive and active optical components on one chip in a scalable manner and have been identified to support a plethora of applications, such as data communication, sensing, astrophotonics, quantum information processing, and national security.[1–4] Photonic circuits are indispensable components in modern optical communication networks and lie at the heart of integrated photonic devices. Currently, to this end, one of the biggest challenges in integrated photonics is establishing a general and flexible method to produce photonic circuits with low loss, high integration density, and high tunability. The unique feature of 3D fabrication geometry promises femtosecond laser direct writing (FLDW) as an on-demand solution to these requirements.

Femtosecond (fs) laser-induced multiphoton absorption enables tailoring the material structures and properties inside transparent bulk materials with high processing precision and triggers a great deal of activity in the field of photonics.[5–13] In particular, the fs laser can induce a permanent refractive index change in glass, which indicates a promising tool to fabricate photonic circuits, waveguides (WGs), and basic elements in integrated optics.[5,14,15] FLDW has been identified to be an effective technique for constructing WGs in a 3D fashion over a large depth from the micrometer to millimeter scale.[5,16–18] WG-based 2D and 3D optical devices have also been demonstrated in various glasses. Compared with the 2D fabrication of silicon photonic circuits by planar lithography, FLDW is a rapid prototyping technique to produce WGs in 3D without needing complex procedures. Thus, up to now, FLDW has been exploited to

*Address all correspondence to Dezhi Tan, wctdz@zju.edu.cn; Jianrong Qiu, qjr@zju.edu.cn

be a highly potential solution to quickly create optical components and integrated photonic devices three-dimensionally in transparent glasses. The intrinsic characteristic of being embedded in bulk makes these devices highly tolerant to variations of the working environment, which is significant for optical network applications.[19,20]

However, although significant advances have been made in writing and applications of WGs, there are still practical challenges that need to be addressed before fully exploiting 3D fabrication capabilities of FLDW and constructing complex WG-based photonic integrated devices. For example, low insertion loss, including low coupling loss and propagation loss, and symmetrical mode field are usually necessary. Unfortunately, propagation effects, such as nonlinear filamentation and refocusing, would influence energy-deposition behavior and the resultant microstructures.[21,22] In general, when a tightly focused fs laser irradiates into glass, a refractive-index mismatch between the air and glass causes spherical aberration (SA), which would distort the energy distribution in the focus and the shape of modified volumes.[23–25] SA increases with increments of numerical aperture (NA), focusing depth, and refractive index of the glass.[26] Other effects such as the self-focusing effect and nonlinear absorption effect can also induce focus distortion. As a result, although the transverse writing geometry with the writing direction perpendicular to the laser propagation axis can realize maximum degrees of processing flexibility, these effects intrinsically lead to an elliptical cross-section in WGs and usually also cause high asymmetry in the mode field of the written WGs along with high coupling loss and propagation loss.[15,27,28] It is a great challenge to maintain the WG circularity, symmetry, and mode-field profiles, which would limit the coupling loss, propagation loss, and 3D capability of the FLDW technique. Furthermore, these issues will be more serious for the deep WGs in glass. However, writing deep WGs is of importance for constructing complex reconfigurable photonic circuits, which is essential for highly integrated on-chip devices with multifunctionality. Furthermore, to push the development and wide-scale implementation of integrated photonic devices beyond the laboratory, the importance of fabricating WGs with high uniformity and efficiency is continuing to grow, which raises concerns over controlling the highly nonlinear process in the WG writing and the stability of the setups. In addition, since the refractive index change induced by fs laser irradiation is generally small (usually smaller than 1%), decreasing the loss, especially the bend loss in the curved WGs, is a tough task. To address these issues, great efforts have been devoted to developing improved strategies to reduce the coupling loss, propagation loss, and bend loss, improve the symmetry of cross-section and that of the mode field, and enhance the processing uniformity and efficiency.

Here, we provide a comprehensive review of the improved techniques along with the mechanisms for controlling the symmetry of the WG cross-section and mode field profile and reducing the loss (including coupling loss, propagation loss, and bend loss), as outlined in Fig. 1. Furthermore, with the ever-increasing data demand, photonic WGs have achieved explosive growth in applications, especially in optical communication devices, topology and quantum science, and astrophotonics. We will also review the state-of-the-art progress of photonic applications in these fields with WGs written by fs lasers.

2 Improved Technologies and Mechanisms for Waveguide Writing by Femtosecond Lasers

2.1 Beam Shaping

The shape of the focal volume affects the energy distribution and the generated cross-section of the WGs, which would determine the morphology of the mode field, the coupling loss, and propagation loss.[15,28] In general, manipulating the beam shape has been proved to be a facile method to control the morphology of the mode field and reduce the coupling loss and propagation loss. For this purpose, several beam shaping techniques were introduced, including slit beam shaping, astigmatic beam shaping, simultaneous spatiotemporal focusing (SSTF), and spatial light modulator (SLM) beam shaping.[23–26,29–32]

2.1.1 Slit beam shaping

In general, as mentioned, WGs written by fs lasers in glass using conventional spherical focusing optics exhibit significant loss and strong core asymmetry with an elongated shape along the fs laser propagation direction with a large aspect ratio. Cheng et al. reported that the aspect ratio in the cross-section of the microchannels could be greatly reduced by inserting a

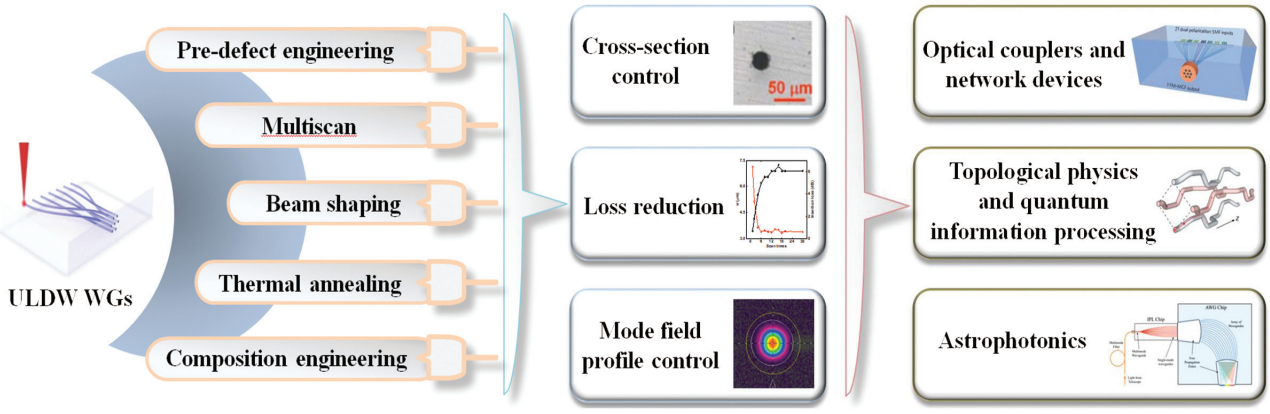

Fig. 1 WGs written by fs lasers in glass: improved fabrication techniques and photonic device applications.

slit before the focusing lens with the slit oriented parallel to the laser scanning direction, which is attributed to the diffraction effect at the slit aperture.[23] This slit beam shaping technique was also adopted to produce low loss, circular WGs in glass with a long working-distance objective lens.[25,33,34]

For a circular Gaussian beam and an elliptical Gaussian beam, the energy distribution near the focal point is described as[23]

$$I_c = \frac{1}{(1+z^2/z_0^2)}\ \exp\left[-2\frac{x^2+y^2}{w_0^2(1+z^2/z_0^2)}\right], \tag{1}$$

$$I_e = \frac{1}{(1+z^2/z_0^2)^{1/2}}\frac{1}{(1+z^2/z_0'^2)^{1/2}}\ \exp\left[-2\frac{x^2}{w_0^2(1+z^2/z_0^2)}\right] \times \exp\left[-2\frac{y^2}{w_0'^2(1+z^2/z_0'^2)}\right], \tag{2}$$

where $w_0 = \lambda/(\mathrm{NA}\cdot\pi)$ is the beam waist at the focus with λ as the laser wavelength, $z_0 = kw_0^2/2$ is the Rayleigh length with k as the wave vector, and $w_0' = (R_x/R_y)w_0^2$ and $z_0' = kw_0'^2/2$ with R_x and R_y as the radii along the x and y axes of the elliptical beam, respectively. Equation (2) indicates that a beam waist can be expanded R_x/R_y times in the y direction, and the beam in the x direction is tightly focused, leading to small Rayleigh length. As a result, for an elliptical Gaussian beam, there is a significant reduction in the aspect ratio that is determined by the ratio of the Rayleigh length to the beam waist at the focal point, which is achievable by inserting a slit.[23,26]

To estimate the optimal slit width (W_y) for generating highly symmetrical cross-section of WGs, the aspect ratio of the slit, W_y/W_x, can be expressed as the following:

$$\frac{W_y}{W_x} = \frac{\mathrm{NA}}{n}\sqrt{\frac{\ln 2}{3}} \quad \text{for } W_x > 3W_y, \tag{3}$$

where W_x is the unapertured beam waist, NA is the numerical aperture of the objective lens, and n is the refractive index of glass.

Compared to the case without a slit, as shown in Fig. 2(a), Fig. 2(d) shows that the transverse width in the y direction has become significantly larger by placing a slit before the focusing lens, which results in much higher symmetry for the energy distribution [Fig. 2(e)]. Figure 2(c) shows that the shape of a WG written without a slit has an elliptical-shaped core with the aspect ratio of about 4:1. A circular WG is fabricated by introducing a slit with width of about 500 μm, as shown in Fig. 2(f). The symmetry of the refractive index distribution and mode field of the guiding light also becomes higher after inserting a slit. Consequently, this slit beam shaping would be favorable for improving the loss performance.

Combining low NA ($0.1-0.2$) focusing optics and the slit beam shaping technique, the fs laser could write deep surface WGs with a circular cross-section and low loss over a large depth range (e.g., from 0.7 to 7 mm), and the aspect ratio reaches nearly 1.[26] Due to the highly symmetrical morphology, Fig. 2(h) shows that the propagation loss is as low as 0.2 dB/cm at the depth of 0.72 mm and remains smaller than 1 dB/cm at the depth beyond 7 mm. The slit beam shaping technique also works in the transverse regime with the laser beam moving along the propagation direction.[35] All of these results reveal that slit beam shaping is a powerful technique to improve the performance of WGs written by fs lasers in glass. In addition, the slit beam shaping technique is also adopted to fabricate WG Bragg gratings with a circular cross-section.[36,37]

2.1.2 Astigmatic beam shaping

Although the slit beam shaping technique is simple, it is not efficient, and most of the laser energy is attenuated by the slit.[32,38] To shape the laser beam, astigmatic shaping is also adopted to reshape the beam with an astigmatic cylindrical telescope before focusing, which allows for writing WGs with a circular cross-section and arbitrary size.[29,31,39–44] The basic principle for the astigmatic beam shaping is that the WG size does not depend on the focal size along the sample translation direction in the transverse writing regime. Focusing very tightly in the x direction will decrease the Rayleigh range z_{Rx}; the increased divergence in the xz plane can significantly reduce the intensity to that below the threshold for nonlinear absorption, and this decreases the focus depth. Consequently, the transverse WG size can be optimized by independently tuning the focal size in the y direction. The intensity profile of a focused astigmatic Gaussian beam can be expressed as

$$I_0(x,y,x) = I_{00}\frac{w_{ox}}{w_x(z)}\frac{w_{oy}}{w_y(z)}\ \exp\left\{-2\left[\frac{x^2}{w_x(z)^2}+\frac{x^2}{w_y(z)^2}\right]\right\}, \tag{4}$$

$$w_x(z) = w_{ox}\sqrt{1+\left(\frac{z}{z_{Rx}}\right)^2}, \quad w_y(z) = w_{oy}\sqrt{1+\left(\frac{z-z_0}{z_{Ry}}\right)^2}, \tag{5}$$

where $z_{Rx,y} = \pi(w_{0x,y}^2/\lambda)$ denotes the Rayleigh ranges of the Gaussian beam for the x and y directions, w_{ox} is the astigmatic beam waist at $z=0$, and z_0 is the offset distance between the beam waists, named the astigmatic difference, which is shown in Fig. 3(a). Increasing the beam size (w_y) in the y direction, with respect to w_{0y}, is achieved by controlling z_0 at the plane with respect to the beam waist in the x direction. Figures 3(a)–3(d) show that the symmetry and size of the electron density profile are highly tunable by modifying the astigmatic difference. Consequently, the WG size perpendicular to the beam propagation direction can be adjusted continuously, and the highly symmetrical WG profile is achievable. Furthermore, manipulating the astigmatic difference allows for not only improving the symmetry of the WG profile but also for varying the WG size. As a result, the coupling loss can reach as low as 0.1 dB/facet to the single mode optical fiber at 1550 nm, and the propagation loss is lower than 0.4 dB/cm.[45] This beam shaping method is also of significance for mass production of identical WGs, which provide a stable and reliable quantum light source.[39,40]

When the microstructure is not purely one-dimensional (1D), slit beam shaping and astigmatic beam shaping require modifying the orientation of the slit or the cylindrical lens pair during laser beam scanning, and an additional complexity is produced. As a result, they are not suitable for writing bending WGs and related devices that restrict their further applications.

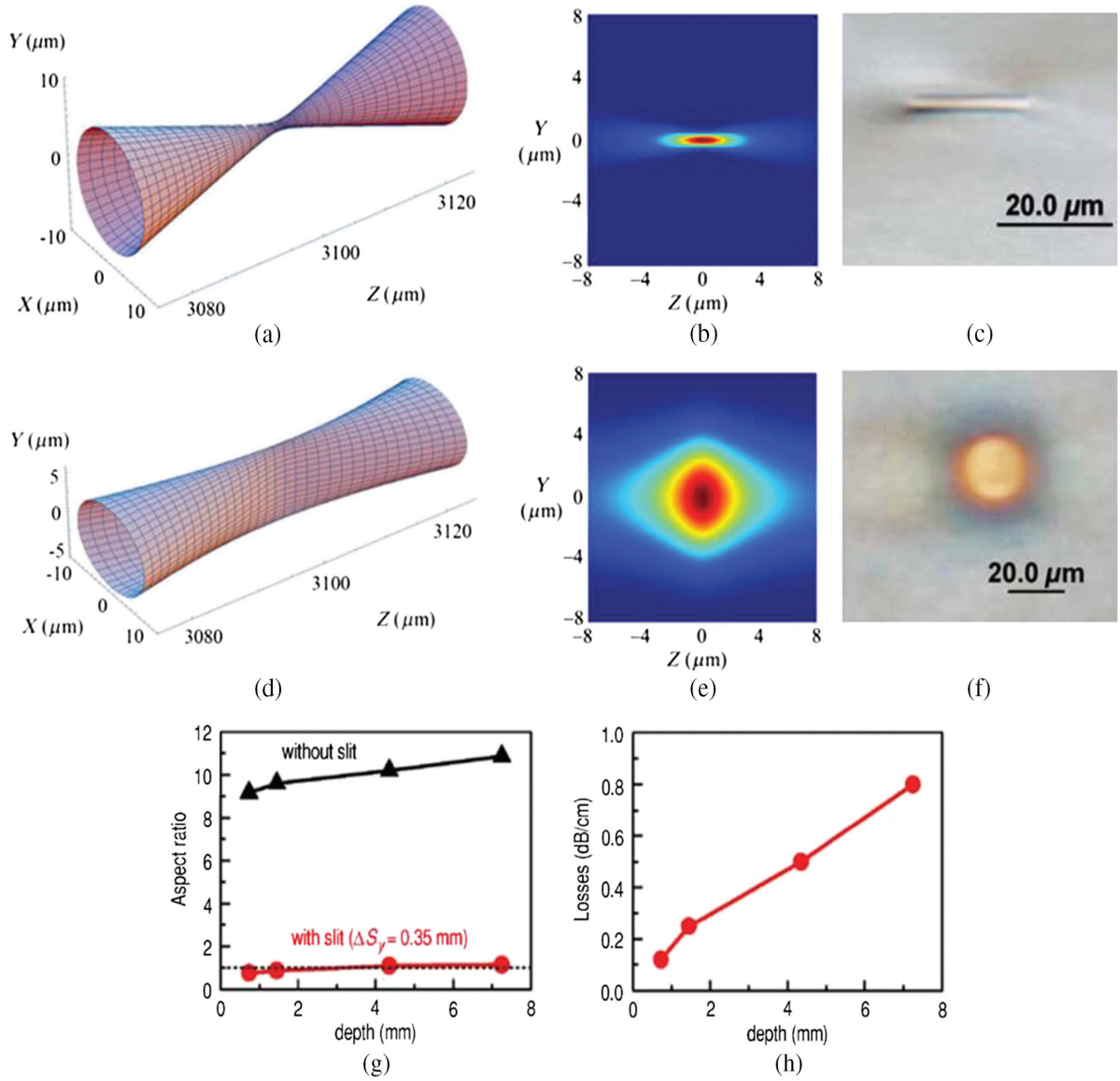

Fig. 2 Beam evolution near focus (a) without and (d) with a slit, energy distribution in the *YZ* plane (b) without and (e) with a slit, optical images of fabricated WGs in phosphate glass (c) without and (d) with a slit ($W_y = 500$ μm). *X* corresponds to the fs laser beam translation direction. Figures reproduced from Ref. 25. (g) Aspect ratio of the WGs produced in the fused silica with a slit W_y of 350 μm. Dotted line: aspect ratio of 1. (h) Propagation loss at 1550 nm as a function of depth ($W_y = 250$ μm). Figures reproduced from Ref. 26.

2.1.3 Simultaneous spatiotemporal focusing

SSTF offers another solution to control the cross-section.[30,46–49] This technique relies on separating the spectral components of the fs laser pulse in space before focusing using a grating pair, which induces spatial chirping in the incident pulse and generates an array of beamlets at various frequencies. As different frequency components overlap spatially only around the focus, temporal focusing happens, and this results in the shortest pulse duration with the highest peak intensity. In such a manner, the spatiotemporally focused pulses are transform-limited in time, diffraction-limited in space, and strongly localized near the geometric focus, and the pulse duration broadens obviously when moving away from the focus, which leads to a rapid decrease in the peak intensity. As a result, this transform-limited SSTF method allows for a significant improvement in the axial resolution of the fs laser writing. The schematic illustration of fs laser SSTF is shown in Fig. 4(a).

In general, the field of a spatially chirped pulse can be written as

$$A_1(x,y,\omega) = A_0 \exp\left[-\frac{(\omega-\omega_0)^2}{\Omega^2}\right] \exp\left\{-\frac{[x-\Delta x(\omega)]^2+y^2}{2W_0^2}\right\}, \tag{6}$$

where A_0 is a field amplitude, $\sqrt{2\ln 2}\Omega$ is the full width at half maximum of the frequency spectrum, ω_0 is the carrier frequency, W_0 is the incident beam waist before the grating pair, and $\Delta x(\omega) = \alpha(\omega-\omega_0)$ is the displacement of each spectral component (α is the groove density of the grating).

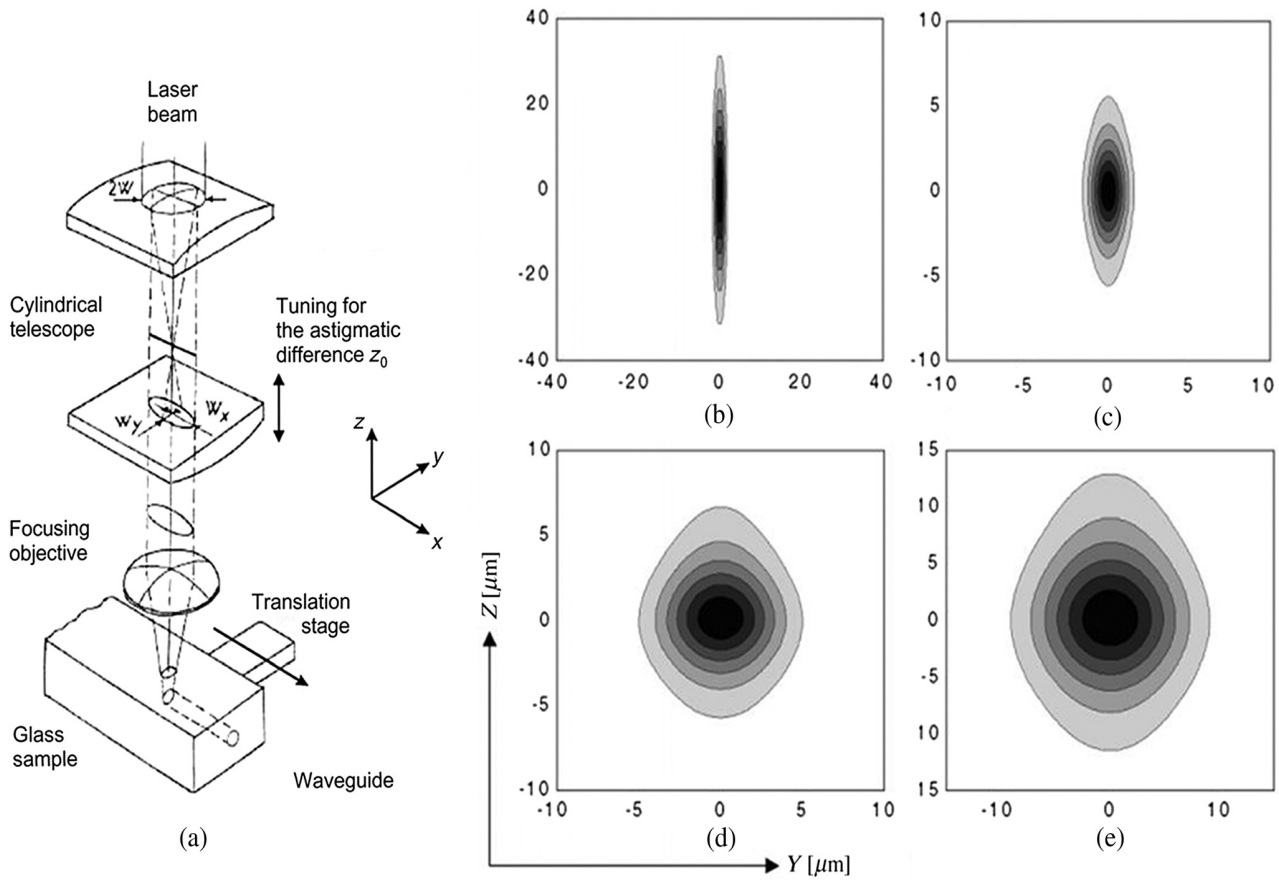

Fig. 3 (a) Schematic of the WG writing setup with astigmatic beam shaping. Figure reproduced from Ref. 31. Simulated electron density profiles (b) without and with astigmatic beam shaping for different focusing parameters (c) $w_{0x} = 1$ μm, $w_{0y} = 3$ μm, $z_0 = 0$, (d) $w_{0x} = 1$ μm, $w_{0y} = 3$ μm, $z_0 = 100$ μm, and (e) $w_{0x} = 1.4$ μm, $w_{0y} = 4.2$ μm, $z_0 = 260$ μm. Figures reproduced from Ref. 29.

The field after the objective lens and near the focus can be expressed as

$$A_2(x, y, \omega) = A_1(x, y, \omega) \exp\left(-ik\frac{x^2 + y^2}{2f}\right), \tag{7}$$

$$A_3(x, y, \omega) = \frac{\exp(ikz)}{i\lambda z} \iint_{-\infty}^{\infty} A_2(\xi, \eta, \omega) \times \exp\left[ik\frac{(x-\xi)^2 + (y-\eta)^2}{2z}\right] \mathrm{d}\xi\, \mathrm{d}\eta, \tag{8}$$

where k is equal to $2\pi c/\omega_0$, c is the velocity of light in vacuum, and f is the focal length of the objective lens.

$$I(x, y, z, t) = |A_3(x, y, z, t)|^2 = \left| \int_{-\infty}^{\infty} A_3(x, y, z, t) \exp(-i\omega t) \mathrm{d}\omega \right|^2. \tag{9}$$

Figures 4(c) and 4(d) show the intensity distributions of the SSTF beam in the XZ and YZ planes calculated by combining Eqs. (6)–(9), and a nearly spherical intensity distribution has been obtained. Furthermore, the axial resolution of fs laser writing is continuously tunable simply either by adjusting the incident beam size or the spatial chirp of the laser pulse via changing the distance between the two gratings. In addition, an objective lens with a relatively high NA (i.e., NA = 0.46) is necessary for generating a nearly spherical distribution of the laser field in the focal volume. However, a low NA objective lens cannot result in a circular lateral cross section.[50]

The aspect ratios of cross-sectional shapes of a focal spot can be manipulated independently in both axial and lateral directions by combining a slit beam shaping technique and an SSTF technique, which enables isotropic resolution in 3D space even for an objective lens with low NA.[51] To suppress the strong aberration in the fabrication at large depth, another double-pass grating compressor (DGC) can be adopted, as shown in Fig. 4(e). The total group delay dispersion of the pulse before the objective lens could be controlled by simultaneously modifying the DGC and the single-pass grating compressor. The longitudinal resolution is improved dramatically, and a nearly perfect circular cross-section is obtained. In this case, a low NA lens also works. The focal lens with low NA allows for writing circular WGs at a large depth (~9 mm), owing to its long working distance.[50] In addition, besides controlling the aspect ratio, SSTF also offers several additional levels of control over the ultrafast laser focus such as an adjustable pulse front tilt (PFT).[52,53] Neighboring foci can be overlapped by exploiting the inherent PFT with an appropriately designed diffractive holographic pattern from SLM irradiated

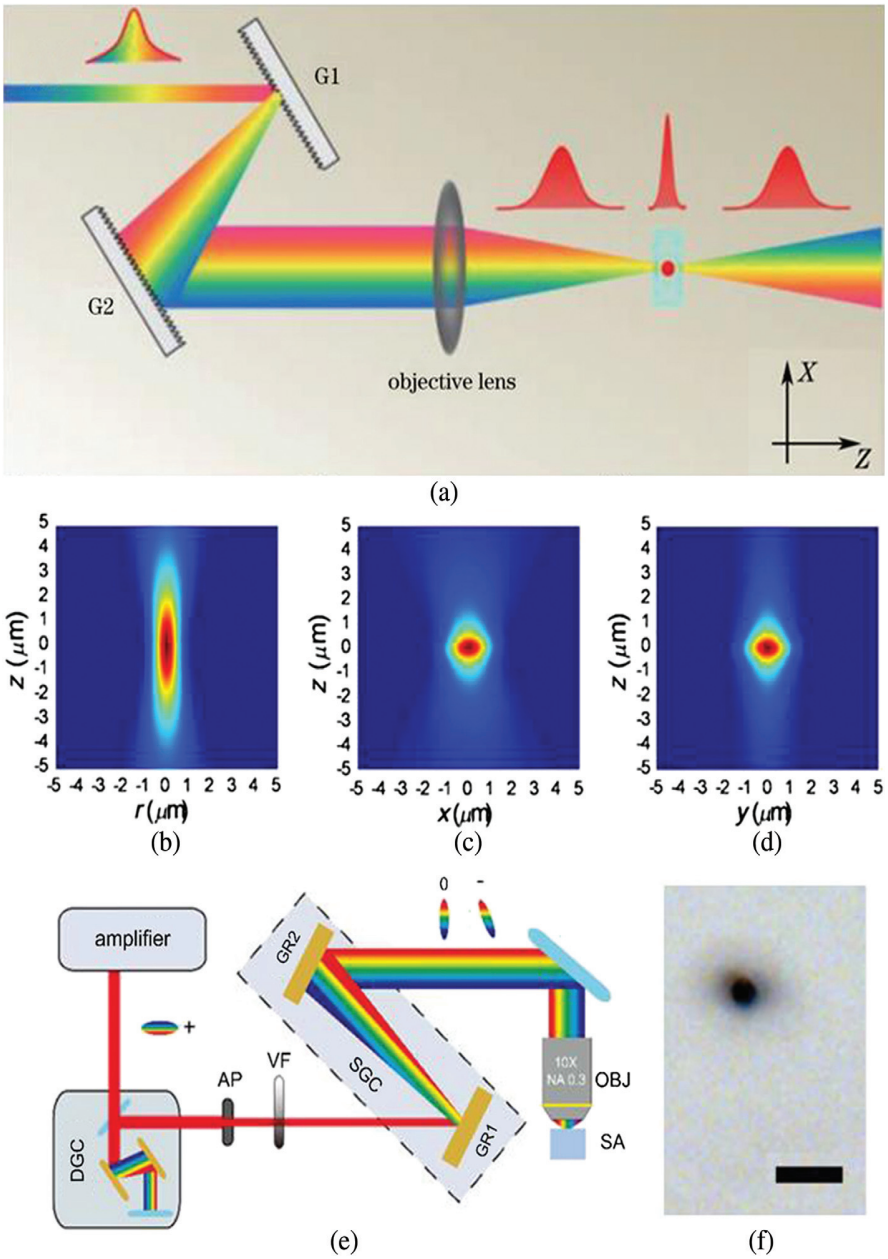

Fig. 4 (a) Schematic illustration of fs laser SSTF. Calculated laser intensity distributions at the focus generated by an objective lens (b) without and (c), (d) with the SSTF technique in the *XZ* and *YZ* planes, respectively. Figures reproduced from Ref. 30. (e) Schematic of the experimental setup for adding an initial temporal chirp on the SSTF. AP, aperture; VF, variable neutral density filter; GR1 and GR2, gratings; OBJ, objective lens; SA, sample. (f) Cross-sectional view optical micrographs of the line written at 9 mm. Scale bar, 20 μm. Figures reproduced from Ref. 50.

by a spatially chirped beam, and overlapping of multiple spots from a single pulse could have occurred in space but separated in time.[47] This technique not only provides a high level of axial confinement but also enables parallel writing for improving the processing efficiency. Temporally chirped SSTF is demonstrated via focusing the light with an off-axis parabola after the grating pairs, which is useful for rapid prototyping to produce high aspect ratio channels in glass and also for biomedical applications (e.g., deep tissue ablation and optical histology).[54] Combining a grating with an SLM or a cylindrical lens, temporally chirped SSTF is also achievable with enhanced axial resolution for accurately tailoring the laser–material interaction.[49,55,56]

In summary, the SSTF of the fs laser pulse strongly reduces nonlinear side effects and offers unique possibilities for fabrication with isotropic 3D resolution.[57] Furthermore, the addition of an initial temporal chirp on the SSTF is favorable for keeping the fabrication resolution nearly unchanged against the SA.

2.1.4 Spatial light modulator beam shaping

An SLM beam shaping technique gives rise to a versatile and energy efficient option for modifying the energy distribution in the focus, allowing not only for the improvement of the aspect-ratio of the focal volume as well as the symmetry of the mode field pattern of WGs but also the dynamic manipulation of it

during fabrication.[24,58–60] Aberration correction is achieved over a large depth using SLM with higher accuracy and flexibility, which enables writing deep WGs with a circular cross-section. To realize the depth-dependent aberration correction, the change in optical path length for the light refracted at the glass surface should be considered, and the SA associated phase in the pupil of the objective can be expressed as[59]

$$\emptyset_{\mathrm{SA}}(\rho) = \frac{-2\pi d_{\mathrm{nom}}}{\lambda}\left[\sqrt{n_2^2 - (\mathrm{NA}\cdot\rho)^2} - \sqrt{n_1^2 - (\mathrm{NA}\cdot\rho)^2}\right], \tag{10}$$

where d_{nom} is the nominal depth in the glass [Fig. 5(a)], λ is the wavelength of the fs laser, n_1 (n_2) is the refractive index of air (glass), ρ is the normalized pupil radius, and NA is the NA of the lens. Equation (10) indicates that the aberration strongly depends on writing depth and the NA of the objective lens. Figure 5(b) shows that the peak intensity (I_p) of the laser beam decreases with increase of focusing depth, especially in the higher NA regime. The full width at half maximum (Δz) of the distribution along the beam propagation direction increases with the depth, as revealed in Fig. 5(c), and this is in agreement with the simulation of energy distribution for focusing at various depths, which shows that the focus becomes distorted, and the cross-section is no longer symmetric and substantially elongated along the laser propagation direction. The distortion and asymmetry become more serious with a depth increase. As a consequence, the cross-section of the fabricated WGs is noncircular at the large depth, as shown in Fig. 5(d). Figure 5(e) shows that the morphology of the WG can be improved significantly after appropriate aberration correction using SLM, and the WG cross-section almost does not depend on the writing depth. Furthermore, Fig. 5(f) shows that the near-field mode profile exhibits high symmetry, and the mode ellipticity reaches nearly 1. In addition, there is also no obvious difference in light transmission of the WGs at different depths after aberration correction. These results indicate that the SLM beam shaping technique allows for fabricating symmetrical WGs through the entire depth of the working objective lens, which will be crucial for fabricating complex WG lattices with high integration density and holds promise for a wide range of applications with 3D photonic circuits.

In addition, the SLM can also enable effective parallel writing. Multiple foci with controlled power distribution and dynamically variable distance can be produced in 3D by modulating the spatial phase distribution of a fs laser beam with a computer-generated hologram, which allows for writing several WGs or multiscan performance over one WG in a single pass.[61–64] Furthermore, for fabricating 3D WG arrays and coupling devices

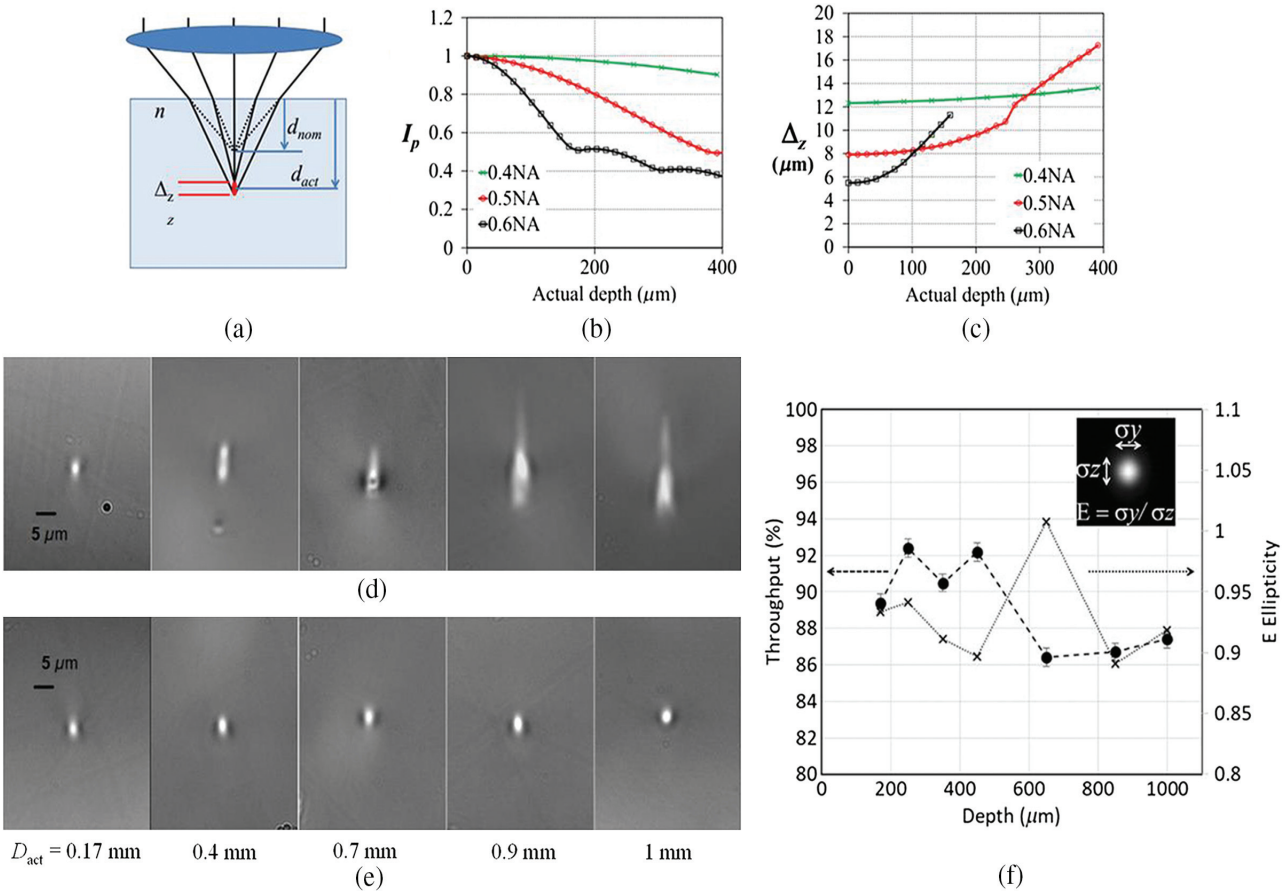

Fig. 5 (a) Schematic of the focusing geometry. (b) Simulated estimate of the focal peak intensity I_p at various depths in glass. (c) Δz as a function of depth. WGs inscribed at different depths (d) without and (e) with aberration correction in the nonthermal writing regime (pulse repetition rate of 1 kHz). Figures reproduced from Ref. 59. (f) Plot of the transmission throughput and mode ellipticity as a function of depth for WGs inscribed with SLM beam shaping at the thermal writing regime (pulse repetition rate of 1 MHz). Figure reproduced from Ref. 24.

using the traditional fs laser writing technique, the substrate is needed to be precisely positioned. With the help of the SLM, a branched WG can be written simultaneously by one pass scanning in glass. Consequently, an SLM not only significantly enhances the fabrication uniformity and efficiency but also eliminates the need for precisely positioning the glass substrate.

2.2 Multiscan

Multiscan is a reliable technique to increase the refractive index change and modify the shape and size of the WGs by scanning the laser beam multiple times.[5,65] In this regime, there is no position shift between consecutive scans. David et al. revealed that the increase in refractive index is about 0.01 and 0.035 in the Ge-doped silica glass generated by 1 and 10 writing passes, which indicates the possibility of reducing insertion loss by the multiscan.[5,65] Bend loss could be also reduced by scanning the WG track multiple times in all curved segments due to the tighter confinement of the modes caused by multiscan-induced large refractive index contrast.[66] Recently, Tan et al. reported that the WG size can be controlled by adjusting the scanning passes [Figs. 6(a)–6(c)].[67] Furthermore, a mechanism of a temperature gradient-assisted process was proposed for the formation of WGs, which locates outside the focus. Consequently, the unique position of WGs allows for abating the distortion of laser energy in the focal volume and inscribing low-loss deep WGs. Usually, a WG core with the largest density and RI locates near the center of the modified zone, which is generated by the matter melting and quenching in thermal writing with high repetition rate pulses (e.g., >100 kHz) or local compression in the nonthermal case with low repetition rate pulses. In temperature gradient-assisted writing, a high temperature with a sharp gradient is generated by ultrafast injection of enough energy in the focus, which is accompanied by pressure wave propagation. As a result, rapid mechanical expansion with structural reorganization is driven during the temperature evolution, and melted and ionized matter would be ejected out from the hot pressurized center to the surrounding zone, resulting in forming a densified "cladding" ring and a rarefied center consisting of less dense structures [Fig. 6(a)]. In addition, in the conical WG structure, a quasidirectional hydrodynamic material flow can be induced by the fast stress relaxation along the laser propagation axis, and the axial densification at the top of the densified ring is generated [Fig. 6(b)]. Multiscan writing is suggested to repeat this material flow process and increase the WG size. The absence of separation between the parallel pass avoids the presence of a nonhomogeneous interface structure between parallel scans. As the guiding core of WGs is at the tips of the densified zone, outside the focal volume, a lowest insertion loss of about 0.6 dB [Fig. 6(c)] for the 1-cm-long WGs with the WG diameter size of around 6 μm is obtained over a large depth range from 300 to 900 μm. Revealing strong dependence of insertion loss on the WG size provides a unique way to improve WG performance in various coupling cases.

The critical issue for the multiscan technique is the relatively low fabrication yield. In addition, the scan speed in the multiscan case is usually the same as that in the single pass scan, and there have been no systematic studies about the optimal speed in the multiscan, uncovering what may enable improvement of the fabrication efficiency with low propagation loss, coupling loss, and bend loss. Our work indicates that monitoring the WG size offers an effective way to optimize the multiscan process efficiently.[67] Furthermore, the optimal processing window for low-loss WGs is usually small, and the fluctuation in the writing process may be detrimental to the reproducibility and the uniformity, especially when the number of the WGs is larger. Multiscan as well as the aforementioned SLM-assisted parallel writing should be helpful for improving the writing reproducibility and the uniformity.

Besides rescanning the laser along the whole path, tapering the WGs close to the end facet was also demonstrated to be a useful technique to increase the refractive index as well as to enlarge the modification region.[68,72] As shown in Fig. 6(d), a spatial power ramp is used. Multiscan is performed at the last few millimeters of a WG with increasing laser power, ranging from just under the modification threshold up to a moderate power level. Figure 6(g) shows that mode field size can be modified by tapering of WGs with the multiscan. Furthermore, the coupling efficiency to the standard single mode fiber is also enhanced.

In another case, the WG cross-section is tunable using the multiscan technique, and an offset is adopted between consecutive parallel scans with a small distance in the direction perpendicular to the laser scanning direction, as shown in Fig. 6(f).[69,70,73–76] This technique does not depend on the intensity distribution at the focal volume and enables WG fabrication with desirable morphologies, such as square cross-sections along with a step index refractive index profile [Fig. 6(g)]. The size of the WG cross-section and the change in refractive index can be controlled independently by varying the scan parameters and the translation speed, respectively, and this is not achievable using beam shaping techniques. Furthermore, integrated photonic lanterns constituted with an array of single mode WGs can be produced using the multiscan technique, which have found many applications in astrophotonics and remote sensing.[77–80]

In addition, writing a pair of parallel structures with a desirable distance to sandwich the curved WG will control the stress and birefringence effect in the WGs.[81,82] The refractive index change would increase from 1.85×10^{-3} to 3.45×10^{-3} in the guiding core, as shown in Fig. 6(h).[71] Consequently, the bend loss is suppressed drastically from 2.7 to 0.3 dB for a bend arc angle of 5 deg. A similar technique is adopted to fabricate a mode field compressor and reduce the mode field size.[83] Birefringence is demonstrated to be tunable in the range from 0 to 4.35×10^{-4}, and this allows great flexibility in designing polarization sensitive and insensitive components devices on one single chip, which adds another degree of freedom in the fabrication of integrated optical devices.[81,82]

2.3 Thermal Annealing

Stress can be induced during the WG writing in glass, and anisotropic and inhomogeneous distribution of the refractive index in the modified region is generated through the photoelastic effect, which would lead to a polarization shift and polarization dependent losses as well as an asymmetrical mode field and large propagation loss.[84,85] The stress in the cladding zone surrounding the WG core also reduces the refractive index contrast between the WG core and the outer region, which can cause high propagation loss and bend loss.[86] Thermal annealing has been demonstrated to be a useful method for stress relaxation and complex material reorganization.[82,85,86] In general, heat increases the atom movement rate in the glass matrix by offering the

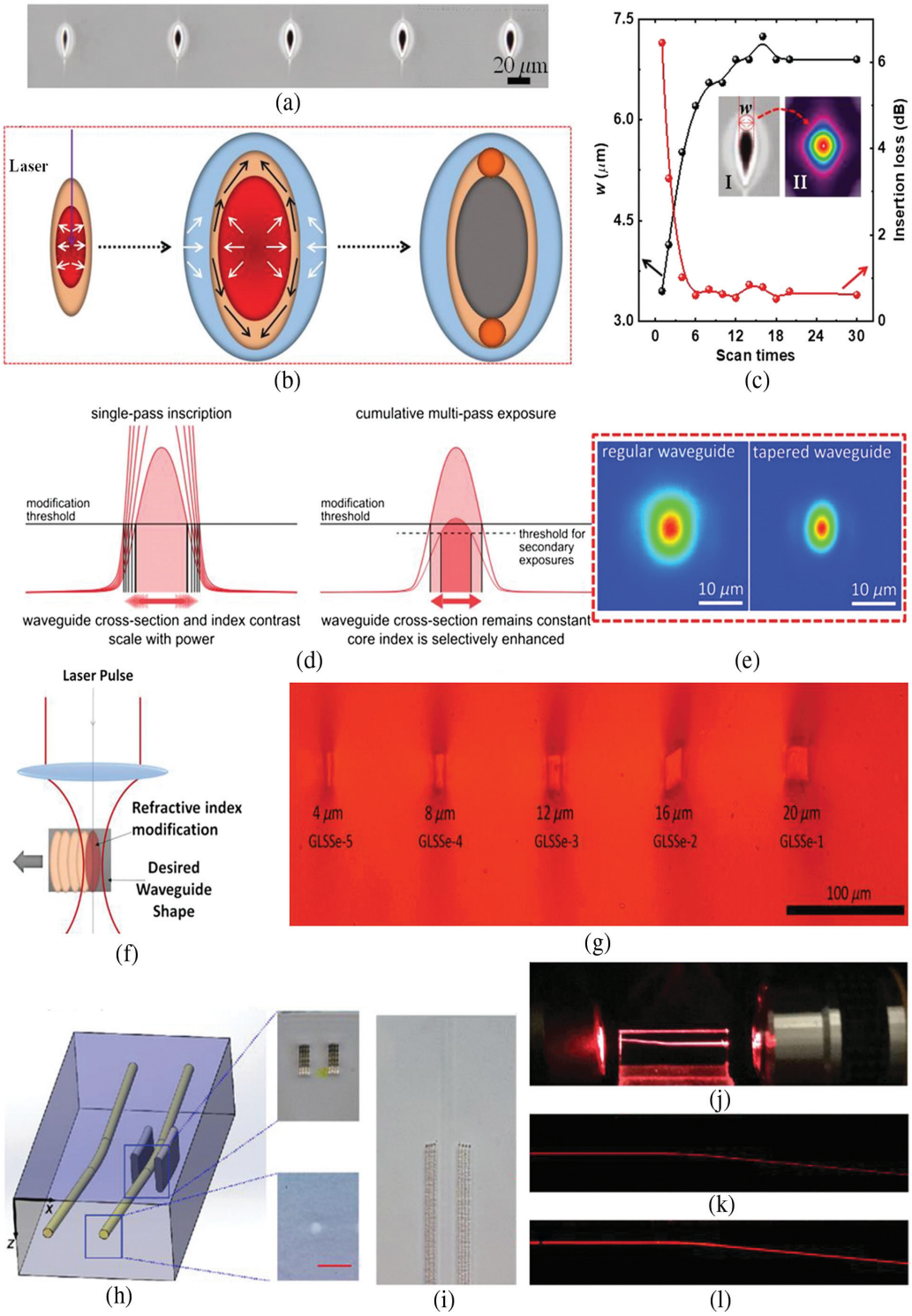

Fig. 6 (a) Cross-sections of WGs written by scanning fs lasers 1, 2, 4, 6, and 10 times. (b) Schematic view of temperature gradient assistant fs laser writing. Black arrow: matter expansion and flow driven by temperature gradient and stress. White arrows: stress. (c) Insertion loss and diameter (w) of WGs fabricated by scanning various times at 300 μm. Inset: I, cross-section; II, near-field mode profile. Figure reproduced from Ref. 67. (d) Left: illustration of the dependency of the WG cross-section on the fs laser power. Right: cross section of WGs tapered by multiscanning with a low power at the end of the WG. Figures reproduced from Ref. 68. (f) Schematic of the multiscan WG fabrication with an offset perpendicular to the writing direction. Figure reproduced from Ref. 69. (g) Size variation with an increase in the number of scans. Figure reproduced from Ref. 70. (h) Schematic of the sandwiched WG. Insets: the cross sections of the WG and bend-loss-suppression walls. Scale bar: 30 μm. (i) Top view of the sandwiched WG. (j) A 633-nm laser beam propagating in the WG. Top view images of a WG bend (k) without and (l) with bend-loss-suppression walls. Figures reproduced from Ref. 71.

energy for breaking bonds and during annealing at temperatures in the vicinity of the glass transition temperature, where the formation of new bonds and structural rearrangement may have occurred, which leads to a decrease in the structural inhomogeneity.[87–89] As a result, the reduction of the structural deformation leads to stress relaxation. In addition, nonbridging oxygen hole center (NBOHC) defects can also disappear at low temperature (e.g., 300°C for silica glass).[33,90] Consequently, the size of the guiding core and the structure anisotropy are reduced, the refractive index contrast in the core/cladding regions increases, and these are accompanied by lower propagation loss and bend loss along with higher mode symmetry.

A typical rate thermal annealing process is adopted for this purpose. The key characteristic of this thermal treatment is the slow cooling rate that enables removing the stress and birefringence effectively. In general, to initiate an erasure and stabilization process, the sample is initially heated above the transformation temperature. Once reaching the maximum temperature that is well below the softening temperature of the glass, a very slow cooling rate is adopted until the glass temperature is cooled down below the strain or transformation point temperature.[82,86] Figures 7(a) and 7(b) show the cross-section of the WGs before and after annealing, respectively, and the refractive index profile is displayed in Figs. 7(c) and 7(d), respectively, which clearly indicate that the outer lower refractive index zone is removed by thermal annealing. As a result, the output power through the WGs increases, and the bend loss decreases significantly, as revealed in Fig. 7(e). Symmetric polarization-insensitive WGs are also available with ultralow birefringence and low propagation loss of 0.3 dB/cm. Babu et al. also reported that insertion loss could be reduced effectively to 1.01 dB at 632.8 nm by an isochronal annealing treatment, which is due to the bleaching of the NBOHC defects.[91,92]

2.4 Predefect Engineering

One of the big challenges for direct writing of WGs by fs lasers is the increase in the refractive index of WGs, which would foster better performances of the devices. As the presence of defects makes great contributions to the refractive index increase, predefect engineering of materials to induce an incipient defect density has been explored to cause an increment in the refractive index.[34] The predefects can be generated by hard (40 keV) X-ray irradiation with accumulated doses up to

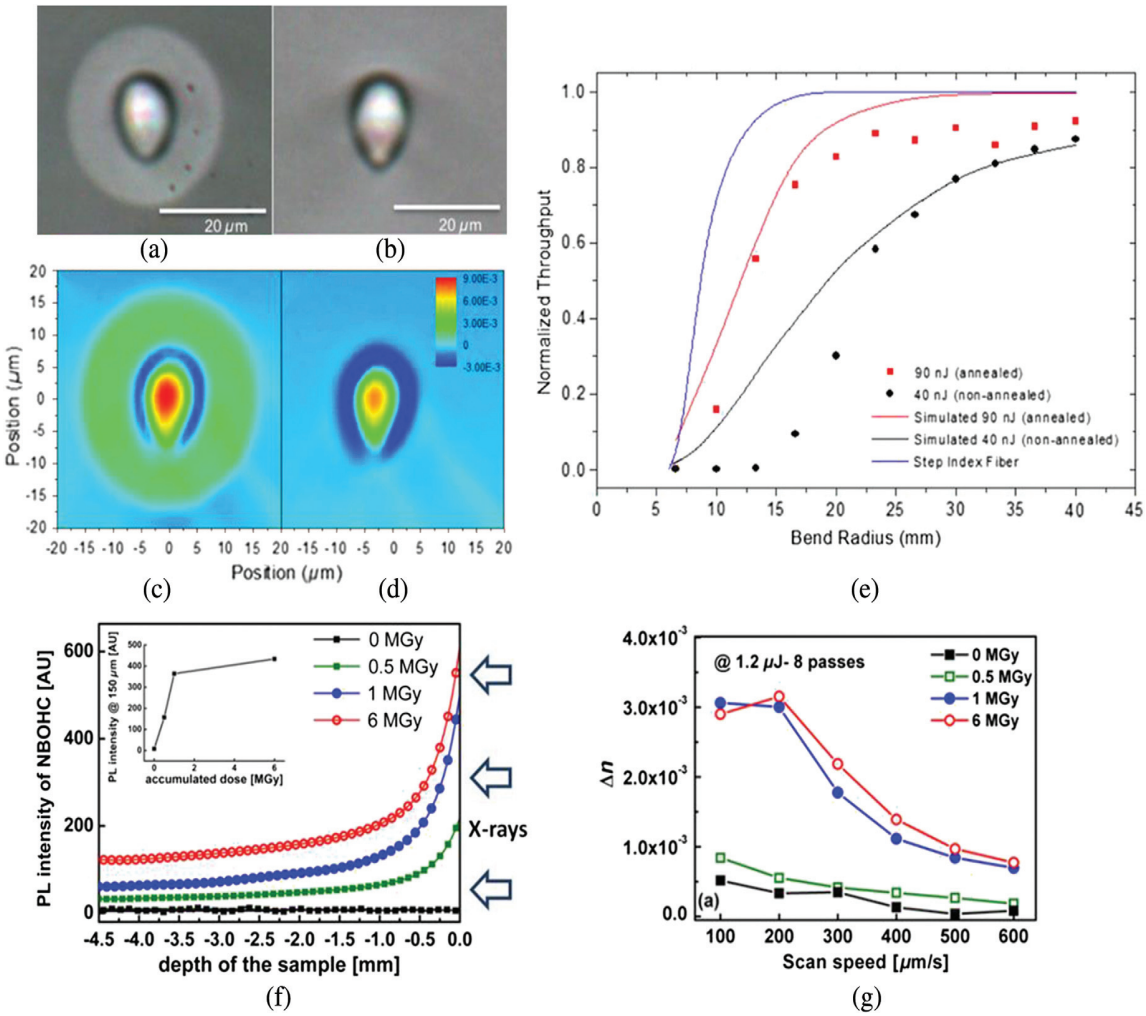

Fig. 7 Cross sections of the WGs (a) before and (b) after thermal annealing. Refractive index profiles of WG (c) before and (d) after annealing. (e) Normalized output through the WGs as a function of bend radii. Figures reproduced from Ref. 86. (f) PL intensity versus depth in the glass after X-ray exposure with various doses. (g) Change of refractive index (Δn) in the WGs as a function of the scan speed at different X-rays doses. Figures reproduced from Ref. 34.

6 MGy, which subsequently serve as precursors for further defect generation induced by fs lasers, along with an overall increase in photosensitivity. As a result, photoinscription efficiency is enhanced, and a higher index change is obtained. Figure 7(f) shows that the PL coming from NBOHC increases with an increase in X-ray doses from 0.5 to 6 MGy, especially in the depth smaller than 500 μm, and the unexposed sample does not emit PL, which indicates the generation of NBOHC after X-ray irradiation. The increase in refractive index is much larger with 1 and 6 MGy doses of X-ray irradiation than that with 0–0.5 MGy doses of irradiation at all scan speed, as shown in Fig. 7(g). In conclusion, predefect engineering is a promising technique to increase the refractive index of WGs, which also enables validating scenarios of defect-assistant densification for the refractive index change. Furthermore, we suggest that UV light or electron and ion beam preirradiation may also lead to similar effects, and further experimental work is needed to verify this proposal.[93,94]

2.5 Composition Engineering

As the optical properties and photoresponse to fs lasers depend on the chemistry of glass, and the fs laser-induced refractive index change would be determined by the structural and elemental reorganization, composition engineering is a simple and promising alternative route to improve the performance of written WGs in glasses, especially in the thermal writing regime with high repetition rate lasers.[95–98] In the fs laser writing process, the local temperature would be higher than that of the softening and working point of glass.[67,98] As a result, the breaking of bonds linking the network modifiers or the network formers will occur in this high-temperature field, and the ions, including O^{2-}, would diffuse and modify the local compositions of glass, which usually leads to formation of two typical zones with positive and negative refractive index change, respectively. Increasing the concentration of the components such as Ca, La, and Al that induce densification and disorder causes a larger increase in refractive index, with Δn reaching 10^{-2}, and reduces the coupling loss and propagation loss significantly.[96,97,99] For example, in typical alkali-free borosilicate glasses, such as Corning Eagle 2000, Corning Eagle XG, and Schott AF32 glasses, the characterizations based on the refractive index mapping, electron microprobe analysis, and Raman spectroscopy clearly suggest that an increase in the concentration of the silicon element causes a decrease in refractive index, and an increase in the concentration of Ca and Al elements leads to an increment in the refractive index.[96] Similar phenomena are also found in other glass systems.[97] Germanium doping in silica glass is suggested to increase the refractive index change.[100] The increment in the concentration of Al_2O_3 in the aluminosilicate glasses could lead to breaking of the Si-O-Si network into four and three-membered ring structures accompanied by structure densification, which is confirmed by the increase of Raman intensity at D_1 (~485 cm^{-1}) and D_2 (~600 cm^{-1}) peaks.[91] The presence of silver was reported to decrease the insertion loss of the WGs in the binary tellurite-zinc glass, but the mechanism is still unclear.[101] However, although composition engineering is a useful method to increase the refractive index change, there have been not as many efforts to optimize the compositions and controll the element migration in a desirable way for achieving better performance, and more systematical studies are still needed.

3 Applications in Optical Coupling and Integrated Devices

WG writing by fs lasers in glass has found various applications in a vast range from scientific researches to technological devices.[14,15,102–107] In this review, we focus the recent progress in the WG applications for photonic integrated devices in communication, topological physics, quantum information processing, and astrophotonics.

3.1 Optical Couplers and Network Devices

Optical couplers are one of the key building blocks for combining and splitting optical signals in photonic integrated circuits.[2,108] A compact, low-loss, broadband power coupler with polarization sensitivity or insensitivity is highly required for many applications, such as power splitters, optical switches, multiplexers, directional couplers, birefringent retarders, and rotated waveplates.[43,68,82,102,105,108–110] The flexibility in photonic circuit configuration and mass production with designability in 3D helps WG writing by fs lasers to build couplers and splitters with arbitrary shapes and tunable coupling ratios in glass.[104,105,111] Especially, achieving polarization transformation is achievable and also desirable in integrated architecture with WGs created by FLDW, and this is critical for quantum applications, as controll over polarization enables performing operations with polarization-encoded photonic qubits.[43,111–113]

For example, an on-chip rotated polarization directional coupler (RPDC) operating at 780 nm with an arbitrary birefringent optical axis can be constructed via writing a double-track, as shown in Fig. 8(a), through which the distribution of the refractive index between adjacent tracks in the fused silica is tuned.[43] In this case, a single-mode WG with an artificially birefringent optical axis and high transmittance could be produced by adjusting the relative radial and azimuthal positions of the tracks. Figure 8(b) shows the polarization analysis of the 45-deg rotated birefringent optical axis measured by two crossed polarizers. The visibility of the input polarized light propagating along the optical axis remains as high as 98% to 99%. Characterization of the transmission power of the 45-deg RPDC with adjusted coupling lengths indicates that coupling lengths are the same for the 0-deg and 45-deg RPDCs, and the parallel coupling length could be determined to be 23 mm. Reconstruction of the Stokes vector was also performed, and the average fidelities reach 98.1% and 96.0% for the 0-deg and 45-deg RPDCs, respectively, with the corresponding average ratios up to 16 dB (0 deg) and 20 dB (45 deg).

Shortening the distance between the coupled WGs in the couplers may induce strong anisotropic mechanical stress, which was exploited to decrease the size of the polarizing directional couplers down to 3.7 mm with WG distance below 5 μm.[116] Importantly, the WGs exhibit low birefringence out of the coupled region. As a result, this approach allows for constructing complex polarization-sensitive integrated circuits with high integration. The extinction ratios at the operation wavelength of 808 nm are determined to be about 16 and 20 dB for the horizontal and vertical polarizations, respectively.

Polarized and polarization insensitive directional couplers, working in the telecom band of 1550 nm, were also fabricated in aluminoborosilicate glass (EAGLE, Corning) just by controlling the interaction length (L) and the separation of two WGs (d), as shown in Fig. 8(c).[111] This paves the way to the integrated

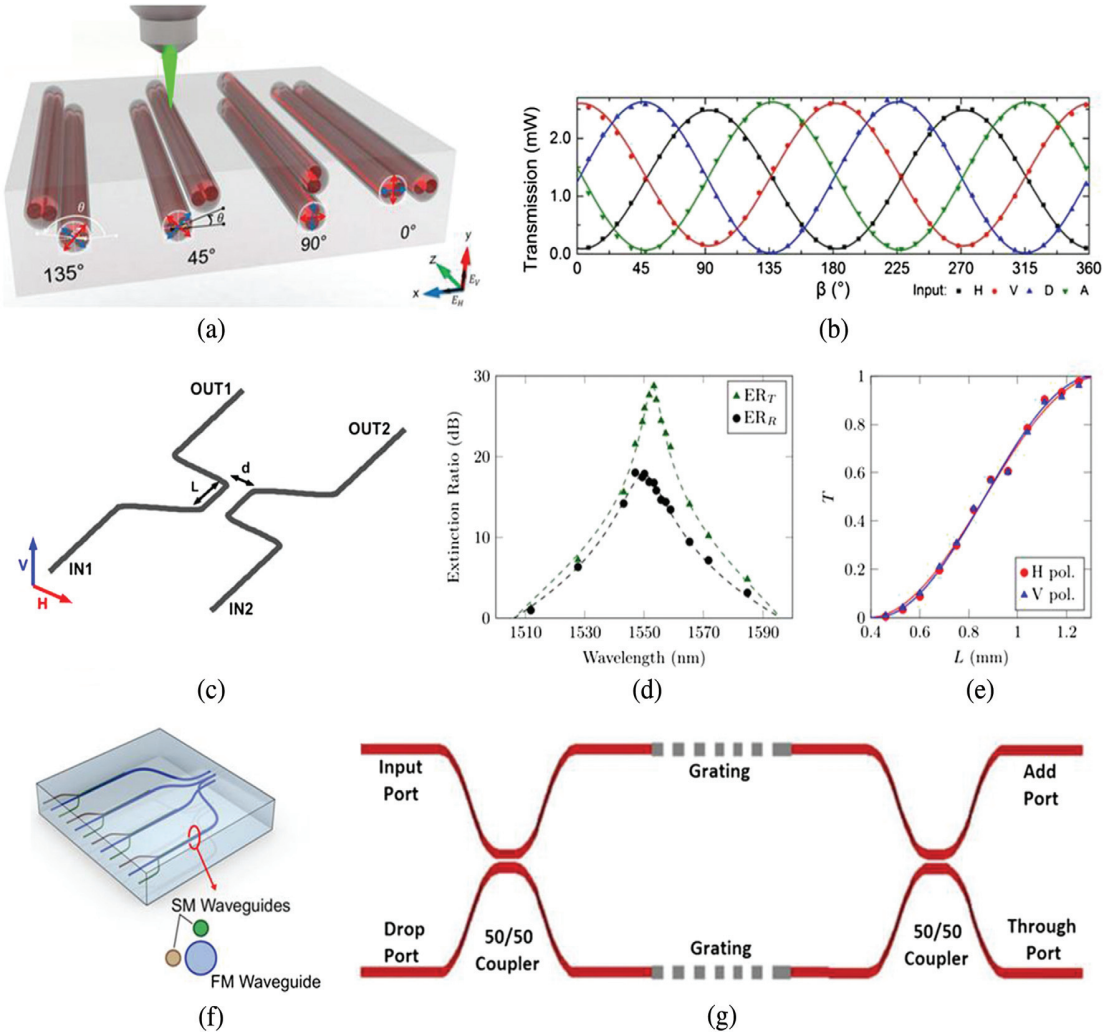

Fig. 8 (a) Illustration of the double-track approach for fabrication of WGs and RPDCs. θ is the geometrically radial and azimuthal offset between two adjacent tracks (dark red) in each WG (gray). (b) Polarization analysis of the 45-deg rotated parallel coupling region with different linear input states [H, V, antidiagonal (135 deg, A Pol.) and diagonal (45 deg, D Pol.)]. Figures reproduced from Ref. 43. (c) Schematic of a DC. Two input (out) ports: IN1 and IN2 (OUT1 and OUT2). (d) Transmission and reflection extinction ratios for a PDC with L of 33.2 mm and d of 12.5 μm in the telecom band. (e) Transmission for polarization insensitive DCs with L of 0.4 to 1.3 mm and d of 8 μm. Figures reproduced from Ref. 111. (f) Diagram of the 4-core few-mode coupler. Figure reproduced from Ref. 114. (g) Schematic of the optical add-drop multiplexer configuration. Figure reproduced from Ref. 115.

controll over polarization encoded photonic qubits and polarization entanglement at the 1550 nm wavelength range. In general, the WG birefringence causes a different periodicity for different polarization states in the power oscillation between the two WGs in the DCs, which can be described as

$$T = \sin^2(kL + \emptyset_0), \quad R = \cos^2(kL + \emptyset_0), \tag{11}$$

where T is the power transmission coefficient, R is the reflection coefficient, k is the coupling coefficient between the optical modes, and $\emptyset_0$ is an offset for the coupling occurring in the curved segments incoming and departing from the coupling region.

Large phase difference could be present with large L. With the appropriate coupler geometrical and coupling parameters, the two oscillations can be in antiphase, which results in a polarized DC. For example, Fig. 8(d) shows that the extinction ratios between the two polarizations are higher than 25 dB at 1550 nm with extinction ratios higher than 15 dB, where L is 33.2 mm, and d is 12.5 μm. While for shorter interaction lengths, the DC exhibits polarization insensitivity. Figure 8(e) shows the transmission for DCs with L of 0.4 to 1.3 mm and d of 8 μm, and the absolute transmission difference for the two polarizations is as low as 10^{-4}, meaning polarization insensitivity. The authors suggested that the alteration of the optical properties caused by the inscription of the second WG to that of the first one in the coupler is the origin of such polarization-insensitive behavior. Techniques, such as birefringence compensation and thermal annealing, were used to improve the symmetry of the WGs and the birefringence, which lead to symmetric polarization-insensitive DCs.[82] These achievements imply that it is possible to integrate polarization

dependent and independent devices in a single circuit by just manipulating the geometrical parameters of the components, which will be vital in future complex photonic devices.

To realize arbitrary photonic waveplate operations on chip, a stress engineering technique via writing an additional modification track near the WG was adopted to create an artificial stress field and rotate the optical axis of the birefringent WG.[108] Higher pulse energy and lower writing velocity were used for writing the second defect track, in which no light propagates. Consequently, Hadamard, Pauli-X, and rotation gates for encoding photonic polarization qubits on chip were achieved with high fidelity on both classical and quantum states of light. In this case, the retardation between ordinary and extraordinary field components was tuned, including half-wave plate and quarter-wave plate operations through modifying the length of the modified track parallel to the WG.

Furthermore, to support the ever-growing demand in transmission bandwidth and capacity over a communication channel, a number of technological features have been developed by the telecommunication community in the past decades.[117] 3D multiplexers and demultiplexers based on WGs were produced and could be integrated on a photonic chip.[19,68,102,114,118,119] Ultrahigh capacity space-division multiplexers systems were built in borosilicate glass.[19] For example, 1.2 Pb/s throughput transmission was demonstrated using the few-mode multicore fiber (four-core, three-mode) with a cladding diameter of 160 μm, as shown in Fig. 8(f).[114] In this case, 368 wavelength division multiplexed spatial super channels across the C and L bands were used. Simultaneous multiplexing of the LP_{01}, LP_{11a}, and LP_{11b} modes of all cores is achievable in this three-mode, four-core fiber with high mode extinction ratios and low insertion losses over a large bandwidth across the S + C + L bands.[111] In addition, optical add–drop multiplexers written in fused silica were demonstrated operating at 1550 nm, as shown in Fig. 8(g).[115] To this end, two DCs with a symmetrical geographical layout were used in a Mach–Zehnder interferometer configuration for the signal routing, and the inserted Bragg grating WGs between the DCs worked for wavelength selectivity. In principle, the input signal is split equally into two WGs by the first DC, which is then guided to two identical Bragg grating WGs. The resonant wavelength is reflected to the drop port and collected. The remaining transmitted signal will leave from the through port. New information at the resonant wavelength can also be added to the output signal through the add port. The versatility of the fs writing technique promises the capability of scalable DM fabrication with more modes and cores and mass production. As a result, practical ultrahigh capacity dense space-division DMs are expected.

Due to the intrinsic flexibility of 3D fabrication, WG-based fan-out devices were also achieved, with one end consisting of a 1D WG array and another end consisting of a 2D WG array, which can be used as multiplexers, demultiplexers (aforementioned), interposers to interconnect silicon photonic chips, as shown in Fig. 9(a), and astrophotonic interferometer integrated chips (discussed later).[78,79,121] For example, WGs in a glass interposer were reported to vertically couple light from an optical fiber to the silicon photonic chip.[122] An 84-channel interposer is also realized for coupling a multicore optical fiber and silicon photonics chips, as shown in Fig. 9(b).[120] However, misalignment causes significant loss in the packaging and stabilizing process. Further improvement in the packaging step for edge coupling of WGs to the silicon photonic chips is one of the biggest challenges. For the future, the optimized 3D WG fan-out devices may promise an attractive balancing of loss, mode matching, high channel density, low crosstalk, and multifunctional integration with other photonic components.

3.2 Topological Physics and Quantum Information Processing

In the past decades, photonic structures consisting of arrays of evanescently coupled WGs have emerged as a major representation of functionalized optical structures, in which the light propagates along the topological states or the light evolution exhibits intrinsic similarities with the quantum evolution of particle wave-functions. As a result, WG arrays have been proposed as a typical model system for researches and applications in topological physics and quantum information processing, such as formation of topological edge states, quantum mechanics emulation, and quantum computing. FLDW has been established as a standard method to construct 3D WGs into a variety of optical bulk materials, which enables the achievement of various innovative topological states, quantum physical concepts, and quantum information applications that are not feasible with other fabrication techniques.[2,14,123,124]

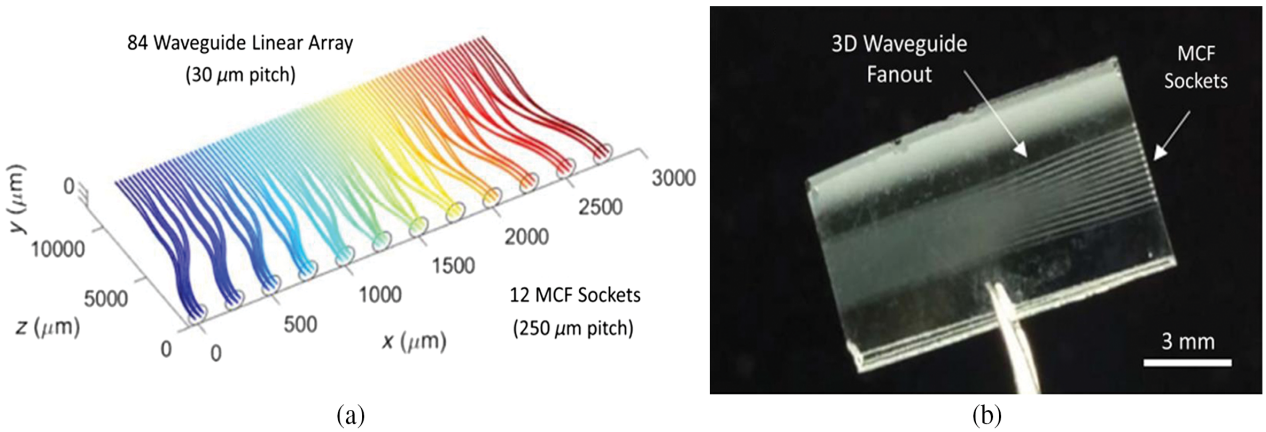

Fig. 9 (a) Schematic for an 84-channel interposer in glass, fanning out from a linear array (silica photonic chip at back) to 12 socket positions for multicore fibers (MCFs) packaging. (b) Optical image of the interposer in silica glass. Figures reproduced from Ref. 120.

Recently, the rise of topology has been one of the most recognizable trends in physics.[125,126] In the topological phases, protected travel is allowed along the edges of the structures in a robust way, giving rise to immunity against backscattering by defects. In particular, topological photonics have attained a burst of interest, as light waves can work as a platform for revealing the nontrivial bulk and edge topological states by carefully structuring photonic crystals.[125–127] WG photonic lattices are frequently adopted to build photonic topological structures for investigating the interplay of topology and interparticle interactions.[128–131] For example, the helicity of the evanescently coupled helical WG array would break the z-reversal symmetry in a honeycomb photonic lattice [Figs. 10(a) and 10(b)], which leads to formation of Floquet topological insulators, and topologically protected transport of visible light is observed on the lattice edges.[127] Photonic Floquet topological insulators in the fractal lattices were proposed theoretically, and robust travel along the outer and inner boundaries of the fractal lattices without scattering was possible.[133] Experimental realization of topological fractal insulators is promising. Solitons were also identified in an anomalous photonic Floquet topological insulator, which exhibited different behavior in that they executed cyclotron-like orbits.[134] For this purpose, the WG lattice was modulated periodically along the axis, and this resulted in a nonzero winding number with the optical Kerr effect-induced nonlinearity. The observation of topological solitons offers new prospective directions for the topological nonlinear optics, complementing other platforms. 2D honeycomb photonic lattices with broken inversion symmetry were also reported to exhibit photonic topological valley Hall edge states and four-dimensional (4D) quantum Hall.[132,135] Detuning the refractive index of the two honeycomb sublattices with varying average writing pulse energy of the fs laser generates an armchair [Fig. 10(c)] and zigzag edges [Fig. 10(d)] at their domains and a boron nitride-like band structure.[132] Consequently, the edge states appear along the domain walls between regions with opposite valley Chern numbers. The valley-Hall effect enables a new mechanism for realizing time-reversal-invariant photonic topological insulators. The fabricated time-reversal invariant WG photonic lattice could possess a zero-dimensional topological defect corner mode, which represents a new type of crystalline topological phase with a topologically protected energy lying at mid-gap and insensitive to disorder.[136]

In addition, sufficiently strong disorder can lead to the close of the topological bandgap, and the system becomes topologically trivial with all states being localized and all transport vanishing, complying with Anderson localization [Figs. 11(b) and 11(e)]; but, adding on-site disorders with random variations in the refractive index of WGs could drive the system from a trivial phase into a topological one, resulting in the emergence of topological Anderson insulators with protected edge states and quantized transport, as revealed in Figs. 11(c) and 11(f). In this case, the refractive index detuning was induced by adjusting the writing speed during the fabrication process, and a slower writing speed leads to a larger refractive index in WGs. The topological Anderson insulator was demonstrated experimentally with sufficiently detuned honeycomb photonic structure of helical WGs.[137] The light propagates only along the edge in the Floquet topological insulator [Fig. 11(d)]. When there is strong disorder, the system becomes topologically trivial, and there is

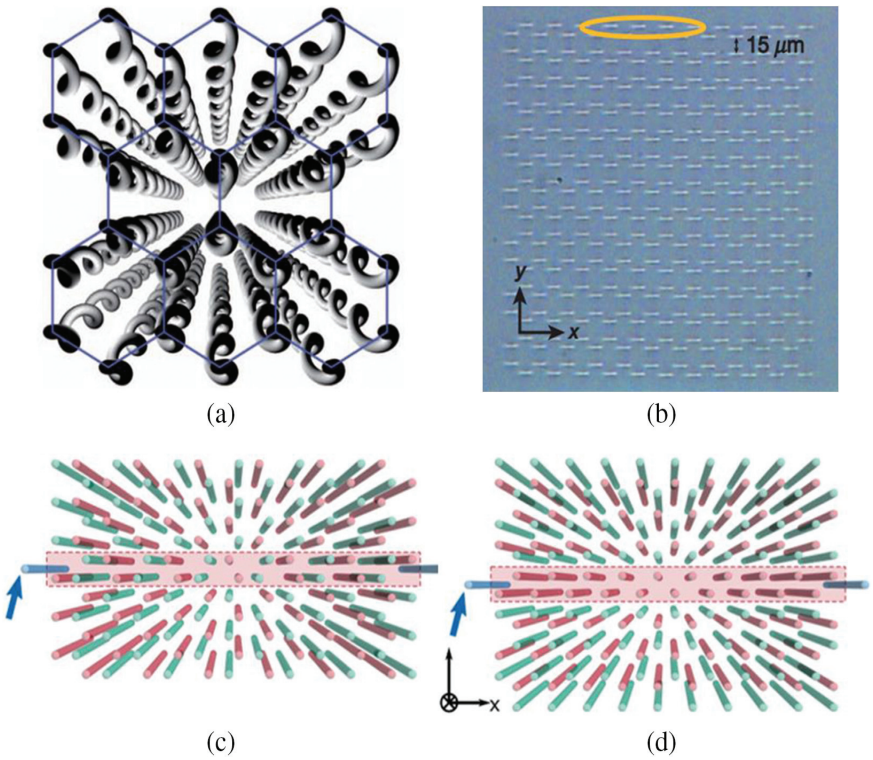

Fig. 10 (a) Sketch of the helical WGs with honeycomb geometry. (b) Optical image of the input facet of the photonic lattice. Figures reproduced from Ref. 127. Schematic diagram of honeycomb lattices with (c) armchair and (d) zigzag edge domain walls. Red and green WGs exhibit a different refractive index, and blue is the excitation WGs. Red-shaded regions are domain walls. Figures reproduced from Ref. 132.

no light along the edge [Fig. 11(e)]. After introduction of sufficiently strong on-site disorder, a photonic topological Anderson insulator is generated, which is confirmed by the presence of the mid-gap excitation-induced coupling to a topological edge state, as shown in Fig. 11(f). A photonic topological insulator in a synthetic dimension with topological edge states was demonstrated successfully.[138] In this case, a 2D WG array was produced with 1D in real space and one synthetic dimension in modal space. As a result, the propagation of the topologically protected edge state was observed at the edge of the synthetic space, but not at the spatial edges of the system. Waveguiding by artificial gauge fields was demonstrated using an array of evanescently coupled identical WGs. In this realization, WGs in the core and cladding follow distinct trajectories during propagation, and the artificial gauge field caused a shift of the dispersion relations from one another in the core and in the cladding in momentum-space.[139]

In contrast to the intricate set-ups with helical optical WGs [Fig. 10(a)], Fig. 12(b) indicates the presence of kagome-based corner states in the straight WGs, which exhibit a high degree of flexibility and control, operating in the visible light range.[140] Furthermore, topological boundary states in a single photon level were established in the WG-based quasicrystal, with the protected topological phases against the decoherence caused by diffusion and the noise.[141]

Quantum computing and quantum communication offer high efficiency in approaching problems of scientific and commercial interests, where processing an extremely large amount of data with fast speed is on-demand.[142,143] Photonic WG lattices give rise to an excellent model system allowing for simulating many quantum statistics for quantum information processing.[144,145] For example, boson sampling experiments against various alternative hypotheses were achieved on larger WG photonic chips fabricated by fs laser writing, which will be critical for boson sampling devices to conform the supremacy of quantum information processing over classical computers.[124] Anderson localization of a pair of noninteracting entangled photons was observed in an integrated quantum walk by employing

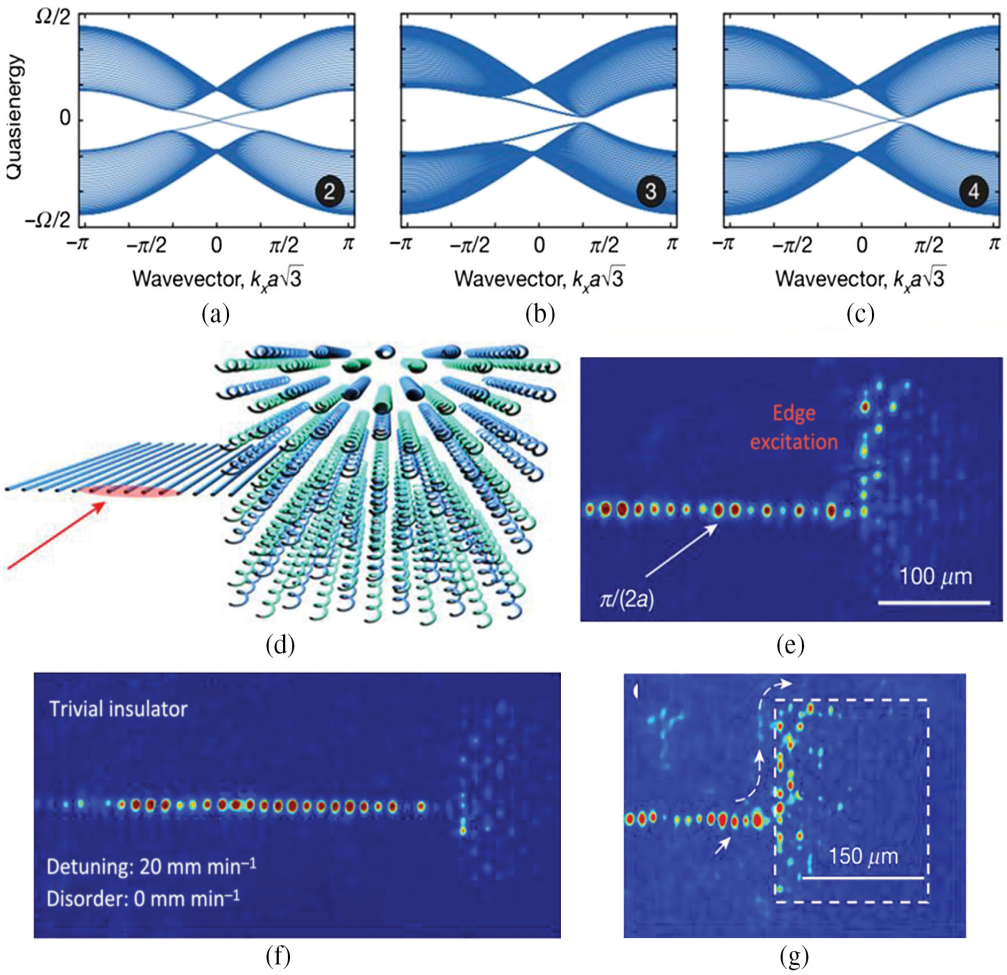

Fig. 11 (a) Topological bandgap for the Floquet topological insulator in a helical honeycomb lattice. (b) Breaking the parity structure symmetry by detuning the sublattices with formation of a trivial bandgap. (c) Forming topological Anderson insulator phase by suppressing the effect of the parity-symmetry breaking terms with sufficiently strong disorder. (d) Hybrid structure with a 1D straw and a 2D honeycomb helical WG lattice. The excited state was controlled by the "straw"—through which the modes of the system were selectively excited. Excitation light along the edge states in the (e) Floquet topological insulator, (f) trivial insulator, and (g) topological Anderson insulator. The input positions were indicated by the white arrows. Figures reproduced from Ref. 137.

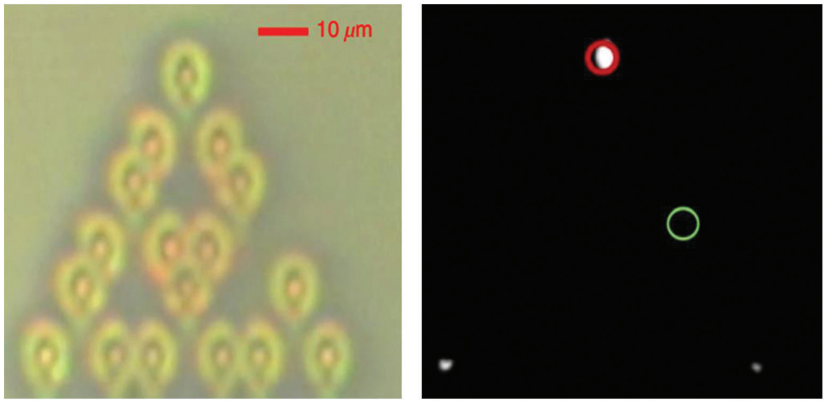

Fig. 12 (a) Triangular photonic lattices with a defect in a straight WG array. (b) Observation of the "fractionalized" corner states. Red circle: injection of 720-nm coherent light into the WG at the corner indicated. Green circle: missing WGs. Figures reproduced from Ref. 140.

polarization entanglement of photons to simulate the quantum statistics in the WG arrays.[146] Genuine many-particle quantum interference and high-visibility quantum interference of single-photon topological states were observed with the fs laser written integrated photonic circuit.[145,147] Two topological edge states were brought into proximity, interfering and undergoing a beamsplitter operation, and the visibility of the Hong–Ou–Mandel interference is as high as $93.1\% \pm 2.8\%$.[147] By integrating a quantum dot-based multiphoton source and a WG photonic chip in glass, scalable platforms exhibiting high-rate many-particle quantum interference were attained.[148] Jin and coauthors reported a 2D continuous-time quantum walk with a single photon on the 2D WG array and quantum fast hitting on hexagonal WG photonic structures with up to 160 nodes and a depth of 16 layers [Figs. 13(a)–13(c)].[149,151,152] They showed that the time for optimal quantum hitting increases linearly with network depth, as shown in Fig. 13(d). In comparison, Fig. 13(d) indicated that classical random walk was characterized by a quadratic relation. As a consequence, quantum speed-up to improve information processing is highly promising, which would initiate breakthroughs into real-life applications. Recently, a scalable photonic computer was developed to solve the subset sum problem. Photons were found to dissipate into the photonic circuits and search for solutions in parallel that result in an exponential superiority over even supercomputers in time consumption, as shown in Fig. 13(e).[150] Furthermore, quantum polarization entangled states could be well topologically protected on a photonic chip, and the linking of photonic topology and quantum information opens the door to topological enhancement in the quantum regime.[153]

Many other applications in the photonic topology and quantum information processing were also reported. For example, using the fs laser written 3D helical WG lattices, type-II Weyl points of light at optical frequencies were observed experimentally, confirmed by the presence of conical diffraction with the frequency corresponding to the Weyl point, and Fermi arc-like surface states.[154] A Weyl exceptional ring was also realized with the upper and lower bands of the topological transitions meeting at a ring, rather than a point, by observing the lack of conical diffraction at the topological transition when the system is non-Hermitian with quantized Berry charge.[155] A scalable approach for the operation of the fast Fourier transform algorithm was developed using 3D WG photonic integrated interferometers.[156] Unique complex photonic quantum structures, such as the fractal network, can be built with 3D fs laser writing, which provides platforms for the investigations about the properties of these structures.[20]

3.3 Astrophotonics

Application of fs laser writing WGs for astrophotonics was proposed in 2009 by Thamson et al., which relies on the capability of 3D designability with high WG density and precision position control.[77] Implementing various optical functions on a single integrated chip enables the reduction of the complexity of traditional astronomical instruments significantly. The typical glass systems for astrophotonics include silica glass, borosilicate glass, chalcogenide glass, and fluoride glass.[78,80,157–164] For the demonstration, integrated photonic lanterns were fabricated, which can couple multimode light to an array of single-mode WGs.[78] These integrated devices [named photonic dicers, as shown in Fig. 14(a)] are also developed as a diffraction limited pseudoslit and used to reformat multimode light into a 1D array for high-resolution diffraction limited spectroscopy.[158–160,165] In this case, multimode light collated from the telescope (I in Fig. 14) is spatially overlapped, and the input modal noise is converted into amplitude and phase changes along the slit, which minimizes the slit length as well as the number of detector pixels for light analysis in the spectrograph. However, during on-sky testing, wavelength-dependent loss was discovered, which manifests as modal noise and makes it difficult to extract and calibrate spectra properly.[160] By integrating WG S-bends, Y-splitters, and directional couplers on one chip, as shown in Fig. 14(b), nulling interferometers were written in gallium lanthanum sulfur (GLS) glass via multiscans of 5.1 MHz fs laser.[162] In this two-port interferometer, the Y-splitters direct half of the light into the outer photometric channels, with another half directed into the two inner channels for interferometric interaction. The starlight is nulled by destructive interference in the coupling region. The remaining light at the output of the coupler may originate from a possible exoplanet near the star. On-sky demonstration was also realized with the nulling interferometer integrated in the borosilicate glass [Fig. 14(c)].[80] In this chip, each WG encountered a Y-splitter with 33% of the light split off that was sent to separate

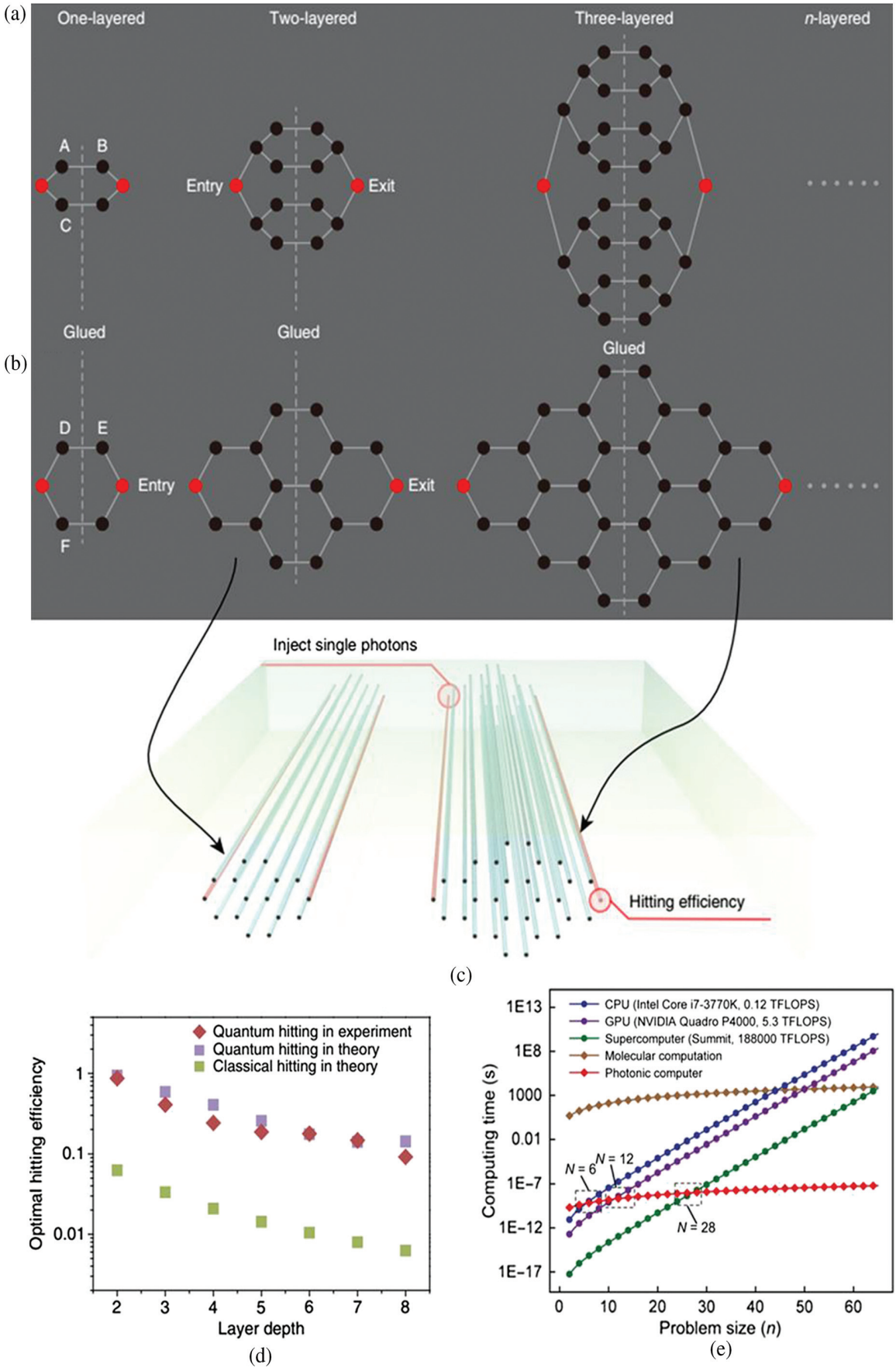

Fig. 13 Schematic diagrams of (a) a photonic-chip-based glued binary tree, (b) the proposed hexagonal WG photonic chips, and (c) the quantum fast hitting experiment on the WG photonic chips. (d) Optimal hitting efficiency for hexagonal photonic chips at different layer depths. Figure reproduced from Ref. 149. (e) The estimated computing time for the photonic computer and other competitors. Figure reproduced from Ref. 150.

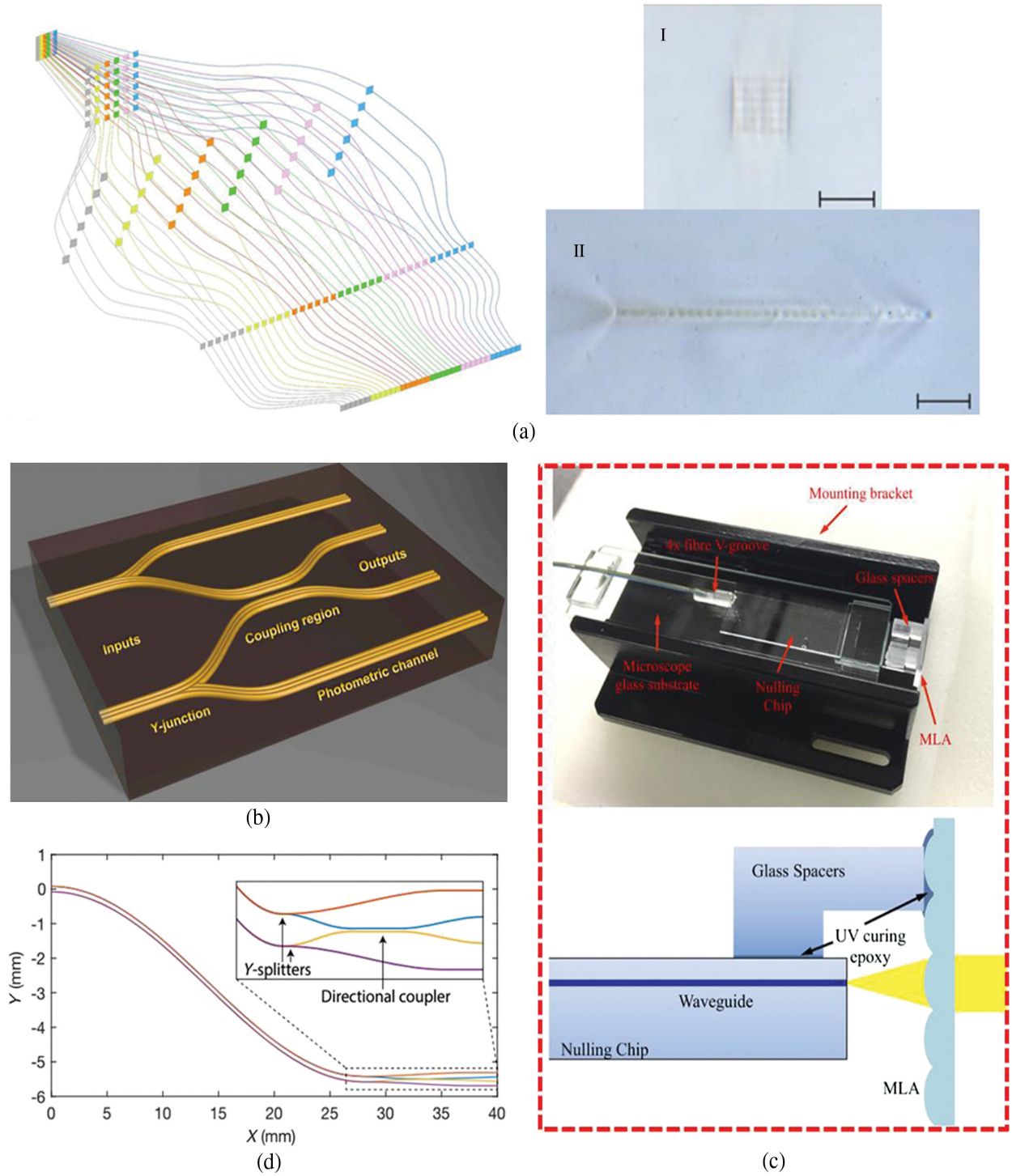

Fig. 14 (a) Schematic of a photonic dicer consisting of the 3D WG lattices combining photonic lantern and reformatting functions. I: multicode input end with 6 × 6 array WGs in 2D; II: pseudoslit output end with 36 array WGs in 1D. Figures reproduced from Ref. 159. (b) Schematic of an on-chip two-port nulling interferometer chip in GLS glass. Figure reproduced from Ref. 162. (c) The photonic assembly includes the nulling chip, the microlens array (MLA), and fiber V-groove. (d) The WG arrangement in the photonic chip. Figure reproduced from Ref. 80.

photometric outputs, as shown in Fig. 14(d). An evanescent directional coupler was created by bringing two input WGs together, and it produced a 50:50 splitting ratio at its two output ports. At the output face, the four WGs were butt-coupled and bonded to a fiber V-groove using UV curing adhesive and sent via single-mode fibers to the photodetectors. A periodic 3D array of WGs is also an excellent platform for light coupling and performing interferometry of the light that comes from telescopes.[157,161,166]

Though laboratory testing and on-sky testing have indicated that the integrated WGs written by fs lasers hold great potential in astrophotonics, there are still some issues hindering their wide application. For example, chalcogenide and fluoride glasses are fascinating alternatives for mid-infrared optic

detecting in the range from 2 to 5 μm, which are in high demand for high angular resolution astrophotonics. Unfortunately, the loss performance of WGs in these mid-infrared glasses (e.g., propagation loss >0.2 dB/cm in chalcogenide glass and >0.3 dB/cm in fluoride glass) is worse than that in silica and borosilicate glasses (that <0.2 dB/cm).[162–164] In fact, the propagation loss will increase in the 3D WG lattices. Second, it is also still difficult to fabricate 3D WG arrays with identical waveguiding performance in each one, especially when the WG number and depth variation are large. As a result, there is a difference between the outputs from different WGs. Beam shaping techniques as discussed above with critical controlling over the writing parameters should be important for writing identical WGs for reliable results and high reproductivity.[40] Third, an oil immersion objective with 1.25 NA is usually necessary for writing loss WGs in mid-infrared glass. As a result, special care should be taken to prevent oil boiling, and the writing depth is also limited. In addition, multiscan is usually adopted for the astrophotonic WG writing with a tunable size of cross-section. Modified alternative techniques (e.g., temperature gradient-assisted fs laser writing) may be helpful to fabricate optimal WGs under more mild conditions for astrophotonics. Fourth, although the laboratory testing implies that WGs in the mid-infrared glass will be a better choice than that in borosilicate glass for the astrophotonic interferometer, the on-sky demonstration has only been achieved in the latter glass until now. Further work is needed to reduce the loss (including propagation loss, coupling loss, and bend loss) of WGs in the mid-infrared glass for the astrophotonic interferometry.

4 Conclusions and Prospects

The far-reaching goal of on-chip multifunctional photonic circuits is to perform complex tasks within a single chip. Though great progress has been made in developing improved techniques and achieving device applications, besides the aforementioned issue, there exist some potential challenges for the practical applications of fs laser writing WGs. For example, the mechanism of RI change induced by fs lasers is still not fully understood. As a result, optimizing the loss performance usually relies on the experimental experience, and the reported optimized laser parameters are varied from different groups. Uncovering the process of fs laser–matter interaction and mechanisms of refractive index change is urgent and also essential to enhance reproductivity of high-performance WGs. Second, although writing low propagation loss (~0.2 dB/cm) WGs in borosilicate glass is realized with the high speed of 1 to 10 cm/s, the optimized scanning speed for achieving typically low propagation loss of ~0.3 dB/cm in silica glass is usually 50 to 200 μm/s, and the effective speed is even much smaller in the multiscan case. Considering that silica glass may be the most important substrate compatible with the modern semiconductor industry, enhancing the writing efficiency of WGs in silica glass will be significant. Third, due to the relatively small refractive index change induced by fs lasers, reducing the bend loss is still a great challenge, and the effective working radius with reasonable performance is generally greater than 20 mm. More work is expected to decrease the bend loss for fabricating 3D complex photonic circuits with high density and purchasing the full fabrication capability of FLDW. Next, combining writing structures (e.g., WGs and nanogratings) with chemical etching and metal deposition will be an important step to construct photonic integrated devices, which also provides the possibility of realizing thermo-optic or electro-optical control over device functionality.[4,167,168] Furthermore, for the photonic integrated circuit devices, reducing the coupling loss between the WGs and other optical components, such as optical fibers, is also important, which can be achieved by modulating the refractive index and size of WGs. For example, temperature gradient-assisted fs laser writing offers a promising technique to tune the size of WGs and reduce the coupling loss significantly.[67] Packaging techniques for integrating various optical components and a large number of WGs are in demand.[169] In addition, WGs also provide a new platform for applications not yet achieved. For example, WGs are fascinating alternatives for programmable photonic circuits. Typically, the 3D designability gives WGs written by fs lasers superiority compared with the traditional 2D planar dielectric WGs.[4] Recently, integrated WGs with low power reconfigurability and reduced crosstalk have been produced by FLDW, and thermal phase shifting has been demonstrated, which indicates a very simple method for dynamic reconfiguration of the WGs.[168,170] These pave the way toward programmable photonic circuits, thus opening exciting perspectives in integrated photonics. WGs supporting orbital angular momentum modes possess an additional degree of freedom for modern optics and allow for the fabrication of a photonic chip for high-capacity communication and high-dimensional quantum information processing.[171,172] Integrated quantum memory may be also achievable by writing WGs in the rare-earth-ion-doped glass.[44]

In conclusion, this review reveals the rapidly growing photonic circuits written by fs lasers in glass. With important achievements and progress including improved technologies, such as beam shaping, multiscan, thermal annealing, predefect engineering, and composition engineering, the mechanisms and the recent photonic device applications, such as optical couplers, network devices, topological physics, quantum information processing, and astrophotonics, have been reviewed in detail. Future challenges and research directions have also been proposed. It is reasonable to expect further progress and additional applications of WGs and FLDW for the benefit of all-photonics networks in the future.

Acknowledgments

This work was financially supported by the National Key R&D Program of China (2020YFB1805900), the National Natural Science Foundation of China (U20A20211, 51902286, 61775192, 61905215, and 51772270), Open Funds of the State Key Laboratory of High Field Laser Physics, Shanghai Institute of Optics and Fine Mechanics, Chinese Academy of Sciences, and the Fundamental Research Funds for the Central Universities. The authors declare no competing financial interest.

References

1. A. W. Elshaari et al., "Hybrid integrated quantum photonic circuits," *Nat. Photonics* **14**(5), 285–298 (2020).
2. M. Gräfe and A. Szameit, "Integrated photonic quantum walks," *J. Phys. B At. Mol. Opt. Phys.* **53**(7), 073001 (2020).
3. L. Li et al., "Integrated flexible chalcogenide glass photonic devices," *Nat. Photonics* **8**(8), 643–649 (2014).
4. W. Bogaerts et al., "Programmable photonic circuits," *Nature* **586**(7828), 207–216 (2020).

5. K. M. Davis et al., "Writing waveguides in glass with a femtosecond laser," *Opt. Lett.* **21**(21), 1729–1731 (1996).
6. E. N. Glezer et al., "Three-dimensional optical storage inside transparent materials," *Opt. Lett.* **21**(24), 2023–2035 (1996).
7. D. Z. Wei et al., "Experimental demonstration of a three-dimensional lithium niobate nonlinear photonic crystal," *Nat. Photonics* **12**(10), 596–600 (2018).
8. Z. Wang, D. Z. Tan, and J. R. Qiu, "Single-shot photon recording for three-dimensional memory with prospects of high capacity," *Opt. Lett.* **45**(22), 6274–6277 (2020).
9. K. J. Sugioka and Y. Cheng, "Ultrafast lasers—reliable tools for advanced materials processing," *Light Sci. Appl.* **3**(4), e149 (2014).
10. W. J. Yang, P. G. Kazansky, and Y. P. Svirko, "Non-reciprocal ultrafast laser writing," *Nat. Photonics* **2**(2), 99–104 (2008).
11. D. Z. Tan et al., "Single-pulse-induced ultra-fast spatial clustering of metal in glass: fine tunability and application," *Adv. Photonics Res.* (2000121) (2021).
12. Y. Hu et al., "Chiral assemblies of laser-printed micropillars directed by asymmetrical capillary force," *Adv. Mater.* **32**(31), 2002356 (2020).
13. S. Jiang et al., "Multifunctional Janus microplates arrays actuated by magnetic fields for water/light switches and bio-inspired assimilatory coloration," *Adv. Mater.* **31**(15), 1807507 (2019).
14. T. Meany et al., "Laser written circuits for quantum photonics," *Laser Photonics Rev.* **9**(4), 363–384 (2015).
15. D. Z. Tan et al., "Femtosecond laser induced phenomena in transparent solid materials: fundamentals and applications," *Prog. Mater. Sci.* **76**, 154–228 (2016).
16. K. Miura et al., "Photowritten optical waveguides in various glasses with ultrashort pulse laser," *Appl. Phys. Lett.* **71**(23), 3329–3331 (1997).
17. S. M. Eaton, H. Zhang, and P. R. Herman, "Heat accumulation effects in femtosecond laser written waveguides with variable repetition rate," *Opt. Express* **13**(12), 4708–4716 (2005).
18. A. Szameit and S. Nolte, "Discrete optics in femtosecond-laser written photonic structures," *J. Phys. B At. Mol. Opt. Phys.* **43**(16), 163001 (2010).
19. R. G. H. van Uden et al., "Ultra-high-density spatial division multiplexing with a few-mode multicore fibre," *Nat. Photonics* **8**(11), 865–870 (2014).
20. X. Y. Xu et al., "Shining light on quantum transport in fractal networks," arXiv:2005.13385v1 (2020).
21. A. Couairona and A. Mysyrowicz, "Femtosecond filamentation in transparent media," *Phys. Rep.* **441**(2-4), 47–189 (2007).
22. Q. Sun et al., "Effect of spherical aberration on the propagation of a tightly focused femtosecond laser pulse inside fused silica," *J. Opt. A Pure Appl. Opt.* **7**(11), 655–659 (2005).
23. Y. Cheng et al., "Control of the cross-sectional shape of a hollow microchannel embedded in photostructurable glass by use of a femtosecond laser," *Opt. Lett.* **28**(1), 55–57 (2003).
24. N. Bisch et al., "Adaptive optics aberration correction for deep direct laser written waveguides in the heating regime," *Appl. Phys. A* **125**(5), 364 (2019).
25. M. Ams et al., "Slit beam shaping method for femtosecond laser direct-write fabrication of symmetric waveguides in bulk glasses," *Opt. Express* **13**(15), 5676–5681 (2005).
26. V. D. Blanco et al., "Deep subsurface waveguides with circular cross section produced by femtosecond laser writing," *Appl. Phys. Lett.* **91**(5), 051104 (2007).
27. D. Liu et al., "Influence of focusing depth on the microfabrication of waveguides inside silica glass by femtosecond laser direct writing," *Appl. Phys. A* **84**(3), 257–260 (2006).
28. S. Gross and M. J. Withford, "Ultrafast-laser-inscribed 3D integrated photonics: challenges and emerging applications," *Nanophotonics* **4**(3), 332–335 (2015).
29. G. Cerullo et al., "Femtosecond micromachining of symmetric waveguides at 1.5 μm by astigmatic beam focusing," *Opt. Lett.* **27**(21), 1938–1940 (2002).
30. F. He et al., "Fabrication of microfluidic channels with a circular cross section using spatiotemporally focused femtosecond laser pulses," *Opt. Lett.* **35**(7), 1106–1108 (2010).
31. R. Osellame et al., "Femtosecond writing of active optical waveguides with astigmatically shaped beams," *J. Opt. Soc. Am. B* **20**(7), 1559–1567 (2003).
32. P. R. Varona et al., "Slit beam shaping technique for femtosecond laser inscription of enhanced plane-by-plane FBGs," *J. Lightwave Technol.* **38**(16), 4526–4532 (2020).
33. V. D. Michele et al., "Near-IR- and UV-femtosecond laser waveguide inscription in silica glasses," *Opt. Mater. Express* **9**(12), 4624–4633 (2019).
34. M. Royon et al., "X-ray preconditioning for enhancing refractive index contrast in femtosecond laser photoinscription of embedded waveguides in pure silica," *Opt. Mater. Express* **9**(1), 65–74 (2019).
35. K. Mishchik et al., "Photoinscription domains for ultrafast laser writing of refractive index changes in BK7 borosilicate crown optical glass," *Opt. Mater. Express* **3**(1), 67–85 (2013).
36. G. D. Marshall et al., "Directly written monolithic waveguide laser incorporating a distributed feedback waveguide-Bragg grating," *Opt. Lett.* **33**(9), 956–958 (2008).
37. D. Marshall, M. Ams, and M. J. Withford, "Direct laser written waveguide–Bragg gratings in bulk fused silica Graham," *Opt. Lett.* **31**(18), 2690–2692 (2006).
38. A. R. De la Cruz et al., "Modeling of astigmatic-elliptical beam shaping during fs-laser waveguide writing including beam truncation and diffraction effects," *Appl. Phys. A* **104**(2), 687–693 (2011).
39. Y. Wang et al., "Quantum topological boundary states in quasicrystals," *Adv. Mater.* **31**(49), 1905624 (2019).
40. R. J. Ren et al., "Identical quantum sources integrated on a single silica chip," arXiv:2005.12918 (2020).
41. J. P. Brub and R. Valle, "Femtosecond laser direct inscription of surface skimming waveguides in bulk glass," *Opt. Lett.* **41**(13), 3074–3077 (2016).
42. J. P. Bérubé et al., "Femtosecond laser direct inscription of mid-IR transmitting waveguides in BGG glasses," *Opt. Mater. Express* **7**(9), 3124–3135 (2017).
43. C. Y. Wang, J. Gao, and X. M. Jin, "On-chip rotated polarization directional coupler fabricated by femtosecond laser direct writing," *Opt. Lett.* **44**(1), 102–105 (2019).
44. C. Liu et al., "On-demand quantum storage of photonic qubits in an on-chip waveguide," *Phys. Rev. Lett.* **125**(26), 260504 (2020).
45. R. Osellame et al., "Lasing in femtosecond laser written optical waveguides," *Appl. Phys. A* **93**(1), 17–26 (2008).
46. Z. H. Wang et al., "Interferometric characterization of pulse front tilt of spatiotemporally focused femtosecond laser pulses," *Opt. Express* **22**(21), 26328–26337 (2014).
47. B. Sun et al., "Four-dimensional light shaping: manipulating ultrafast spatiotemporal foci in space and time," *Light Sci. Appl.* **7**(1), 17117 (2018).
48. A. Patel et al., "Non-paraxial polarization spatio-temporal coupling in ultrafast laser material processing," *Laser Photonics Rev.* **11**(3), 1600290 (2017).
49. R. Kammel et al., "Simultaneous spatial and temporal focusing: a route towards confined nonlinear materials processing," *Proc. SPIE* **9736**, 97360T (2016).
50. P. Wang et al., "Aberration-insensitive three-dimensional micromachining in glass with spatiotemporally shaped femtosecond laser pulses," *Opt. Lett.* **43**(15), 3485–3488 (2018).
51. F. He et al., "Independent control of aspect ratios in the axial and lateral cross sections of a focal spot for three-dimensional femtosecond laser micromachining," *New J. Phys.* **13**(8), 083014 (2011).
52. E. Block et al., "Integrated single grating compressor for variable pulse front tilt in simultaneously spatially and temporally focused systems," *Opt. Lett.* **39**(24), 6915–6918 (2014).

53. J. Squier et al., "High average power Yb:CaF femtosecond amplifier with integrated simultaneous spatial and temporal focusing for laser material processing," *Appl. Phys. A* **114**(1), 209–214 (2014)
54. D. N. Vitek et al., "Temporally focused femtosecond laser pulses for low numerical aperture micromachining through optically transparent materials," *Opt. Express* **18**(17), 18086–18094 (2010).
55. G. Zhu et al., "Simultaneous spatial and temporal focusing of femtosecond pulses," *Opt. Express* **13**(6), 2153–2159 (2005).
56. B. Leshem et al., "When can temporally focused excitation be axially shifted by dispersion?" *Opt. Express* **22**(6), 7087–7098 (2014).
57. R. Kammel et al., "Enhancing precision in fs-laser material processing by simultaneous spatial and temporal focusing," *Light Sci. Appl.* **3**(5), e169 (2014).
58. P. S. Salter et al., "Adaptive slit beam shaping for direct laser written waveguides," *Opt. Lett.* **37**(4), 470–472 (2012).
59. L. Huang et al., "Aberration correction for direct laser written waveguides in a transverse geometry," *Opt. Express* **24**(10), 10565–10574 (2016).
60. P. S. Salter et al., "Adaptive optics in laser processing," *Light Sci. Appl.* **8**(1), 110 (2019).
61. M. Sakakura et al., "Fabrication of three-dimensional 1 × 4 splitter waveguides inside a glass substrate with spatially phase modulated laser beam," *Opt. Express* **18**(12), 12136–12143 (2010).
62. M. Pospiech et al., "Single-sweep laser writing of 3D-waveguide devices," *Opt. Express* **18**(7), 6994–7001 (2010).
63. C. Mauclair et al., "Dynamic ultrafast laser spatial tailoring for parallel micromachining of photonic devices in transparent materials," *Opt. Express* **17**(5), 3531–3542 (2009).
64. P. S. Salter and M. J. Booth, "Dynamic optical methods for direct laser written waveguides," *Proc. SPIE* **8613**, 86130A (2013).
65. Y. Nasu, M. Kohtoku, and Y. Hibino, "Low-loss waveguides written with a femtosecond laser for flexible interconnection in a planar light-wave circuit," *Opt. Lett.* **30**(7), 723–725 (2005).
66. R. Keil et al., "Hybrid waveguide-bulk multi-path interferometer with switchable amplitude and phase," *APL Photonics* **1**(8), 081302 (2016).
67. D. Z. Tan et al., "Fabricating low loss waveguides over a large depth in glass by temperature gradient assisted femtosecond laser writing," *Opt. Lett.* **45**(14), 3941–3944 (2020).
68. S. Gross et al., "Three-dimensional ultra-broadband integrated tapered mode multiplexers," *Laser Photonics Rev.* **8**(5), L81–L85 (2014).
69. R. Mary, D. Choudhury, and A. K. Kar, "Applications of fiber lasers for the development of compact photonic devices," *IEEE J. Sel. Top. Quantum. Electron* **20**(5), 72–84 (2014).
70. M. D. Mackenzie et al., "GLS and GLSSe ultrafast laser inscribed waveguides for mid-IR supercontinuum generation," *Opt. Mater. Express* **9**(2), 643–651 (2019).
71. Z. M. Liu et al., "Suppression of bend loss in writing of three-dimensional optical waveguides with femtosecond laser pulses," *Sci. China-Phys. Mech. Astron.* **61**(7), 070322 (2018).
72. R. Heilmann et al., "Tapering of femtosecond laser-written waveguides," *Appl. Opt.* **57**(3), 377–381 (2018).
73. N. D. Psaila et al., "Femtosecond laser inscription of optical waveguides in Bismuth ion doped glass," *Opt. Express* **14**(22), 10452–10459 (2006).
74. H. L. Butcher et al., "Ultrafast laser-inscribed mid-infrared evanescent field directional couplers in GeAsSe chalcogenide glass," *OSA Continuum.* **1**(1), 221–228 (2018).
75. L. Helen et al., "Demonstration and characterization of ultrafast laser-inscribed mid-infrared waveguides in chalcogenide glass IG2," *Opt. Express* **26**(8), 10930–10943 (2018).
76. G. Demetriou et al., "Nonlinear refractive index of ultrafast laser inscribed waveguides in gallium lanthanum sulphide," *Appl. Opt.* **56**(19), 5407–5411 (2017).
77. R. R. Thomson, A. K. Kar, and J. Allington-Smith, "Ultrafast laser inscription: an enabling technology for astrophotonics," *Opt. Express* **17**(3), 1963–1969 (2009).
78. R. R. Thomson et al., "Ultrafast laser inscription of an integrated photonic lantern," *Opt. Express* **19**(6), 5698–5705 (2011).
79. G. Douglass et al., "Femtosecond laser written arrayed waveguide gratings with integrated photonic lanterns," *Opt. Express* **26**(2), 1497–1505 (2018).
80. B. R. M. Norris et al., "First on-sky demonstration of an integrated-photonic nulling interferometer: the GLINT instrument," *Mon. Not. R. Astron. Soc.* **491**(3), 4180–4193 (2020).
81. L. A. Fernandes et al., "Stress induced birefringence tuning in femtosecond laser fabricated waveguides in fused silica," *Opt. Express* **20**(22), 24103–24114 (2012).
82. G. Corrielli et al., "Symmetric polarization-insensitive directional couplers fabricated by femtosecond laser writing," *Opt. Express* **26**(12), 15101–15109 (2018).
83. Z. M. Liu et al., "Fabrication of an optical waveguide-mode-field compressor in glass using a femtosecond laser," *Materials* **11**(10), 1926 (2018).
84. M. Sakakura et al., "Thermal and shock induced modification inside a silica glass by focused femtosecond laser pulse," *J. Appl. Phys.* **109**(2), 023503 (2011).
85. V. R. Bhardwaj et al., "Stress in femtosecond-laser-written waveguides in fused silica," *Opt. Lett.* **29**(12), 1312–1314 (2004).
86. A. Arriola et al., "Low bend loss waveguides enable compact, efficient 3D photonic chips," *Opt. Express* **21**(3), 2978–2986 (2013).
87. O. S. Narayanaswamy, "Annealing of glass," *Glass Sci. Technol.* **3**, 275–318 (1986).
88. H. E. Hagy, "Fine annealing of optical glass for low residual stress and refractive index homogeneity," *Appl. Opt.* **7**(5), 833–835 (1968).
89. N. Ollier et al., "Relaxation study of pre-densified silica glasses under 2.5 MeV electron irradiation," *Sci. Rep.* **9**(1), 1227 (2019).
90. J. J. Witcher et al., "Thermal annealing of femtosecond laser written structures in silica glass," *Opt. Mater. Express* **3**(4), 502–510 (2013).
91. B. H. Babu et al., "Systematic control of optical features in aluminosilicate glass waveguides using direct femtosecond laser writing," *Opt. Mater.* **72**, 501–507 (2017).
92. P. Dekker et al., "Annealing dynamics of waveguide Bragg gratings: evidence of femtosecond laser induced colour centres," *Opt. Express* **18**(4), 3274–3283 (2010).
93. J. D. Musgraves, K. Richardson, and H. Jain, "Laser-induced structural modification, its mechanisms, and applications in glassy optical materials," *Opt. Mater. Express* **1**(5), 921–935 (2011).
94. X. W. Wang et al., "Analysis of defects patterned by femtosecond pulses inside KBr and SiO_2 glass," *Appl. Phys. A* **122**(3), 194 (2016).
95. T. T. Fernandez et al., "Ion migration assisted inscription of high refractive index contrast waveguides by femtosecond laser pulses in phosphate glass," *Opt. Lett.* **38**(24), 5248–5251 (2013).
96. T. T. Fernandez et al., "Revisiting ultrafast laser inscribed waveguide formation in commercial alkali-free borosilicate glasses," *Opt. Express* **28**(7), 10153–10164 (2020).
97. P. Moreno-Zarate et al., "Role of the La/K compositional ratio in the properties of waveguides written by fs-laser induced element redistribution in phosphate-based glasses," *Materials* **13**(6), 1275 (2020).
98. T. T. Fernandez et al., "Bespoke photonic devices using ultrafast laser driven ion migration in glasses," *Prog. Mater. Sci.* **94**, 68–113 (2018).
99. M. Macias-Montero et al., "Waveguide tapers fabrication by femtosecond laser induced element redistribution in glass," *J. Lightwave Technol.* **38**(23), 6578–6583 (2020).

100. L. Bressel et al., "Femtosecond laser induced density changes in GeO_2 and SiO_2 glasses: fictive temperature effect," *Opt. Mater. Express* **1**(4), 605–613 (2011).
101. J. M. Oliveira et al., "Waveguides written in silver-doped tellurite glasses," *Opt. Mater.* **101**, 109767 (2020).
102. N. Riesen et al., "Femtosecond direct-written integrated mode couplers," *Opt. Express* **22**(24), 29855–29861 (2014).
103. Y. Duan et al., "Time dependent study of femtosecond laser written waveguide lasers in Yb-doped silicate and phosphate glass," *Opt. Mater. Express* **5**(2), 416–422 (2015).
104. K. Minoshima et al., "Fabrication of coupled mode photonic devices in glass by nonlinear femtosecond laser materials processing," *Opt. Express* **10**(15), 645–652 (2002).
105. K. Suzuki et al., "Characterization of symmetric $[3 \times 3]$ directional couplers fabricated by direct writing with a femtosecond laser oscillator," *Opt. Express* **14**(6), 2335–2343 (2006).
106. S. Gross et al., "Ultrafast laser-written sub-components for space division multiplexing," in *Opt. Fiber Commun. Conf.*, OSA, p. W1A.1 (2020).
107. J. Lapointe et al., "Making smart phones smarter with photonics," *Opt. Express* **22**(13), 15473–15483 (2014).
108. R. Heilmann et al., "Arbitrary photonic wave plate operations on chip: realizing Hadamard, Pauli-X and rotation gates for polarisation qubits," *Sci. Rep.* **4**(1), 4118 (2015).
109. L. A. Fernandes et al., "Femtosecond laser fabrication of birefringent directional couplers as polarisation beam splitters in fused silica," *Opt. Express* **19**(13), 11992–11999 (2011).
110. W. J. Yang et al., "Low loss photonic components in high index bismuth borate glass by femtosecond laser direct writing," *Opt. Express* **16**(20), 16215–16226 (2008).
111. I. Pitsios et al., "Geometrically controlled polarisation processing in femtosecond-laser-written photonic circuits," *Sci. Rep.* **7**(1), 11342 (2017).
112. G. Corrielli et al., "Rotated waveplates in integrated waveguide optics," *Nat. Commun.* **5**(1), 4249 (2014).
113. L. Sansoni et al., "Polarization entangled state measurement on a chip," *Phys. Rev. Lett.* **105**(20), 200503 (2010).
114. R. S. Luís et al., "1.2 Pb/s throughput transmission using a 160 μm cladding, 4-core, 3-mode fiber," *J. Lightwave Technol.* **37**(8), 1798–1804 (2019).
115. V. A. Amorim et al., "Monolithic add–drop multiplexers in fused silica fabricated by femtosecond laser direct writing," *J. Lightwave Technol.* **35**(17), 3615–3621 (2017).
116. I. V. Dyakonov et al., "Laser-written polarizing directional coupler with reduced interaction length," *Opt. Lett.* **42**(20), 4231–4234 (2017).
117. T. Mizuno et al., "Dense space-division multiplexed transmission systems using multi-core and multi-mode fiber," *J. Lightwave Technol.* **34**(2), 582–592 (2016).
118. N. Riesen et al., "Monolithic mode-selective few-mode multicore fiber multiplexers," *Sci. Rep.* **7**(1), 6971 (2017).
119. B. Guan et al., "Free-space coherent optical communication with orbital angular, momentum multiplexing/demultiplexing using a hybrid 3D photonic integrated circuit," *Opt. Express* **22**(1), 145–156 (2014).
120. G. Djogo et al., "Femtosecond laser additive and subtractive micro-processing: enabling a high-channel-density silica interposer for multicore fibre to silicon-photonic packaging," *Int. J. Extreme. Manuf.* **1**(4), 045002 (2019).
121. R. R. Thomson et al., "Ultrafast-laser inscription of a three dimensional fan-out device for multicore fiber coupling applications," *Opt. Express* **15**(18), 11691–11697 (2007).
122. M. Mirshafiei et al., "Glass interposer for short reach optical connectivity," *Opt. Express* **24**(11), 12375–12384 (2016).
123. C. Mikael et al., "Photonic Floquet topological insulators," *Nature* **496**(7444), 196–200 (2013).
124. N. Spagnolo, "Experimental validation of photonic boson sampling," *Nat. Photonics* **8**(8), 615–620 (2014).
125. L. Lu, J. D. Joannopoulos, and M. Soljačić, "Topological photonics," *Nat. Photonics* **8**(11), 821–829 (2014).
126. M. Kim, Z. Jacob, and J. Rho, "Recent advances in 2D, 3D and higher-order topological photonics," *Light Sci. Appl.* **9**(1), 130 (2020).
127. M. C. Rechtsman et al., "Photonic Floquet topological insulators," *Nature* **496**(7444), 196–200 (2013).
128. M. Kremer et al., "A square-root topological insulator with non-quantized indices realized with photonic Aharonov-Bohm cages," *Nat. Commun.* **11**(1), 907 (2020).
129. L. J. Maczewsky et al., "Fermionic time-reversal symmetry in a photonic topological insulator," *Nat. Mater.* **19**(8), 855–860 (2020).
130. S. Weimann et al., "Topologically protected bound states in photonic parity–time-symmetric crystals," *Nat. Mater.* **16**(4), 433–438 (2017).
131. G. G. Pyrialakos et al., "Symmetry-controlled edge states in the type-II phase of Dirac photonic lattices," *Nat. Commun.* **11**(1), 2074 (2020).
132. J. Noh et al., "Observation of photonic topological valley Hall edge states," *Phys. Rev. Lett.* **120**(6), 063902 (2018).
133. Z. J. Yang et al., "Photonic Floquet topological insulators in a fractal lattice," *Light Sci. Appl.* **9**(1), 128 (2020).
134. S. Mukherjee and M. C. Rechtsman, "Observation of Floquet solitons in a topological bandgap," *Science* **368**(6493), 856–859 (2020).
135. O. Zilberberg et al., "Photonic topological boundary pumping as a probe of 4D quantum Hall physics," *Nature* **553**(7686), 59–62 (2018).
136. J. Noh et al., "Topological protection of photonic mid-gap defect modes," *Nat. Photonics* **12**(7), 408–415 (2018).
137. S. Stützer et al., "Photonic topological Anderson insulators," *Nature* **560**(7719), 461–465 (2018).
138. E. Lustig et al., "Photonic topological insulator in synthetic dimensions," *Nature*, **567**(7748), 356–360 (2019).
139. Y. Lumer et al., "Light guiding by artificial gauge fields," *Nat. Photonics* **13**(5), 339–345 (2019).
140. A. E. Hassan et al., "Corner states of light in photonic waveguides," *Nat. Photonics* **13**(10), 697–700 (2019).
141. Y. Wang et al., "Quantum topological boundary states in quasicrystals," *Adv. Mater.* **31**(49), 1905624 (2019).
142. J. W. Wang et al., "Integrated photonic quantum technologies," *Nat. Photonics* **14**(5), 273–284 (2020).
143. D. J. Brod et al., "Photonic implementation of boson sampling: a review," *Adv. Photonics* **1**(3), 034001 (2019).
144. N. Spagnolo et al., "Three-photon bosonic coalescence in an integrated tritter," *Nat. Commun.* **4**(1), 1606 (2013).
145. T. Giordani et al., "Experimental statistical signature of many-body quantum interference," *Nat. Photonics* **12**(3), 173–178 (2018).
146. A. Crespi et al., "Anderson localization of entangled photons in an integrated quantum walk," *Nat. Photonics* **7**(4), 322–328 (2013).
147. J. L. Tambasco et al., "Quantum interference of topological states of light," *Sci. Adv.* **4**(9), eaat3187 (2018).
148. C. Antón et al., "Interfacing scalable photonic platforms: solid-state based multi-photon interference in a reconfigurable glass chip," *Optica* **6**(12), 1471–1477 (2019).
149. H. Tang et al., "Experimental quantum fast hitting on hexagonal graphs," *Nat. Photonics* **12**(12), 754–758 (2018).
150. X. Y. Xu et al., "A scalable photonic computer solving the subset sum problem," *Sci. Adv.* **6**(5), eaay5853 (2020).
151. H. Tang et al., "Experimental two-dimensional quantum walk on a photonic chip," *Sci. Adv.* **4**(5), eaat3174 (2018).
152. Z. Y. Shi et al., "Quantum fast hitting on glued trees mapped on a photonic chip," *Optica* **7**(6), 613–618 (2020).
153. Y. Wang et al., "Topologically protected quantum entanglement," arXiv:1903.03015v1 (2019).

154. J. Noh et al., "Experimental observation of optical Weyl points and Fermi arc-like surface states," *Nat. Phys.* **13**(6), 611–617 (2017).
155. A. Cerjan et al., "Experimental realization of a Weyl exceptional ring," *Nat. Photonics* **13**(9), 623–628 (2019).
156. A. Crespi et al., "Suppression law of quantum states in a 3D photonic fast Fourier transform chip," *Nat. Commun.* **7**(1), 10469 (2016).
157. A. Saviauk et al., "3D-integrated optics component for astronomical spectro-interferometry," *Appl. Opt.* **52**(19), 4556–4565 (2013).
158. D. G. MacLachlan et al., "Development of integrated mode reformatting components for diffraction-limited spectroscopy," *Opt. Lett.* **41**(1), 76–79 (2016).
159. R. J. Harris et al., "Photonic spatial reformatting of stellar light for diffraction-limited spectroscopy," *Mon. Not. R. Astron. Soc.* **450**(1), 428–434 (2015).
160. N. Cvetojevic et al., "Modal noise in an integrated photonic lantern fed diffraction-limited spectrograph," *Opt. Express* **25**(21), 25546–25565 (2017).
161. R. Diener et al., "Towards 3D-photonic, multi-telescope beam combiners for midinfrared astrointerferometry," *Opt. Express* **25**(16), 19262–19274 (2017).
162. T. Gretzinger et al., "Towards a photonic mid-infrared nulling interferometer in chalcogenide glass," *Opt. Express* **27**(6), 8626–8638 (2019).
163. J. Tepper et al., "Ultrafast laser inscription in ZBLAN integrated optics chips for mid-IR beam combination in astronomical interferometry," *Opt. Express* **25**(17), 20642–20653 (2017).
164. A. Arriola et al., "Mid-infrared astrophotonics: study of ultrafast laser induced index change in compatible materials," *Opt. Mater. Express* **7**(3), 698–711 (2017).
165. N. Jovanovic et al., "Integrated photonic building blocks for next-generation astronomical instrumentation I: the multimode waveguide," *Opt. Express* **20**(15), 17029–17043 (2012).
166. J. Tepper et al., "Integrated optics prototype beam combiner for long baseline interferometry in the L and M bands," *Astron. Astrophys.* **602**, A66 (2017).
167. N. Psaila, "3D laser direct writing for advanced photonic integration," *Proc. SPIE* **10924**, 109240U (2019).
168. F. Ceccarelli et al., "Low power reconfigurability and reduced crosstalk in integrated photonic circuits fabricated by femtosecond laser micromachining," *Laser Photonics Rev.* **14**(10), 2000024 (2020).
169. E. Perez et al., "Automated on-axis direct laser writing of coupling elements for photonic chips," *Opt. Express* **28**(26), 39340–39353 (2020).
170. F. Ceccarelli et al., "Thermal phase shifters for femtosecond laser written photonic integrated circuits," *J. Lightwave Technol.* **37**(17), 4275–4281 (2019).
171. Y. Chen et al., "Mapping twisted light into and out of a photonic chip," *Phys. Rev. Lett.* **121**(23), 233602 (2018)
172. Y. Chen et al., "Vector vortex beam emitter embedded in a photonic chip," *Phys. Rev. Lett.* **124**(15), 153601 (2020).

Dezhi Tan is an associate professor in the College of Optical Science and Engineering at Zhejiang University, China. He received his BS and PhD degrees in materials science and engineering from Zhejiang University in 2009 and 2014, respectively. He worked as a postdoc at Polytechnique Montreal (Canada), the JSPS fellow in Kyoto University (Japan), and a research professor in the Institute for Basic Science (Korea). His current research interest is focused on the study of ultrafast laser–matter interaction and the fabrication of micro/nanostructures and devices in transparent media.

Jianrong Qiu is a professor in the College of Optical Science and Engineering at Zhejiang University, China. He specializes in laser–matter interaction and optical materials. He is the chair professor of the Cheung Kong Scholars Program, and a fellow of the Optical Society of America (OSA), the American Ceramic Society (ACS), the International Glass Commission, and the Chinese Ceramics Society. He is also the vice chairman of Photoelectronic Glasses Branch and an associate editor (or international advisory board member) of *Asian J. Ceram Soc.*, *Int. J. Appl. Glass Sci.*, and *J. Non-Cryst. Solids*.

Biographies of the other authors are not available.

https://doi.org/10.1186/s43074-023-00101-8

PhotoniX

REVIEW

Open Access

Ultrafast laser-induced self-organized nanostructuring in transparent dielectrics: fundamentals and applications

Bo Zhang[1*], Zhuo Wang[1], Dezhi Tan[2] and Jiangrong Qiu[1*]

*Correspondence: zhangbob@zju.edu.cn; qjr@zju.edu.cn

[1] State Key Laboratory of Modern Optical Instrumentation, College of Optical Science and Engineering, Zhejiang University, Hangzhou, China
[2] Zhejiang Lab, Hangzhou, China

Abstract

Inscribing functional micro-nano-structures in transparent dielectrics enables constructing all-inorganic photonic devices with excellent integration, robustness, and durability, but remains a great challenge for conventional fabrication techniques. Recently, ultrafast laser-induced self-organization engineering has emerged as a promising rapid prototyping platform that opens up facile and universal approaches for constructing various advanced nanophotonic elements and attracted tremendous attention all over the world. This paper summarizes the history and important milestones in the development of ultrafast laser-induced self-organized nanostructuring (ULSN) in transparent dielectrics and reviews recent research progresses by introducing newly reported physical phenomena, theoretical mechanisms/models, regulation techniques, and engineering applications, where representative works related to next-generation light manipulation, data storage, optical detecting are discussed in detail. This paper also presents an outlook on the challenges and future trends of ULSN, and important issues merit further exploration.

Keywords: Ultrafast laser, Self-organization, Nanostructuring, Transparent dielectrics

Introduction

As Moore's law going close to its limit, integrated photonics aiming for on-chip functionalization is fast-rising and has brought up a boom in searching for next-generation optoelectronic substrate materials. Especially, all-inorganic transparent dielectrics such as various glasses and crystals have been established as excellent modular platforms for light emission [1–5], transmission [6–9], and modulation [10–15]. Predictably, next-generation integrated photonic elements and systems will largely rely on various three-dimensional (3D) micro-nano structures inscribed in transparent dielectrics [16–22], such as optical waveguides [23–26], optical couplers [27–29], photonic crystals [30–32], and optical storage voxels [33–35], which has arisen an ever-growing demand for the fabrication of highly integrated all-inorganic optical devices and systems. Currently, it remains difficult and a major challenge to build complex 3D micro-nano structures in multiple all-inorganic transparent dielectrics by using conventional lithography fabrication technologies, owing to the extremely low linear optical absorption and high

modification threshold of these materials. Therefore, novel approaches for tailoring transparent dielectrics to efficiently construct complicated functional micro-nano structures are urgently needed.

Ultrafast laser is among the greatest scientific breakthroughs in the twentieth century. Benefiting from its extremely high peak power (up to the PW level [36]), an ultrafast laser can easily excite a strong non-linear light absorption, enabling various intriguing strong field material modifications [37–43], which greatly expands human's understanding of light-matter interaction under extreme physical conditions. As a consequence, a large number of new phenomena induced by ultrafast laser have been observed one after another since entering the twenty-first century, giving birth to many advanced processing technologies, such as nanomaterial synthesis [44–48], two-photon polymerization [49–51], laser ablation [52–55], selective crystallization [56–58], ion valence manipulation [59–61], and etching assisted laser modification [62–64], etc. Among them, ultrafast laser-induced self-organized nanostructuring (ULSN) is especially fascinating and has established itself to be a fertile ground for exploring novel optical fabrication methodologies because of its high efficiency, super-resolution, and controllability in creating functional surface nanostructures [65–70]. After nearly 30 years of development, ULSN optics is currently developing into a systematic research topic that covers new phenomenon observation, fundamental theory establishment, regulation technique exploration, and engineering applications. Especially in recent years, boosted by multidisciplinary fields such as big data, artificial intelligence, integrated optics, advanced sensing and detecting, 3D spatial ULSN in transparent dielectrics has become a rising new hotspot and attracted extensive attention.

In this paper, we review the developmental path of ULSN in transparent dielectrics and focus on important phenomena, hypotheses, theories, and applications. The milestone research works in recent ten years made by major research groups all over the world are introduced in detail and the existing issues as well as research gaps are discussed. Finally, the future development trend of ULSN methodology and ULSN-related technologies is prospected.

Ultrafast laser-induced self-organization phenomena in transparent dielectrics

Although photo-induced periodic self-organization has been extensively discussed on the surfaces of different materials (including transparent dielectrics) since the laser was invented in 1960 [71], it was not until 2003 that the first report on ULSN in transparent dielectrics appeared [72]. Up to now, a universal physical picture of ULSN in various transparent dielectrics remains far from being achieved, which is attributed to the particularity of ULSN in transparent dielectrics. For ULSN on surfaces, the inherent substrate-air interface and its initial nanoroughness provide suitable conditions for plasma excitation and local field enhancement where the optical field evolution study can be well set on a 2D plane [73–76]. However, no naturally existing interface is available in transparent dielectrics, and physical models for describing ULSN processes are generally needed to be considered in 3D space [77–79]. The observation, manipulation, and characterization of the structures induced in transparent dielectrics are also much more difficult than those on surfaces. For ULSN in transparent dielectrics, more factors will participate in the laser-matter interaction process and usually cannot be ignored [80, 81],

for example, intrinsic structural properties of the matrix (defects and inhomogeneities in lattices or glass networks) [82], light propagation behaviors in the media (refraction, scattering, and self-focusing, etc.) [83], and state changes of materials (metallization, phase transition, and refractive index change, etc.) in 3D space [84, 85], which makes ULSN phenomena in transparent dielectrics widely divergent. Therefore, it is necessary to conduct a targeted review and discussion on the phenomena, mechanisms, and applications of ULSN in different transparent media.

With the substantial development of ultrafast laser processing and material characterization technologies over the last 20 years, a large number of ultrafast laser-induced self-organization phenomena that involve new light-matter interaction mechanisms have been successively uncovered in various transparent dielectrics, serving as the origin of novel ULSN technologies. Representative examples include periodic crystallization, periodic micro-nano voids/pores, and nanogratings in glasses and crystals. These phenomena lead to the birth of multiple ULSN technical routes of near-field enhancement patterning, self-organized lithography, and laser-assisted etching, which is followed by a series of unique ULSN-based applications, such as micro-nano photonic elements, multi-dimensional optical data storage, and micro-nano fluidic devices (Fig. 1).

Nanogratings

The discovery of nanograting structure can be traced back to the year 1999 when L. Sudrie et al. [86] reported an extraordinary anisotropic light scattering induced

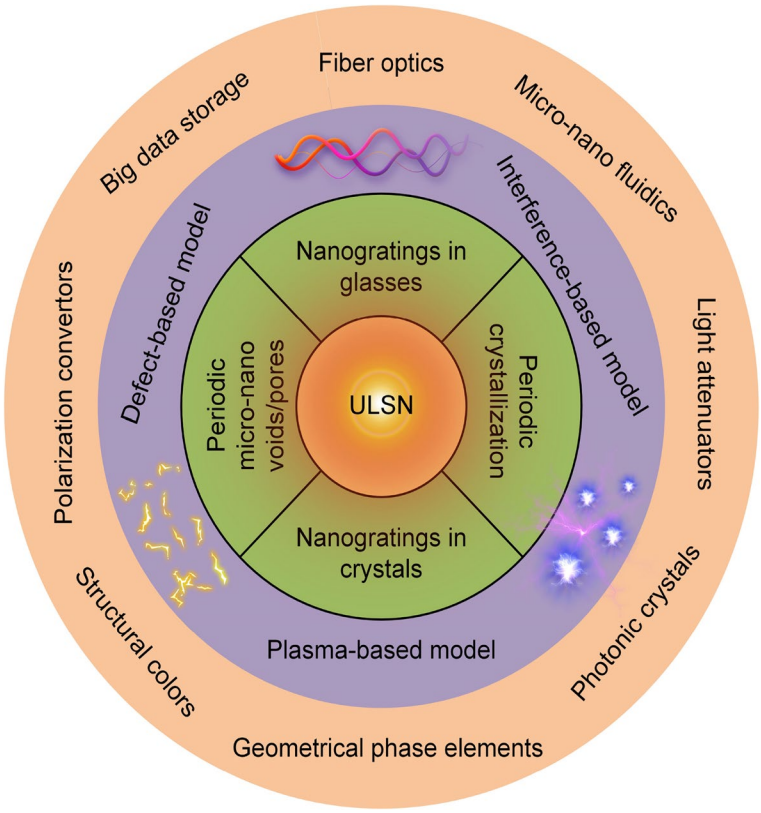

Fig. 1 Schemes for ULSN-induced phenomena, corresponding mechanisms and applications of the created structures

by femtosecond laser irradiation in fused silica. In the same year, Kazansky et al. [87] observed a similar phenomenon inside germanium-doped silica glass. Qiu et al. [88] then reported a polarization-dependent optical scattering in a fluoroaluminate glass, and attributed this phenomenon to the creation of a permanent nanostructure in the laser-irradiated area. In 2003, Shimotsuma et al. [72] finally revealed an unprecedented polarization-dependent nanometer-sized grating structure in the plane perpendicular to the ultrafast laser propagation direction by using backscattering electron microscopy (Fig. 2(a)). Further characterization indicates that nanograting is formed in a carrot-shaped 3D region along the laser propagation direction (Fig. 2(b)) [89–91], which is considered caused by the self-focusing effect, spherical aberration effect, and other nonlinear effects of ultrafast laser-matter interaction [92–94]. In the following ten years, various physicochemical characteristics of nanograting were revealed one after another, including structural anisotropic periodicity [82, 95], polarization-dependent birefringence (Fig. 2(c)) [96], selective etching (Fig. 2(d)) [91, 97], erasing and rewriting capacity (Fig. 2(e)) [98], and heat resistance (Fig. 2(f)) [99, 100], which lays the foundation of the establishment of ULSN technology and ULSN-based applications.

As a symbolic feature of nanograting, periodicity is essentially reflected by periodic material modulations. The most common example is periodic oxygen modulation [99, 101]. Auger electron spectroscopic analysis of the nanograting formed in fused silica shows that oxygen in the laser-irradiated area is periodically modulated [72]. The oxygen content in the dark regions of the periodic fringes is lower, while silicon remains almost unchanged. Shimotsuma et al. [102] subsequently confirmed that oxygen-deficient zones are periodically arranged nanoplates that are filled with nanopores with a feature size of about 10 nm. These oxygen-deficient nanoplates possess a much lower refractive index (RI) compared with the

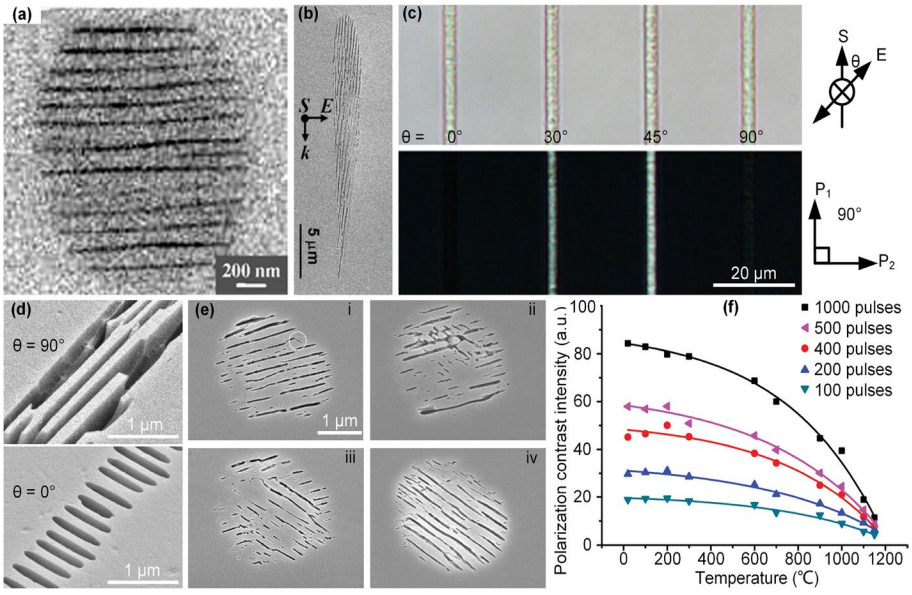

Fig. 2 **a** Nanogratings induced in fused silica [72]. Copyright 2003, American Physical Society. **b** Cross section view of nanogratings [91]. Copyright 2006, Springer Nature. **c** Polarization-dependent birefringence of nanogratings [96]. Copyright 2014, Optica Publishing Group. **d** Polarization-dependent selective etching of nanogratings [97]. Copyright 2005, Optica Publishing Group. **e** Erasing and rewriting capacity of nanogratings [98]. Copyright 2007, Optica Publishing Group. f Heat resistance of nanogratings [100]. Copyright 2012, Laser Institute of America

surrounding glass matrix (RI change can be as high as 0.2 [103]) and are highly susceptible to hydrofluoric acid (Fig. 2(d)) [97]. These physicochemical anisotropies of nanograting make the originally isotropic glass matrix possess some crystalline properties.

In 2004, Bricchi et al. [104] investigated the birefringence of nanograting and attributed this phenomenon to the optical phase modulation caused by the subwavelength periodic refractive-index distribution. Numerous subsequent studies have confirmed that the appearance of polarization-dependent optical birefringence is a basic criterion for the formation of nanogratings [96, 105]. This artificial birefringence signal can not only be used to optimize the processing parameters of ULSN but also serve as an information carrier, playing an important role in high-density optical storage. In 2008, Taylor et al. [90] presented the erasing and overwriting process of nanogratings in fused silica. There, the rewritten structures emerge immediately within the first three ultrafast laser pulses and gradually grow along the direction perpendicular to the rewrite laser polarization with the increase of incident pulses (Fig. 2(e)). In this process, the origin nanograting is gradually erased and replaced by the rewritten one with a new orientation, which can also be characterized by the birefringence signal of the rewriting area. The rewritable property makes nanograting an ideal tool for ULSN-based optical data storage.

Heat resistance is a key performance of various all-inorganic functional elements. However, many ultrafast laser-produced structures are metastable state structures that are easily changed through thermal excitation, such as color centers and excitons [106, 107]. Therefore, investigating the heat resistance of nanograting is necessary. In 2012, Richter et al. [100] studied the thermal stability of the nanograting induced in fused silica with different incident pulse numbers by detecting the birefringence intensity (Fig. 2(f)). Experiments indicate that heat treatment gradually weakens the birefringence signal of nanograting, indicating that nanograting is deteriorating. Notably, the birefringence signal does not disappear before the melting temperature of fused silica is reached and remains 13% of the initial intensity after being treated with a temperature of 1150 ℃. In 2022, Wang et al. [108] systematically examined the thermal stability of nanogratings induced in silica-based glasses and confirmed that high levels of OH and Cl impurities will reduce the thermal stability, but the overall excellent heat resistance of nanograting still makes nanogratings a promising candidate in building highly robust elements.

As the most fundamental and widely reported structure induced by ULSN in transparent dielectrics, nanogratings possess plenty of representative features that can be universally extended to other ULSN-produced self-organization forms. With the development of characterization techniques and detecting methods, more work is needed to further generalize the theoretical framework of nanogratings, boosting the mechanism and application research on ultrafast laser-matter interaction physics.

Periodic crystallization

Since the discovery of nanograting in fused silica, researchers have been working on extending ULSN to more functional transparent dielectrics [109]. Studies have shown that most nanogratings consist of periodic defect phases, while, in some unconventional glasses, similar grating structures can appear in the form of periodic crystallization.

In 2016, Cao et al. [110] first reported an extraordinary periodic crystallization phenomenon in Li_2O-Nb_2O_5-SiO_2 glass and have done systematic works on this structure in the following years [111–113]. Crystallographic characterization indicates that this self-assembled nanostructure consists of periodically arranged nanocrystals embedded in the glass matrix. These nanocrystal polar axes are aligned perpendicular to the laser polarization, which preliminarily indicates that the ultrafast laser-induced periodic crystallization in the unconventional glass is polarization-dependent (Fig. 3(a)-(c)). The research group believes that these layered crystalline nanostructures hold the potential to support tunable second-harmonic generation and serve as nonlinear photonic elements. However, limited by the poor regularity of this nanostructure, they have not demonstrated its practical application.

In 2018, Shimotsuma et al. [114] observed another polarization-dependent periodic crystallization structure in Al_2O_3-Dy_2O_3 glass (Fig. 3(d)), and found that by adjusting the content of Dy_2O_3 in the glass, two types of crystallites can be precipitated. Raman spectroscopy indicates that for Al-30Dy glass (Dy_2O_3 content is 30 mol%), the precipitated crystal is $Dy_3Al_5O_{12}$ garnet, while for Al-40Dy glass (Dy_2O_3 content is 40 mol%), the precipitated crystal can be $Dy_3Al_5O_{12}$ garnet or $DyAlO_3$ perovskite crystals according to the pulse energy. Structural characterization shows that the periodic crystallization induced in Al_2O_3-Dy_2O_3 glass possesses fairly high regularity and controllability, which confers its broader application prospects.

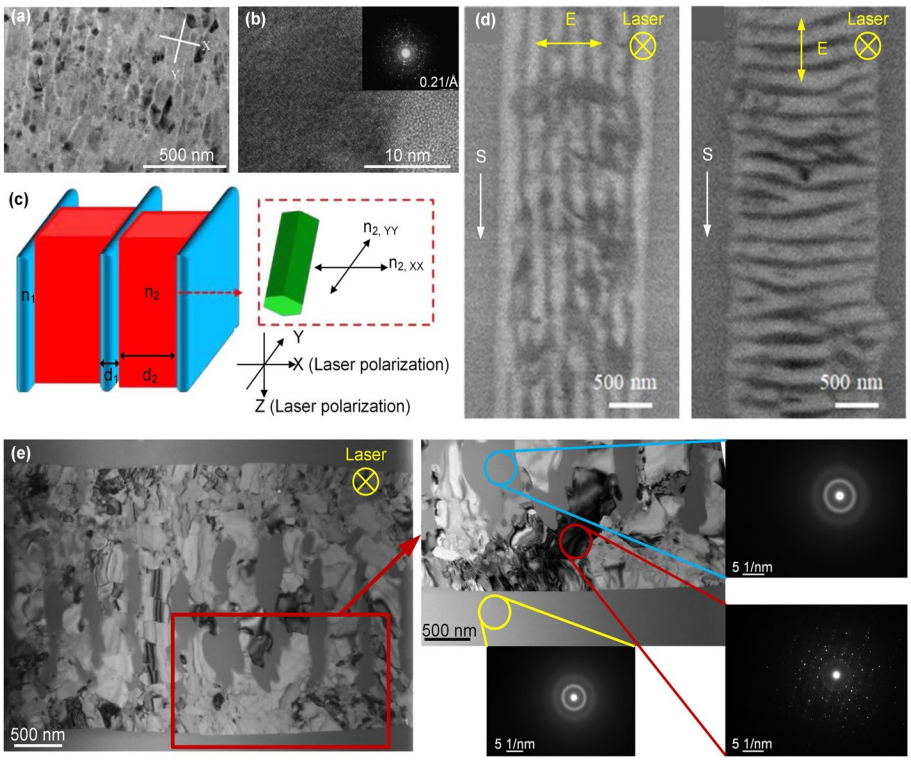

Fig. 3 **a** Periodic crystallization induced in lithium niobium silicate glass and **b**) corresponding high-resolution transmission electron microscopy (HRTEM) image of the crystal-glass interface. **c** Schematic of ULSN-produced periodic crystallization [110]. Copyright 2016, Optica Publishing Group. **d** Periodic crystallization induced in Al_2O_3-Dy_2O_3 glass [114]. Copyright 2018, Springer Nature. **e** Periodic crystallization induced in LTN glass and corresponding transmission electron microscopy (TEM) structural characterization [115]. Copyright 2019, Wiley–VCH

In 2019, Zhang et al. [115] reported a periodic crystalline structure in a La_2O_3-Ta_2O_5-Nb_2O_5 (LTN) glass system (Fig. 3(e)), and studied the effects of glass composition and laser parameters on the ultrafast laser-induced periodic crystallization process. Experiments indicate that the birefringence signal of the induced periodic crystalline structure increases significantly with the increase of Ta_2O_5 content, while in La_2O_3-Nb_2O_5 glass without Ta_2O_5, it is extremely difficult to induce periodic crystallization. This is because the addition of Ta_2O_5 enhances the crystallization ability of the glass system and plays a role in promoting nucleation. Notably, this study also demonstrated the polarization-dependent light attenuation performance of periodic crystalline structures in the near-infrared region, which is the first application demo based on this structure. In 2021, Zhang et al. [116] further demonstrated that the birefringence signal of periodic crystallization structures can be erased and rewritten by an ultrafast laser with a different polarization state, implying a considerable degree of similarity between periodic crystallization and nanogratings.

Ultrafast laser-induced periodic crystallization has just been revealed in recent years and is still in its infancy, but is rapidly developing to become a brand new research field where a large number of research gaps related to physical phenomena, theoretical models, and engineering applications are waiting to be addressed. In the future, by combining various frontier optical technologies like spatial light modulation (SLM), beam shaping, multi-beam interference, and super-resolution processing, ultrafast laser-induced periodic crystallization is expected to serve as a highly efficient and universal method for in situ constructing functional phase transition structures in various mainstream optical media, empowering next-generation integrated optics research.

Other self-organization forms

Owing to the complexity of ultrafast laser-matter interaction in transparent dielectrics, the material modifications induced by ultrafast laser vary widely depending on the irradiation conditions and the types of target materials. Since the discovery of nanogratings, more and more ULSN-produced peculiar phenomena and micro-nano structures in transparent materials have been uncovered, such as periodic micro-nano voids, anomalous polarization-dependent structures, and periodic structures in crystals, which greatly expands ULSN-based material modification and deepens people's understanding of strong field light-matter interaction physics.

In 2005, Kanehira et al. [117] first reported a periodically aligned nanovoid structure in conventional borosilicate glass via single femtosecond laser irradiation. The induced nanoscaled spherical voids were self-organized with a period along the laser propagation direction and can be manipulated by tuning laser parameters and focusing position (Fig. 4(a)). Since then, ultrafast laser-induced periodic micro-nano voids have been observed in fused silica [118], $SrTiO_3$ crystal [119], CaF_2 crystal [120], Al_2O_3 crystal [121], and glasses [122] one after another, revealing the high universality of this process. For structural manipulation, Hu et al. [123] presented that by moving the laser focusing position close to the surface perpendicular to the horizontal surface (XY plane) of the sample, the one-step creation of two perpendicular strings of periodic voids can be achieved. Song et al. [124] reported that by employing different types of objective lens, inverted periodic voids with opposite directions can be

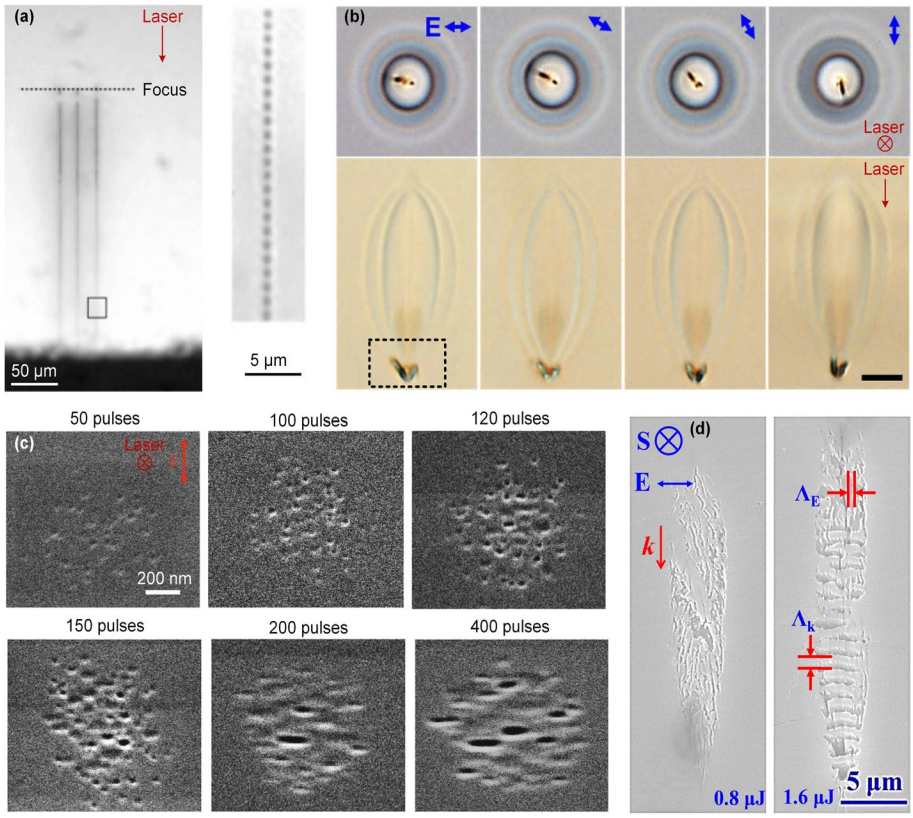

Fig. 4 **a** Periodically aligned nanovoids induced in borosilicate glass [117]. Copyright 2005, American Chemical Society. **b** Polarization-dependent V-shaped structure (marked by dotted box) induced in aluminosilicate glass [126]. Copyright 2021, Optica Publishing Group. **c** SEM images of the polarization-dependent nanopores written with different pulse numbers [127]. Copyright 2020, Nature Springer. **d** SEM images of cross sections of the multiple periodic structures inscribed in quartz crystal [128]. Copyright 2019, Optica Publishing Group

induced. In 2011, Luo et al. [125] presented that inverted periodic voids can also be achieved by tuning the objective's immersion liquid, showing the flexible controllability of this self-organized structure.

In 2016, Zhang et al. [129] observed an anomalous polarization-dependent dumbbell-shaped structure by using ultrafast laser static irradiation in an aluminosilicate glass. This dumbbell-shaped structure is formed at the top of the laser focal volume and can be erased by further irradiation. Interestingly, O^2 bubbles are revealed to appear at the periphery of the incident laser beam and distribute along the laser polarization direction. In 2021, they further reported a V-shaped crack that forms at the bottom of the laser-modified volume and is oriented parallel to the laser polarization (Fig. 4(b)) [126]. These findings enrich the family of non-periodic self-organized structures. Sakakura et al. [127] recently presented brand new polarization-dependent nanopores by ULSN in fused silica that share many optical properties of nanogratings, such as structural anisotropy, birefringence, and polarization-dependence (Fig. 4(c)). The formation of this structure is considered attributed to the interstitial oxygen generation caused by ultrafast laser-induced multiphoton and avalanche ionization. Notably, these nanopores are superior to conventional nanogratings in terms of reducing incident pulse number, pulse energy, and optical loss, which make them

competitive in constructing ultralow-loss optical elements and high-speed optical data storage.

Except for glasses, ULSN has been demonstrated in more types of dielectrics. In 2016, Karpinski et al. [130] induced a self-organized periodic planar structure in MgO-doped $LiNbO_3$ crystal by using ultrafast laser continuous writing. Scanning electron microscopy (SEM) images confirm that such a periodic structure is periodically assembled and aligned perpendicular to the laser polarization, which is highly similar to the nanogratings formed in glasses. In 2019, Zhang et al. [128] reported another unique self-organization phenomenon in bulk quartz crystal (Fig. 4(d)). There, three types of periodic structures with different periods are simultaneously induced in the irradiation volume. The first one is similar to nanogratings and the second one is formed in the laser writing direction. The third one is formed in the laser propagation direction. In 2021, Xu et al. [131] and Zhai et al. [132] inscribed nanograting-like self-organized periodic structures in sapphire that possess optical phase modulation, erasing, and rewriting abilities. Notably, a new class of ULSN mediating between the surface and the interior has also been rising in recent years. In these studies, metal nanoparticles (NPs) or clusters with nonlinear optical responses are introduced into transparent dielectrics to modulate incident light waves and establish a periodic field distribution, thereby activating ULSN [133–135]. The self-assembled periodic structures are usually produced in thin films or near-surface regions owing to the limitation of ion deposition or implantation depth [136]. These results expand ULSN methods to more functional materials like bulk crystals, films, and composite materials, which helps to clarify the linkages of different ULSN phenomena and enriches the potentially available materials.

As important branches of ULSN, the discovery of these novel self-organization phenomena is encouraging, as they greatly generalize ULSN approach in product categories, manipulation degrees of freedom, and available materials. By utilizing the optical modulation abilities of the created structures, various novel tools for constructing photonic elements can be developed in the future. However, the research on these structures is still not thorough and limited to the interpretation of experimental observations, and their formation mechanisms remain largely unclear. As a result, these ULSN methods are currently far from mature whether in theory or technological practice. Therefore, more studies need to be carried out to fully clarify the physical processes behind them, improve the regularity of products, and explore structural manipulation methods.

Mechanisms of ultrafast laser-induced self-organization in transparent dielectrics

The ultrafast laser-matter interaction is a highly complex multi-physics coupling process involving various nonlinear effects that are currently still far from fully clarified. As a typical instance of ultrafast laser-matter interaction, ULSN in transparent dielectrics remains largely enigmatic. In the last 20 years, researchers have invested tremendous efforts to uncover its physical mechanisms and a series of inspiring hypotheses, models, and concepts have been proposed, which greatly promotes the process of fully understanding and utilizing ULSN. Here, we mainly focus on the representative research progress and important milestones in recent years.

Interference-based model

The theoretical frameworks for early discovered ULSN phenomena are relatively well established. With the first observation of the nanogratings in fused silica, Shimotsuma et al. [72, 137] preliminarily proposed an interference model similar to the formation mechanism of surface periodic structures [71]. In this model, the nonlinear ionization process in the laser irradiation area releases plenty of free electrons, resulting in the creation of electron plasmas. This process will greatly promote light absorption and then lead to the excitation of plasma waves. The interference between this electron plasma wave and subsequent incident light wave finally induces the creation of nanogratings in transparent media. This model well explains the structural periodicity (Fig. 5(a)) and has been considered the most important origin theory for nanograting phenomena. Since then, a series of studies have been carried out to improve the original interference theory [79, 138, 139]. These works revealed that the periodic field distribution can be established and modulated by various scattering centers originating from inhomogeneities, electronic defects, and laser-induced nanopores/voids in the media (Fig. 5(b)). In a simple view, the interference of the incident waves and the scattered waves from scattering results in the wavelength-scaled periodicity perpendicular to the laser polarization [138], and the coherent superposition of multiple

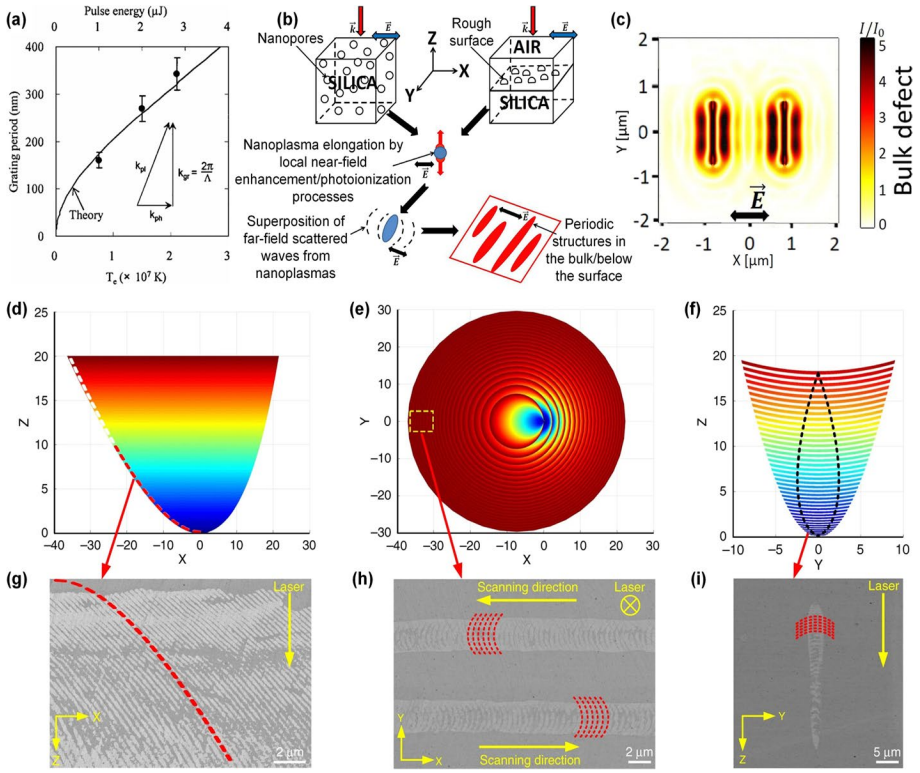

Fig. 5 **a** Nanograting period evolution based on the plasma interference model [72]. Copyright 2003, American Physical Society. **b** Schematic of nanopore-mediated interference mechanisms for describing periodicity formation in bulk and on surfaces. **c** Secondary field modulation induced by the coherent superposition of the scattered waves from two adjacent nanoplanes [79]. Copyright 2017, Springer Nature. **d-f** Theoretically calculated 3D focal-area interference field presented by the equal-phase surfaces in d) XZ plane, e XY plane, and f YZ plane. **g-i** Corresponding SEM images of the actually produced structures by ULSN [78]. Copyright 2021, Springer Nature

scattered waves from different scattering centers enables a further reduction of the initial period, leading to the subwavelength periodicity (Fig. 5(c)) [79]. These models reasonably explain the polarization-dependence and multi-pulse accumulation-driven structure creation of nanogratings [110, 140], which promotes the maturity of interference-based models.

For new types of ULSN phenomena, the establishment and discussion of theoretical models are still rarely reported. In 2021, Zhang et al. [78] presented an extraordinary periodic crystallization structure in the LTN glass system that is polarization-independent but direction-dependent. This nanograting tilts opposite to the laser scanning direction and possesses a curved spatial morphology, which subverts the conventional understanding of the nanograting formation mechanism based on the interference model discussed above. To clarify this puzzle, the group proposed a brand new interference model where a single scattering center is introduced to replace the randomly distributed ionization centers or plasmas. According to this model, the interference is established by the scattered spherical waves from the scattering center and oblique incident waves that are distributed at the periphery of the focused beam (Fig. 5(d)-(f)). This model can quantitatively describe the intensity distribution of the interference field and the theoretically calculated result is in good agreement with the experimentally generated structures (Fig. 5(g)-(i)). They further demonstrated that this model is highly universal and can explain a series of similar ULSN phenomena not only in glasses but also in crystals. This study further extended the conventional interference model and greatly expand the application scope of this theory, which lays the foundation for further manipulating and utilizing different types of self-organized periodic structures. Notably, the interference model proposed here is conceptually different from the previous ones for explaining polarization-dependent nanogratings, which is reflected in the interference excitation, the scattering source, and the spatial morphology of the interference. In this model, the interference field is actively excited by ultrafast laser irradiation without relying on intrinsic defects or inhomogeneities in the glass network where the scattering field originates from the spherical light waves emitted by a single scattering center in the focal area rather than multiple inhomogeneous scattering centers or plasma waves. In addition, the spatial morphology of the interference field here is highly regular and strictly defined by the interference equations, rather than depending on ambiguous evolution processes.

With the deepening of research, the framework of the interference model for explaining early ULSN phenomena has become much clearer than before. However, with the discovery of new self-organized structures in multiple transparent media, plenty of disagreements and contradictions have been emerging in various branches of this theory. So far, different types of interference models are still largely isolated, and a highly general physical model that can offer a full understanding of ULSN has not yet been obtained. Therefore, more efforts need to be invested to disentangle the interrelationships and commonalities of different concepts to achieve a more refined and comprehensive theory.

Plasma-based model

Bhardwaj et al. [141, 142] proposed a nanoplasmonic model to explain the ultrafast laser-induced periodic modifications in transparent dielectrics where the local field enhancement effect at the boundary of the initially sphere-shaped nanoplasmas causes an asymmetric growth in the orientation perpendicular to the laser polarization and form disk-shaped plasmas (Fig. 6(a)). During laser irradiation, these disk-shaped plasmas will become quasi-metallic and interact with subsequent incident light waves, which results in the periodic modulation of the plasmas and finally creates periodically assembled nanoplanes (Fig. 6(b)). According to this model, the regularly arranged nanoplanes will first form at the top of the irradiation volume and eventually fill the whole laser-modified area, and the period of these nanoplanes is estimated to be about λ/2n where λ is the ultrafast laser wavelength and n is the refractive index of the medium. This model provides a picture of the structural evolution process of ultrafast laser-induced periodic self-organization under multi-pulse interaction.

Liao et al. [77] presented that the standing plasma waves excited at the interfaces between modified and unmodified zones play an important role in the formation of

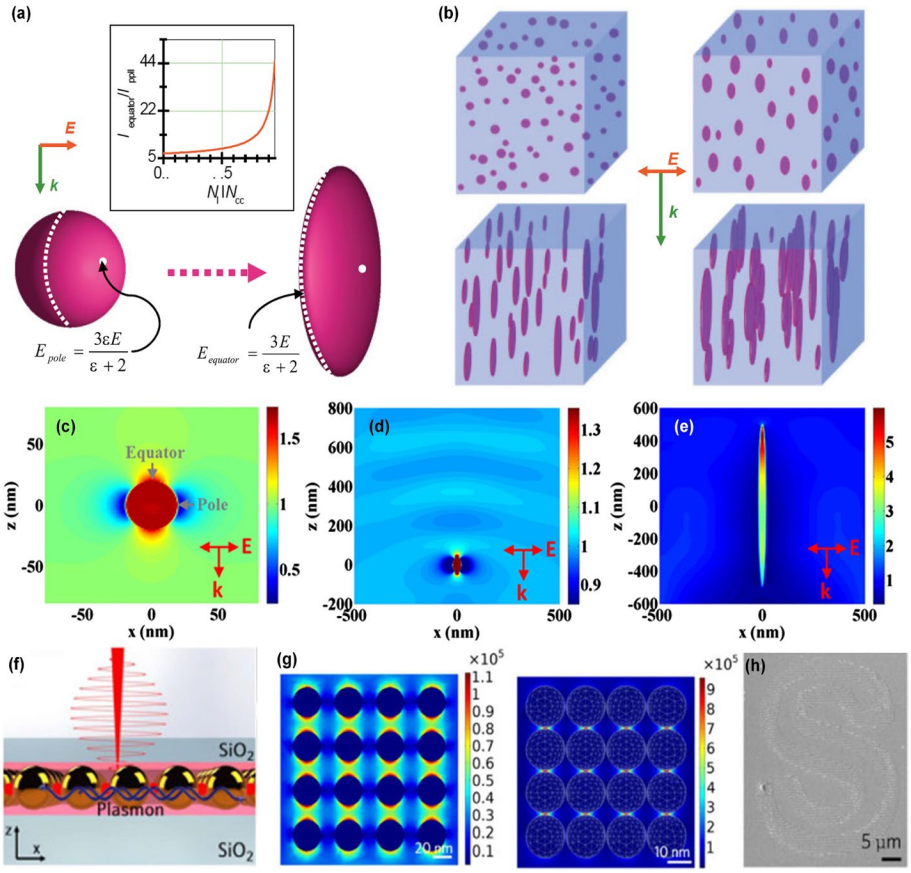

Fig. 6 **a** Evolution mechanism of nanoplasmas based on asymmetric field enhancement and **b**) scheme of evolution of nanoplasmas into nanoplanes [90]. Copyright 2008, Wiley–VCH. **c-e** Theoretical distribution of light-filed intensity in XZ plane near **c**) a spherical nanoplasma, **d** an elliptical nanoplasma, and **e** an elliptical nanoplasma with a larger ellipticity [77]. Copyright 2015, Optica Publishing Group. **f** Schematic of ULSN in fused silica with ion-implanted Ag NPs. **g** Simulated electric field distribution for 15 nm (left) and 1 nm (right) spaced NPs. **h** SEM image of the letter "S" formed by self-assembled grating structures [136]. Copyright 2023, Elsevier

nanogratings by periodically modulating the electronic field intensity to excite nanoplasmas and induce periodic nanopores. According to this study, local field enhancement initially occurs at the equator of spherical nanoplasmas perpendicular to the polarization direction (Fig. 6(c)), which will induce an asymmetric ablation and thus lead to the formation of elliptical nanoplasmas. They also presented that the field enhancement occurs at the tips of elliptical nanoplasmas with different ellipticities (Fig. 6(d) and (e)), which further promotes the anisotropic growth of nanoplasmas and drives the nanopores to evolve into nanogratings with the increase of incident laser pulses. This interface-mediated mechanism is similar to that of ultrafast laser-induced surface ripples and explains many similarities between nanogratings and surface periodic structures. Notably, ultrafast laser-induced standing plasma waves are also used to interpret the formation of self-organized nanovoids in transparent dielectrics [143], which indicates the intercommunity of the formation mechanism of different ULSN-produced structures. In 2015, Liao et al. [144] further demonstrated that the coherent superposition of the scattering waves from early-formed nanogratings will create secondary optical intensity maxima. Such a local field enhancement is generally created between two nanoplanes and leads to the birth of new "son" nanoplanes, which explains the period reduction of nanogratings under the incidence of a large number of ultrafast pulses. Recently, Wu et al. [136] proposed a plasmon-enhanced ULSN by using ion implantation techniques (Fig. 6(f)). In this study, Ag ions are injected 100 nm below the surface and formed into homogeneous NPs in fused silica. Assisted by the significant light-field enhancement and localization of the NPs, the incident pulses excite and form a standing wave that can interfere with the subsequent laser pulses (Fig. 6(g)). This process enables establishing a periodic field distribution that drives the creation of subwavelength grating structures (Fig. 6(h)).

Plasma-based models are widely applied to describe the emergence and anisotropic growth of ultrafast laser-induced polarization-dependent periodic structures, such as the polarization-dependent nanopores [145], nanogratings [141], and nanoslits [146]. However, the lifetime of the light-excited electron plasma is only ~ 150 fs [147, 148], much shorter than the pulse interval of ultrafast laser, which limits the effectiveness of these models in explaining the subsequent interaction between nanoplasmas and incident waves. Thus, more in-depth works are still needed to clarify the bridging process from plasma generation to the activation of ULSN and thus complete plasma-based models.

Defect-based model

To bridge the temporal gap between the previously excited state and subsequently incident pulses, Richter et al. [100, 149] proposed a defect-assisted nanostructuring model where the self-trapped excitons (STEs) and defects induced by an ultrafast laser play a critical role in the formation of nanogratings (Fig. 7(a)). They investigated the coupling mechanism between individual pulses by tuning the temporal pulse separation from 500 fs to several ms. Experiments indicate that STEs are formed after the initial nonlinear absorption of ultrafast laser pulses and decay to point defects in about 500 ps. For very short pulse separations, the STEs promote the absorption of the following incident pulses, increasing the coupling between laser pulses and the material. When the pulse

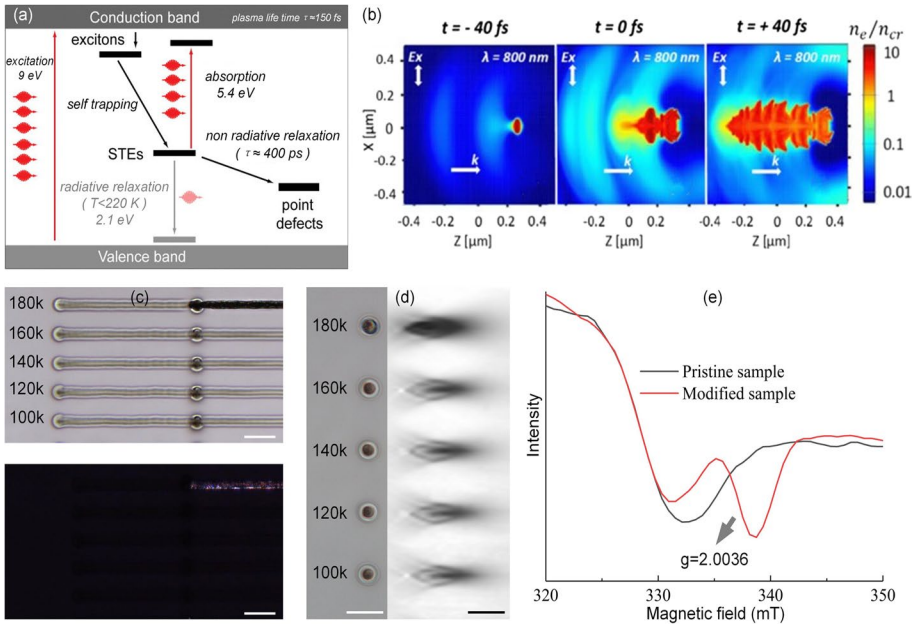

Fig. 7 **a** Evolution process of STEs into point defects [100]. Copyright 2011, Laser Institute of America. **b** Evolution of electron density near a single inhomogeneity in glass [138]. Copyright 2016, American Physical Society. **c** Crystallite seeds assisted periodic crystallization test with different incident pulses and **d**) crystallite seed induction test with different incident pulses, and **e** EPR spectra of crystallite seeds and glass matrix [116]. Copyright 2021, Wiley–VCH

separation exceeds the lifetime of the STEs, the cumulative process of incident pulses is mediated by permanent defects.

Rudenko et al. [79, 138, 139] numerically investigated the formation mechanism of ultrafast laser-induced periodic structures in fused silica. According to their simulation, randomly distributed inhomogeneities in the material play an important role in forming scattering centers, creating different types of nanogratings, and tuning the nanograting period (Fig. 7(b)). Notably, these models are established mainly relying on the inherent defects or inhomogeneities in the fused silica and its universality in more other transparent dielectrics remains to be examined. In 2021, Zhang et al. [116] first reported a defect-assisted periodic crystallization in unconventional glasses where an auxiliary effect originates from photo-induced defects plays a decisive role (Fig. 7(c)). It is shown that the pre-irradiation of the medium with an ultrafast laser can locally induce defective crystallite seeds that can provide a unique domino-like assisting effect to activate and maintain continuous periodic phase transitions (Fig. 7(d)). The working principle of this auxiliary effect is to greatly reduce the pulse number and energy threshold for triggering ULSN process. Especially, the pulse density threshold can be reduced to 21–150 pulse/μm, nearly 10,000 times lower than that for inducing local crystallization by static laser irradiation. Electron paramagnetic resonance (EPR) measurement indicates that this auxiliary effect essentially originates from the laser-induced hole-trapped defect centers in the glass networks (Fig. 7(e)). Experiments also show that this mechanism is highly universal in multiple glass systems. This study sustains that ULSN process can be activated by the actively excited defects and changes the conventional concept that ULSN process relies on the intrinsic defects and heterogeneity of the matrix. The proposed model is especially suitable for explaining the continuous phase transition-typed ULSN phenomena in transparent dielectrics, which further extends the defect-based ULSN mechanisms.

Although many studies have confirmed the important role of various types of defects in mediating ULSN processes, the effectiveness of proposed models largely depends on the materials and experimental conditions. Consequently, there is still on consensus on the nature of these defects, specifically, where they come from, what they are, or how they work. In the next stage, more work is needed to clarify the spatiotemporal characteristics of the defects-assisted energy deposition and explore the defect-mediated ULSN in more different transparent dielectrics other than fused silica, including various unconventional glasses and crystals, to further complete the theory.

Model improvements

Beam properties also play an important role in creating and manipulating structures during ULSN process. One important model is the pulse intensity forward tilt (PFT)-based ULSN. In 2012, Dai et al. [150] reported a controllable 3D-spatial rotation of the nanogratings in fused silica and proposed that this rotation depends on the angle between the PFT and the laser polarization direction (k). Specifically, PFT introduces an angle between the Poynting vector (p) and the wave vector, which decomposes the incident electric field into two electric field components perpendicular ($E_{\perp}$) and parallel ($E_{\parallel}$) to the laser propagation direction. The electric field component $E_{\perp}$ determines the orientation of nanogratings in the plane perpendicular to the laser propagation direction, while the electric field component $E_{\parallel}$ makes nanogratings rotate in the plane parallel to the laser propagation direction (Fig. 8(a)). According to this mechanism, an

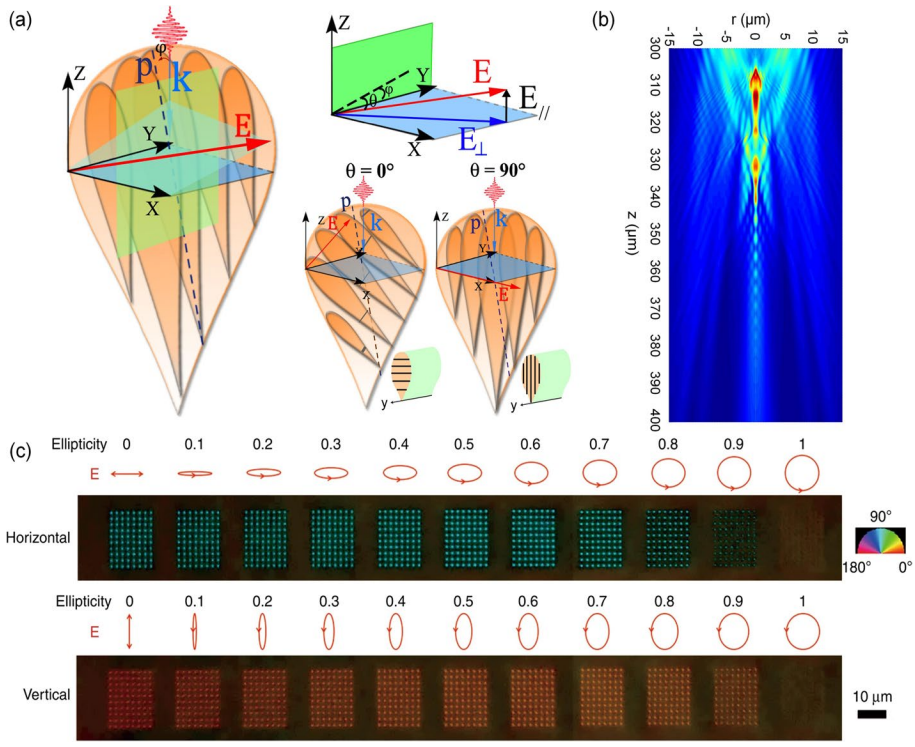

Fig. 8 **a** Schematic of PFT-based 3D structural manipulation of nanogratings [150]. Copyright 2012, Optica Publishing Group. **b** Theoretically calculated fluence distribution at the focus [118]. Copyright 2008, AIP Publishing. **c** Birefringence images of imprinted nanopore-voxels. Pseudo colors show the orientation of the slow axis [151]. Copyright 2023, Springer Nature

ultrafast laser beam with PFT can be applied to simultaneously rotate nanogratings on two orthogonal planes and thus manipulate ULSN in 3D space [150].

Another representative example is the creation of self-organized periodic nanovoids where Gauss–Bessel beam [152], truncated Gaussian beam [122], and tightly focused Gaussian beam [117] were widely applied to achieve this class of ULSN. In the modeling, these beams are generally set as incident fields and combined with different light propagation and light-matter interaction models to obtain the theoretical fluence distribution. For example, Gaizauskas et al. [152] applied a zero-order Gauss-Bessel beam as the incident field to calculate the fluence distribution by using the nonlinear Schrodinger equation neglecting the plasma defocusing effect. The periodicity of the calculated fluence is similar to the experimentally induced structure. Mauclair et al. [122] applied a truncated Gaussian beam as the incident field and simulated the light field in the focal region by using the Fresnel linear propagation formalism. It was found that a series of fluence peaks appeared before the main focus, agreeing well with their experimental results. In 2008, Song et al. [118] took a tightly focused Gaussian beam as the incident field and proposed a composite model by combining the ultrafast laser nonlinear propagation model with the spherical aberration effect caused by the interface of two media with different refractive indices. Specifically, they applied a spherical aberration theory to obtain the light field after passing through the interface and set this light field as a new incident field, and then the fluence distribution in the medium is solved by incorporating the nonlinear Schrodinger equation and the electron density evolution equation (Fig. 8(b)). Their model and corresponding experimental results demonstrated the interface spherical aberration effect caused by the refractive index mismatch between air and the medium is the main reason for the ULSN creation of periodic nanovoids by a tightly focused ultrafast laser.

Recently, Lei et al. [151] observed that ULSN with an elliptically polarized beam in silica glass can create anisotropic nanopores whose birefringence signal intensity is about twice that induced by a linearly polarized beam, where the maximum birefringence is created by the elliptically polarized beam with an ellipticity of 0.6 (Fig. 8(c)). This is counterintuitive because the nonlinear absorption of an elliptically polarized ultrafast laser by fused silica is much weaker than that of a linearly polarized one. They attributed this abnormal phenomenon to the enhanced interaction of circularly polarized ultrafast laser with randomly oriented bonds and hole polarons in the glass network, and the high-efficiency ULSN creation of this birefringent structure can be interpreted as the result of a balance between the maximum concentration of nanopores at circular polarization and their anisotropic shaping driven by the linear polarization component.

To sum up, these studies discussed above further expand and refine the important roles of beam properties, interference, plasmas, and defects in ULSN process, and also illustrate the complexity of ULSN in transparent dielectrics, because there are cooperative effects between different models and various external factors. For example, the presence of nanostructures, optical aberration, and defects may affect the excitation and modulation of optical fields and also affect the role of beam polarization states in ULSN, which requires greater efforts in the future to gain a deeper understanding of how these mechanisms work together to activate and manipulate ULSN processes in different types of media.

Applications based on ultrafast laser-induced self-organization in transparent dielectrics

As a high-resolution volume optical processing tool, ULSN is highly effective in creating complex all-inorganic mico-nano structures in various transparent dielectrics, which greatly enhances people's ability to construct integrated elements with ultrahigh stability, lifetime, and robustness. In recent years, more and more ULSN-based applications have been demonstrated in different functional materials. Here, we focus on representative research progress, including micro-nano optical elements, multidimensional data storage, and super-resolution etching, and briefly introduce some emerging novel applications.

Micro-nano optical elements

In 2002, Bricchi et al. [153] demonstrated a birefringent Fresnel zone plate in silica fabricated by using ULSN (Fig. 9(a)), which is considered the earliest optical application based on ULSN methods. Since then, various intriguing micro-nano optical elements have emerged by using ULSN approaches (Fig. 9(b) and (c)), such as wave plates

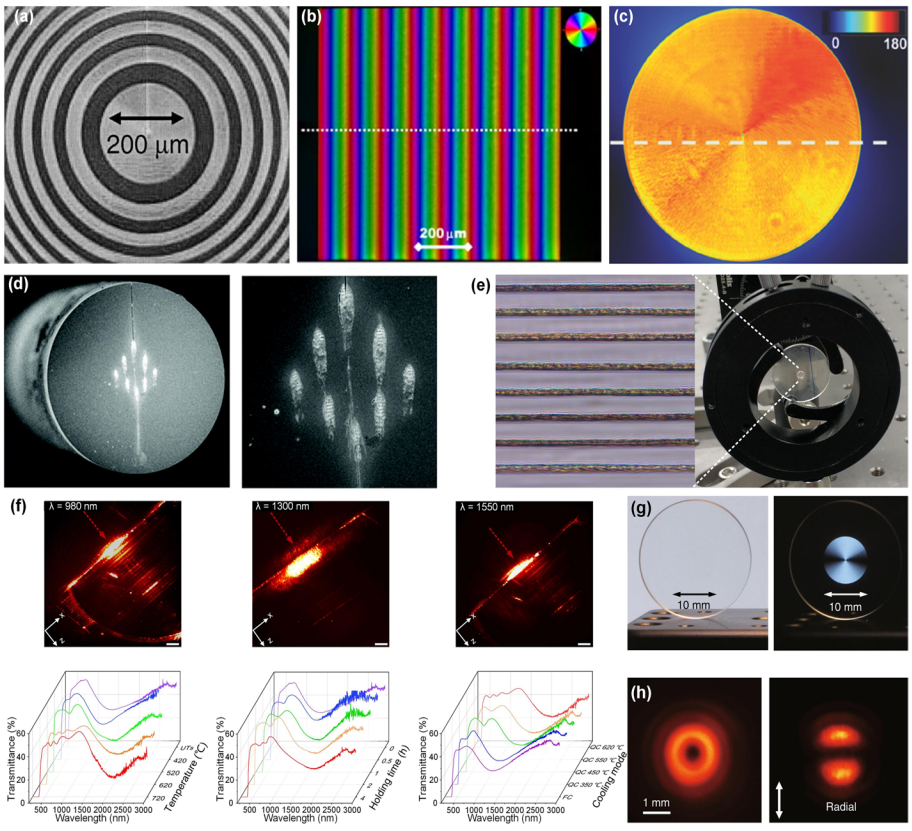

Fig. 9 **a** Fresnel zone plate made of nanogratings in fused silica [153]. Copyright 2002, Optica Publishing Group. **b** Polarization diffraction gratings made of nanogratings in fused silica [157]. Copyright 2010, Optica Publishing Group. **c** Optical vortex converter made of nanogratings in GeO_2 glass [166]. Copyright 2017, Wiley–VCH. **d** In-line polarizer made by inscribing nanogratings in a single mode fiber [169]. Copyright 2019, Royal Society of Chemistry. **e** Near-infrared light attenuator made of periodic crystallization induced in LTN glass [115]. Copyright 2019, Wiley–VCH. **f** Tunable photonic crystal fabricated by ULSN-induced periodic crystallization [78]. Copyright 2021, Springer Nature. **g** Ultralow-loss polarization convertor made of self-organized nanopores in fused silica and **h**) corresponding beam conversion results [127]. Copyright 2020, Springer Nature

[154–156], polarization diffraction gratings [157], polarization selective holograms [158], light attenuators [115, 159, 160], Bragg gratings [161–164], and polarization converters [165–167]. Most of these applications are based on nanogratings in glasses due to a relatively complete understanding of the physicochemical characteristics and formation mechanisms of this structure [168]. Recently, with the expansion of application scenarios and the discovery of different types of self-organization phenomena, more pioneering applications emerge and greatly accelerate the maturing of ULSN.

Fiber is among the greatest innovations of human beings and provides an excellent platform for next-generation high-performance communication, sensing, measurement, and computing technologies [170]. Recently, ULSN-based fiber optics is fast developing to become a hot research field [171]. In 2019, Lu et al. [169] combined ULSN with fiber optics and first induced self-organized fiber nanogratings (FNGs) by ultrafast laser direct writing in a single mode silica fiber (Fig. 9(d)). In this work, an in-line polarizer is demonstrated based on FNGs, boosting the application of ULSN in all-fiber polarization mode control and high-order vector mode selection. In 2021, Wang et al. [172] demonstrated distributed fiber optical sensors by continuously inscribing FNGs in silica fiber core point by point. The insertion loss of single point sensor element can be as low as 0.001 dB and due to the excellent heat resistance of nanogratings, the fabricated fiber sensors can sustain long-term stability in high temperatures up to 1000 ℃. Notably, this study first demonstrated the application of FNGs based sensors in nuclear reactors, confirming the great potential of ULSN in fabricating robust optical devices for extreme environments.

In recent years, new types of ULSN-produced modifications have sprung up and remarkable progress has been made in practical applications. In 2019, Zhang et al. [115] presented a polarization-dependent light attenuation effect of the periodic crystallization in LTN glass system and demonstrated that a broadband light attenuator made of the periodic crystallization can work in the near-infrared region (Fig. 9(e)). This is the first report on the periodic crystallization-based optical application. In 2021, they further uncovered the dual optical modulation capability of periodic crystallization, including polarization-dependent light attenuation and wavelength-dependent selective optical transmittance [78]. Based on this, they further inscribed a multi-functional all-inorganic photonic crystal in the glass (Fig. 9(f)). Notably, by engineering a reversible secondary-phase transition of the crystal part in the periodic crystallization structure, the optical modulation performances of this photonic crystal can be broadly manipulated, which shows the excellent flexibility of ULSN-produced all-inorganic optical elements.

In 2020, Sakakura et al. [127] demonstrated geometrical phase optical elements based on ULSN-produced polarization-dependent nanopores in fused silica, such as geometrical phase prism, lens, and polarization convertor (Fig. 9(g) and (h)). Compared with the nanograting-based optical elements, the nanopore-based optical elements have an extremely high optical transmittance of about 99% in the visible and near-infrared waveband and higher than 90% even in the ultraviolet range, which is attributed to the ultralow scattering loss of the nanopores. In 2021, Xu et al. [131] inscribed periodic structures in sapphire and demonstrated the application of geometric phase elements, including geometric phase lens and Q-plate. These optical elements are demonstrated to

possess high imaging and focusing performances which may find applications in various harsh environments, such as high-power optics.

Although these newly presented ULSN technique routes are still in the early stage of investigation, they have already shown remarkable advantages in fabricating all-inorganic optical elements with excellent integration, robustness, flexibility, and high transmittance in 3D space. To give full play to these advantages, normalized and quantitative fabrication processes aiming for ULSN is needed to be established and completed to improve the regularity of the self-organized structures. And more potential application scenarios related to optical sensing, displaying, imaging, precision measurement, and signal processing are waiting for further exploration.

High-density data storage

With the rapid development of big data and artificial intelligence technologies, the amount of data generated by human society has been fast exploding [173–175]. Faced with the long-term ultra-large-scale data storage, currently applied technologies inherently have many drawbacks such as insufficient reliability, limited lifespan, and low storage density, resulting in considerably huge energy consumption [176–178]. If people continue to rely on conventional technologies, it will further exacerbate the global energy shortage. Therefore, there is an ever-urgent demand to develop long-term, energy saving, and high-density data storage technologies.

The erasable and rewritable polarization-dependent birefringence properties of nanogratings make this structure highly favorable for high density data storage. In 2008, Taylor et al. [90] demonstrated the in situ information rewriting based on the nanograting structures in fused silica where data voxels are effectively rewritten by following pulses with new polarization angled 45° to the initial one. In 2010, Shimotsuma et al. [179] demonstrated five-dimensional (5D) optical data storage by introducing the optical retardance and the azimuth angle of the slow axis of nanogratings as information multiplexing channels on the basis of XYZ spatial coordinates (Fig. 10(a)) whose storage density can be as large as 300 Gbit/cm^3, about 10 times as that of a 12 cm BlueRay disk. In 2015, Zhang et al. [180] characterized the lifetime of nanograting-based 5D optical data storage by thermally accelerated aging measurements. According to Arrhenius law, the room temperature decay time of nanogratings can be as long as $\sim 3 \times 10^{20}$ years (Fig. 10(b)), implying that the theoretical lifetime of the nanograting-based 5D optical data storage in fused silica is comparable to the age of the Universe, namely, an unlimited data storage lifetime.

However, as the formation of nanogratings in transparent dielectrics generally requires multi-pulses incidence, the recording speed of the nanograting-based data storage is limited by the incident pulse number per unit time. Besides, the pulse energy for nanograting creation is considerably high and the readout accuracy remains not enough, which is unfavorable for developing low-power data storage. Recently, Yan et al. [181] proposed a quasi-single-pulse approach to generate anisotropic nanostructures with birefringence properties in fused silica that allow high-speed data recording. In their proposal, the anisotropic nanostructure is induced by the spatiotemporal manipulation of a picosecond laser. The temporal manipulation is achieved by a beam splitter or a birefringence crystal that can split a single ultrafast pulse into two pulses. The spatial manipulation is achieved

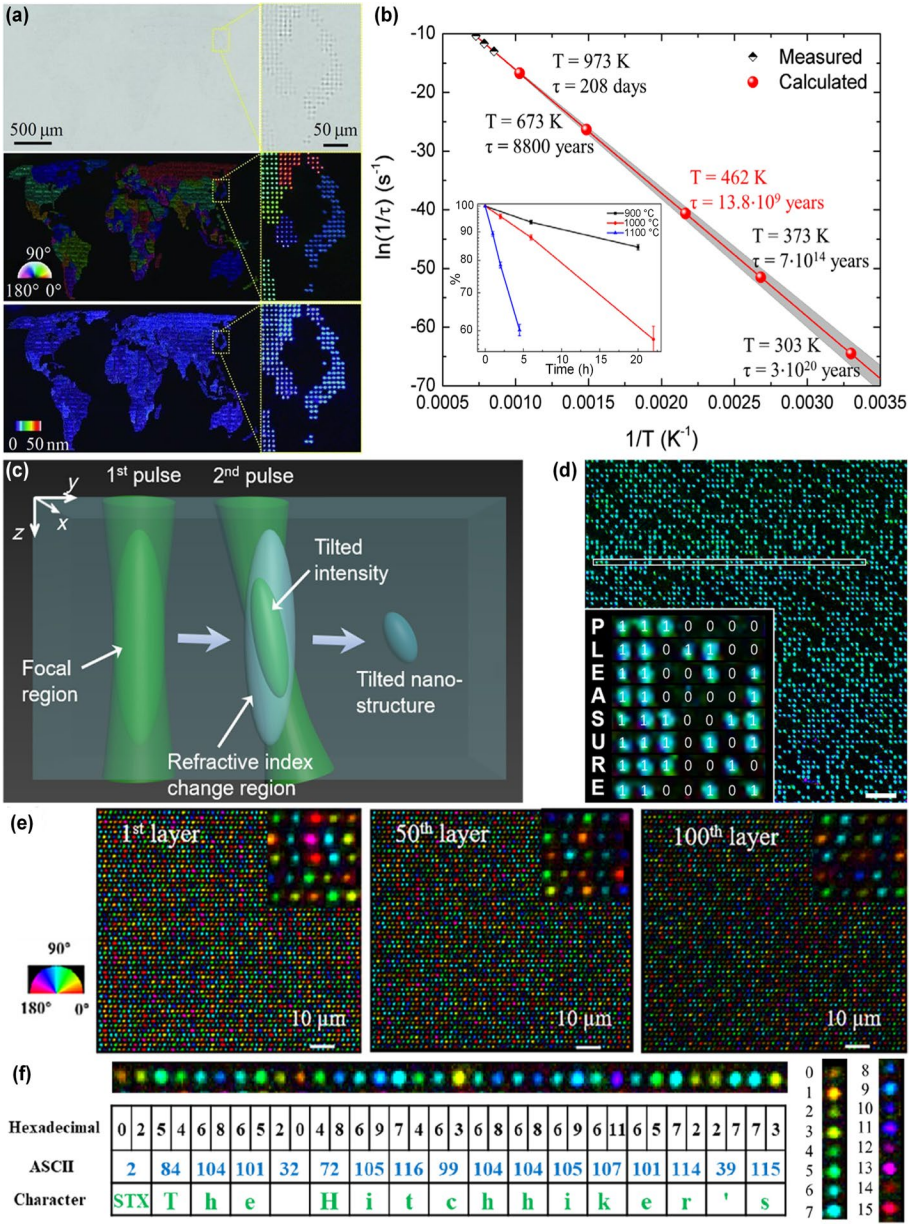

Fig. 10 **a** 5D optical data storage with nanogratings in fused silica, including XYZ coordinates (up), slow axis orientation (middle), and optical retardance (below) [179]. Copyright 2010, Wiley–VCH. **b** Theoretical nanograting decay times at certain temperatures [180]. Copyright 2015, American Physical Society. **c** Schematic of formation mechanism of tilted anisotropic nanostructure and **d**) corresponding decoded data [181]. Copyright 2021, Optica Publishing Group. e 100-layer optical data storage with nanopores in fused silica [182]. Copyright 2022, Wiley–VCH. **f** Energy-efficient data storage with nanovoids induced by near-field enhancement effect [145]. Copyright 2021, Optica Publishing Group

by an SLM device that can dynamically manipulate the relative location of the first pulse and second pulse. The first pulse is used to excite STEs to induce a temporary high absorption and positive refractive index change. Then the second pulse partly interacts with the pre-modified area, creating a tilted intensity distribution, which is the origin of the anisotropic nanostructure (Fig. 10(c)). The readout accuracy of the written information can be up to 99.09% (Fig. 10(d)). Wang et al. [182] reported a high capacity multilayer 5D optical data storage based on ultrafast laser-induced polarization-dependent

nanopores that can greatly reduce the scattering loss of light. Benefitting from the high transmittance (99%), the readout accuracy of this multi-layer data storage can be considerably high. As proof, they demonstrated the recording of "The Hitchhiker's Guide to the Galaxy" into 100 layers of birefringent voxels in fused silica and the readout accuracy is examined as high as 100% (Fig. 10(e)). Lei et al. [145] demonstrated a fast and energy-efficient data recording approach by near-field enhancement mediated energy deposition manipulation. There, an isotropic circular nanovoid (~130 nm) is first induced by seeding pulses with pulse energy higher than the micro-explosion threshold and an anisotropic nano lamella-shaped structure (~460 nm) is then created by low-power writing pulses via the near-field enhancement effect (Fig. 10(f)). In the data recording, the incident pulse train consists of one seeding pulse (30 nJ) and seven (13.5 nJ) writing pulses for high retardance (~3 nm) or one seeding pulse (24 nJ) and four (13.5 nJ) writing pulses for low retardance (~1 nm). The information writing speed can be 225 Kb/s (6×10^5 voxels/s) and the readout accuracy is examined at 99.5% and 96.3% for the top layer and the bottom layer (50 layers).

In summary, multiple types of ULSN-produced structures have shown great potential in developing next-generation optical storage technologies with considerably high data density, readout accuracy, and storage lifetime. However, current ULSN-based multi-dimensional data recording largely relies on multi-pulse incidence or seed pulse pre-modification in fused silica, which greatly limits the data writing speed. Besides, the optical setups for multi-dimensional information readout are too complex and bulky to satisfy the requirements of commercial applications. Therefore, real single pulse data recording routes still need to be exploited, where new storage media, data writing/readout mechanisms, algorithms for fast data extraction, and especially the miniaturization of memory systems are waiting for further investigation.

Micro-nano fluidic devices

The rapid development of ULSN greatly boosts the field of advanced manufacturing. Especially, ultrafast laser micromachining in transparent media produces various types of material modifications, such as defects, refractive index changes, cracks/voids, and so forth. By utilizing the unique physicochemical properties of the ULSN-modified area, on-demand subtractive nanostructuring with higher resolution and controllability can be further achieved. One representative example is ULSN-assisted 3D fluidic channel fabrication in transparent dielectrics.

In 2013, Liao et al. [183] proposed a sub-50 nm nanostructuring approach based on ULSN-induced nanogratings in a homemade high-silicate SiO_2-B_2O_3-Na_2O porous glass. There, the induced nanogratings are induced as polarization-dependent periodic hollow nanovoids in the porous glass. By fixing the laser polarization perpendicular to the scanning direction and reducing the pulse energy to a certain value (~60 nJ), a single central nanovoid elongated in the writing path with a width of ~37 nm can be solely induced (Fig. 11(a) and (b)). The single nanovoid can be connected into a continuous nano-channel by using a low laser writing speed of 5–10 μm/s and a post-annealing treatment is applied to collapse the inherent nanopores in the glass matrix. The fluidic functionality is confirmed by filling the nano-channels with an observable fluorescent dye solution. They further fabricated integrated micro-nano fluidic systems by simultaneously inscribing

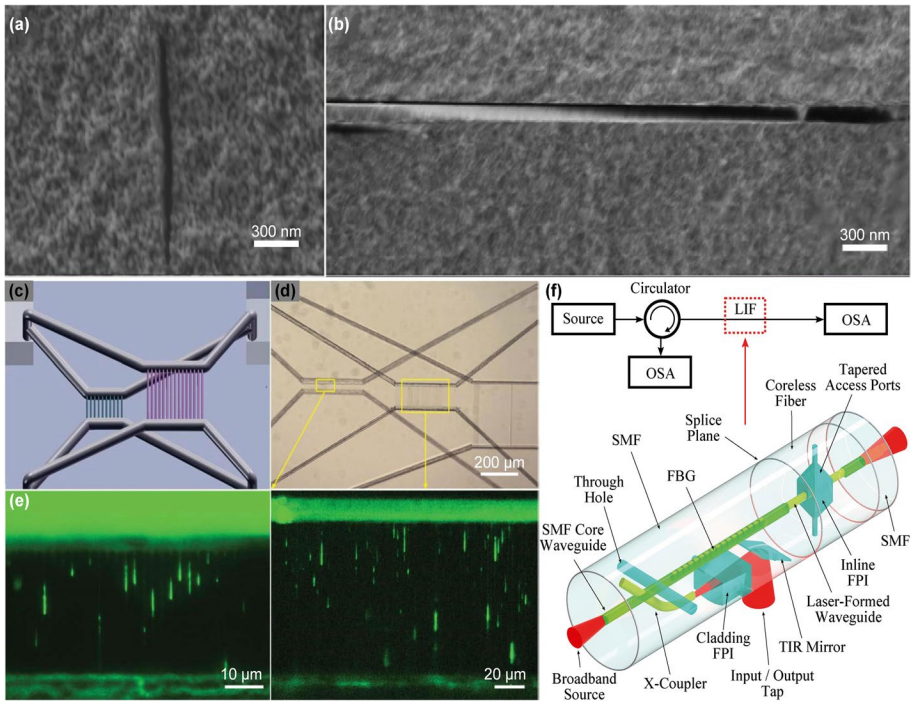

Fig. 11 **a** Cross section and **b** top view SEM image of a single nanochannel induced in SiO_2-B_2O_3-Na_2O porous glass by ULSN [183]. Copyright 2013, Optica Publishing Group. **c** Schematic and **d**) top-view optical image of 3D fluidic systems for DNA analysis, and **e**) fluorescent images of DNA stretching in nanochannels [184]. Copyright 2013, Royal Society of Chemistry. **f** Schematic of integrated LIF optofluidic systems [185]. Copyright 2014, Royal Society of Chemistry

conventional micro-channels and ULSN-based nano-channels into 3D fluidic configurations in the glass matrix [184]. The micro-nano fluidic systems are demonstrated as lab-on-a-chip devices for deoxyribonucleic acid (DNA) analysis and the stretching behaviors of DNA molecules are clearly observed in the nano-channels (Fig. 11(c)-(e)), opening up new approaches for the investigation of single molecular behaviors.

Recently, ultrafast laser-assisted subtractive fabrication has developed to become an effective tool for structuring all-inorganic transparent dielectrics in 3D by utilizing the great etching rate difference in chemical etchants of the irradiated and unirradiated zones [186–189]. ULSN process has been confirmed to possess multi-dimensionally controllable super-resolution material modification abilities that are well suited for higher precision etching in transparent dielectrics, namely, ULSN-assisted etching. Hnatovsky et al. and Cheng et al. [91, 97, 190, 191] systematically studied the selective etching properties of nanogratings in glasses and revealed the highly differential etching rate inside nanogratings, which lays the foundation for ULSN-assisted microfluidic channel fabrication. Haque et al. [185] further combined ULSN-assisted etching and ultrafast laser 3D structuring inside optical fibers to construct highly integrated lab-in-fiber (LIF) optofluidic systems that consist of various microfluidic channels and optical resonators (Fig. 11(f)). The fabricated LIF devices are demonstrated to possess broad prospects in in-line bend, strain, refractive index, and temperature sensing.

ULSN-assisted micro-nano fabrication provides a facile and powerful approach for constructing advanced micro-fluidic devices. However, current studies largely focus on structure minimizing and efficiency improvement. There are still research gaps in

on-demand channel shape control, inner-surface engineering, and modular integration of micro-fluidic systems. With the advent of various new types of ULSN phenomena, mechanisms, and materials, more novel ULSN-assisted micro-nano fluidic technologies aiming for fields like personalized medicine, fast virus detection, and efficient microreactors, are expected to be new hotspots in this field.

Other applications

In addition to the classic applications, some intriguing ULSN-based applications have also begun to sprout in recent years, providing new insights into frontier fields like extreme fabrication, structural coloration, and chiral optics.

For example, Yan et al. [146] proposed a direct optical nanofabrication approach that enables 3D processing in fused silica with a considerably high spatial resolution down to 40 nm and a lateral spacing down to 200 nm. This technology is based on the creation of a polarization-dependent single nanoslit structure by using ULSN. Specifically, the laser polarization is set perpendicular to the scanning direction to activate the continuous growth of the structure along the writing path and thus form a high-aspect-ratio single nanoslit structure, where the near-field redistribution induced by the presence of the nanoslit allows for achieving a lateral spacing much smaller than the laser beam size. As a proof of concept, they demonstrated the fabrication of customized 3D nanostructures formed by nanoslits (Fig. 12(a)). This ULSN process can serve as a general

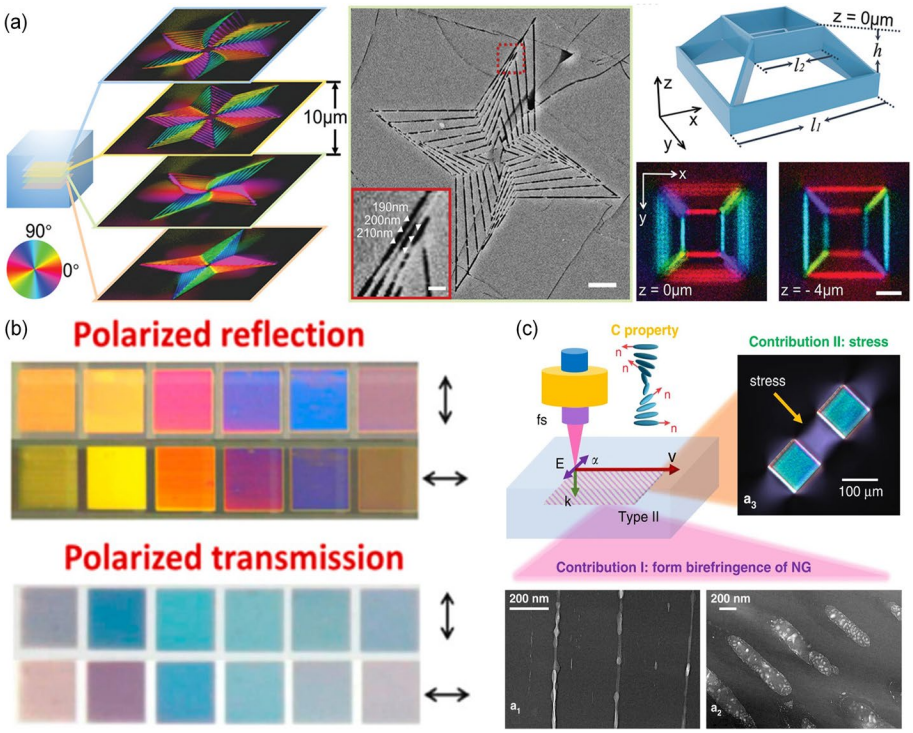

Fig. 12 **a** 3D nanofabrication based on the ULSN creation of self-organized nanosilts, including nanopatterns in four layers (left), SEM image of the nanopattern in the third layer (middle), and truncated pyramid structure (right) [146]. Pseudo colors show the orientation of the slow axis. Copyright 2021, Wiley–VCH. **b** Polarization-sensitive color generated by grating structures in nanocomposite films [133]. Copyright 2017, American Chemical Society. **c** ULSN creation of nanogratings possessing circular properties [192]. Copyright 2023, Springer Nature

nanofabrication approach that is broadly applicable in constructing functional structures for nanophotonics, nanofluidics, nanomechanics, metamaterials, and information recording.

In 2017, Liu et al. [133] reported a novel coloration route based on ULSN-produced 3D metallic nanostructures in a nanocomposite thin film (Ag NPs: TiO_2). In this work, they presented that the irradiation of a linearly polarized ultrafast laser on the film can simultaneously excite two independent propagating optical modes (a surface mode and a guided mode) and both of these modes can interact with incident waves to establish periodic field distributions, leading to the creation of composite self-assembled nanostructures with two periodicities. By utilizing the diffractive and polarization-sensitive properties of the induced nanostructures, they demonstrated the high potential of this ULSN strategy in structural coloration and multiplexed optical image encoding (Fig. 12(b)). This work also prospected the potential of such nanostructured composite films in applications like solar energy harvesting, photocatalysis, and photochromic devices.

Recently, Lu et al. [192] reported the tailoring of chiral optical properties in 3D by ULSN in an initially achiral material (silica glass). In a simple view, they observed that there are two major contributions that ULSN-produced nanogratings own to its aggregate birefringent response, namely, a form and a stress-related one (Fig. 12(c)), and then respectively investigated the polarization-dependence properties of these two contributions and established a two-layer model based on Mueller formalism to describe the generation of chiral optical properties of the laser-modified area. Under the guidance of this model, they demonstrated two types of chiral optical elements, including nanograting-based waveplates and stress-based waveplates to achieve customized optical rotation. Predictably, the presented principle allows for flexibly designing 3D structured light beams in terms of phase, amplitude, and polarization, providing a novel perspective on tailoring the optical properties of transparent dielectrics.

Although still in their infancy, these studies are impressive enough to represent an important milestone in shaping ULSN into a highly flexible and versatile tool for promoting advanced material modification and light-matter interaction physics. However, many of the envisioned application scenarios in these reports are still to be implemented and a more exhaustive performance characterization of the corresponding devices or elements is required. Towards practical applications, more work is still required in the future to improve manufacturing efficiency, structural controllability, as well as the uniformity of mass production.

Conclusions and outlook

ULSN in transparent dielectrics has made remarkable progress in creating a versatile platform for ultrafast laser-matter interactions and extreme material processing, giving birth to a large number of new phenomena, theoretical models, and engineering applications, which offers competitive solutions to many challenging problems in various multidisciplinary fields, including quantum technology, big data storage, advanced optical sensing, detecting, imaging, and communication. Predictably, ULSN will continue to be a hot research topic in strong-field physics in the future and bring us more fascinating discoveries.

In this review, we comb recent progress and key milestones in ULSN and ULSN-based technologies. Nanograting, as the most widely researched object, has established itself as an important mother structure for predicting and exploiting more ULSN approaches due to its highly general physicochemical characteristics. Excitingly, we note that a rising number of unprecedented phenomena have emerged in recent years one after another, and gradually developed into important branches of ULSN. Inspired by the formation mechanism of nanogratings, novel theories and physical models have been proposed to explain newly discovered ULSN phenomena and direct the structural manipulation, which is followed by a burst of pioneering applications based on these ULSN-produced structures. We excitingly witness a giant improvement in the performances of various elements and devices fabricated by ULSN, which benefits from the favorable properties of the created structures. However, the fast progress of ULSN is accompanied by plenty of conflicts and puzzles between new concepts and established theoretical frameworks. The specific roles of optical scattering, interference, and field enhancement effect in ULSN process are still controversial and the plasma and defect-mediated structural evolution process remain largely unclear. As a result, it is still far away from achieving a consensus on the essence of ULSN. In the future, advanced ultrafast dynamics detection approaches like pump-probe spectroscopy [193], ultrafast photography [194], and ultrafast electro-optical imaging [195] would be useful to provide more intuitive experimental evidence for different models and unravel these mysteries. Moreover, we have recently witnessed the booming of various optical modulation technologies, including super-resolution microscopy [196], adaptive aberration control [197], SLM [198], and optical parametric amplifier (OPA) [199], etc. We believe these technologies can serve as powerful tools during ULSN process to achieve much more flexible structural manipulation of the period, height, and uniformity of the self-organized structures in the near future.

The rapid expansion of technologies like data mining, machine learning, and artificial intelligence, has brought human society into the era of information on explosion. Light, as a powerful information carrier, represents the future of information technologies where transparent dielectrics provide a versatile platform for light manipulation. ULSN in transparent dielectrics offers a tremendously attractive brand new idea for artificially tailoring natural materials to realize on-demand manipulation of light at micro-nano scale. Therefore, the future orientation of ULSN would be the enabler for highly integrated optical information processing, transmission, and storage. Technically, the coupling between ULSN-produced micro-nano optical elements and commercial optoelectronic devices is desired to be optimized. Multifunctional integrated optical systems across materials and elements have not been effectively demonstrated by ULSN. In addition, standardized, efficient, and mass ULSN fabrication is urgently needed to be achieved. For ULSN-based multi-dimensional data storage, there is still significant space to improve the information recording and readout speed. Higher density data storage with more information multiplexing channels, such as light frequency and photon orbital angular momentum (OAM) [200–202], remains to be further explored by ULSN in transparent dielectrics. In addition, the data writing and reading systems are not integrated and facile enough for commercial use. Thus, more efforts are needed to be invested in solving these problems.

ULSN in transparent dielectrics has developed into a broad research field rather than a small subdivision. Therefore, future research should be systematic and intrinsically associated with physics, optics, material science, computer science, and mechanical engineering. It is exciting to combine ULSN with diverse frontier cross-disciplinary technologies to establish a family of universal multifunctional material modification methods that can freely manipulate ULSN processes and construct arbitrary geometries and complicated systems in arbitrary materials.

Abbreviations

ULSN	Ultrafast laser-induced self-organized nanostructuring
3D	Three-dimensional
RI	Refractive index
LTN	La_2O_3-Ta_2O_5-Nb_2O_5
SEM	Scanning electron microscopy
HRTEM	High-resolution transmission electron microscopy
TEM	Transmission electron microscopy
NPs	Nanoparticles
STEs	Self-trapped excitons
EPR	Electron paramagnetic resonance
FNGs	Fiber nanogratings
5D	Five-dimensional
DNA	DeoxyriboNucleic acid
LIF	Lab-in-fiber
SLM	Spatial light modulation
OPA	Optical parametric amplifier
OAM	Photon orbital angular momentum

Acknowledgements
Not applicable.

Authors' contributions
Writing-original draft preparation: BZ, ZW. Writing-review and editing: DT, JQ. BZ was a major contributor in writing the manuscript. All authors read and approved the final manuscript.

Funding
This work was financially supported by the National Natural Science Foundation of China (Grant Nos. U20A20211, 51902286, 61905215, and 62005164); the National Key R&D Program of China (No. 2021YFB2800500); the Key Research Project of Zhejiang Lab; China Postdoctoral Science Foundation (2021M702799).

Availability of data and materials
The datasets and figures used and analyzed during the current study are available from the corresponding author on reasonable request.

Declarations

Competing interests

The authors declare that they have no competing interests.

Received: 23 November 2022 Revised: 24 June 2023 Accepted: 12 July 2023
Published online: 25 July 2023

References

1. Wang X-J, Fang H-H, Sun F-W, Sun H-B. Laser Writing of Color Centers. Laser Photonics Rev. 2022;16:2100029. https://doi.org/10.1002/lpor.202100029.
2. Du Y, et al. Precipitation of CsPbBr 3 quantum dots in borophosphate glasses inducted by heat-treatment and UV-NIR ultrafast lasers. Chem Eng J. 2020;401:126132. https://doi.org/10.1016/j.cej.2020.126132.
3. Mizuochi N, et al. Electrically driven single-photon source at room temperature in diamond. Nat Photonics. 2012;6:299–303. https://doi.org/10.1038/nphoton.2012.75.
4. Jin D, et al. 22.5-W narrow-linewidth diamond Brillouin laser at 1064 nm. Opt Lett. 2022;47:5360–3. https://doi.org/10.1364/OL.471447.
5. Yu M, et al. Integrated femtosecond pulse generator on thin-film lithium niobate. Nature. 2022. https://doi.org/10.1038/s41586-022-05345-1.

6. Fang J, et al. 3D waveguide device for few-mode multi-core fiber optical communications. Photon Res. 2022;10:2677–85. https://doi.org/10.1364/PRJ.465174.
7. Wang P, Wang Y, Tong L. Functionalized polymer nanofibers: a versatile platform for manipulating light at the nanoscale. Light Sci Appl. 2013;2:102. https://doi.org/10.1038/lsa.2013.58.
8. Tan D, et al. Fabricating low loss waveguides over a large depth in glass by temperature gradient assisted femtosecond laser writing. Opt Lett. 2020;45:3941–4. https://doi.org/10.1364/OL.396861.
9. Xu P, et al. Elastic ice microfibers. Science. 2021;373:187–92. https://doi.org/10.1126/science.abh3754.
10. Zhang X-L, et al. Non-Abelian braiding on photonic chips. Nat Photonics. 2022;16:390–5. https://doi.org/10.1038/s41566-022-00976-2.
11. Li L, et al. Integrated flexible chalcogenide glass photonic devices. Nat Photonics. 2014;8:643–9. https://doi.org/10.1038/nphoton.2014.138.
12. Pelucchi E, et al. The potential and global outlook of integrated photonics for quantum technologies. Nat Rev Phys. 2022;4:194–208. https://doi.org/10.1038/s42254-021-00398-z.
13. Wang T, et al. Periodically poled LiNbO3 crystals from 1D and 2D to 3D. SCIENCE CHINA Technol Sci. 2020;63:1110–26. https://doi.org/10.1007/s11431-019-1503-0.
14. Zhu D, et al. Integrated photonics on thin-film lithium niobate. Adv Opt Photon. 2021;13:242–352. https://doi.org/10.1364/AOP.411024.
15. Juodkazis S, et al. Optical third harmonic generation during femtosecond pulse diffraction in a Bragg grating. J Phys D Appl Phys. 2006;39:50. https://doi.org/10.1088/0022-3727/39/1/009.
16. Dezhi T, Zhuo W, Beibei X, Jianrong Q. Photonic circuits written by femtosecond laser in glass: improved fabrication and recent progress in photonic devices. Adv Photonic. 2021;3:1–24. https://doi.org/10.1117/1.AP.3.2.024002.
17. Meany T, et al. Laser written circuits for quantum photonics. Laser Photonics Rev. 2015;9:363–84. https://doi.org/10.1002/lpor.201500061.
18. Sun K, et al. Three-dimensional direct lithography of stable perovskite nanocrystals in glass. Science. 2022;375:307–10. https://doi.org/10.1126/science.abj2691.
19. Chen F, de Aldana JRV. Optical waveguides in crystalline dielectric materials produced by femtosecond-laser micromachining. Laser Photonics Rev. 2014;8:251–75. https://doi.org/10.1002/lpor.201300025.
20. Zhang X-L, et al. Non-Abelian braiding on photonic chips. Nat Photonics. 2022. https://doi.org/10.1038/s41566-022-00976-2.
21. Pezzagna S, Meijer J. Quantum computer based on color centers in diamond. Appl Phys Rev. 2021;8:011308. https://doi.org/10.1063/5.0007444.
22. Lenzini F, Gruhler N, Walter N, Pernice WHP. Diamond as a Platform for Integrated Quantum Photonics. Adv Quantum Technol. 2018;1:1800061. https://doi.org/10.1002/qute.201800061.
23. Ams M, Marshall GD, Spence DJ, Withford MJ. Slit beam shaping method for femtosecond laser direct-write fabrication of symmetric waveguides in bulk glasses. Opt Express. 2005;13:5676–81. https://doi.org/10.1364/OPEX.13.005676.
24. Kowalevicz AM, Sharma V, Ippen EP, Fujimoto JG, Minoshima K. Three-dimensional photonic devices fabricated in glass by use of a femtosecond laser oscillator. Opt Lett. 2005;30:1060–2. https://doi.org/10.1364/OL.30.001060.
25. Marshall GD, et al. Laser written waveguide photonic quantum circuits. Opt Express. 2009;17:12546–54. https://doi.org/10.1364/OE.17.012546.
26. Sun Y-K, et al. Non-Abelian Thouless pumping in photonic waveguides. Nat Phys. 2022;18:1080–5. https://doi.org/10.1038/s41567-022-01669-x.
27. Crespi A, et al. Integrated photonic quantum gates for polarization qubits. Nat Commun. 2011;2:566. https://doi.org/10.1038/ncomms1570.
28. Crespi A, et al. Integrated multimode interferometers with arbitrary designs for photonic boson sampling. Nat Photonics. 2013;7:545–9. https://doi.org/10.1038/nphoton.2013.112.
29. Wang C-Y, Gao J, Jin X-M. On-chip rotated polarization directional coupler fabricated by femtosecond laser direct writing. Opt Lett. 2019;44:102–5. https://doi.org/10.1364/OL.44.000102.
30. Xu T, et al. Three-dimensional nonlinear photonic crystal in ferroelectric barium calcium titanate. Nat Photonics. 2018;12:591–5. https://doi.org/10.1038/s41566-018-0225-1.
31. Wei D, et al. Efficient nonlinear beam shaping in three-dimensional lithium niobate nonlinear photonic crystals. Nat Commun. 2019;10:4193. https://doi.org/10.1038/s41467-019-12251-0.
32. Wei D, et al. Experimental demonstration of a three-dimensional lithium niobate nonlinear photonic crystal. Nat Photonics. 2018;12:596–600. https://doi.org/10.1038/s41566-018-0240-2.
33. Ouyang X, et al. Synthetic helical dichroism for six-dimensional optical orbital angular momentum multiplexing. Nat Photonics. 2021;15:901–7. https://doi.org/10.1038/s41566-021-00880-1.
34. Wang Z, Tan D, Qiu J. Single-shot photon recording for three-dimensional memory with prospects of high capacity. Opt Lett. 2020;45:6274–7. https://doi.org/10.1364/OL.409171.
35. Gao L, Zhang Q, Evans RA, Gu M. 4D Ultra-High-Density Long Data Storage Supported by a Solid-State Optically Active Polymeric Material with High Thermal Stability. Adv Opt Mater. 2021;9:2100487. https://doi.org/10.1002/adom.202100487.
36. Sung JH, et al. 4.2 PW, 20 fs Ti:sapphire laser at 0.1 Hz. Opt Lett. 2017;42:2058–61. https://doi.org/10.1364/OL.42.002058.
37. Tan D, Sharafudeen KN, Yue Y, Qiu J. Femtosecond laser induced phenomena in transparent solid materials: Fundamentals and applications. Prog Mater Sci. 2016;76:154–228. https://doi.org/10.1016/j.pmatsci.2015.09.002.
38. Gattass RR, Mazur E. Femtosecond laser micromachining in transparent materials. Nat Photonics. 2008;2:219–25. https://doi.org/10.1038/nphoton.2008.47.
39. Huang X, et al. Reversible 3D laser printing of perovskite quantum dots inside a transparent medium. Nat Photonics. 2020;14:82–8. https://doi.org/10.1038/s41566-019-0538-8.
40. Guo B, et al. Femtosecond Laser Micro/Nano-manufacturing: Theories, Measurements, Methods, and Applications. Nanomanufacturing Metrol. 2020;3:26–67. https://doi.org/10.1007/s41871-020-00056-5.

41. Jia Y, Wang S, Chen F. Femtosecond laser direct writing of flexibly configured waveguide geometries in optical crystals: fabrication and application. Opto-Electronic Advances. 2020;3, 190042-190041-190042-190012, https://doi.org/10.29026/oea.2020.190042.
42. Lin Z, Hong M. Femtosecond Laser Precision Engineering: From Micron, Submicron, to Nanoscale. Ultrafast Science. 2021;2021:9783514. https://doi.org/10.34133/2021/9783514.
43. Tan D, Zhang B, Qiu J. Ultrafast Laser Direct Writing in Glass: Thermal Accumulation Engineering and Applications. Laser Photonics Rev. 2021;15:2000455. https://doi.org/10.1002/lpor.202000455.
44. Hu Y, Zhang W, Ye Y, Zhao Z, Liu C. Femtosecond-Laser-Induced Precipitation of CsPbBr 3 Perovskite Nanocrystals in Glasses for Solar Spectral Conversion. ACS Applied Nano Materials. 2020;3:850–7. https://doi.org/10.1021/acsanm.9b02362.
45. Eliezer S, et al. Synthesis of nanoparticles with femtosecond laser pulses. Physical Review B. 2004;69:144119. https://doi.org/10.1103/PhysRevB.69.144119.
46. Maximova K, Aristov A, Sentis M, Kabashin AV. Size-controllable synthesis of bare gold nanoparticles by femtosecond laser fragmentation in water. Nanotechnology. 2015;26:065601. https://doi.org/10.1088/0957-4484/26/6/065601.
47. Liu S-F, et al. 3D nanoprinting of semiconductor quantum dots by photoexcitation-induced chemical bonding. Science. 2022;377:1112–6. https://doi.org/10.1126/science.abo5345.
48. Yuan Y, et al. Ultrafast Shaped Laser Induced Synthesis of MXene Quantum Dots/Graphene for Transparent Supercapacitors. Adv Mater. 2022;34:2110013. https://doi.org/10.1002/adma.202110013.
49. Xing J-F, Zheng M-L, Duan X-M. Two-photon polymerization microfabrication of hydrogels: an advanced 3D printing technology for tissue engineering and drug delivery. Chem Soc Rev. 2015;44:5031–9. https://doi.org/10.1039/C5CS00278H.
50. Geng Q, Wang D, Chen P, Chen S-C. Ultrafast multi-focus 3-D nano-fabrication based on two-photon polymerization. Nat Commun. 2019;10:2179. https://doi.org/10.1038/s41467-019-10249-2.
51. Kotz F, et al. Two-Photon Polymerization of Nanocomposites for the Fabrication of Transparent Fused Silica Glass Microstructures. Adv Mater. 2021;33:2006341. https://doi.org/10.1002/adma.202006341.
52. Hua JG, Liang SY, Chen QD, Juodkazis S, Sun HB. Free-Form Micro-Optics Out of Crystals: Femtosecond Laser 3D Sculpturing. Advanced Functional Materials n/a, 2200255, https://doi.org/10.1002/adfm.202200255 (2022).
53. Fang Y, et al. Liquid-Infused Slippery Stainless Steel Surface Prepared by Alcohol-Assisted Femtosecond Laser Ablation. Adv Mater Interfaces. 2021;8:2001334. https://doi.org/10.1002/admi.202001334.
54. Balling P, Schou J. Femtosecond-laser ablation dynamics of dielectrics: basics and applications for thin films. Rep Prog Phys. 2013;76:036502. https://doi.org/10.1088/0034-4885/76/3/036502.
55. Yu L, et al. Nanochannels with a 18-nm feature size and ultrahigh aspect ratio on silica through surface assisting material ejection. Adv Photonics Nexus. 2022;1:026004. https://doi.org/10.1117/1.APN.1.2.026004.
56. Stone A, et al. Directionally controlled 3D ferroelectric single crystal growth in LaBGeO5 glass by femtosecond laser irradiation. Opt Express. 2009;17:23284–9. https://doi.org/10.1364/OE.17.023284.
57. Miura K, Qiu J, Mitsuyu T, Hirao K. Space-selective growth of frequency-conversion crystals in glasses with ultrashort infrared laser pulses. Opt Lett. 2000;25:408–10. https://doi.org/10.1364/OL.25.000408.
58. Stone A, et al. Formation of ferroelectric single-crystal architectures in LaBGeO5 glass by femtosecond vs. continuous-wave lasers. J Non-Cryst Solids. 2010;356:3059–65. https://doi.org/10.1016/j.jnoncrysol.2010.03.048.
59. Zheng Y, et al. Valence state manipulation of Sm3+ ions via a phase-shaped femtosecond laser field. Photon Res. 2018;6:144–8. https://doi.org/10.1364/PRJ.6.000144.
60. Qiu J, et al. Space-selective valence state manipulation of transition metal ions inside glasses by a femtosecond laser. Appl Phys Lett. 2001;79:3567–9. https://doi.org/10.1063/1.1421640.
61. Royon A, et al. Silver Clusters Embedded in Glass as a Perennial High Capacity Optical Recording Medium. Adv Mater. 2010;22:5282–6. https://doi.org/10.1002/adma.201002413.
62. Tokel O, et al. In-chip microstructures and photonic devices fabricated by nonlinear laser lithography deep inside silicon. Nat Photonics. 2017;11:639–45. https://doi.org/10.1038/s41566-017-0004-4.
63. Liu X-Q, et al. Biomimetic sapphire windows enabled by inside-out femtosecond laser deep-scribing. PhotoniX. 2022;3:1. https://doi.org/10.1186/s43074-022-00047-3.
64. Liu X-Q, Bai B-F, Chen Q-D, Sun H-B. Etching-assisted femtosecond laser modification of hard materials. Opto-Electronic Advances. 2019;2:190021–190021. https://doi.org/10.29026/oea.2019.190021.
65. Geng J, Yan W, Shi L, Qiu M. Surface plasmons interference nanogratings: wafer-scale laser direct structuring in seconds. Light. 2022;11:189. https://doi.org/10.1038/s41377-022-00883-9.
66. Li Z-Z, et al. O-FIB: far-field-induced near-field breakdown for direct nanowriting in an atmospheric environment. Light. 2020;9:41. https://doi.org/10.1038/s41377-020-0275-2.
67. Chen L, et al. Large-area straight, regular periodic surface structures produced on fused silica by the interference of two femtosecond laser beams through cylindrical lens. Opto-Electronic Advances. 2021;4, 200036–200031–200036–200039, https://doi.org/10.29026/oea.2021.200036
68. Yong J, Chen F, Yang Q, Jiang Z, Hou X. A Review of Femtosecond-Laser-Induced Underwater Superoleophobic Surfaces. Adv Mater Interfaces. 2018;5:1701370. https://doi.org/10.1002/admi.201701370.
69. Vorobyev AY, Guo C. Direct femtosecond laser surface nano/microstructuring and its applications. Laser Photonics Rev. 2013;7:385–407. https://doi.org/10.1002/lpor.201200017.
70. Qiao M, Yan J, Jiang L. Direction Controllable Nano-Patterning of Titanium by Ultrafast Laser for Surface Coloring and Optical Encryption. Adv Opt Mater. 2022;10:2101673. https://doi.org/10.1002/adom.202101673.
71. Bonse J, Gräf S. Maxwell Meets Marangoni—A Review of Theories on Laser-Induced Periodic Surface Structures. Laser Photonics Rev. 2020;14:2000215. https://doi.org/10.1002/lpor.202000215.
72. Shimotsuma Y, Kazansky PG, Qiu J, Hirao K. Self-Organized Nanogratings in Glass Irradiated by Ultrashort Light Pulses. Phys Rev Lett. 2003;91:247405. https://doi.org/10.1103/PhysRevLett.91.247405.
73. Öktem B, et al. Nonlinear laser lithography for indefinitely large-area nanostructuring with femtosecond pulses. Nat Photonics. 2013;7:897–901. https://doi.org/10.1038/nphoton.2013.272.

74. Mastellone M, et al. Deep-Subwavelength 2D Periodic Surface Nanostructures on Diamond by Double-Pulse Femtosecond Laser Irradiation. Nano Lett. 2021;21:4477–83. https://doi.org/10.1021/acs.nanolett.1c01310.
75. Sun X-C, et al. Wafer-scale high aspect-ratio sapphire periodic nanostructures fabricated by self-modulated femtosecond laser hybrid technology. Opt Express. 2022;30:32244–55. https://doi.org/10.1364/OE.463575.
76. Huang M, Zhao F, Cheng Y, Xu N, Xu Z. Origin of Laser-Induced Near-Subwavelength Ripples: Interference between Surface Plasmons and Incident Laser. ACS Nano. 2009;3:4062–70. https://doi.org/10.1021/nn900654v.
77. Liao Y, et al. High-fidelity visualization of formation of volume nanogratings in porous glass by femtosecond laser irradiation. Optica. 2015;2:329–34. https://doi.org/10.1364/OPTICA.2.000329.
78. Zhang B, et al. Self-organized phase-transition lithography for all-inorganic photonic textures. Light. 2021;10:93. https://doi.org/10.1038/s41377-021-00534-5.
79. Rudenko A, et al. Spontaneous periodic ordering on the surface and in the bulk of dielectrics irradiated by ultrafast laser: a shared electromagnetic origin. Sci Rep. 2017;7:12306. https://doi.org/10.1038/s41598-017-12502-4.
80. Beresna M, Gecevičius M, Kazansky PG. Ultrafast laser direct writing and nanostructuring in transparent materials. Adv Opt Photon. 2014;6:293–339. https://doi.org/10.1364/AOP.6.000293.
81. Buividas R, et al. Mechanism of fine ripple formation on surfaces of (semi)transparent materials via a half-wavelength cavity feedback. Nanotechnology. 2011;22:055304. https://doi.org/10.1088/0957-4484/22/5/055304.
82. Beresna M, Gecevičius M, Lancry M, Poumellec B, Kazansky PG. Broadband anisotropy of femtosecond laser induced nanogratings in fused silica. Appl Phys Lett. 2013;103:131903. https://doi.org/10.1063/1.4821513.
83. Cho S-H, Kumagai H, Midorikawa K. In situ observation of dynamics of plasma formation and refractive index modification in silica glasses excited by a femtosecond laser. Optics Communications. 2002;207:243–53. https://doi.org/10.1016/S0030-4018(02)01410-4.
84. Davis KM, Miura K, Sugimoto N, Hirao K. Writing waveguides in glass with a femtosecond laser. Opt Lett. 1996;21:1729–31. https://doi.org/10.1364/OL.21.001729.
85. Buividas R, Mikutis M, Juodkazis S. Surface and bulk structuring of materials by ripples with long and short laser pulses: Recent advances. Prog Quantum Electron. 2014;38:119–56. https://doi.org/10.1016/j.pquantelec.2014.03.002.
86. Sudrie L, Franco M, Prade B, Mysyrowicz A. Writing of permanent birefringent microlayers in bulk fused silica with femtosecond laser pulses. Opt Commun. 1999;171:279–84. https://doi.org/10.1016/S0030-4018(99)00562-3.
87. Kazansky PG, et al. Anomalous Anisotropic Light Scattering in Ge-Doped Silica Glass. Phys Rev Lett. 1999;82:2199–202. https://doi.org/10.1103/PhysRevLett.82.2199.
88. Qiu J, et al. Memorized polarization-dependent light scattering in rare-earth-ion-doped glass. Appl Phys Lett. 2000;77:1940–2. https://doi.org/10.1063/1.1311956.
89. Hnatovsky C, et al. Pulse duration dependence of femtosecond-laser-fabricated nanogratings in fused silica. Appl Phys Lett. 2005;87:014104. https://doi.org/10.1063/1.1991991.
90. Taylor R, Hnatovsky C, Simova E. Applications of femtosecond laser induced self-organized planar nanocracks inside fused silica glass. Laser Photonics Rev. 2008;2:26–46. https://doi.org/10.1002/lpor.200710031.
91. Hnatovsky C, et al. Fabrication of microchannels in glass using focused femtosecond laser radiation and selective chemical etching. Appl Phys A. 2006;84:47–61. https://doi.org/10.1007/s00339-006-3590-4.
92. Sudrie L, et al. Femtosecond Laser-Induced Damage and Filamentary Propagation in Fused Silica. Phys Rev Lett. 2002;89:186601. https://doi.org/10.1103/PhysRevLett.89.186601.
93. Ohfuchi T, et al. Shape control of femtosecond-laser-induced birefringent structures by controlling spherical aberration. J Laser Appl. 2016;28:022603. https://doi.org/10.2351/1.4944115.
94. Lancry M, Brisset F, Poumellec B. In the heart of nanogratings made up during femtosecond laser irradiation, in Advanced Photonics & Renewable Energy, OSA Technical Digest (CD) (Optica Publishing Group, 2010), paper BWC3. https://opg.optica.org/abstract.cfm?URI=BGPP-2010-BWC3.
95. Ramirez LPR, et al. Tuning the structural properties of femtosecond-laser-induced nanogratings. Appl Phys A. 2010;100:1–6. https://doi.org/10.1007/s00339-010-5684-2.
96. Zhang F, Zhang H, Dong G, Qiu J. Embedded nanogratings in germanium dioxide glass induced by femtosecond laser direct writing. J Opt Soc Am B. 2014;31:860–4. https://doi.org/10.1364/JOSAB.31.000860.
97. Hnatovsky C, et al. Polarization-selective etching in femtosecond laser-assisted microfluidic channel fabrication in fused silica. Opt Lett. 2005;30:1867–9. https://doi.org/10.1364/OL.30.001867.
98. Taylor RS, et al. Femtosecond laser erasing and rewriting of self-organized planar nanocracks in fused silica glass. Opt Lett. 2007;32:2888–90. https://doi.org/10.1364/OL.32.002888.
99. Bricchi E, Kazansky PG. Extraordinary stability of anisotropic femtosecond direct-written structures embedded in silica glass. Appl Phys Lett. 2006;88:111119. https://doi.org/10.1063/1.2185587.
100. Richter S, et al. Nanogratings in fused silica: Formation, control, and applications. J Laser Appl. 2012;24:042008. https://doi.org/10.2351/1.4718561.
101. Wang J, Liu X, Dai Y, Wang Z, Qiu J. Effect of sodium oxide content on the formation of nanogratings in germanate glass by a femtosecond laser. Opt Express. 2018;26:12761–8. https://doi.org/10.1364/OE.26.012761.
102. Asai T, et al. Systematic Control of Structural Changes in GeO2 Glass Induced by Femtosecond Laser Direct Writing. J Am Ceram Soc. 2015;98:1471–7. https://doi.org/10.1111/jace.13482.
103. Lancry M, et al. Ultrafast nanoporous silica formation driven by femtosecond laser irradiation. Laser Photonics Rev. 2013;7:953–62. https://doi.org/10.1002/lpor.201300043.
104. Bricchi E, Klappauf BG, Kazansky PG. Form birefringence and negative index change created by femtosecond direct writing in transparent materials. Opt Lett. 2004;29:119–21. https://doi.org/10.1364/OL.29.000119.
105. Hnatovsky C, Shvedov V, Krolikowski W, Rode A. Revealing Local Field Structure of Focused Ultrashort Pulses. Physical Review Letters. 2011;106:123901. https://doi.org/10.1103/PhysRevLett.106.123901.
106. Shugaev MV, et al. Fundamentals of ultrafast laser–material interaction. MRS Bull. 2016;41:960–8. https://doi.org/10.1557/mrs.2016.274.
107. Musgraves JD, Richardson K, Jain H. Laser-induced structural modification, its mechanisms, and applications in glassy optical materials. Opt Mater Express. 2011;1:921–35. https://doi.org/10.1364/OME.1.000921.

108. Wang Y, Lancry M, Cavillon M, Poumellec B. Lifetime prediction of nanogratings inscribed by a femtosecond laser in silica glass. Opt Lett. 2022;47:1242–5. https://doi.org/10.1364/OL.449486.
109. Richter S, et al. Laser induced nanogratings beyond fused silica - periodic nanostructures in borosilicate glasses and ULE™. Opt Mater Express. 2013;3:1161–6. https://doi.org/10.1364/OME.3.001161.
110. Cao J, et al. Form birefringence induced in multicomponent glass by femtosecond laser direct writing. Opt Lett. 2016;41:2739–42. https://doi.org/10.1364/OL.41.002739.
111. Cao J, Mazerolles L, Lancry M, Brisset F, Poumellec B. Modifications in lithium niobium silicate glass by femtosecond laser direct writing: morphology, crystallization, and nanostructure. J Opt Soc Am B. 2017;34:160–8. https://doi.org/10.1364/JOSAB.34.000160.
112. Cao J, Poumellec B, Brisset F, Lancry M. Pulse energy dependence of refractive index change in lithium niobium silicate glass during femtosecond laser direct writing. Opt Express. 2018;26:7460–74. https://doi.org/10.1364/OE.26.007460.
113. Cao J, et al. Femtosecond Laser-Induced Crystallization in Glasses: Growth Dynamics for Orientable Nanostructure and Nanocrystallization. Cryst Growth Des. 2019;19:2189–205. https://doi.org/10.1021/acs.cgd.8b01802.
114. Shimotsuma Y, et al. Self-assembled glass/crystal periodic nanostructure in Al2O3-Dy2O3 binary glass. Appl Phys A. 2018;124:82. https://doi.org/10.1007/s00339-017-1507-z.
115. Zhang B, et al. Self-Organized Periodic Crystallization in Unconventional Glass Created by an Ultrafast Laser for Optical Attenuation in the Broadband Near-Infrared Region. Advanced Optical Materials. 2019;7:1900593. https://doi.org/10.1002/adom.201900593.
116. Zhang B, et al. Ultrafast Laser Inducing Continuous Periodic Crystallization in the Glass Activated via Laser-Prepared Crystallite-Seeds. Adv Opt Mater. 2021;9:2001962. https://doi.org/10.1002/adom.202001962.
117. Kanehira S, Si J, Qiu J, Fujita K, Hirao K. Periodic Nanovoid Structures via Femtosecond Laser Irradiation. Nano Lett. 2005;5:1591–5. https://doi.org/10.1021/nl0510154.
118. Song J, et al. Formation mechanism of self-organized voids in dielectrics induced by tightly focused femtosecond laser pulses. Appl Phys Lett. 2008;92:092904. https://doi.org/10.1063/1.2841066.
119. Song J, et al. Polarization dependence of the self-organized microgratings induced in SrTiO3 crystal by a single femtosecond laser beam. Opt Express. 2013;21:18461–8. https://doi.org/10.1364/OE.21.018461.
120. Hu X, et al. Self-formation of quasiperiodic void structure in CaF2 induced by femtosecond laser irradiation. Journal of Applied Physics. 2007;101:023112. https://doi.org/10.1063/1.2430911.
121. Hu X, et al. Self-formation of void array in Al2O3 crystal by femtosecond laser irradiation. Chin Opt Lett. 2008;6:388–90.
122. Mauclair C, et al. Single-pulse ultrafast laser imprinting of axial dot arrays in bulk glasses. Opt Lett. 2011;36:325–7. https://doi.org/10.1364/OL.36.000325.
123. Hu X, et al. Self-organized microvoid array perpendicular to the femtosecond laser beam in CaF2 crystals. Laser Phys Lett. 2008;5:394–7. https://doi.org/10.1002/lapl.200810006.
124. Song J, et al. Mechanism of femtosecond laser inducing inverted microstructures by employing different types of objective lens. J Phys D. 2011;44:495402. https://doi.org/10.1088/0022-3727/44/49/495402.
125. Luo F, et al. Femtosecond laser-induced inverted microstructures inside glasses by tuning refractive index of objective's immersion liquid. Opt Lett. 2011;36:2125–7. https://doi.org/10.1364/OL.36.002125.
126. Zhang F, et al. Polarization-dependent microstructural evolution induced by a femtosecond laser in an aluminosilicate glass. Opt Express. 2021;29:10265–74. https://doi.org/10.1364/OE.420595.
127. Sakakura M, Lei Y, Wang L, Yu Y-H, Kazansky PG. Ultralow-loss geometric phase and polarization shaping by ultrafast laser writing in silica glass. Light. 2020;9:15. https://doi.org/10.1038/s41377-020-0250-y.
128. Zhang F, et al. Self-assembled three-dimensional periodic micro-nano structures in bulk quartz crystal induced by femtosecond laser pulses. Opt Express. 2019;27:6442–50. https://doi.org/10.1364/OE.27.006442.
129. Zhang F, et al. Evolution of polarization dependent microstructures induced by high repetition rate femtosecond laser irradiation in glass. Opt Express. 2016;24:21353–63. https://doi.org/10.1364/OE.24.021353.
130. Karpinski P, Shvedov V, Krolikowski W, Hnatovsky C. Laser-writing inside uniaxially birefringent crystals: fine morphology of ultrashort pulse-induced changes in lithium niobate. Opt Express. 2016;24:7456–76. https://doi.org/10.1364/OE.24.007456.
131. Xu S, et al. Ultrafast laser-inscribed nanogratings in sapphire for geometric phase elements. Opt Lett. 2021;46:536–9. https://doi.org/10.1364/OL.413177.
132. Zhai Q, et al. Evolution of self-organized nanograting from the pre-induced nanocrack-assisted plasma–laser coupling in sapphire. Appl Phys B. 2021;127:74. https://doi.org/10.1007/s00340-021-07625-6.
133. Liu Z, et al. Three-Dimensional Self-Organization in Nanocomposite Layered Systems by Ultrafast Laser Pulses. ACS Nano. 2017;11:5031–40. https://doi.org/10.1021/acsnano.7b01748.
134. Loeschner K, Seifert G, Heilmann A. Self-organized, gratinglike nanostructures in polymer films with embedded metal nanoparticles induced by femtosecond laser irradiation. J Appl Phys. 2010;108:073114. https://doi.org/10.1063/1.3490191.
135. Eles B, et al. Mechanisms driving self-organization phenomena in random plasmonic metasurfaces under multipulse femtosecond laser exposure: a multitime scale study. 2022;11, 2303-2318, https://doi.org/10.1515/nanoph-2022-0023
136. Wu, B. et al. (2023). Plasmon guided assembly of nanoparticles in solids. Materials Today Nano 21, 100299, https://doi.org/10.1016/j.mtnano.2022.100299.
137. Shimotsuma Y, Hirao K, Qiu J, Kazansky PG. Nano-modification inside transparent materials by femtosecond laser single beam. Mod Phys Lett B. 2005;19:225–38. https://doi.org/10.1142/S0217984905008281.
138. Rudenko A, Colombier J-P, Itina TE. From random inhomogeneities to periodic nanostructures induced in bulk silica by ultrashort laser. Physical Review B. 2016;93:075427. https://doi.org/10.1103/PhysRevB.93.075427.
139. Rudenko A, Colombier J-P, Itina TE, Stoian R. Genesis of Nanogratings in Silica Bulk via Multipulse Interplay of Ultrafast Photo-Excitation and Hydrodynamics. Adv Opt Mater. 2021;9:2100973. https://doi.org/10.1002/adom.202100973.

140. Muzi E, Cavillon M, Lancry M, Brisset F, Que R, Pugliese D, et al. Towards a Rationalization of Ultrafast Laser-Induced Crystallization in Lithium Niobium Borosilicate Glasses: The Key Role of the Scanning Speed. Crystals. 2021;11(3):290. https://doi.org/10.3390/cryst11030290.
141. Bhardwaj VR, et al. Optically Produced Arrays of Planar Nanostructures inside Fused Silica. Phys Rev Lett. 2006;96:057404. https://doi.org/10.1103/PhysRevLett.96.057404.
142. Rajeev PP, et al. Transient nanoplasmonics inside dielectrics. J Phys B: At Mol Opt Phys. 2007;40:S273–82. https://doi.org/10.1088/0953-4075/40/11/s03.
143. Sun H, et al. Standing electron plasma wave mechanism of void array formation inside glass by femtosecond laser irradiation. Appl Phys A. 2007;88:285–8. https://doi.org/10.1007/s00339-007-4012-y.
144. Liao Y, et al. Formation of in-volume nanogratings with sub-100-nm periods in glass by femtosecond laser irradiation. Opt Lett. 2015;40:3623–6. https://doi.org/10.1364/OL.40.003623.
145. Lei Y, et al. High speed ultrafast laser anisotropic nanostructuring by energy deposition control via near-field enhancement. Optica. 2021;8:1365–71. https://doi.org/10.1364/OPTICA.433765.
146. Yan Z, Gao J, Beresna M, Zhang J. Near-Field Mediated 40 nm In-Volume Glass Fabrication by Femtosecond Laser. Adv Opt Mater. 2022;10:2101676. https://doi.org/10.1002/adom.202101676.
147. Martin P, et al. Subpicosecond study of carrier trapping dynamics in wide-band-gap crystals. Phys Rev B. 1997;55:5799–810. https://doi.org/10.1103/PhysRevB.55.5799.
148. Petite G, Daguzan P, Guizard S, Martin P. Conduction electrons in wide-bandgap oxides: a subpicosecond time-resolved optical study. Nucl Instrum Methods Phys Res, Sect B. 1996;107:97–101. https://doi.org/10.1016/0168-583X(95)00845-4.
149. Richter S, et al. The role of self-trapped excitons and defects in the formation of nanogratings in fused silica. Opt Lett. 2012;37:482–4. https://doi.org/10.1364/OL.37.000482.
150. Dai Y, Wu G, Lin X, Ma G, Qiu J. Femtosecond laser induced rotated 3D self-organized nanograting in fused silica. Opt Express. 2012;20:18072–8. https://doi.org/10.1364/OE.20.018072.
151. Lei Y, et al. Efficient ultrafast laser writing with elliptical polarization. Light. 2023;12:74. https://doi.org/10.1038/s41377-023-01098-2.
152. Gaizauskas E, et al. Discrete damage traces from filamentation of Gauss-Bessel pulses. Opt Lett. 2006;31:80–2. https://doi.org/10.1364/OL.31.000080.
153. Bricchi E, Mills JD, Kazansky PG, Klappauf BG, Baumberg JJ. Birefringent Fresnel zone plates in silica fabricated by femtosecond laser machining. Opt Lett. 2002;27:2200–2. https://doi.org/10.1364/OL.27.002200.
154. Tian J, et al. A Comparison between Nanogratings-Based and Stress-Engineered Waveplates Written by Femtosecond Laser in Silica. Micromachines. 2020;11, https://doi.org/10.3390/mi11020131
155. Ohfuchi T, et al. Polarization imaging camera with a waveplate array fabricated with a femtosecond laser inside silica glass. Opt Express. 2017;25:23738–54. https://doi.org/10.1364/OE.25.023738.
156. Lammers K, et al. Embedded nanograting-based waveplates for polarization control in integrated photonic circuits. Opt Mater Express. 2019;9:2560–72. https://doi.org/10.1364/OME.9.002560.
157. Beresna M, Kazansky PG. Polarization diffraction grating produced by femtosecond laser nanostructuring in glass. Opt Lett. 2010;35:1662–4. https://doi.org/10.1364/OL.35.001662.
158. Cai W, Libertun AR, Piestun R. Polarization selective computer-generated holograms realized in glass by femtosecond laser induced nanogratings. Opt Express. 2006;14:3785–91. https://doi.org/10.1364/OE.14.003785.
159. Zhang F, Yu Y, Cheng C, Dai Y, Qiu J. Fabrication of polarization-dependent light attenuator in fused silica using a low-repetition-rate femtosecond laser. Opt Lett. 2013;38:2212–4. https://doi.org/10.1364/OL.38.002212.
160. Zhang F, et al. Wavelength response and thermal stability of embedded nanograting structure light attenuator fabricated by direct femtosecond laser writing. Appl Phys B. 2014;117:53–8. https://doi.org/10.1007/s00340-014-5797-y.
161. Cavillon M, et al. Overview of high temperature fibre Bragg gratings and potential improvement using highly doped aluminosilicate glass optical fibres. J Phys. 2019;1:042001. https://doi.org/10.1088/2515-7647/ab382f.
162. Mihailov SJ, Hnatovsky C, Grobnic D, Chen K, Li M. Fabrication of Bragg Gratings in Random Air-Line Clad Microstructured Optical Fiber. IEEE Photonics Technol Lett. 2018;30:209–12. https://doi.org/10.1109/LPT.2017.2782368.
163. Hnatovsky C, Grobnic D, Coulas D, Barnes M, Mihailov SJ. Self-organized nanostructure formation during femtosecond-laser inscription of fiber Bragg gratings. Opt Lett. 2017;42:399–402. https://doi.org/10.1364/OL.42.000399.
164. Li J, Ho S, Haque M, Herman PR. Nanograting Bragg responses of femtosecond laser written optical waveguides in fused silica glass. Opt Mater Express. 2012;2:1562–70. https://doi.org/10.1364/OME.2.001562.
165. Beresna M, Gecevičius M, Kazansky PG, Gertus T. Radially polarized optical vortex converter created by femtosecond laser nanostructuring of glass. Appl Phys Lett. 2011;98:201101. https://doi.org/10.1063/1.3590716.
166. Zhang F, Cerkauskaite A, Drevinskas R, Kazansky PG, Qiu J. Microengineering of Optical Properties of GeO2 Glass by Ultrafast Laser Nanostructuring. Adv Opt Mater. 2017;5:1700342. https://doi.org/10.1002/adom.201700342.
167. Beresna M, Gecevičius M, Kazansky PG. Polarization sensitive elements fabricated by femtosecond laser nanostructuring of glass [Invited]. Opt Mater Express. 2011;1:783–95. https://doi.org/10.1364/OME.1.000783.
168. Zhang B, Liu X, Qiu J. Single femtosecond laser beam induced nanogratings in transparent media - Mechanisms and applications. J Materiomics. 2019;5:1–14. https://doi.org/10.1016/j.jmat.2019.01.002.
169. Lu J, et al. Fiber nanogratings induced by femtosecond pulse laser direct writing for in-line polarizer. Nanoscale. 2019;11:908–14. https://doi.org/10.1039/C8NR06078A.
170. He J, Xu B, Xu X, Liao C, Wang Y. Review of Femtosecond-Laser-Inscribed Fiber Bragg Gratings: Fabrication Technologies and Sensing Applications. Photonic Sens. 2021;11:203–26. https://doi.org/10.1007/s13320-021-0629-2.
171. Pallarés-Aldeiturriaga, D., Roldán-Varona, P., Rodríguez-Cobo, L. López-Higuera, J. M. (2020).Optical Fiber Sensors by Direct Laser Processing: A Review. Sensors 20, https://doi.org/10.3390/s20236971
172. Wang M, et al. Femtosecond laser fabrication of nanograting-based distributed fiber sensors for extreme environmental applications. Int J Extreme Manuf. 2021;3:025401. https://doi.org/10.1088/2631-7990/abe171.
173. Kaisler S, Armour F, Espinosa JA. Money, W. in 2013 46th Hawaii International Conference on System Sciences. 995–1004.
174. Gu M, Zhang Q, Lamon S. Nanomaterials for optical data storage. Nat Rev Mater. 2016;1:16070. https://doi.org/10.1038/natrevmats.2016.70.

175. Zhang Q, Xia Z, Cheng Y-B, Gu M. High-capacity optical long data memory based on enhanced Young's modulus in nanoplasmonic hybrid glass composites. Nat Commun. 2018;9:1183. https://doi.org/10.1038/s41467-018-03589-y.
176. Gu M, Li X, Cao Y. Optical storage arrays: a perspective for future big data storage. Light. 2014;3:e177–e177. https://doi.org/10.1038/lsa.2014.58.
177. Zhu L, et al. Near-perfect fidelity polarization-encoded multilayer optical data storage based on aligned gold nanorods. Opto-Electronic Advances. 2021;4:210002. https://doi.org/10.29026/oea.2021.210002.
178. Wang Z, Zhang B, Tan D, Qiu J. Ostensibly perpetual optical data storage in glass with ultra-high stability and tailored photoluminescence. Opto-Electronic Advances. 2023;6, 220008–220001–220008–220008, https://doi.org/10.29026/oea.2023.220008
179. Shimotsuma Y, et al. Ultrafast Manipulation of Self-Assembled Form Birefringence in Glass. Adv Mater. 2010;22:4039–43. https://doi.org/10.1002/adma.201000921.
180. Zhang J, Gecevičius M, Beresna M, Kazansky PG. Seemingly Unlimited Lifetime Data Storage in Nanostructured Glass. Phys Rev Lett. 2014;112:033901. https://doi.org/10.1103/PhysRevLett.112.033901.
181. Yan Z, et al. Anisotropic nanostructure generated by a spatial-temporal manipulated picosecond pulse for multidimensional optical data storage. Opt Lett. 2021;46:5485–8. https://doi.org/10.1364/OL.443370.
182. Wang H, et al. 100-Layer Error-Free 5D Optical Data Storage by Ultrafast Laser Nanostructuring in Glass. Laser & Photonics Reviews 2022;n/a, 2100563, https://doi.org/10.1002/lpor.202100563
183. Liao Y, et al. Femtosecond laser nanostructuring in porous glass with sub-50 nm feature sizes. Opt Lett. 2013;38:187–9. https://doi.org/10.1364/OL.38.000187.
184. Liao Y, et al. Direct laser writing of sub-50 nm nanofluidic channels buried in glass for three-dimensional micro-nanofluidic integration. Lab Chip. 2013;13:1626–31. https://doi.org/10.1039/C3LC41171K.
185. Haque M, Lee KKC, Ho S, Fernandes LA, Herman PR. Chemical-assisted femtosecond laser writing of lab-in-fibers. Lab Chip. 2014;14:3817–29. https://doi.org/10.1039/C4LC00648H.
186. Ródenas A, et al. Three-dimensional femtosecond laser nanolithography of crystals. Nat Photonics. 2019;13:105–9. https://doi.org/10.1038/s41566-018-0327-9.
187. Sima F, et al. Three-dimensional femtosecond laser processing for lab-on-a-chip applications. 7, 613-634, doi:https://doi.org/10.1515/nanoph-2017-0097 (2018).
188. Osellame R, Hoekstra HJWM, Cerullo G, Pollnau M. Femtosecond laser microstructuring: an enabling tool for optofluidic lab-on-chips. Laser Photonics Rev. 2011;5:442–63. https://doi.org/10.1002/lpor.201000031.
189. Marcinkevičius A, et al. Femtosecond laser-assisted three-dimensional microfabrication in silica. Opt Lett. 2001;26:277–9. https://doi.org/10.1364/OL.26.000277.
190. Qi J, et al. Femtosecond laser induced selective etching in fused silica: optimization of the inscription conditions with a high-repetition-rate laser source. Opt Express. 2018;26:29669–78. https://doi.org/10.1364/OE.26.029669.
191. Yu X, et al. Tuning etch selectivity of fused silica irradiated by femtosecond laser pulses by controlling polarization of the writing pulses. J Appl Phys. 2011;109:053114. https://doi.org/10.1063/1.3555080.
192. Lu J, et al. Tailoring chiral optical properties by femtosecond laser direct writing in silica. Light. 2023;12:46. https://doi.org/10.1038/s41377-023-01080-y.
193. Ashoka A, et al. Extracting quantitative dielectric properties from pump-probe spectroscopy. Nat Commun. 2022;13:1437. https://doi.org/10.1038/s41467-022-29112-y.
194. Yao Y, et al. Single-Shot Real-Time Ultrafast Imaging of Femtosecond Laser Fabrication. ACS Photonics. 2021;8:738–44. https://doi.org/10.1021/acsphotonics.1c00043.
195. Yang C, et al. Single-Shot Receive-Only Ultrafast Electro-Optical Deflection Imaging. Phys Rev Appl. 2020;13:024001. https://doi.org/10.1103/PhysRevApplied.13.024001.
196. Lamon S, Wu Y, Zhang Q, Liu X, Gu M. Nanoscale optical writing through upconversion resonance energy transfer. Science Advances 7, eabe2209, https://doi.org/10.1126/sciadv.abe2209.
197. Salter PS, Booth MJ. Adaptive optics in laser processing. Light. 2019;8:110. https://doi.org/10.1038/s41377-019-0215-1.
198. Wang H, et al. Two-Photon Polymerization Lithography for Optics and Photonics: Fundamentals, Materials, Technologies, and Applications. Advanced Functional Materials. 2023; n/a, 2214211, https://doi.org/10.1002/adfm.202214211
199. Malevich P, et al. High energy and average power femtosecond laser for driving mid-infrared optical parametric amplifiers. Opt Lett. 2013;38:2746–9. https://doi.org/10.1364/OL.38.002746.
200. Fang X, Ren H, Gu M. Orbital angular momentum holography for high-security encryption. Nat Photonics. 2020;14:102–8. https://doi.org/10.1038/s41566-019-0560-x.
201. Xinyuan F, et al. High-dimensional orbital angular momentum multiplexing nonlinear holography. Adv Photonics. 2021;3:1–7. https://doi.org/10.1117/1.AP.3.1.015001.
202. Bozinovic N, et al. Terabit-Scale Orbital Angular Momentum Mode Division Multiplexing in Fibers. Science. 2013;340:1545–8. https://doi.org/10.1126/science.1237861.

Publisher's Note